Sensorless Control of Permanent Magnet Synchronous Machines

Sigurd Øvrebø

Norwegian University of Science and Technology
Faculty of Information Technology, Mathematics and Electrical Engineering

Department of Electrical Power Engineering

December - 2004

Printed format: ISBN 82-471-6523-6

Electronic format: ISBN 82-471-6522-8
(With corrcections)
2004:147

ABSTRACT

As the cost for permanent magnets are decreasing and the quality of the magnets are increasing the Permanent Magnet Synchronous Machine (PMSM) are becoming more popular. The PMSM is superior to induction machines both in torque per kilograms and efficiency. Typical applications for these machines are applications where machine volume or efficiency is important. In order to control a PMSM the rotor position needs to be known. This can be obtained by usage of sensor or by usage of a sensorless control scheme. Sensorless Control schemes typically divide into two categories; schemes that give good controllability from 2-5 Hz and schemes that gives good controllability at all speeds including zero speed. The focus for this thesis is sensorless control schemes with good controllability at low and zero speeds. Sensorless control is a multi physics challenge where the machine, inverter and control scheme are equally important for the quality of the drive system. In order to describe the saliency in the machine a new saliency machine model is developed in this thesis. The model includes yoke saturation, teeth saturation and induced currents in magnets. In injection based sensorless control the high frequency flux distribution in the machine is of great interest. In this thesis the frequency dependency in inductance is estimated in two machines by using injection of test signals in a large frequency range. Based on the measurements and the new saliency model the high frequency flux distribution is estimated and the frequency dependency of the saliency is described. A variety of different sensorless schemes are published over the last two decades. As the publications uses different test criteria it is challenging to determine the characteristics for the different schemes: three different control schemes are evaluated in terms of determining the scheme characteristics. A new scheme based on [1, 7] is presented in this thesis. The new scheme enables integration of transient excitation and position estimation in every switching period. The continuous injection based schemes evaluated in this work is rotating high frequency carrier injection [2,13,39] and pulsating high frequency carrier injection [3,26]. The different schemes sensitivity to the inverter non linearity is modelled and evaluated. A comparison of the three schemes is presented. Surface mounted PMSM typically has a small saliency. The saliency in a surface mounted PMSM can be increased in several ways. The last part of this thesis presents a redesign approach for an axial flux PMSM. Several approaches are evaluated in terms of synergy effects with the machine cost and performance. An approach based on insertion of semi-magnetic slot wedges are realised in a prototype.

ACKNOWLEDGMENTS

This thesis is not a result of a one person effort but rather the sum of the effort from the author and all the persons I have met and discussed with during the last five years. At first I want to thank Professor Roy Nilsen at the Department of Electrical Power Engineering for convincing me to start with the Dr.Ing studies and for being my supervisor. He's industrial background and expertise has been very important for my work. Secondly I want to thank Professor Robert Nilsen for his contributions during numerous discussions on machine design and FEM simulations. Also I want to thank all the colleagues and fellow students at the department. In particular I want to thank Richard Lund for always being a good colleague, discussion partner and friend.

During my Master studies and Dr.Ing studies I have had the pleasure of spending two periods with the WEMPEC group at The University of Wisconsin Madison. I want to thank Professor R.D. Lorenz for being a great inspiration for my interest for sensorless control and the WEMPEC group for the great hospitality. Special thanks to Michael Harke for being a good friend and helping out in all possible ways.

Some industrial contributors also have to be mentioned: SmartMotor AS contributed with software/hardware and personnel for discussions on machine design and control. A special thanks to Ulf Aaknes for believing in my work. Surehamar and Høganes contributed with detailed information on laminations and iron powder material. Comsol contributed with guidance with FEMLab. Clawmai electronics delivered semi magnetic slot wedges.

The person that deserves the most thanks is my friend and wife to be, Kirsti Hammer. Unfortunately she had to listen to all my complains during times of trouble, but she would still comfort me and encourage me to go on with the work. Our two children Ida(4) and Isak(1) have given me a better perspective of life. At last I need to thank my close family: my parents and my brother have always encouraged me to pursue my dreams and believe in myself.

TABLE OF CONTENTS

INTRODUCTION

Sensorless control of electric machines has been a research topic for more than two decades. The objective for this work is to eliminate the need for a position sensor by using the machine as the position sensor. The position sensor and cable connection has been a source of failure for motor control applications. For small drives the sensor contributes considerable to the overall cost. Sensorless control is divided into two speed regions; a high speed region and a low speed region. In the high speed region the back EMF can be used for the rotor position estimate. In the low and zero speed region the back EMF becomes too small for position estimation. In this region second order effects in the machine can be utilized in order to make a position estimate. Induction machines have been the main focus for the research in this field [1, 2, 13, 21, 22, 28, 35]. Research on sensorless control of PMSM has been going on simultaneously [1, 3, 26, 39]. In later years Permanent Magnet Synchronous Machines has been increasingly popular as the cost of permanent magnets is decreasing and the quality of the magnets improves. The activity on sensorless control of PMSM has increased as the application ranges of the PMSM are expanding.

Project overview

There are a variety of different schemes and patents within the field of sensorless control. The test conditions differs from author to author and it is difficult to determine what the characteristics of each scheme really are. Part of this project was focused on determining the characteristics of the different schemes. In order to limit the number of schemes a selection of schemes was made upon the following system criteria:

- High or medium bandwidth estimation capability
- Two current sensors
- Measurement of DC bus voltage
- Varying load inertia

From these criteria the following schemes where selected: Rotating High Frequency Carrier Injection (HFCI-R) [2, 13, 39], Pulsating High Frequency Carrier Injection (HFCI-P) [3, 26] and Transient based excitation (TE) [1, 7]. In order to make a direct comparison the Transient based Excitation scheme was modified to a new scheme where the position could be estimated in every switching period. The methods where evaluated on a PMSM with interior magnets (IPMSM).

A surface mounted PMSM have typically very little saliency. If machine design are to be used in order to cerate more saliency in the machine, increased understanding of the mechanisms of saliency are needed. Part of this project has been focused on modelling the mechanisms of saliency for PMSM's. A prototype axial flux PMSM was tested in the initial work. There where no detectable saliency in the machine when the applied test signal had frequency larger than 125 Hz. Part of this project has been evaluating redesign approaches in order to increase the saliency ratio for the axial flux machine.

Contributions

Most of the detailed work done on sensorless control has been focusing on induction machine control. There are several large differences in the machine structure and control strategy for Permanent Magnet Synchronous Machines (PMSM). In this thesis the main components in the drive system is analysed in order to increase the understanding of the system. The main contributions from this work are:

- Detailed Single Saliency Modelling for Radial- and Axial PMSM
- Analyses and measurements of the frequency dependency of saliency in radial and axial PMSM
- Development of a new sensorless scheme based on transient excitation.
- Implementation, test and comparison of three of the most promising excitation methods for sensorless control.
- Detailed description of inverter non linearity impact on the different sensorless schemes
- Sensorless control aspects integrated in the machine design process for an axial flux PMSM

Overview of Chapters

Chapter 1 describes the standard machine equations for radial flux PMSM and a more detailed description of modelling for an axial flux PMSM.

Chapter 2 gives a brief overview of the most common sensorless control methods. The back EMF based methods are presented first in order to see their limitations and their ability to include low and zero speed techniques. Then a brief overview of the state of the art low and zero speed sensorless control methods are given.

Chapter 3 presents a new modelling approach for single saliency PMSM's. The main idea is to model the main and leakage inductance separate in a dq-oriented system. The spatial variation in the main and leakage inductance are 90 electrical degrees apart. These variations are represented in a machine model that incorporates rotor saliency and saturated induced saliency from the permanent magnet and the load current. The

saliency modelling can be used as a tool when increased saliency ratio is wanted by use of machine design.

Chapter 4 describes the frequency dependency of the saliency. As the frequency of the injected signal increase there will be skin effects in the stator conductors and the machine laminations. These mechanisms are described and measurements with carrier frequency from 100 to 8100 Hz are presented for the IPMSM. In addition the IPMSM was tested with transient excitation (20 kHz equivalent). The saliency ratio for the axial flux PMSM is tested with carrier frequency from 125 to 500 Hz.

Chapter 5 describes the experimental set up. The main focus in this chapter is the inverter and the dead time introduced in order to prevent cross-conduction in the inverter legs. The dead time effect was one of the major disturbances to all the schemes evaluated. A brief description of the experimental work strategy is given at the end of the chapter.

Chapter 6 describes the scheme based on rotating high frequency carrier injection (HFCI-R). In the first section the basics of the scheme are presented. The observer structure used for all the schemes is described. A simple decoupling technique is suggested in order to remove the dead time effects. In the final part of the chapter the experimental work with the HFCI-R scheme is presented.

Chapter 7 describes the scheme based on pulsating injection of high frequency carrier injection (HFCI-P). In the first section the basics of the scheme is presented. Usage of a synchronous frame filter is suggested for the HFCI-P scheme in order to allow higher current regulator bandwidth. In the final part the experimental work done on the HFCI-P scheme is presented.

Chapter 8 describes a new scheme based on transient excitation (TE). The scheme is based on [1, 7] and a position estimate is generated in every switching period. A modified scheme applies the transient excitation in intervals in order to evaluate the performance with lower switching losses. In the final part of the chapter the experimental work with the TE scheme is presented.

Chapter 9 contains an evaluation of the implemented methods. A detailed analysis of the dead time effects is presented.

Chapter 10 describes saliency ratio enhancement by machine design. In the first section the state of the art redesign for sensorless control are presented. Then a design example is given for an axial flux machine. A new prototype is built and tested.

Chapter 11 gives a summary of the main conclusions and suggestions for future work.

NOMENCLATURE

Symbol	definition
s	integral operator
i_{sa}^{S}	phase current in a-phase
i_{sb}^{S}	phase current in b-phase
i_{sc}^{S}	phase current in c-phase
$\underline{i}_{s}^{s}$	stator current in stationary reference frame
$i_{s\alpha}^{s}$	alpha component of stator current, stationary reference frame
$i_{s\beta}^{s}$	beta component of stator current, stationary reference frame
$\underline{i}_{s}^{r}$	stator current in rotor reference frame (dq-frame)
i_{q}	q-axis component of the stator current, rotor reference frame (dq-frame)
i_{d}	d-axis component of the stator current, rotor reference frame (dq-frame)
$\underline{i}_{s\_c}^{s}$	carrier signal component of the stator current, stationary ref frame
$\underline{i}_{s\_cp}^{s}$	carrier signal component of the stator current due to the positive sequence carrier signal voltage
$\underline{i}_{s\_cn}^{s}$	carrier signal component of the stator current due to the negative sequence carrier signal voltage
$I_{s\_cn}^{s}$	magnitude of the positive sequence component of the carrier signal current
$I_{s\_cn}^{s}$	magnitude of the negative sequence component of the carrier signal current magnitude
$\underline{u}_{s}^{s}$	stator voltage, stationary reference frame

$u^s_{s\alpha}$	stator voltage, alpha component, stationary ref. frame
$u^s_{s\beta}$	stator voltage, beta component, stationary ref. frame
$\underline{u}^r_s$	stator voltage, rotor reference frame
u_d	stator voltage, direct component, rotor ref. frame
u_q	stator voltage, quadrature component, rotor ref. frame
$\underline{u}^s_{s\_c}$	carrier signal component of the stator voltage
$u^s_{s\alpha\_c}$	alpha component of carrier signal
$u^s_{s\beta\_c}$	beta component of carrier signal
$U^s_{s\_c}$	carrier signal voltage magnitude
$\underline{\psi}_s$	stator flux linkage
ψ_m	permanent magnet flux linkage
θ_c	carrier signal angle
θ	rotor position (electrical degrees)
ω	rotor angular speed (radians per seconds-referred electrical)
ω_n	rated rotor angular speed
ω_c	carrier angular speed
θ_{mek}	rotor position - mechanical
Ω_{mek}	rotor angular speed - mechanical
ε	error signal
r_s	stator resistance
L_s	stator self inductance
L_{s0}	average stator self inductance minus leakage inductance
$L_{s\sigma}$	stator leakage inductance
L_g	stator mutual inductance (position dependent)
L_{ab}	stator mutual inductance between a and b phase
$\sum L$	average stator inductance

ΔL	differential stator inductance

Inductance terms from Saliency modelling

L_0	average main inductance with no magnets or saturation in the machine
L_{0rd}	rotor design saliency in main inductance (including relative permeability and induced currents in magnets)
L_{0ts}	stator teeth saturation (main flux path)
L_{0ys}	stator yoke saturation (main flux path)
L_σ	average leakage inductance
$L_{\sigma ts}$	variation in leakage inductance due to stator teeth saturation
$L_{\sigma ys}$	variation in leakage inductance due to yoke saturation
L_{lds}	load dependent saturation
L_{0cs}	influence on main inductance from core saturation when core is in the d- axis
L_{0lcs}	influence on main inductance from local core saturation when core is in q- axis
$L_{\sigma cs}$	influence on leakage inductance from core saturation when core is in the d- axis
$L_{\sigma lcs}$	influence on leakage inductance from local core saturation when core is in q-axis

Superscripts	definition
^	estimated quantity
*	commanded or reference quantity
s	(lower case) stationary reference frame quantity, two axis
S	(upper case) stationary reference frame quantity, three axis
r	rotor position synchronous reference frame quantity
k	general synchronous reference frame

1 MACHINE MODELLING

In order to discuss the different aspects of sensorless control a basic understanding of the machine equations are needed. This chapter describes the machine equations for Permanent Magnet Synchronous Machines (PMSM). In the first section the equations for an Interior Permanent Magnet Synchronous Machine (IPMSM) is derived. In the second section the equations for a double air gap axial flux PMSM is derived.

1.1 Radial flux machine model

This chapter describes the basic machine equations for the permanent magnet machines (PMSM). The derivations are based on basic machine theory from [8-11]. First part describes the standard equations for a radial flux permanent magnet machine with interior magnets (IPMSM). Second part will cover the equations for an axial flux PMSM with surface mounted magnets. Some simplifications are used to derive the equations for the IPMSM:

- Magnetic saturation in the iron is not considered
- The permanent magnet material is assumed to have linear, temperature independent demagnetizing curve.
- The flux from the magnets and the windings are assumed sinusoidal distributed over the air gap. The distributed windings are simplified by representing them as one concentrated winding.
- Iron losses (hysteresis and eddy current losses) are neglected.
- Resistance and inductance are assumed independent of temperature and frequency, thus skin effects are neglected.
- The three phase stator windings are assumed to be y- connected, thus no zero sequence currents can appear (and no zero sequence flux is assumed).

1.1.1 Radial flux IPMSM machine equations

The radial flux IPMSM has a designed saliency in the rotor due to the different permeability in iron and permanent magnet. The d and q-axis inductance will be different; in Figure 1.1.1 and Figure 1.1.2 the d-axis inductance will be smaller than the q-axis inductance. This is due to the magnet permeability is close to unity and the iron permeability is typical three decades bigger.

In this sub chapter the design in Figure 1.1.1 and Figure 1.1.2 will be used for the derivations. The inductance in each phase can be described in two parts; one due to self-inductance and one due to mutual inductance. The self-inductance has three terms:

$$L_a(\theta) = L_{s\sigma} + L_{s0} + L_g \cos(2\theta) \tag{1.1}$$

$$L_b(\theta) = L_{s\sigma} + L_{s0} + L_g \cos(2\theta + 120) \tag{1.2}$$

$$L_c(\theta) = L_{s\sigma} + L_{s0} + L_g \cos(2\theta - 120) \tag{1.3}$$

$L_{s\sigma}$ - Leakage inductance

L_{s0} - Average inductance minus the leakage inductance

L_g - Amplitude of the sinus varying part

The mutual inductance has two terms; one constant term and one sinus varying;

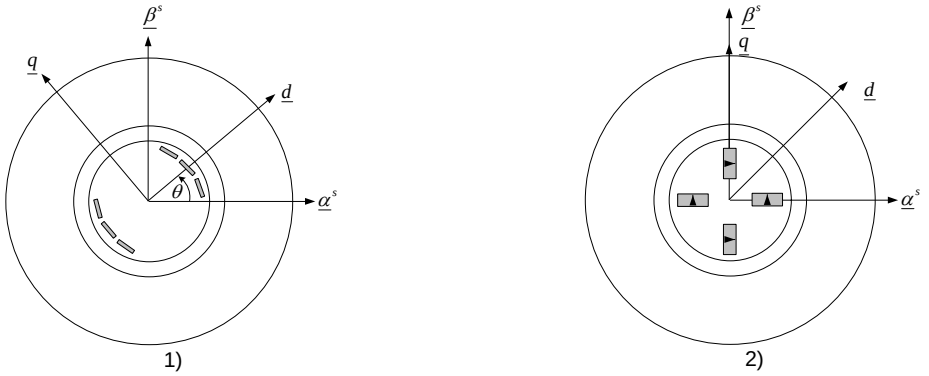

Figure 1.1 IPMSM basic designs

$$L_{ab}(\theta) = L_{ba}(\theta) = -\frac{1}{2}L_{s0} + L_g \cos(2\theta - 120) \tag{1.4}$$

$$L_{bc}(\theta) = L_{cb}(\theta) = -\frac{1}{2}L_{s0} + L_g \cos(2\theta) \tag{1.5}$$

$$L_{ac}(\theta) = L_{ca}(\theta) = -\frac{1}{2}L_{s0} + L_g \cos(2\theta - 240) \tag{1.6}$$

For the PMSM in Figure 1.1.1 L_g becomes negative. For all three phases we get an inductance matrix;

$$\underline{L}_s^S = \begin{bmatrix} L_a(\theta) & L_{ab}(\theta) & L_{ac}(\theta) \\ L_{ba}(\theta) & L_b(\theta) & L_{bc}(\theta) \\ L_{ca}(\theta) & L_{cb}(\theta) & L_c(\theta) \end{bmatrix} \tag{1.7}$$

The voltage equation in the tree phase system becomes:

$$\underline{U}_s^S = \underline{I}_s^S R_s + \frac{d\underline{\Psi}_s^S}{dt} \tag{1.8}$$

Where:

$$\underline{\Psi}_s^S = \underline{L}_s^S \cdot \underline{I}_s^S + \underline{\Psi}_m^S \tag{1.9}$$

The equations can be represented in a two axis model in different reference frames. The transformation (and the transformation matrixes) of the three phase representation to the two axis model is given in Appendix A. The inductance matrix becomes:

$$\underline{L}_s^r = \begin{bmatrix} L_{s\sigma} + \frac{3}{2}(L_{s0} + L_g) & 0 \\ 0 & L_{s\sigma} + \frac{3}{2}(L_{s0} - L_g) \end{bmatrix} = \begin{bmatrix} L_d & 0 \\ 0 & L_q \end{bmatrix} \tag{1.10}$$

The dq-inductances are expressed as:

$$\mathrm{L_d} = \mathrm{L_{s\sigma}} + \frac{3}{2}(\mathrm{L_{s0}} + \mathrm{L_g}) \tag{1.11}$$

$$\mathrm{L_q} = \mathrm{L_{s\sigma}} + \frac{3}{2}(\mathrm{L_{s0}} - \mathrm{L_g}) \tag{1.12}$$

If these inductances are used to describe the inductance matrix in the stator stationary reference frame the simplified expression becomes:

$$\underline{L}_s^s = \begin{bmatrix} \sum L - \Delta L\cos(2\theta) & \Delta L\sin(2\theta) \\ \Delta L\sin(2\theta) & \sum L + \Delta L\cos(2\theta) \end{bmatrix} \tag{1.13}$$

Where the average and difference inductance are defined as:

$$\sum \mathrm{L} = \frac{\mathrm{L_d} + \mathrm{L_q}}{2} = \mathrm{L_{s\sigma}} + \frac{3}{2}\mathrm{L_{s0}} \tag{1.14}$$

$$\Delta \mathrm{L} = \frac{\mathrm{L_d} - \mathrm{L_q}}{2} = \frac{3}{2}\mathrm{L_g} \tag{1.15}$$

The voltage equations in synchronous frame fixed to rotor are:

$$\underline{U}_s^r = \underline{I}_s^r R_s + \frac{d\underline{\Psi}_s^r}{dt} + j\omega\Psi_s^r \tag{1.16}$$

$$\underline{\Psi}_s^r = \underline{L}_s^r \underline{I}_s^r + \underline{\Psi}_m^r \tag{1.17}$$

The voltage equations in stationary reference frame:

$$\underline{U}_s^s = \underline{I}_s^s R_s + \frac{d\underline{\Psi}_s^s}{dt} \tag{1.18}$$

$$\underline{\Psi}_s^s = \underline{L}_s^s \underline{I}_s^s + \underline{\Psi}_m^s \tag{1.19}$$

The electromagnetic torque produced in the machine can be expressed as:

$$M_e = \frac{3}{2} p(\Psi_d I_q - \Psi_q I_d) = \frac{3}{2} p(\Psi_m I_q - (L_q - L_d) I_d I_q) \tag{1.20}$$

Where p represent the pole pairs in the machine. The relation between torque and acceleration can be expressed as:

$$J \cdot \frac{d\Omega_{mek}}{dt} = M_e - M_L \tag{1.21}$$

The relation between mechanical and electrical angular speed and angle is:

$$\omega = p \cdot \Omega_{mek} \tag{1.22}$$

$$\theta = p \cdot \theta_{mek} \tag{1.23}$$

1.1.2 Scaled model

The basis values for the scaled model are the amplitude values from the rated phase quantities.

$$U_{base} = \sqrt{2}U_{f,n} = \sqrt{\frac{2}{3}}U_n \tag{1.24}$$

$$I_{base} = \sqrt{2}I_{f,n} = \sqrt{2}I_n \tag{1.25}$$

The rated speed is the basis for the angular velocity;

$$\omega_{base} = 2\pi f_n \tag{1.26}$$

The rest of the basis values are derived from the first three;

$$\Psi_{base} = \frac{U_{base}}{\omega_n} \tag{1.27}$$

$$S_{base} = \frac{3}{2}U_{base}I_{base} \tag{1.28}$$

$$\Omega_{base} = \frac{\omega_n}{p} \tag{1.29}$$

$$M_{base} = \frac{S_{base}}{\Omega_{base}} \tag{1.30}$$

$$Z_{base} = \frac{U_{base}}{I_{base}} \tag{1.31}$$

$$L_{base} = \frac{\Psi_{base}}{I_{base}} = \frac{U_{base}}{\omega_n I_{base}} \tag{1.32}$$

Substituting these reference values into (1.16) gives;

$$u_d = r_s i_d + \frac{1}{\omega_n}\frac{d\psi_d}{dt} - n\psi_q \tag{1.33}$$

$$u_q = r_s i_q + \frac{1}{\omega_n}\frac{d\psi_q}{dt} + n\psi_d \tag{1.34}$$

And the flux linkages becomes;

$$\psi_d = x_d i_d + \psi_m \tag{1.35}$$

$$\psi_q = x_q i_q \tag{1.36}$$

and

$$x_d = \frac{\omega_n L_d}{Z_{base}} = \frac{(L_{s\sigma} + \frac{3}{2}(L_{s0} + L_g))\omega_n I_{base}}{U_{base}} \tag{1.37}$$

$$x_q = \frac{\omega_n L_q}{Z_{base}} = \frac{(L_{s\sigma} + \frac{3}{2}(L_{s0} - L_g))\omega_n I_{base}}{U_{base}} \tag{1.38}$$

The mechanical equations can be expressed as:

$$m_e = \psi_m \cdot i_q - (x_q - x_d) \cdot i_d \cdot i_q \tag{1.39}$$

$$T_m \frac{dn}{dt} = m_e - m_L \tag{1.40}$$

$$\frac{d\theta}{dt} = \omega_n \cdot n \tag{1.41}$$

$$T_m = \frac{J \cdot \Omega_{mek,n}^2}{S_n} \tag{1.42}$$

1.2 Axial flux machine model

There are a variety of different axial flux machines. Some machines are “toroide wound” as in [42], some are realized without iron core, and some are wound on separate iron cores or as for the toroide wound on a common iron core. In this chapter the axial flux machine is a prototype Machine from SmartMotor AS. The machine realized with concentrated iron powder cores and two air gaps. The derivations will be made on a general machine with the same characteristics. In Figure 1.2.1 principal view of the machine is presented. Figure 1.2.1 shows the stator where the grey areas represent the iron powder cores and the yellow areas represents the windings. Figure 1.2.2 represents the rotor, the blue segments are the permanent magnets that are mounted on a iron disk that forms the rotor yoke. Figure 1.2.3 shows the assembled machine. The wires to the stator is fed trough the shaft.

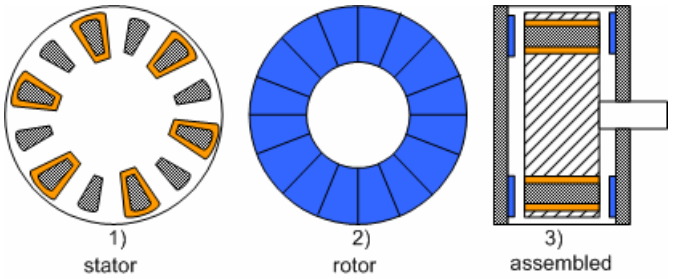

Figure 1.2 Principal view of the axial flux machine

1.2.1 Machine model

In the derivation of a machine model for the axial flux PMSM we include one position dependent term due to saturation in the yoke between the magnets. This is merely done to illustrate how position dependencies in the coils are modelled as one winding. There is several other saturation effects that may introduce position dependent inductance, these effects are discussed in detail in Chapter 3. In Figure 1.3 the saturation in the yoke is represented by the red areas between the permanent magnets. The coupling between the coils is very small in this type of machines. This is mainly due to the structure with every second core has a surrounding winding. Some assumptions are made in order to simplify the modelling:

- the permeability of the yoke is assumed to vary sinusoidal as a result of the saturation
- the flux in the yoke is assumed to be dominated by the flux from the permanent magnets
- the air gap flux is assumed to be sinusoidal distributed
- magnetic coupling between the coils are neglected
- only yoke saturation (due to permanent magnets) is included in the model

If we assume no magnetic coupling between Coil2 and Coil3 and that we have a position dependent variation of the inductance in each coil, the resulting inductance from the series coupling of coil 1 and 2 becomes:

$$L_{coil2} = L_{av} + L_g^{'} \cdot \cos(2 \cdot \theta) \tag{1.43}$$

$$L_{coil3} = L_{av} + L_g^{'} \cdot \cos(2 \cdot (\theta + \Delta\theta)) \tag{1.44}$$

$$L_{phase} = 2 \cdot L_{av} + L_g \cdot \cos(2 \cdot \theta + \gamma) \tag{1.45}$$

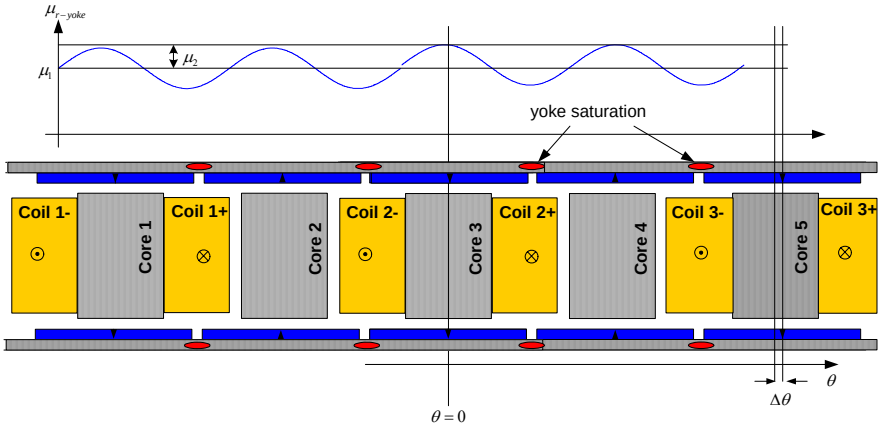

Figure 1.3 Principal view of concentrated windings with yoke saturation between cores

Where

$$L_g = L_g^{'}\sqrt{1+\cos(2\cdot\Delta\theta)^2} \tag{1.46}$$

$$\gamma = a\tan\left[\frac{\sin(2\cdot\Delta\theta)}{1+\cos(2\cdot\Delta\theta)}\right] \tag{1.47}$$

A typical coil configuration could be three coils in series. If we derive the resulting inductance and place the coil in the centre of the series coupling in the same position as coil1 in Figure 1.3 the resulting phase inductance (labelled "a" for phase a) can be written as:

$$L_a = L_{s\sigma} + L_{s0} + L_g\cos(2\theta+\gamma) \tag{1.48}$$

Where:

$$L_{s0} + L_{s\sigma} = 3L_{av} \tag{1.49}$$

$$L_g = L_g^{'}\sqrt{1+2\cdot(\cos(2\cdot\Delta\theta))^2} \tag{1.50}$$

$$\gamma = a\tan\left[\frac{\sin(2\cdot\Delta\theta)-\sin(2\cdot\Delta\theta)}{1+2\cdot\cos(2\cdot\Delta\theta)}\right] \equiv 0 \tag{1.51}$$

Thus with a series coupling of three coils the self inductance can be writes on the same form as for the IPMSM modelling in the previous chapter:

$$L_a = L_{s\sigma} + L_{s0} + L_g\cos(2\theta) \tag{1.52}$$

The two remaining phases are placed 120 electrical degrees shifted compared to the a-phase. Thus the phase inductance terms get the same as IPMSM modelling also for the two remaining phases:

$$L_b = L_{s\sigma} + L_{s0} + L_g \cos(2\theta + 120) \tag{1.53}$$

$$L_c = L_{s\sigma} + L_{s0} + L_g \cos(2\theta - 120) \tag{1.54}$$

If we assume no coupling between the coils there will be no mutual inductance between the phases and the resulting inductance matrix becomes:

$$\underline{L}_s^S = \begin{bmatrix} L_a & 0 & 0 \\ 0 & L_b & 0 \\ 0 & 0 & L_c \end{bmatrix} \tag{1.55}$$

The machine equation can be found in the same manner as for the IPMSM modelling. The only difference will be a different definition of the direct and quadrature inductance:

$$\underline{L}_s^r = \begin{bmatrix} L_{s\sigma} + L_{s0} + \dfrac{L_g}{2} & 0 \\ 0 & L_{s\sigma} + L_{s0} - \dfrac{L_g}{2} \end{bmatrix} = \begin{bmatrix} L_d & 0 \\ 0 & L_q \end{bmatrix} \tag{1.56}$$

The scaled equations become identical with the IPMSM modelling ((1.33) -(1.42)) only with the expressions for L_d and L_q for the axial flux machine used instead of the expressions in (1.11) and (1.12).

The assumptions made in the modelling of the axial flux machine may seem crude. In particular the assumption of sinusoidal flux density in the air gap flux is especially crude. The assumption was tested by a simple test: the induced voltage between two phases was measured while the machine was rotated by hand (Figure 1.4). The sinusoidal shape of the induced voltage indicates that the air gap flux can be modelled as sinusoidal distributed without introducing any large errors. The sinusoidal shape of the induced voltage does not indicate that the flux density is sinusoidal but rather indicates that the six (six coils in series between two phases) sums up like a sinusoidal flux. The assumption that there is no coupling between the individual coils also may seem like a crude approximation. The coupling between the phases was measured in the prototype machine by applying a step voltage to a phase (return in neutral) and measuring the induced voltage in the two open phases. The mutual inductance between the coils where found to be approximately 4 % of the phase self inductance.

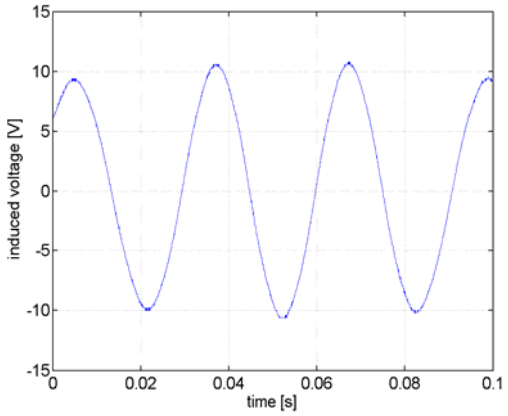

Figure 1.4 Induced voltage for the axial flux machine; shaft turned by hand, voltage measured by oscilloscope

The effect of this coupling was analyzed in detail in [54] and position dependent terms was found in the zero sequence flux if the mutual inductance was position dependent. This could potentially be used as a basis for sensorless control if the neutral point of the machine was made available. In this work voltage measurements for the neutral point was not considered and the modelling was done without including the zero sequence components.

1.3 Chapter conclusions

A machine model for an axial flux machine is presented. The derivation of the machine model shows how the saliency effect from three coils in series will be in the resulting phase inductance. The average values in each coil sums up and the position dependent parts must be added as vectors. The pole pitch ($(360-\Delta\theta)/360$) determines how the position dependent parts adds up. If the pole pitch is unequal unity the resulting saliency ratio will always be smaller for the series coupling than for the single coils. The saliency ratio (SR) for a single coil can be expressed as:

$$SR = \frac{L_g^{'}}{L_{av}} \tag{1.57}$$

Three coils in series gives:

$$SR = \frac{L_g^{'}\sqrt{1+(2\cdot\cos(2\cdot\Delta\theta))^2}}{3\cdot L_{av}} \tag{1.58}$$

The machine equation for the axial flux machine can be expressed on the same form as the standard equations for the radial flux PMSM if the expressions for L_d (1.11) and L_q (1.12) substituted with the expressions found in(1.56).

2 STATE OF THE ART

The term sensorless control is used to cover a variety of different sensorless schemes. There is a distinct difference in the usage of the different schemes. Some applications needs speed or torque control and may not need accurate control around zero speed (for example pumps, propulsion, fans etc.). For this type application sensorless control based on FOC (Field Oriented Control) or a DTC (Direct Torque Control) scheme typically apply. For applications where servo control is needed a position sensor has traditionally been used. In the last two decades techniques based on second order effects has been proposed in order to enable servo control. In order to classify the schemes one can separate the schemes based on the machine model used and if signal injection is used. In the classical machine models the first harmonic of the MMF is used to model a sinusoidal stator MMF. In these models saturation, harmonics due to stator and rotor slotting and skin effect are typically not included. This type machine model will be referred to as fundamental wave machine model. The machine models that incorporate second order effects will be referred to as the non fundamental wave machine model. Table 2.1 shows the classification of schemes [46] and the subchapters devoted to the different classes.

Table 2.1 Classification of Sensorless control Schemes for PMSM

	Fundamental-wave Machine model	Non fundamental wave Machine model
Fundamental wave Excitation	Chapter 2.1, 2.2, 2.3	
Signal injection	Chapter 2.3	Chapter 2.4

2.1 Classical Control Methods

There are two methods for torque production in a PMSM: Vector control or direct torque control (DTC). Vector control drives where introduced in Germany over 25 years ago by Hasse [52] and Blaschke [53]. DTC was first introduced by Takahashi and Noguchi in 1985. The first commercial DTC where introduced by ABB in 1995. Most commercial sensorless drives are based on these two control methods and estimation of flux or rotor position based on the fundamental wave machine model and excitation.

2.2 Vector Control

The most common control strategy for PMSM is rotor oriented Vector Control with a voltage source inverter. The commanded voltages are modulated with a pulse with modulator (PWM) and a fixed switching frequency. In order to get the state variables in rotor reference frame the rotor position is required. The rotor position can be obtained with a position sensor or by estimation of the rotor position. A machine model for a surface mounted PMSM is used to illustrate how the position estimate can be derived from the applied voltage and measured currents. A comparable scheme for IPMSM can be found in [50]. The second term in (2.2) represents the back EMF and contains information of the rotor position.

$$\underline{u}_s^s = \underline{i}_s^s r_s + \frac{1}{\omega_N}\frac{d\underline{\psi}_s^s}{dt} \tag{2.1}$$

$$\underline{\psi}_s^s = \underline{x}_s \cdot \underline{i}_s^s + \psi_m \cdot e^{j\theta} \tag{2.2}$$

There are several methods that derive the flux estimate (and rotor position) from the voltage equations:

- Open loop integration [50]
- Observer based estimation [51, 20]

The simplest (and most common) form uses open integration of the stator voltage minus the resistive drop:

$$\underline{\psi}_s^s = \omega_N \int (\underline{u}_s^s - r_s \underline{i}_s^s)dt + \omega_N \underline{\psi}_{s0}^s \tag{2.3}$$

The rotor position can be derived by considering the real and imaginary parts of the flux linkages from the permanent magnets in the stationary reference frame:

$$\psi_m e^{j\theta} = \begin{bmatrix} \psi_m \cos(\theta) \\ \psi_m \sin(\theta) \end{bmatrix} = \begin{bmatrix} \psi_{s\alpha}^s - x_s i_{s\alpha}^s \\ \psi_{s\beta}^s - x_s i_{s\beta}^s \end{bmatrix} \tag{2.4}$$

There are several aspects of the open integration that may lead to problems: the sensors involved with current and voltage measurements may have offsets, dead time in power electronics distorts the output voltage, and estimate of the stator resistance may be incorrect. These problems may lead to drifting of the integral and failure of the sensorless operation. Examples of compensation schemes that keep the integral parts within bounds are presented in [12, 27, 50]. In a surface mounted PMSM the torque production is proportional to the q-axis current. The large effective air gap due to the low permeability of the permanent magnets leads to a small stator inductance. Field weakening is not possible for a wide speed range. The control of the machine becomes simple as the q component of the stator current is proportional with the torque production.

$$m_e = \psi_m i_q \tag{2.5}$$

Figure 2.1 shows a simple control scheme for the PMSM. The speed and position is derived form an encoder (replaced by estimates for sensorless operation). The speed regulator gives the commanded torque, this is proportional to i_q reference value. The d axis current component does not contribute to torque production and the reference value is set to zero. In order to get the two current regulators decoupled a decoupling block is included. After adding the decoupling terms the commanded voltage is transformed from a rectangular value in rotor reference frame to polar values in stationary reference frame. The voltage angle is corrected for delay in the DSP and converter with the block containing $k_n T_s$. Finally the reference values are used in a space vector modulation in

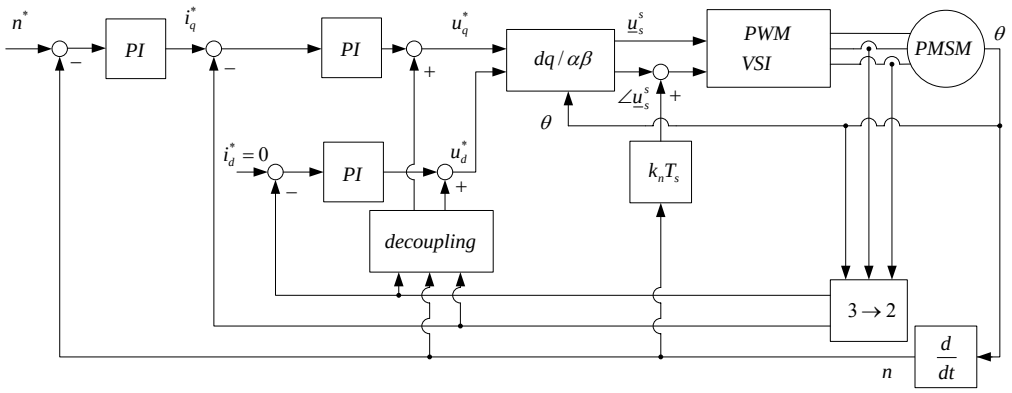

Figure 2.1 Block diagram of the PMSM control

order to obtain register values for pulse with modulation in the voltage source inverter. In a IPMSM the electromagnetic torque has two components. One torque component is due to the interaction between the permanent magnet flux and the stator flux. The other component is caused by a reluctance torque due to the difference in the magnetic structure. The reluctance torque size is proportional to the difference in the direct and quadrature inductance and the product of the current components:

$$m_e = \psi_m i_q - (x_q - x_d) i_d i_q \tag{2.6}$$

The maximum torque per ampere trajectory can be found tracking the derivative of (2.6) with respect to the current in the q-axis:

$$i_q = \pm \sqrt{i_d^2 - \frac{\psi_m i_d}{x_q - x_d}} \tag{2.7}$$

The torque relation is derived from (2.6).

$$i_q = \frac{m_e}{[\psi_m + (x_d - x_q) i_d]} \tag{2.8}$$

Maximum torque per ampere trajectories is plotted in Figure 2.2. The intersections between (2.7) and (2.8) gives the relation between commanded torque and optimal reference current. The optimal current reference is obtained from the torque demand and a lookup table (analytical solution can also apply). The rest of the control scheme is identical with the scheme presented in Figure 2.1. When the speed increases the back EMF increases. There is a limit determined by the DC link voltage that gives the maximum speed without field weakening. When this speed is reached a negative d-axis current is applied in order to reduce the resulting stator flux and the induced voltage.

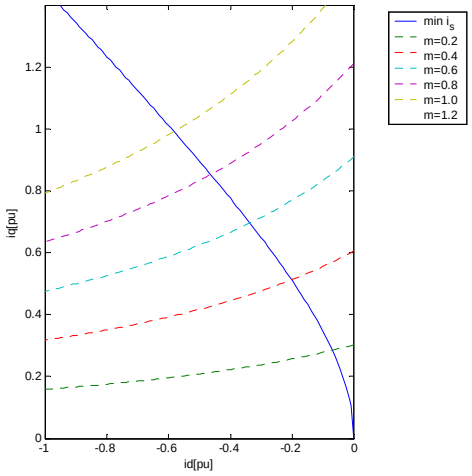

Figure 2.2 Constant toque loci and maximum torque per ampere trajectory

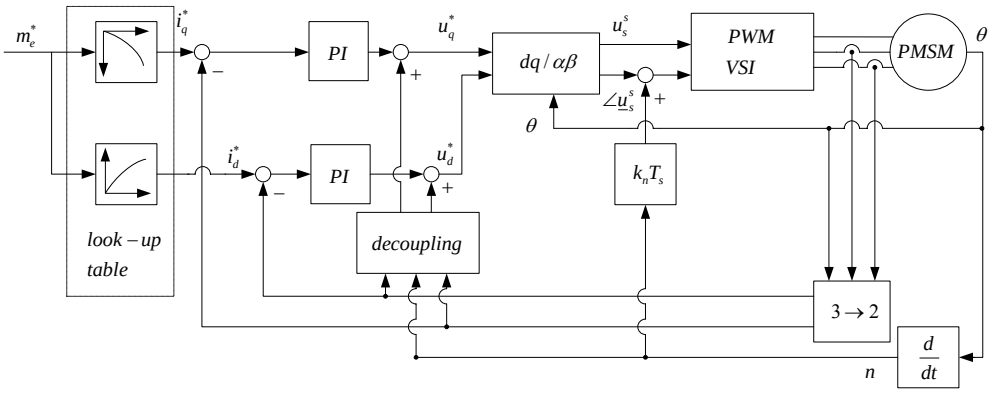

Figure 2.3 Block diagram of the IPMSM maximal torque per ampere controller

2.3 DTC

In a PMSM drive direct torque control is typically realized by controlling the q-axis current for PMSM. DTC was commercialised by ABB in 1995. The DTC scheme is based on controlling the stator flux (and torque) with hysteresis controllers. The idea is that the torque can be controlled without transformations to the rotor reference frame and with very simple hysteresis controllers. The torque can be expressed as:

$$m_e = \underline{\psi}_s^s \times \underline{i}_s^s \tag{2.9}$$

There are several control strategies for DTC, two of them are: the stator flux and torque, the quadrature axis current and the torque (PMSM). In this section the scheme based on flux control is covered. For this scheme maximum torque per ampere is used as control criteria for the speed region up to field weakening, in the field weakening region maximum torque per unit flux will be used as the criteria. DTC is based on the possible voltage vectors from the inverter and optimal selection of these vectors according to the overlaying criteria and the hysteresis controllers.

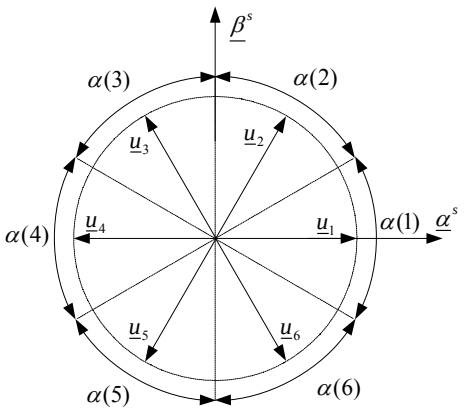

Figure 2.4 The six active switching vectors

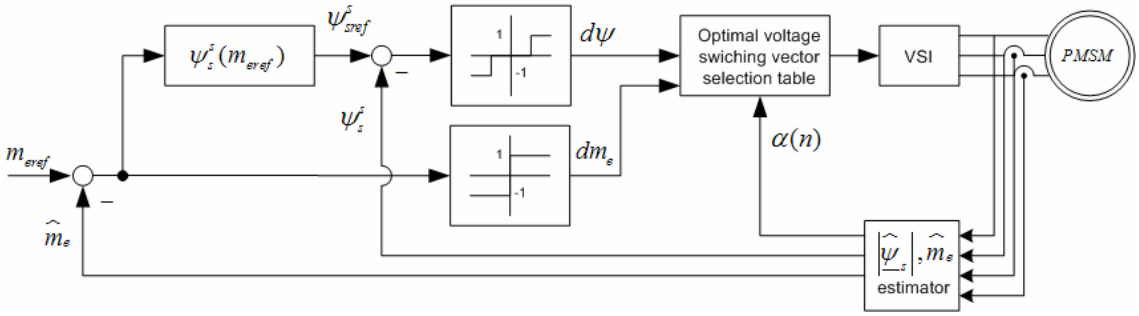

Figure 2.5 DTC control scheme for flux and torque control

The three leg inverter has six active voltage vectors (u(1)..u(6)) and two vectors that short circuits the stator windings. Figure 2.4 shows the six active voltage vectors and the sectors (α(1).. α(6)) that are used for the voltage vector selection. The direction of the stator flux derivative can be derived from the stator voltage equations; if the resistive voltage drop is neglected $d\underline{\psi}_s/dt=\underline{u}_s$. Thus the stator flux will change in the direction of the voltage vector. If no change in the flux is needed the zero vector is applied. Figure 2.5 shows a control structure for DTC control of a PMSM machine. Two hysteresis controllers are used in order to keep the flux and the torque at reference value. Figure 2.6 shows the four possible active voltage vectors in sector 1. For example if the stator flux is located in sector α(1) and the stator flux should be increased and the torque should be positive ($d\psi=1, dm_e=1$) voltage vector $\underline{u}_2$ is selected. The scheme based on hysteresis controllers results in a variable switching frequency. This makes the classical DTC scheme harder to combine with the signal injection based methods compared to Vector control schemes. In [47] an alternative DTC scheme was presented. In this scheme the switching frequency was held constant, thus in this DTC scheme the carrier signals could easier be integrated.

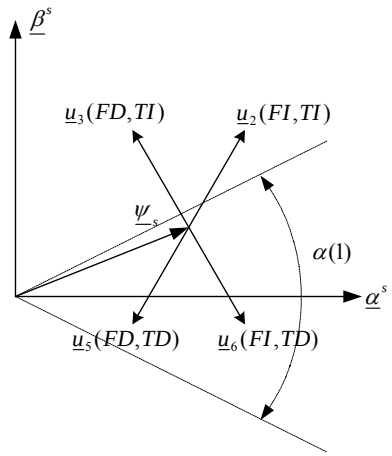

Figure 2.6Selection of optimum switching voltage vectors. FI: flux increase, FD: flux decrease, TI: torque increase, TD: torque decrease.

2.4 Low frequency signal injection

The progress in power electronics and microcontrollers allowed online realization of injection based estimates. In 1982 Gabriel [16] presented his PhD thesis with online parameter estimation of rotor time constant based on injection of pseudo random noise in the estimated d-axis of an induction machine. The position was measured and acceleration of the machine was used as input to an estimator for the rotor time constant. The concept was presented by using step commands in d-axis current while monitoring the acceleration of the rotor. If the pulses were shorter than the time constant in the rotor flux there was no torque response when the estimated position equalled the actual position. The injection based estimation in [16] was realized online with relative low frequency pseudorandom signal (100 Hz). Correlation functions where used to produce the error signal to an estimator. Low frequency injection in the d-axis has also been used for sensorless control of induction machines by Leppanen and Sng[46, 48]. A low frequency signal is injected in the estimated d-axis. Fundamental wave machine model is used and the principle of torque ripple as a result of miss alignment of the estimated d-axis compared to the actual d-axis is the basis to establish an error signal proportional to the position error. As these methods are based on torque production they can be used for machines with no saliency. The latest contribution on this field is presented in [46]. In this work the mechanical relation was used in order to establish an error term proportional with the estimated speed error. Additional excitation was used in order to cancel the torque ripples when the estimated d-axis is aligned with the d-axis. The error term for speed estimation is based upon that there is an oscillation in the actual speed of the machine. This leads to some limitations for the usage of the scheme: the bandwidth of the scheme will be low and the inertia of the system (machine and load) must be limited in order to enable small speed oscillations. Several machine parameters are also used in order to produce the error signal. In [49] the low frequency signal based sensorless control that is tested on a surface mounted PMSM. The operation of the PMSM system was presented (speed reversal tests) but no data on bandwidth performance or disturbance rejection was presented. In general all schemes based on low frequency signal injection will inherently have low bandwidth due to the low frequency of the injected signal.

2.5 High frequency Carrier injection

Of all the carrier injection based schemes for sensorless control the schemes based on high frequency carrier injection has been the scheme with the highest activity during the 90-ties. These schemes use saliency in the machine as the basis for the flux or position estimate. The saliency may be present due to saturation, slot variations, slot harmonics or inherent saliency due to machine geometry. The goal for this type schemes are to enable high performance control at all speeds including zero speed.

2.5.1 Rotating High Frequency Carrier Injection

Rotating high frequency carrier injection for online flux and position estimate was introduced by Professor R.D. Lorenz and the graduate students at University of Madison Wisconsin during the late 80-ties [13]. During the 90-ties there was a large activity sensorless control in Madison covering induction machines [2, 13], linear induction machines [13], Permanent magnet synchronous machines [3], Switched reluctance motors [55] and Universal Motors [56]. There was also several other universities that worked with this type of technology during the 90-ties: at the university of Nottingham Asher, Bradley, Cilia, Teske [21, 35] worked with sensorless control and redesign of induction machines for sensorless control. A detailed description of the scheme based on injection of a rotating high frequency carrier will be given in Chapter 6. In this chapter the evolution of the method is described:

The scheme is based on injection a balanced high frequency carrier superimposed on the fundamental excitation. The response to this carrier signal will contain saliency position information if the machine has a saliency. In early stage both current and voltage injection was evaluated. The scheme based on voltage injection vas preferred as the current based injection needed very high bandwidths for the current regulators (larger than the carrier frequency). The early work on induction machines [13] used saturation induced saliency as basis for the flux position estimate. The saturation induced saliencies where depending on the operating condition of the machine, this made the saturation induced saliency difficult to use. Slot harmonics where also evaluated as a basis for flux position estimate in [2]. In this approach the position dependent part of the current was very small and current sensor (and digital resolution in analogue to digital converters) accuracy became problematic. Finally the induction machine was redesigned with spatial variation in the rotor slot openings [2]. The redesign approach introduced a position dependent variation in the leakage inductance of the induction machine. The redesigned machine in [2] was successfully tested at low load (not at rated torque). In [21] a saliency where introduced in an induction machine by modifying the rotor bars. The effects of inverter non linearity on the position dependent terms in the current where evaluated and a compensation scheme was suggested [35]. The redesigned induction machine in [35] was successfully tested under all operating conditions. As a result of the compensation of the inverter non linearity a standard induction machine was also tested sensor less by using the slot harmonics. Despite the progress on rotating high frequency carrier injection there is still no universal method that will work for all “off the shelf” induction machines. A limited numbers of publications are presented for rotating high frequency carrier injection for PMSM. In 1995 the rotating high frequency carrier injection was tested on an IPMSM [39]. The bandwidth of the position estimate exceeded 100 Hz. The observer used in this experiments use the estimated inertia and a feed forward torque. The scheme used in this paper is described in detail in Chapter 6.

2.5.2 Pulsating high frequency carrier injection

The schemes based on pulsating high frequency carrier injection are also based on a saliency present in the machine. The scheme is described in detail in Chapter 7. In this chapter only a brief overview of the evolution of the method is described. In 1996 Corley and Lorenz [4] applied pulsating high frequency carrier (voltage) injection in the estimated q-axis on an IPMSM. The response in the d-axis current was demodulated by multiplication of sinus to the injected angle. The demodulated signal was proportional to the position error. The error signal was used in a Luenberger style observer comparable to [2] and [13]. In a later paper [5] the bandwidth for the speed loop was found experimentally to be limited to 10 Hz for the q-axis injection based scheme. D-axis voltage injection with a different criteria function for the position estimate was used by Sul, Jung and Ha [22-23] in 1997-1998. The searching criteria were made on assumptions of different high frequency impedance in the d- and q axis. The response from the carrier signal was transformed to a coordinate system $\pi/4$ displaced form the estimated d-axis. The difference of the squared current components in this reference system gives a term that is proportional with the sine of the double angular displacement of the estimated d-axis compared to the real d-axis. For small errors the error term is approximately linear dependent on the angular displacement of the estimated d-axis. In a later paper by Jang and Sul [26] the position estimate was implemented with an alternative error term: the q-axis current was multiplied with sinus to the carrier angle and the resulting term was low pass filtered (this is essentially the same as in [4] but the injection in [4] is done in the q-axis, and the measurement is done in d-axis). This method (d-axis injection) was tested for IPMSM, PMSM, IM and SRM machines with promising results [22-26].

2.5.3 Third harmonic based estimation

Third harmonic based flux position methods was presented by Moreira and Lipo [31, 32] in 1990. Saturation in the induction machine creates a third harmonic component in the air gap flux. The machines that were used had Y-connected stator and therefore no zero sequence current, this leads to a fixed relation between the third harmonic air gap flux and the main flux independent on machine loading. The voltage at the neutral point is in quadrature with the third harmonic air-gap flux and this voltage was used to detect the air gap flux position. The scheme could not give high performance control at low and zero speed due to the small amplitude of the third harmonic voltage. In 2000 Consoli, Scarcella and Testa [28] presented a scheme based on measured voltage from the neutral point of the machine in combination with high frequency carrier injection was presented. The concept is based on the interaction between the carrier signal and the direct axis flux from the permanent magnets. The idea in this method is to use the relation between the direction of the carrier MMF compared to the main MMF. When the two MMF components are aligned the third harmonic flux component increase, when the two MMF components are in opposite directions the third harmonic flux

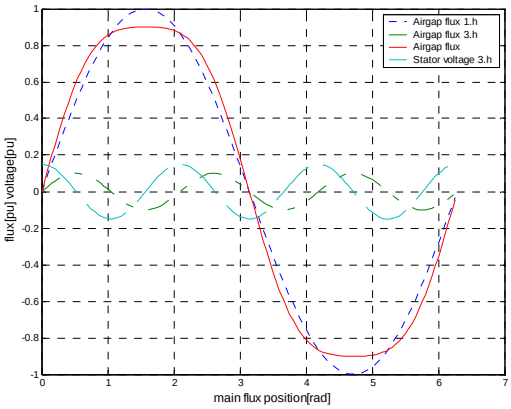

Figure 2.7 Air gap flux components and third harmonic stator voltage

component decreases. When the carrier MMF is orthogonal there is no change in the third harmonic flux. Thus the high frequency flux component is maximum when the high frequency MMF is aligned with the main MMF. The third harmonic flux and the third harmonic voltage at the neutral point is related by a π/2 phase shift. Thus by detecting the maximum, minimum and zero crossings of the high frequency neutral voltage the main flux position can be derived from the relation between the known injection angle and the max, min and zero crossing of the high frequency neutral voltage. This relationship is shown in Figure 2.8

The proposed scheme gives four updates on the position estimate for every period of the injected carrier voltage. The influence of loading is very small as the air-gap flux position is the goal for this estimation. If position estimate is needed one have to include some machine parameters is order to correct for loading. For surface mount PMSM the air-gap flux position is very close to the rotor position.

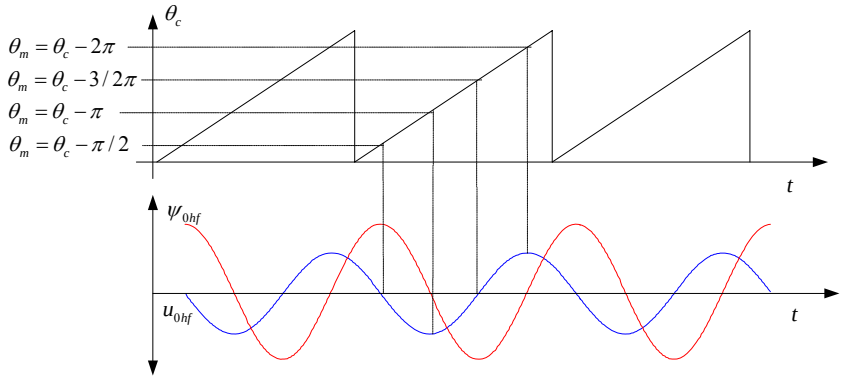

Figure 2.8 Relationship between maximum, zero and minimum of the measured hf zero point voltage and the injected hf signal angle

2.6 Transient excitation

Transient excitation has been used for parameter estimation and initial position estimation for more than three decades. Blaschke [17] used voltage steps in the field winding on a salient pole synchronous machine and determined the rotor position from the response as early as 1975. The method was performed in the commissioning stage in order to determine the initial position of the rotor. The progress in power electronics and microcontrollers allow online realization of these principles. Schroedl presented his thesis in 1993 [1] where the inductance of a surface mounted PMSM was estimated online and used for position estimation. The scheme is described in detail in Chapter 8. Only a brief overview of the evaluation of the method is given in this chapter. In the first implementation the INFORM-method (Indirect Flux detection by On-line Reactance Measurement) was implemented with a measurement sequence that included measurements in all three basis axis (a,b,c-axis). The measurements where done by applying voltage pulses and measure the current change. The fundamental operation of the drive system had to be halted during the measurement sequence. This was a limiting factor as the measurements sequence used several hundred micro seconds. In order to have sufficient torque production the intervals between the measurements had to be long. An alternative approach [58] was presented by Ogasawara and Akagi in 1998. The PWM modulator was rearranged and all six active vectors where active for a minimal time during each switching period. This enabled measurements of the derivative of the current at zero speed. A hardware sampling arrangement where presented in [59] that increased the effective resolution of the analogue to digital converter. The scheme was tested with a IPMSM and the performance where described as: 20 rad/s position response and 300 ms settling time. In a later paper (2002) from Robeischl and Schroedl [60] the measurement sequence was limited to one direction in each measurement sequence. This reduced the measurement time dramatically and the measurement sequence could be performed in all three axis (abc) in intervals with 2 ms between the measurement sequences. In the next paper [61] one additional vector was applied in the measurement sequence in order to minimize the deviation from the stator current before the measure sequence was applied. This modification reduced the audio noise and additional losses in the machine. In [7] Wolbank and Machl integrated the excitation sequence in the zero vector (symmetrical space vector modulation). The performance (or operation) of this excitation schemes was not showed in [7]. The INFORM method [60, 61] was integrated as a commercial product in 2002.

2.7 Chapter conclusions

The rotor oriented Vector control schemes need a position estimate in order make the transformation to rotor reference frame. This is usually done by estimation the stator flux and deriving the position from the relation between stator flux and rotor position. Equation (2.1) and (2.2) shows the simplicity of EMF based position estimate but also the limitation: as the derivative of the permanent magnet flux (ψ_m) is the bases for the

estimation the machine must rotate in order to have any position dependent terms in the voltage. At low speeds the resistive voltage drop, dead time in inverters and voltage drop in power electronics will influence the integral in (2.3). The lower limit for this type sensorless control is 1-2 Hz . Below this frequency an alternative control strategy must be used . Due to the PWM modulation used in Vector control it is easy to integrate high (or low) frequency carrier injection in these schemes. Transient excitation becomes a little more challenging to implement as the interrupt structure in the DSP must be changed.

In [12] the DTC scheme advantages over the standard back EMF methods are described: absence of coordinate transforms, absence of separate voltage modulation block, absence of voltage decoupling, only the sector of the stator flux vector needs to be known and minimal torque response time is achieved. The DTC scheme is also based on the stator flux estimate and it will eventually have the same low and zero speed problems as the Vector control scheme. The classical DTC scheme has varying switching frequency, which makes integration of high (or low) frequency carrier injection difficult.

As all sensorless schemes based on the stator flux estimate will have issues at low and zero speed the need for alternative methods are evident. It is hard to separate the properties of the different schemes found in the literature as different criteria often is used by each author. Also the machines and inverters used in the different setups are different. In order to make a comparison a selection of methods are tested in this work.

The selection of schemes was based on the following requirements and assumptions:

- PMSM application (interior and surface mounted)
- Saliency present in the machine
- Measurements of two phase currents (standard LEM sensors) and DC bus voltage
- Industrial fix point DSP (TMS320F2812)
- High bandwidth
- High quality low and zero speed sensorless control (no position sensor)
- Must work for low and high values of system inertia

From these criteria's the following schemes are candidates: rotating high frequency carrier injection, pulsating high frequency carrier injection and transient excitation. The schemes are described, implemented and tested in Chapter 6, 7 and 8. In Chapter 9 a comparison of the schemes are presented.

3 SALIENCY MODELLING

In the literature saliency modelling is usually based on Fourier analysis [2, 62]. This type analysis is useful when considering saliency based on slot harmonics or other types of saliencies that gives high harmonic order terms. In this chapter the sources of single saliencies are evaluated. The main idea is to model how the different sources of saliency sums up to a resulting single saliency. Saliency contributions in leakage and main inductance are modelled separately. This type of modelling is very useful when considering different flux distribution for the carrier flux [45]. Depending on the lamination used and the carrier frequency the carrier flux may distribute in the leakage flux path or in the main flux path (or in both). The resulting saliency model can also be used when saliency is increased by machine design.

3.1 Concept of Saliency

There are several sources of saliencies in AC machines:

- Rotor inherent saliency
- Saturation based saliency (yoke, teeth)
- Rotor and Stator teeth harmonics
- Lamination direction based saliency
- Eddy current based saliency (for example in permanent magnets)
- Rotor eccentricity based saliency

In this Chapter PMSM machines are evaluated and the saliencies based on rotor inherent saliency and saturation based saliency are the most dominating. Saliency based on rotor stator slotting is not present as the rotor structure has a magnetic smooth surface compared to the slots found in an induction machine. In order to define the term saliency a salient pole synchronous machine in Figure 3.1 is considered. The direct axis

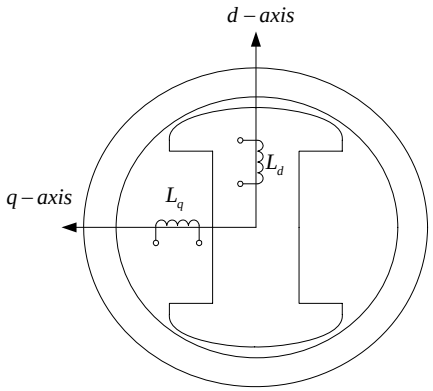

Figure 3.1 Salient pole synchronous machine

magnetic properties is dominated by the two small air gaps, and the quadrature axis magnetic property is dominated by the two much larger air gaps. The inductance for two fictive coils with equal number of turns in these two axis will be different. In the machine model this is represented with $L_d > L_q$. If this was the only saliency present the machine would be considered as a machine with a single saliency. The presence of a single saliency leads to the 2θ dependent terms in the stator oriented machine model (1.13). In order to describe the saturation based saliencies it is helpful to first consider a simple magnetic circuit. Inductance variation is often used as the basis for description of saliency in electric machines. Figure 3.2 illustrates a core with two different materials. The permeability for the two materials differs as illustrated in the figure. The magnetic reluctance in the circuit can be defined as:

$$R_{mag} = \frac{l}{\mu_0 \mu_{r1} A} + \frac{g}{\mu_0 \mu_{r1} A} \tag{3.1}$$

In (3.1) μ_0 defines the permeability for vacuum, and μ_r defines the relative permeability for materials other than vacuum. A defines the area of the cross section of the core, l and g defines the average core lengths. The inductance can be expressed as:

$$L = \frac{N^2}{R_{mag}} \tag{3.2}$$

The inductance in (3.2) depends on the relative permeability in the two core parts, the core dimensions and the number of turns. The relative permeability for standard iron is often in the region 1000 – 10000. The relative permeability for vacuum is 1.0. The relative permeability changes when current is increased in the coil (Figure 3.2.1). Figure 3.2.2 describes the relationship between the magnetic flux density (B) and the magnetic field (H) for a laminate material (Congent M235-35A). Equation (3.3) gives the resulting permeability.

$$\mu_0 \mu_r = \frac{B}{H} \tag{3.3}$$

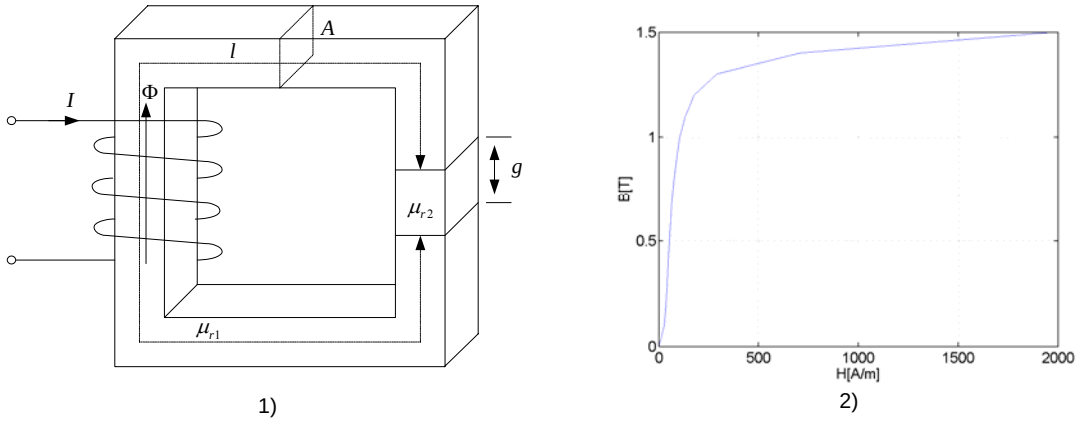

Figure 3.2 Simple magnetic circuit (1) and BH curve for lamination (Congent M235-35A) (2)

When the magnetic field increases towards infinity the relative permeability converges to 1.0. At this operating point an increase in the current will only result in a flux increase comparable to a coil with no iron core.

In addition to the saliency based on electrical phenomena there may be saliencies due to mechanical phenomena: two types rotor eccentricity can be found in electric machines: static and dynamic eccentricity. The static eccentricity is illustrated in Figure 3.3.1. The rotor rotates about the rotor centre. This type eccentricity gives no position dependent terms in the inductance in the stator reference frame. The dynamic eccentricity is illustrated in Figure 3.3.2. The rotor rotates about the centre of the stator. This type of eccentricity will give position dependent terms in the inductance in the stator reference frame due to the air gap variations as the rotor rotates. Several publications [2, 62] analyses the effects of rotor eccentricity but in this work these effects will not be included in the model.

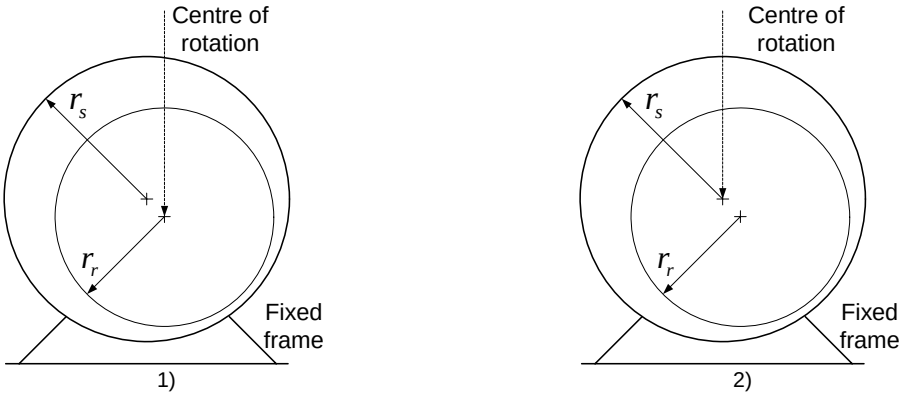

Figure 3.3 Rotor eccentricity. 1: Static Eccentricity, 2: Dynamic Eccentricity

3.2 Radial Flux Machines

In analyses of electric machines simplifications often needs to be done. Typical simplifications are related: windings in stator are distributed in discrete slots, the air gap flux density is not sinusoidal, magnetic material is non linear. In the following some simplifications has been made to simplify the work:

- The permanent magnet material is assumed to have linear, temperature independent demagnetizing curve.
- The flux from the magnets and the windings are assumed sinusoidal distributed over the air gap. The distributed windings are simplified by representing them as two concentrated windings (dq-two axis representation).
- Iron losses (hysteresis and eddy current losses) are neglected.
- Resistance is assumed independent of temperature and frequency, thus skin effects are neglected.
- The three phase stator windings are assumed to be y- connected, thus no zero sequence currents can appear.
- Relative permeability assumed to vary linear with flux density

The last simplification is rather crude: the relation between flux density and relative permeability may be extremely nonlinear depending on material type. In the lamination material used in the IPMSM there is an approximately linear relationship between 0.4 and 1.3 T (Figure 4.4.2). In the definition of inductance [8] the total flux linkage and the current in the coil defines the inductance. Thus in order to describe the inductance in a coil the leakage flux and the main flux must be considered. Figure 3.4 shows the current distribution, the current space vector, the main flux and leakage flux. In the following chapters the main inductance will be derived in the direction of the main flux. The leakage flux is concentrated 90 electrical degrees spatially displaced compared to the main flux. Modelling of the leakage inductance is therefore derived separately in order to incorporate position dependent variations in the inductance.

When the machine is controlled in a standard drive system the flux in the rotor appears as a static flux as the stator current is controlled to be aligned to the q-axis (or to the maximum torque angle if optimal control). The flux path for this flux will be used as the main flux path, and the inductance from these flux linkages will be called main inductance.

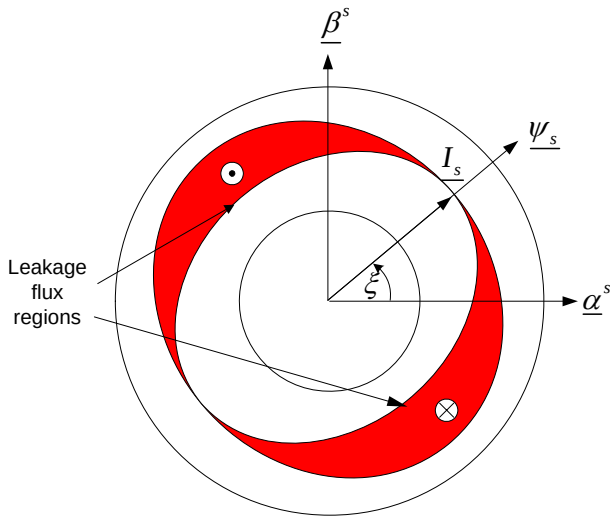

Figure 3.4 Current distribution , current and flux space vectors

Two types radial flux PMSM are common: interior and surface mounted magnets. IPMSM has a saliency present in the rotor. Surface mount PMSMs are typically symmetrical ($L_d = L_q$) if saturation is neglected. In the following chapters saliency models for IPMSM are modelled as these cover both types of machines. In order to make a saliency model the flux from the permanent magnets are considered as the source for saturation in the first step. Saliency and stator flux movement due to load current are included after the no load model is derived. In order to visualize the regions of saturation a representative model of Test Machine 1 is simulated in FEMLab. The machine has 8 poles and interior magnets. Both stator and rotor is made of 0.35 mm lamination (M235-35A) from Congent. The magnet remanence Br is 1.1 T in the model. The relative permeability as a function of flux density was derived from data supplied from the manufacturer of the laminations. In order to reduce the simulation time one pole of the machine is simulated. In Figure 3.5 the flux density (surface) and the magnetic vector potential (lines) is plotted. Flux density is high in the stator teethes (maximum 1.5 T) and in the stator yoke (maximum 1.3 T). Relative permeability is plotted in Figure 3.6. Both the stator teeth and rotor yoke has reduced permeability due to saturation. Due to the colour code and range of the relative permeability it is hard to determine the exact saturation level from Figure 3.6. The three stator teeth in the middle have approximately $\mu_r \approx 150$, the saturated yoke region has approximately $\mu_r \approx 800$-3000.

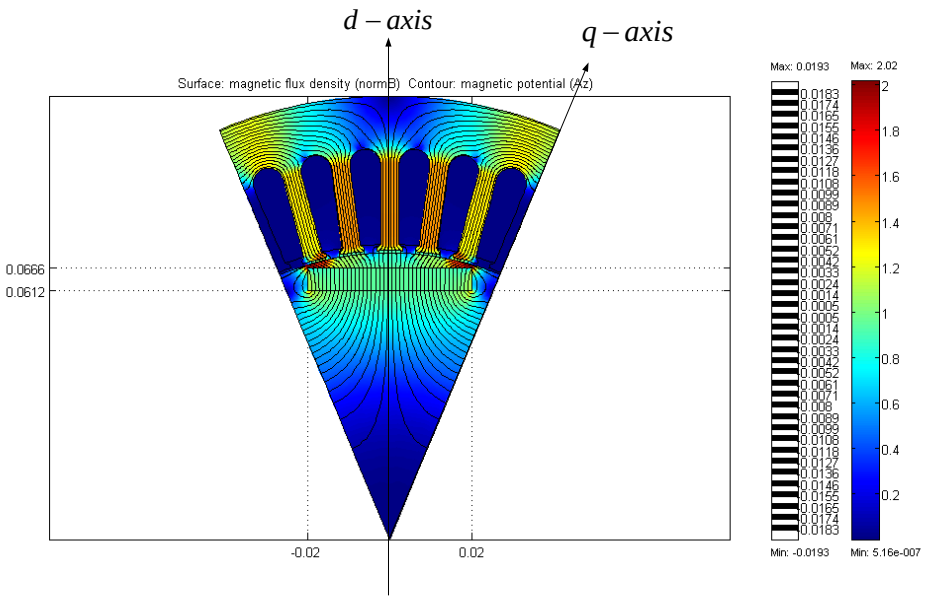

Figure 3.5 IPMSM FEM simulation, Flux density (8 poles total)

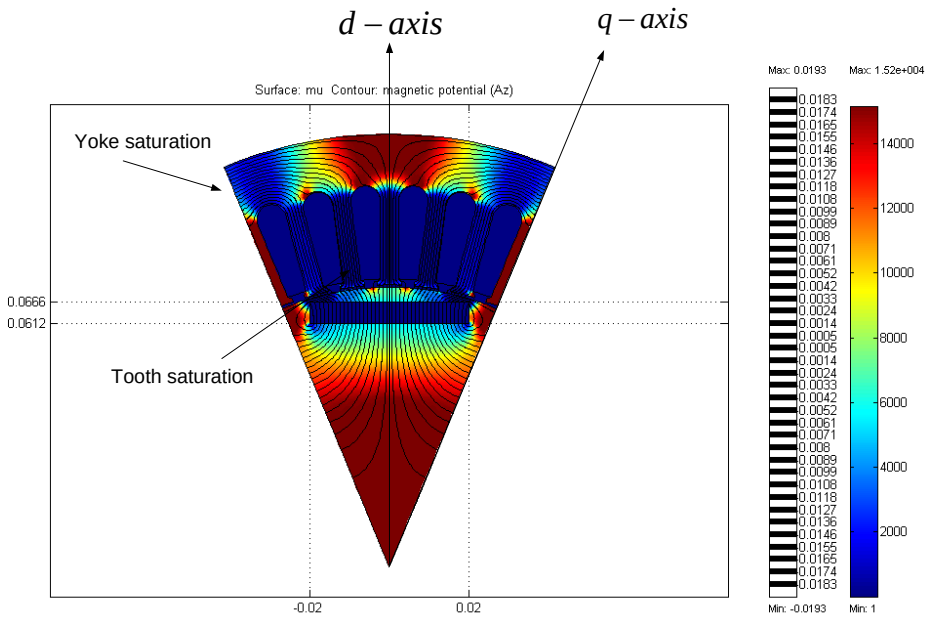

Figure 3.6 IPMSM FEM simulation, relative permeability (8 poles total)

3.2.1 Main flux path

Figure 3.7 shows the regions of saturation and the rotor saliency at no load condition. The permanent magnets in the rotor have relative permeability close to unity. The iron in the rotor has relative permeability in the region of 1000 – 10000. The difference in the relative permeability leads to a different inductance in q and d axis. In Figure 3.7 the q axis main inductance will be larger than the d axis main inductance.

The basis for the saliency model is chosen to be constant and equal inductance in both axis. This represents a structure with no saturation, and relative permeability in the permanent magnets equal to the relative permeability in the rotor iron.

$$L_{d-main} = L_0 \tag{3.4}$$

$$L_{q-main} = L_0 \tag{3.5}$$

The effect from the permanent magnets (relative permeability close to unity) in the rotor is included by subtracting a proper term from the d-axis inductance (L_{0rd}).

$$L_{d-main} = L_0 - L_{0rd} \tag{3.6}$$

In addition to the rotor structure the stator teeth can be saturated in the same axis as the permanent magnets. This leads to further difference in the dq- inductance. This can be modelled as an additional term (L_{0ts}) in the d-axis inductance.

$$L_{d-main} = L_0 - L_{0rd} - L_{0ts} \tag{3.7}$$

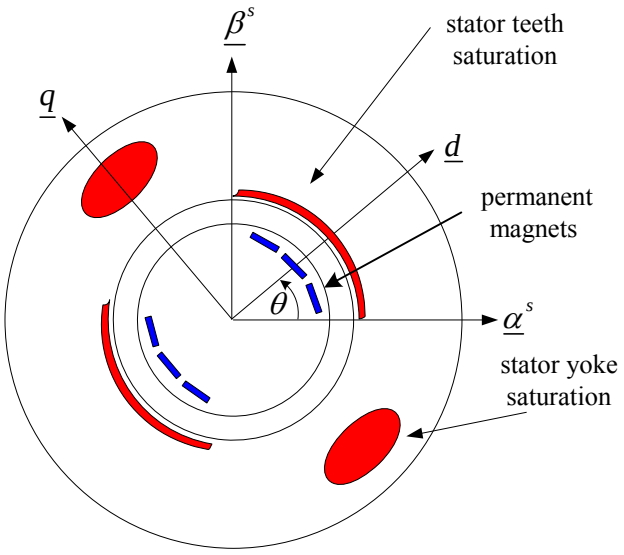

Figure 3.7 Sources for saliency at no load condition

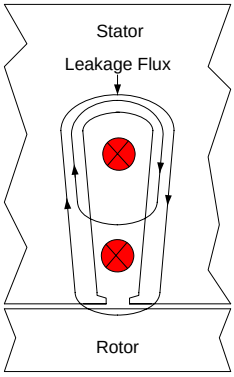

Figure 3.8 Leakage flux path

In the stator yoke there may also be saturation due to the flux from the permanent magnets. In the main flux path this saliency acts in the same manner as the previous saliencies. This can be modelled as an additional term (L_{0ys}) in the d-axis inductance.

$$L_{d-main} = L_0 - L_{0rd} - L_{0ts} - L_{0ys} \tag{3.8}$$

3.2.2 Leakage flux path

In the regions around the stator windings there are leakage flux. The leakage flux is concentrated around the end windings and the stator teeth area. Figure 3.8 shows the leakage flux paths for one stator tooth; some of the leakage flux crosses over the winding area and closes in the yoke over the slot and some portion crosses the air gap and links through the rotor surface.

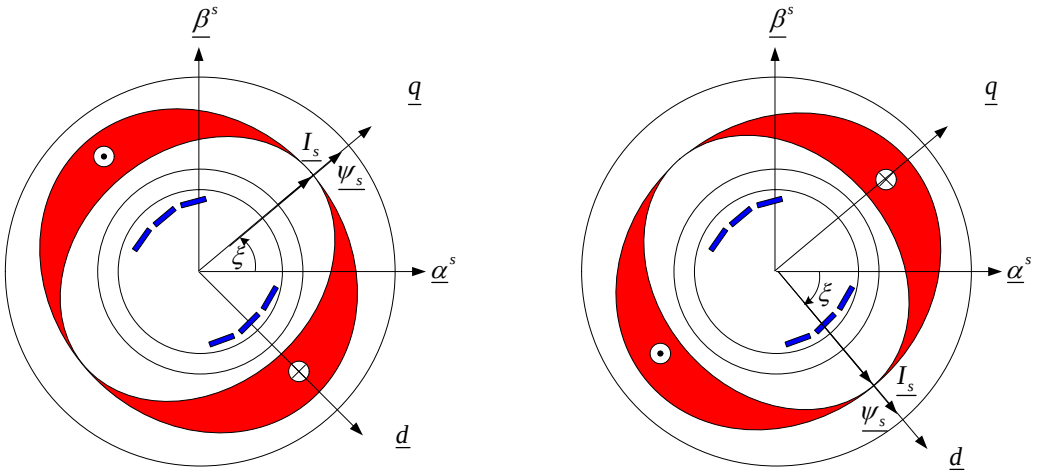

Figure 3.9 Carrier current distribution 1)Current vector in q-axis, 2)Current vector in d-axis

Stator teeth are for most machines partially saturated by the flux from the permanent magnets. The leakage flux path is concentrated around the stator teeth, thus it is natural to include a position dependent term to include the tooth saturation in the leakage inductance term. Figure 3.9 shows a fictive carrier current distribution when the stator current coincides with the q- and d- axis. In order to derive the variations in the leakage inductance we consider an inductance estimate based on the carrier current distribution in Figure 3.9: the leakage flux will be smaller in Figure 3.9.1 compared to the leakage flux in Figure 3.9.2 due to the tooth saturation. This saliency is spatially shifted 90 degrees compared to the main inductance variations. If we model the leakage inductance in the same manner as the main inductance we consider the same inductance in the two axes (L_σ) and the make the correction for the saturated teeth:

$$L_{d-leakage} = L_\sigma \tag{3.9}$$

$$L_{q-leakage} = L_\sigma - L_{\sigma ts} \tag{3.10}$$

Yoke saturation can influence the leakage inductance as well but as the yoke saturation is located 90 electrical degrees apart from the tooth saturation it will reduce the d-axis leakage inductance.

$$L_{d-leakage} = L_\sigma - L_{\sigma ys} \tag{3.11}$$

3.2.3 Resulting no load inductance

The resulting no load inductance consist of both the leakage and the main inductance. The d and q inductance becomes:

$$L_d = L_{d-main} + L_{d-leakage} = L_0 - L_{0rd} - L_{0ts} - L_{0ys} + L_\sigma - L_{\sigma ys} \tag{3.12}$$

$$L_q = L_{q-main} + L_{q-leakage} = L_0 + L_\sigma - L_{\sigma ts} \tag{3.13}$$

L_0 - average main inductance with no magnets or saturation in the machine

L_{0rd} -rotor design saliency in main inductance

L_{0ts} - stator teeth saturation (main flux path)

L_{0ys} -stator yoke saturation (main flux path)

L_σ -average leakage inductance

$L_{\sigma ts}$ -variation in leakage inductance due to stator teeth saturation

$L_{\sigma ys}$ -variation in leakage inductance due to yoke saturation

The difference between L_q and L_d is the basis for saliency in the machine. From (3.12) and (3.13) it can be seen that the saliency from the main inductance and the saliency from the leakage inductance acts in different axis (assumed $L_{\sigma ts} >> L_{\sigma ys}$). The resulting inductance in vector form becomes:

$$\underline{L} = \Sigma L + \Delta_1 L e^{j2\theta} \tag{3.14}$$

Where

$$\Sigma L = \frac{L_d + L_q}{2} = \frac{2L_0 - L_{0rd} - L_{0ts} - L_{ys} + 2L_\sigma - L_{\sigma ts} - L_{\sigma ys}}{2} \tag{3.15}$$

$$\Delta_1 L = \frac{L_q - L_d}{2} = \frac{-L_{\sigma ts} + L_{\sigma ys} + L_{0rd} + L_{0ts} + L_{0ys}}{2} \tag{3.16}$$

3.2.4 Load dependency

When evaluating the load dependency the influence from leakage and main flux are modelled separately. In order to simplify we assume the control strategy to be I_d=0 and I_q=I_s (optimal control can be evaluated in the same manner including I_d*L_d). If the load current increases the stator flux get a phase shift.

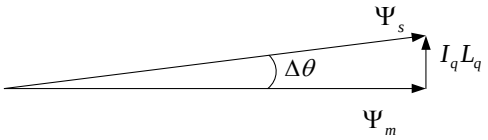

Figure 3.10 Load dependency on stator flux

The shift in the stator flux angle results in a shift in the stator teeth saturation region and the saturated stator yoke region. The angle between the direct axis and the location of the stator flux can be expressed as:

$$\Delta\theta \approx a\sin\left[\frac{i_q L_q}{\sqrt{\psi_M{}^2 + (i_q L_q)^2}}\right] \tag{3.17}$$

Before the resulting saliency model is derived the leakage flux from the load current must be considered. Figure 3.11 illustrates the regions that typically will saturate during a large load current: the region over the slot and the region close to the slot opening. If we consider the control strategy to be I_q =I_s the load dependent saturation will decrease the q-axis leakage inductance.

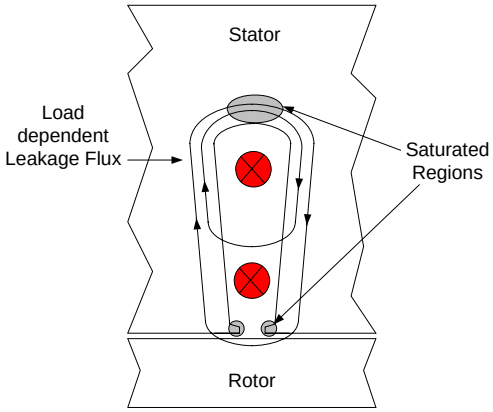

Figure 3.11 Saturation due to Leakage flux from load current

The decrease in the q-axis leakage inductance can be included in the modelled as an additional term in (L_{lds}) the q-axis inductance:

$$L_{q-leakage} = L_{\sigma} - L_{\sigma ts} - L_{lds} \tag{3.18}$$

$$L_{q} = L_{q-main} + L_{q-leakage} = L_{0} + L_{\sigma} - L_{\sigma ts} - L_{lds} \tag{3.19}$$

The angular offset of the air gap flux from the d – axis result in an angular offset for the inductance model:

$$\underline{L} = \Sigma L_{loaded} + \Delta_2 L e^{-j2\theta} + \Delta_3 L e^{-j2(\theta+\Delta\theta)} \tag{3.20}$$

Where:

$$\Delta_2 L = \frac{L_{0rd}}{2} \tag{3.21}$$

$$\Delta_3 L = \frac{-L'_{\sigma ts} + L'_{\sigma ys} + L'_{0ts} + L'_{0ys} - L_{lds}}{2} \tag{3.22}$$

The upper index in the inductance terms indicates that the flux level may increase due to loading (the increase can approximately be assumed to be proportional to Ψ_{ag} / Ψ_{m}). Since the variation in the inductance is modelled as sinusoidal variations the two position varying terms in (3.20) can be modelled as one resulting term:

$$\underline{L} = \Sigma L_{loaded} + \Delta_4 L e^{j\xi} \tag{3.23}$$

Where

$$\xi = a\tan\left(\frac{\sin(\Delta\theta)\Delta_3 L}{\Delta_2 L + \cos(\Delta\theta)\Delta_4 L}\right) \tag{3.24}$$

$$\Delta_4 L = \sqrt{\left(\Delta_2 L + \cos(\Delta\theta)\Delta_3 L\right)^2 + \left(\sin(\Delta\theta)\Delta_3 L\right)^2} \tag{3.25}$$

The inductance model in (3.23) describes the relation between saturation based variations and the rotor design based variations in the leakage and main inductance. In addition the load dependency is included as both a phase shift in the stator flux and local saturation due to heavy load current. The inductance model is by no means an accurate description of the inductance values. The model is developed to increase the understanding of the physics involved when evaluating saliency in different machines at different excitation frequency. This type of modelling can be useful in several ways:

- Selecting of proper excitation frequency for sensorless control
- Development of compensation schemes for sensorless schemes
- Improvement of the saliency ratio for sensorless control purposes trough special machine design

3.2.5 Inductance modulation due to carrier signal

In sensorless control, based on signal injection, the carrier signal can have an influence on the inductance. Two types of modulation will typically occur: induced currents in the permanent magnets and influence of the magnetic work point due to the carrier flux. The permanent magnets are not laminated and the high frequency flux in the rotor can induce currents in the magnets. The flux from the induced currents opposes the carrier flux. This effect will be at maximum when the carrier flux is aligned with the d-axis. In the inductance modelling this effect will lead to a decrease in the d-axis main inductance (this effect has also been modelled as a resistive variation in [6]). The term L_{0rd} includes the effect of relative permeability in the permanent magnets. In order to simplify the model the effects of induced currents in the magnets will also be included in L_{0rd}. Thus:

L_{0rd} -rotor design saliency in main inductance (including relative permeability and induced currents in magnets)

The induced currents will in general be frequency dependent. The frequency dependency is not modelled in detail in this work. The flux from the carrier signal can influence the magnetic work point of the machine. This effect is highly undesirable for some sensorless schemes based on saliency sensing [2-5]. Other sensorless schemes are based on this effect: Consoli [28] use the carrier signal flux influence on the resulting magnetic field as the basis for the sensorless control. This means that the carrier flux alters the saturation in the materials in the machine. In the PMSM used in this work the flux from the permanent magnets are much larger than the carrier flux. The influence of the carrier flux or transient flux on the resulting flux is therefore neglected.

3.2.6 High frequency Inductance measurements on a IPMSM

Prior work in [1] suggested that the high frequency flux resulting from the high frequency current mainly consist of leakage flux. This is natural for an induction machine: in the squirrel cage structure in the rotor there will be induced currents that oppose the high frequency flux. Sensorless control for IPMSM is often regarded advantageous due to the large difference in L_d and L_q. The large difference in L_d and L_q is often considered to exist due to the rotor design. Thus if the high frequency injection methods are supposed to sense this saliency the carrier flux must penetrate into the rotor structure. In order to describe the high frequency machine model the phase and mutual inductance was measured on an IPMSM. The set up is illustrated in Figure 3.12. One of the phases where excited by voltage steps. The first harmonic representation of the transient excitation is a 20 kHz sinus signal (transient excitation further described in Chapter 8). The phase-a current where measured and the induced voltages in the open phases (b and c) where measured. All measurements where measured both within the control system (LEM/ADC/DSP) and with oscilloscopes. The shaft was rotated and the inductance where estimated as a function of the electrical position. Self and mutual inductance estimates are presented in Figure 3.12. In Chapter 1 the basic machine modelling was described. The self and mutual inductance are repeated here for convenience, and the sign of the position dependent term is corrected according to a machine structure shown in Figure 1.1.1:

$$L_a(\theta) = L_{s\sigma} + L_{s0} - L_g \cos(2\theta) \tag{3.26}$$

$$L_{ab}(\theta) = -\frac{L_{s0}}{2} - L_g \cos(2\theta - 120) \tag{3.27}$$

The measurements indicate that there is a difference in the magnitudes of the position dependent terms in the self and mutual inductance. If we assume a position dependent leakage inductance in the phase inductance located in accordance to the saliency modelling in the previous chapter we get:

$$L_{s\sigma}(\theta) = L_{s\sigma 0} - (L_{s\sigma ts} - L_{s\sigma ys})\cos(2\theta) \tag{3.28}$$

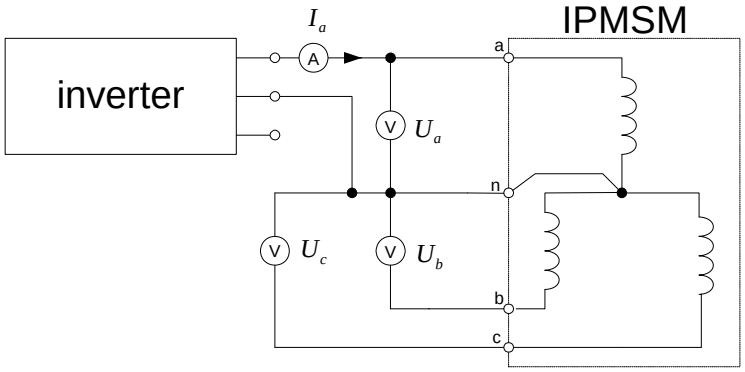

Figure 3.12 Measurements of self and mutual inductance

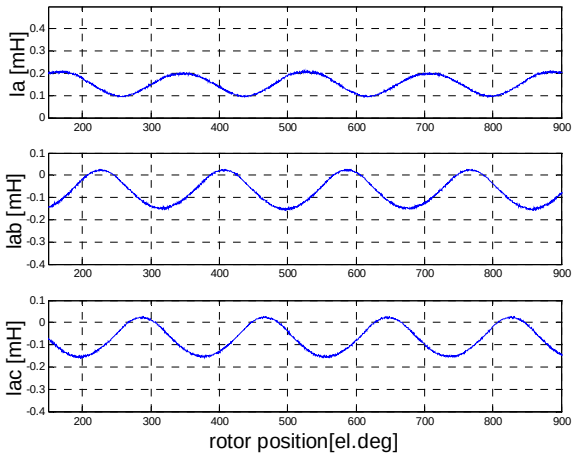

Figure 3.13 Self and mutual (high frequency) inductance phase a, measured with transient excitation

The tooth saturation effect is assumed to dominate over the yoke dependent saturation for the leakage variation. This assumption is based on the FEM simulation where the minimum relative permeability in the teeth where approximately 150 compared to 800 in the stator yoke (Figure 3.6). The leakage flux is not assumed to link with the other phases and the self and mutual inductance high frequency model becomes:

$$L_a(\theta) = L_{s\sigma 0} + L_{s0} + (L_{s\sigma ts} - L_{s\sigma ys} - L_g)\cos(2\theta) \tag{3.29}$$

$$L_{ab}(\theta) = -\frac{L_{s0}}{2} - L_g \cos(2\theta - 120) \tag{3.30}$$

The ratio between the position dependent terms indicates what portion of the saliency that stems from the leakage and main flux. In this case $L_g/(L_g - L_{s\sigma ts} + L_{s\sigma ys})$ is approximately 1.75. In order to relate the saliency modelling to the measured quantities the high frequency machine measurement model ((3.29), (3.30)) is transformed to the dq-frame.

$$L_s^s = \begin{bmatrix} \frac{3L_{s0}}{2} + L_{s\sigma 0} - \frac{3L_g}{2} + \frac{L_{s\sigma ts}}{2} - \frac{L_{s\sigma ys}}{2} & 0 \\ 0 & \frac{3L_{s0}}{2} + L_{s\sigma 0} + \frac{3L_g}{2} - \frac{L_{s\sigma ts}}{2} + \frac{L_{s\sigma ys}}{2} \end{bmatrix} \tag{3.31}$$

Where:

$$\sum L = \frac{3}{2} L_{s0} + L_{s\sigma} \tag{3.32}$$

$$\Delta L = \frac{L_d - L_q}{2} = -\frac{L_{s\sigma ys}}{2} - \frac{3L_g}{2} + \frac{L_{s\sigma ts}}{2} \tag{3.33}$$

Table 3.1 Relation between Theoretical model and Modified standard model

Theoretical model	Modified standard model(measurements)
$L_0 + L_\sigma$	$\frac{3L_{s0}}{2} + L_{s\sigma}$
$L_{0rd} + L_{0ts} + L_{0ys}$	L_g
$L_{\sigma ts}$	$\frac{L_{s\sigma ts}}{2}$
$L_{\sigma ys}$	$\frac{L_{s\sigma ys}}{2}$

In order to describe the relationship between the measured quantities and the theoretical model the no load theoretical model in (3.15) and (3.16) must be compared to (3.32) and (3.33). The mapping of the variables is necessary due to the difference in derivation of the theoretical saliency modelling and the standard saliency modelling. The modelling in this chapter was performed by assuming equal inductance in both axis and subtracting the effects of saturation and rotor structure. In the standard modelling the average inductance term is the basis for the model the variations are superimposed sinus variations. Some of the components in the inductance model can be estimated from the self and mutual inductance. These estimates are given in Table 3.2.

Table 3.2 Estimated inductance terms

L_{s0} [mH]	$L_{s\sigma}$ [mH]	$L_{s\sigma ts} - L_{s\sigma ys}$ [mH]	L_g [mH]	L_d [mH]	L_q [mH]
0.125	0.025	0.0375	0.0875	0.1	0.325

Table 3.1 and 3.2 shows how the difference in the position dependent term in the self and mutual inductance can be included in the machine model by adding a position dependent term in the leakage inductance. In the next main chapter the same estimates will be used in order to estimate the flux distribution in the machine.

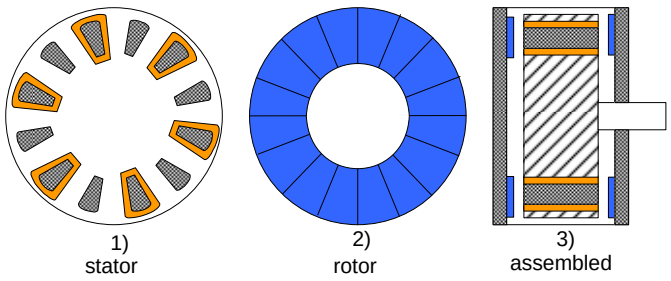

Figure 3.14 Axial flux PMSM

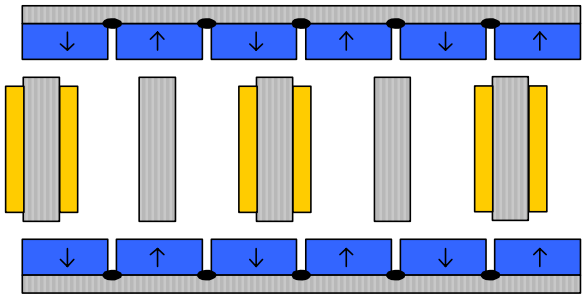

Figure 3.15 Radial Cross section

3.3 Axial flux machines

There are a variety of different axial flux PM designs. In this chapter a double air gap axial flux PM design will be used as an example. The axial flux machine used in this thesis is a prototype machine; a fictive machine is used in this chapter to model the saliency in the machine. In order to model the inductance in the machine one coil will be modelled. The resulting phase inductance can be derived by adding the inductance in the coils as described in Chapter 1. If second order effects (saturation, eccentricity, induced currents) are neglected the axial flux machine has no saliency. The saliency modelling of the axial flux PMSM is therefore only based on second order effects. There are several common factors with the modelling of the radial flux PMSM: the iron powder cores in the axial flux machine can be evaluated in the same manner as the stator teeth of the radial flux machine, the effect of yoke saturation also contributes in the same manner as the yoke saturation of the radial flux machine, and effect of induced currents in the magnets contributes in the same manner as for the radial flux model.

3.3.1 Magnetic loading from permanent magnets

In order to model saliency in the machine saturation effects has to be encountered. The first step in this analysis is to determine the parts of the machine structure that may go into saturation due to the flux from the permanent magnets. The d-axis of the machine will be regarded as the position where the iron powder core is centred under a permanent magnet. The q-axis will be used as the position where the iron powder core is located between two magnets; this is illustrated in Figure 3.16. Some portions of the flux (φ_{2q}) crosses the upper section of the core and in the air between the magnets. The remaining flux (φ_{1q}) flow trough the full length of the core.

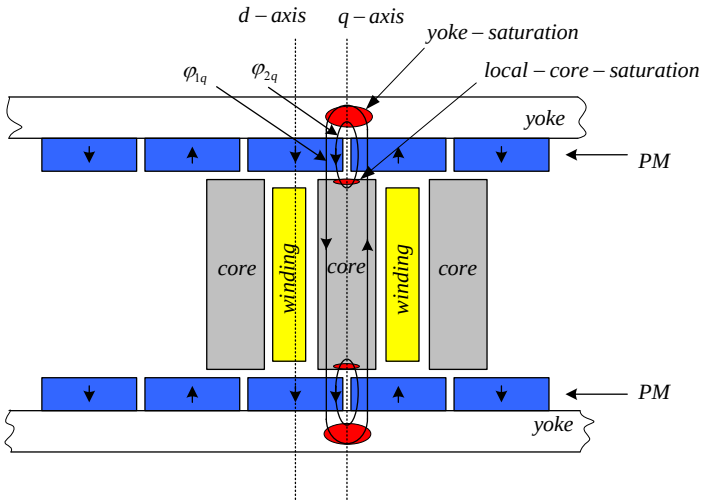

Figure 3.16 Magnetic loading from permanent magnet – core in q- axis

The resulting flux in the core is relative small due to the opposing magnetic field from magnets in different directions. Two areas can potentially be partially saturated due to the magnetic loading from the permanent magnets when the core is located in the q-axis: the top section of the core and the yoke between the magnets. Figure 3.17 shows the flux from the permanent magnets when the core is located in the d-axis. In this position a large portion of the flux (φ_{1d}) links trough the core. A smaller portion of the flux (φ_{2d}) does not link trough the coil but links in the air between the magnets. Two areas can potentially be partially saturated due to the magnetic loading

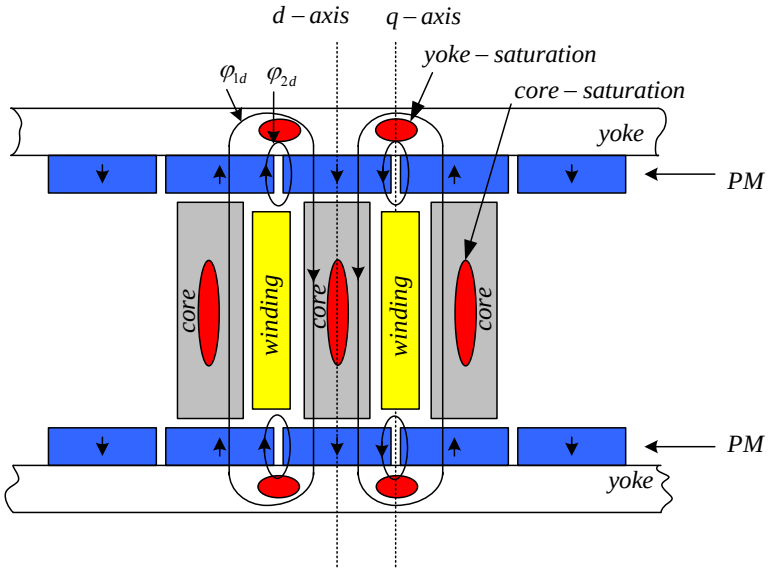

Figure 3.17 Magnetic loading from permanent magnet in d – axis

from the permanent magnets when the core is located in the d-axis: the yoke between the magnets (same as for q-axis position) and the core. The actual design was implemented as a FEM lab model (not presented here as this is a commercial product) and the saturation levels where identified. The yoke saturation between the magnets was found to be large. The local core saturation and core saturation was found to be modest. In the saliency model all the potential areas of saturation is included in order to describe the relations between them.

3.3.2 Main flux path

In the previous section the magnetic loading due to the permanent magnets was considered. Based on the magnetic loading the potential areas of saturation were identified. In this section the inductance of a single coil is derived based on the magnetic loading from the previous section. From the principal view in Figure 3.18 a magnetic equivalent circuit is presented in Figure 3.19. There are two regions that typically saturates due to the magnetic loading from the permanent magnets; the yoke and the core. The core has an average maximum flux density when the core is located in the d- axis. When the core is located in the q- axis there may be local saturation in the core section close to the magnets. The basis for the dq inductance derivation is two equal values for both axes;

$$L_{d-main} = L_0 \tag{3.34}$$

$$L_{q-main} = L_0 \tag{3.35}$$

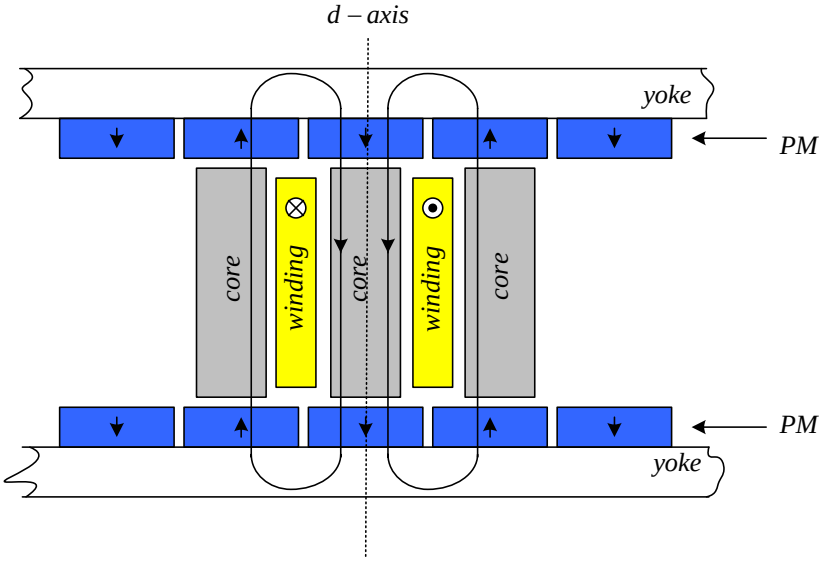

Figure 3.18 Main flux from the stator winding

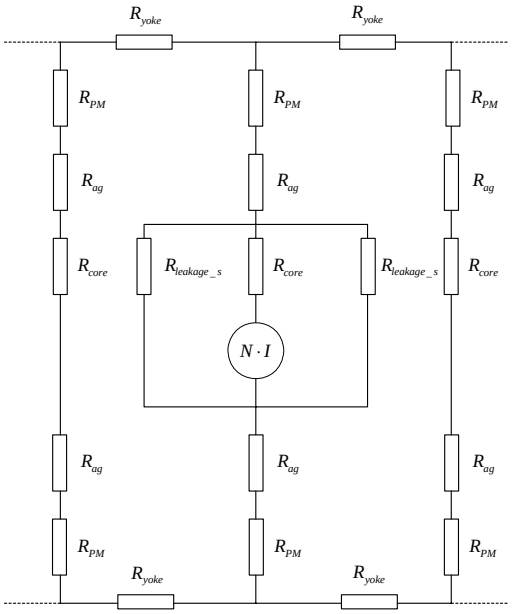

Figure 3.19 Magnetic equivalent scheme for one coil (flux from winding considered, flux form permanent magnet only considered as input to saturation evaluation)

The core saturation in d-axis is included by the term L_{0cs} and the local saturation in the q- axis is included by the term L_{0lcs}. The inductance terms then become:

$$L_{d-main} = L_0 - L_{0cs} \tag{3.36}$$

$$L_{q-main} = L_0 - L_{0lcs} \tag{3.37}$$

The yoke saturation between the magnets has maximum impact when the core is in the d-axis. The term L_{0ys} includes the effect of yoke saturation:

$$L_{d-main} = L_0 - L_{0lcs} - L_{0ys} \tag{3.38}$$

3.3.3 Leakage flux path

The leakage flux paths can be expressed as two constant terms initially.

$$L_{d-leakage} = L_\sigma \tag{3.39}$$

$$L_{q-leakage} = L_\sigma \tag{3.40}$$

A position dependency in the leakage inductance is hard to imagine due to the fact that the flux will have to cross the winding section twice. A position dependent term will be added anyway in order to incorporate this effect for redesign procedures. The core saturation will be included as $L_{\sigma cs}$ and the local core saturation as $L_{\sigma lcs}$. The core saturation will be at maximum when the core is centred in the d-axis (Figure 3.20). The local core saturation will be at maximum when the core is in the q-axis.

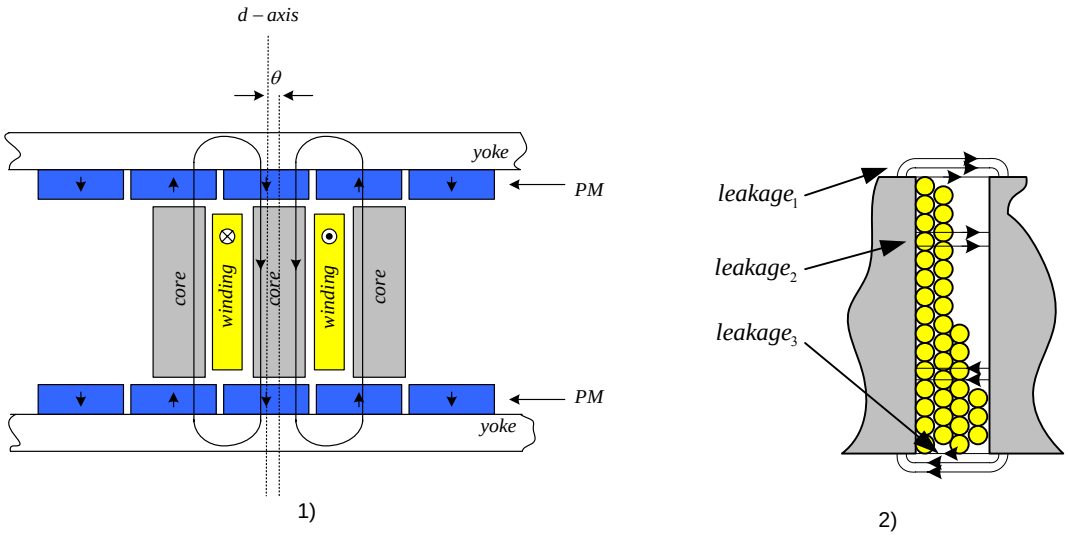

Figure 3.20 Leakage inductance flux path.1: winding in d-axis, 2:leakage flux paths in structure

.The position dependent leakage inductance expressions become:

$$L_{d-leakage} = L_{\sigma} - L_{\sigma cs} \tag{3.41}$$

$$L_{q-leakage} = L_{\sigma} - L_{\sigma lcs} \tag{3.42}$$

3.3.4 Resulting no load inductance

The resulting no load inductance can be represented by the sum of the main and leakage inductance. In order to describe the saliency in the machine the phasor representation of the resulting inductance is presented:

L_0 -basis main inductance evaluated with no saturation

L_{0cs} -influence on main inductance from core saturation when core is in the d- axis

L_{0lcs} - influence on main inductance from local core saturation when core is in q- axis

L_{0ys} -yoke saturation between magnets

L_{σ} -basis main inductance evaluated with no saturation

$L_{\sigma cs}$ -influence on leakage inductance from core saturation when core is in the d- axis

$L_{\sigma lcs}$ - influence on leakage inductance from local core saturation when core is in q-axis

$$L_d = L_{d-main} + L_{d-leakage} = L_0 - L_{0cs} - L_{0ys} + L_{\sigma} - L_{\sigma cs} \tag{3.43}$$

$$L_q = L_{q-main} + L_{q-leakage} = L_0 - L_{0lcs} + L_{\sigma} - L_{\sigma lcs} \tag{3.44}$$

The resulting inductance on vector form becomes:

$$\underline{L} = \Sigma_2 L + \Delta_5 L e^{j2\theta} \tag{3.45}$$

$$\Sigma_2 L = \frac{L_d + L_q}{2} = \frac{2L_0 - L_{0cs} - L_{0lcs} - L_{0ys} + 2L_\sigma - L_{\sigma cs} - L_{\sigma lcs}}{2} \tag{3.46}$$

$$\Delta_5 L = \frac{L_d - L_q}{2} = \frac{-L_{0cs} - L_{0ys} + L_{0lcs} - L_{\sigma cs} + L_{\sigma lcs}}{2} \tag{3.47}$$

3.3.5 Load dependency

In this application the control strategy is typically: I_d=0, I_q=I_s due to the symmetrical structure of the machine. This type of control strategy will be used in this analysis in order to simplify the analyses (optimal control based on $L_d \neq L_q$ not considered). The load dependency from a load current in the q-axis is illustrated in Figure 3.21. The black flux lines illustrates the flux from the windings, the red flux lines represent the flux from the magnets. The area with yoke saturation can potentially be shifted due to high load currents (I_d=0, I_q=I_s) as indicated in Figure 3.21. This is comparable to the saliency shift found in radial flux machines. As the load current increases the flux density in the core increase, this is included in the machine model as load dependent decrease in the q-axis inductance.

$$L_q = L_{q-main} + L_{q-leakage} + L_{q-load-dependent} = L_0 - L_{0lcs} + L_\sigma - L_{\sigma lcs} - L_{\sigma ldcs} \tag{3.48}$$

The loading of the machine will potentially have two effects: the yoke saturation is shifted and the saliency ratio changed (due to the reduction of q-axis inductance). The resulting inductance on vector form becomes:

$$\underline{L} = \Sigma_2 L_{loaded} + \Delta_5 L e^{j2\theta} + \Delta_6 L e^{j2(\theta+\Delta\theta)} \tag{3.49}$$

Where:

$$\Sigma_2 L_{loaded} = \frac{L_d^{'} + L_q^{'}}{2} = \frac{2L_0^{'} - L_{0cs}^{'} - L_{0ys}^{'} - L_{0lcs}^{'} - L_{0ldcs}^{'} + 2L_\sigma^{'} - L_{\sigma cs}^{'} - L_{\sigma lcs}^{'}}{2} \tag{3.50}$$

$$\Delta_5 = \frac{-L_{0cs}^{'} + L_{0lcs}^{'} + L_{0ldcs}^{'} - L_{\sigma cs}^{'} + L_{\sigma lcs}^{'}}{2} \tag{3.51}$$

$$\Delta_6 L = \frac{-L_{0ys}^{'}}{2} \tag{3.52}$$

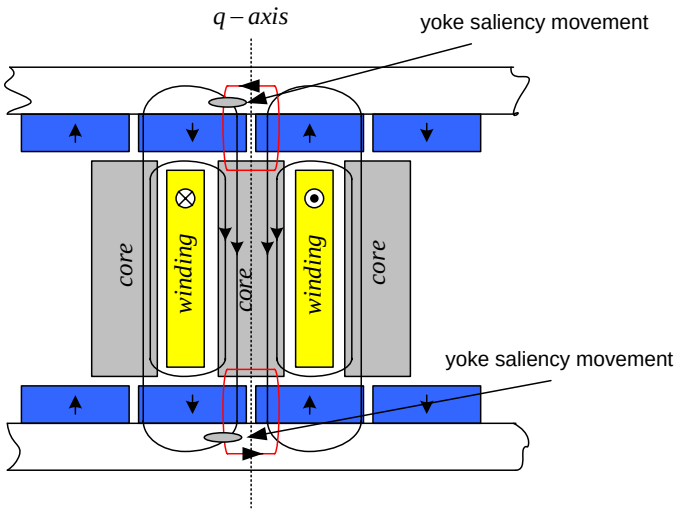

Figure 3.21 Loaded machine. Red lines represent flux from coil, blue lines flux from magnets

The upper index on the inductance terms indicated that these quantities may change due to loading. Since the variation in the inductance is modelled as a sinusoidal variation the two position varying terms becomes:

$$\underline{L} = \Sigma_2 L_{loaded} + \Delta_7 L e^{j\xi} \tag{3.53}$$

$$\xi = a\tan\left(\frac{\sin(\Delta\theta)\Delta_6 L}{\Delta_5 L + \cos(\Delta\theta)\Delta_6 L}\right) \tag{3.54}$$

$$\Delta_7 L = \sqrt{\left(\Delta_5 L + \cos(\Delta\theta)\Delta_6 L\right)^2 + (\sin(\Delta\theta)\Delta_6 L)^2} \tag{3.55}$$

3.3.6 Inductance modulation due to carrier signal

As for the radial flux PMSM there may be some effects from the carrier signal if a carrier signal is used to estimate the inductance. Two phenomena's will typically occur: induced currents in the magnets and influence on the magnetic work point due to the flux from the carrier signal. The permanent magnets are not laminated and the high frequency flux in the rotor may induce currents in the magnets. The flux from the induced currents opposes the carrier flux. This effect will be at maximum when the carrier flux is aligned with the d-axis. In the inductance modelling this effect will lead to a decrease in the d-axis main inductance. The term L_{0rd} includes the effect of relative permeability in the permanent magnets. In order to simplify the model the effects of induced currents in the magnets will also be included in L_{0rd}. Thus:

L_{0rd} -rotor design saliency in main inductance (including relative permeability and induced currents in magnets)

The induced currents will in general be frequency dependent but this is not included in this work. The flux from the carrier signal can influence the magnetic work point of the machine. In the axial flux PMSM used in this work the flux from the permanent magnets are much larger than the carrier flux. The influence of the carrier flux or transient flux on the resulting flux is therefore neglected.

3.3.7 Model validation

The axial flux PMSM and the converter are still in the prototype phase. Due to limited access to the converter for this machine the experimental work and verification of the machine model are limited. In the next main chapter the saliency of the axial flux machine (Test Machine 2) is documented by using a rotating carrier signal at difference frequencies (Figure 4.7 and Figure 4.8). The measurements show a frequency dependency in the saliency: at a carrier frequency equal 100 Hz the saliency ratio is approximately 0.08, when the frequency was increase to 250 Hz the saliency ratio was close to zero. This frequency dependency indicates that the saliency detected at 100 Hz is the saturation in the yoke between the magnets. When the frequency was increased induced currents in the magnets and the stator yoke prevented the carrier flux from penetrating into the yoke. At carrier frequencies at 250 Hz and higher the flux was assumed to distribute in the leakage flux paths. At these frequencies no saliency was detectable. Thus the local core saturation and the core saturation were not detectable in this design (Test Machine 2). The effect of induced currents in the magnets due to the carrier signal was not tested on this machine. In order to test for such phenomena the carrier signal must be varied over a much larger frequency. An extended experimental study of the saliency phenomena's in this machine is scheduled for future work.

3.4 Chapter conclusions

In this chapter new saliency models has been developed for two machines: an axial flux PMSM and a radial flux IPMSM. The saliency models developed in this chapter includes: saturation, rotor designed saliency and saliency due to induced currents in the magnets. The model is based on separate modeling of main and leakage inductance in this way the saliency can be evaluated based on what flux path a carrier flux will distribute in. Due to the many simplifications in the modeling the models are not exact models but rather models that describe the relation between the different sources of saliency. In the first part a radial flux IPMSM (Test Machine 1) was modeled. The saliency model includes a position dependent term in the leakage inductance 90 electrical degrees spatially shifted from the variations in the main inductance. Measurements performed on the IPMSM showed that the position dependent terms in the main and mutual inductance had different magnitude. This can be included in the machine model by using position dependent leakage inductance.

4 HIGH FREQUENCY FLUX DISRIBUTION FOR DIFFERENT EXCITATION METHODS

In this chapter the two major excitation methods for sensorless control is evaluated in order to determine the high frequency flux component distribution in machines. For sensorless control it is of great interest to establish knowledge of whereas the high frequency or transient signals produce flux in the main or in the leakage regions of the machines.

4.1 Basic excitation methods

There are a lot of different low and zero speed sensorless schemes, but the common factor for most of them is the use of additional excitation in order to extract the saliency information. The additional excitation can be divided into two categories:

- High Frequency Carrier Injection (HFCI-R and HFCI-P)
- Transient Excitation

In the HFCI based schemes the carrier frequency can be chosen in a wide frequency range depending on the switching frequency. For a drive with switching frequency at 10 kHz the typical range for the carrier would be 500 – 2000 Hz. The lower frequency is determined by the need of frequency separation in filtering and torque oscillations due to the carrier. The upper frequency limit is given by the ability of producing a high resolution in the modulation of the carrier signal. The frequency of the carrier signal will influence the resulting carrier flux in the machine. When transient excitation is applied the resulting "frequency" is not given. One approach is presented in [36] where the 1. harmonic of the pulse is used to indicate the frequency of the transient excitation.

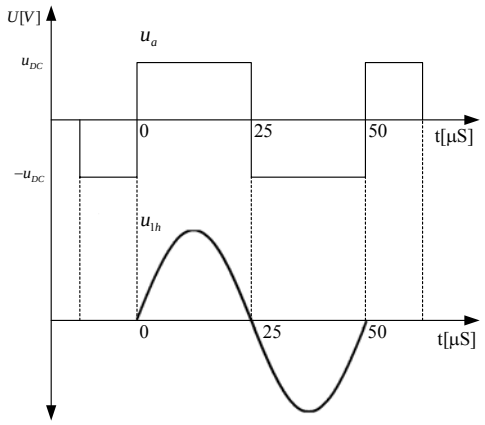

Figure 4.1 First harmonic representation of the transient excitation

In Figure 4.1 the transient excitation used in this work is shown in the upper part. The derivative of the current is calculated by sampling the current at time instances 0, 25 and 50 us. The first harmonic of the transient excitation is indicated in the lower plot in Figure 4.1. The first harmonic representation has a frequency equal 20 kHz.

4.2 Flux penetration in laminates

High frequency flux distribution in laminations has been focus for several papers and dissertations [13, 45, 64, 65]. Usually the focus for these publications [64, 65] is loss calculations: the flux density and eddy currents in each lamination are often the goal for this type of work. In this work the losses are not the main focus but rather the flux distribution in the radial direction. The FEM tool available for this work has been a 2D simulation tool. The physics involved is of a three dimensional nature. Thus in order to understand how the skin effect influence the flux distribution a simple model is used: Figure 4.2.1 illustrates an AC-machine with sinusoidal current distribution in the stator (direction/location represented by two conductors). The main flux is indicated with two flux lines. Side view of one lamination is shown in Figure 4.2.2. The thickness of the lamination (d) is not representative for the real machine (the thickness is made much larger in order to illustrate the flux directions). In the IPMSM (Test Machine 1) the ratio between d/h is 34. When the d/h ratio is large (and the thickness d is small) the skin effect in the radial direction is small compared to the skin effects in the axial direction. One way of illustrating the lamination skin effect [75] is to consider the same flux density at the surface (B_0) of the lamination for different frequencies. In order to define the flux distribution the penetration depth, δ, must be calculated (4.1).

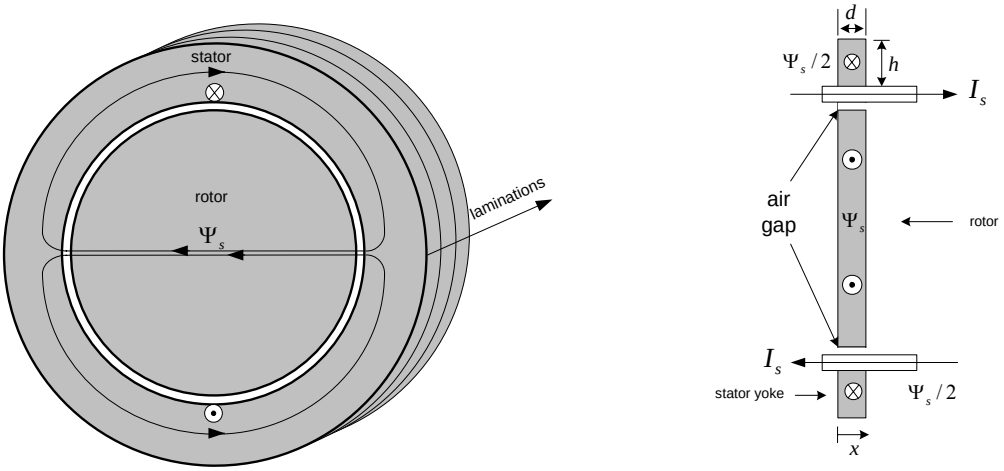

Figure 4.2 AC-machine, 1: main flux in front view, 2: side view one lamination

$$\delta = \sqrt{\frac{2}{\mu\sigma\omega}} \tag{4.1}$$

Where σ is the conductivity, ω angular frequency and μ the permeability of the core material. The normalized flux distribution can be expressed as:

$$B(x) = B_0 \frac{(e^{-x/\delta} + e^{(x-d)/\delta})}{1 + e^{-d/\delta}} \tag{4.2}$$

Where $0 < x < d$. The relative flux distribution for different frequencies is plotted in Figure 4.3.1. In this example a relative permeability equal 10000 is used. The "effective area" is reduced with increasing frequency. If the same amount of flux is passing in the laminate the flux density increases. In order to represent the effective relative permeability several factors must be considered: the effective area reduces, the flux density increases (locally) and the area close to the surface may go into saturation. In order to get an idea of the relations the effective area can be compared to the total area:

$$\frac{effective\_A}{total\_A} = \frac{\int_0^d \frac{(e^{-x/\delta} + e^{(x-d)/\delta})}{1 + e^{-d/\delta}} dx}{d} = \frac{2\sqrt{2}}{d\sqrt{\mu\sigma\omega}} \tanh\left(\frac{d\sqrt{\mu\sigma\omega}}{2\sqrt{2}}\right) \tag{4.3}$$

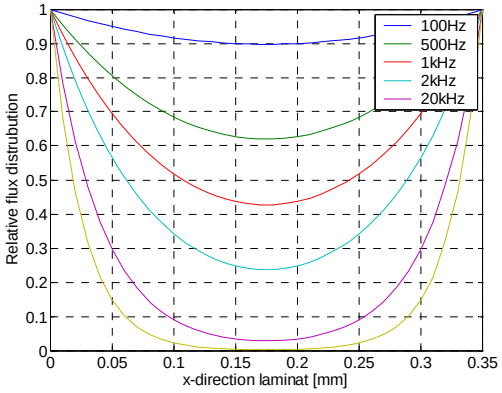

1)

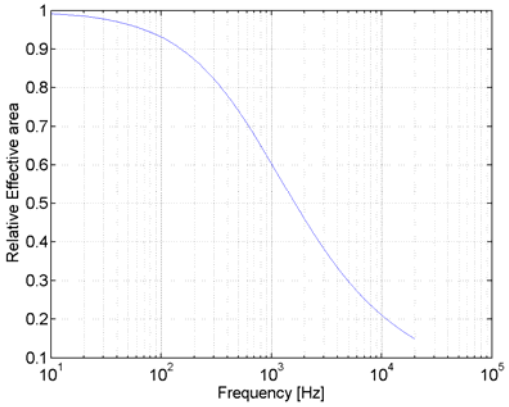

2)

Figure 4.3 1:relative flux distribution, 2: Relative effective area in percentage $\mu_r = 10000$, $\sigma = 1.85x10^6 S/m$

The effective area in percentage of the total area is shown in Figure 4.3.2. The skin effect can be evaluated in several ways. If the radial flux distribution is the point of interest the skin effect can be evaluated as a frequency dependency in the relative permeability. The "relative effective area" curve in Figure 4.3.2 can be used as an approximation to the relative permeability reduction factor.

The laminations in Test Machine 1 were supplied from Congent. The laminations (M235-35A) where 0.35 mm thick and had a conductivity equal $1.85x10^6$S/m. BH curves (from supplier) for this material is plotted in Figure 4.4.1, the relative permeability (Figure 4.4.2) is derived from the BH curves (measurement error distorts the relative permeability curves for 100 and 200 Hz). From Figure 4.3 and lamination data it is likely that the laminations will have skin effect for the frequency region from 500 Hz to 20 kHz. The distribution of the high frequency flux will tend to be higher near the surface of the laminations and the reluctance will increase when the frequency increase. In sensorless control the radial distribution of the high frequency flux is of great interest. As for the saliency modelling the main flux and the leakage flux components will be evaluated separately. The frequency dependency for the *main flux* is evaluated first.

The main flux is illustrated in Figure 4.2.1. The flux flows trough the stator yoke and rotor structure. Compared to the leakage flux the main flux path consists of a long path trough the laminate material. Skin effects are will appear as the frequency increases; Figure 4.3.2 shows a theoretical approximation of the skin effects in the laminates for the main flux. The *leakage flux path* is illustrated in Figure 3.8. This flux path is dominated by a large air gap and a relative short path trough the laminate; the skin effects in the laminations is assumed to have less influence on the leakage flux magnitude.

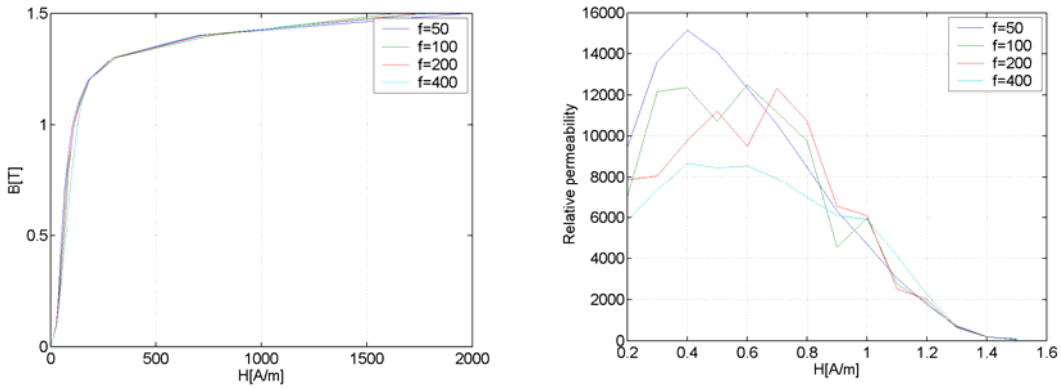

1) 2)

Figure 4.4 Congent M235-35 lamination, 1:BH curves, 2: relative permeability

The resulting radial distribution is assumed to be dominated by the main flux for lower frequencies. As the frequency is increased the main flux is reduced and at high frequencies the leakage flux is assumed to dominate the radial flux distribution. Inductance measurements was performed on an IPMSM and an axial flux PMSM in order to determine the frequency regions where the main flux dominates and where the leakage flux dominates,.

The permanent magnets have a certain level of conductivity; circulating currents can be induced in the magnets when the high frequency flux tries to penetrate into the magnets. This effect adds to the saliency effect that the magnets have for IPMSM (i.e. reduces the d-axis inductance). This effect was included in the saliency model in the previous chapter. In the surface mounted PMSM's the effect could in fact be used as a saliency effect. This is used in [6] for initial position estimate.

4.3 Inductance measurements

The simplest way of determining the frequency dependency in the inductance is to perform measurements of the inductance as a function of position and frequency. This has been done in several papers and PhD reports [3, 13, 25] for a variety of machines. In [3] inductance measurements where performed on an IPMSM. The frequency range in [3] was 500 to 2000 Hz and the inductance where approximately constant in this frequency region. In [25] an IPMSM was also applied; the frequency range was 100 to 700 Hz. In this work the saliency ratio was approximately constant for the actual frequency region. In [13] an induction machine with modified rotor slots was tested. A larger frequency range was cowered (60Hz – 30kHz). The saliency ratio ($\Delta Z / \sum Z$) had a characteristic maximum in the region 1-5kHz. For higher carrier frequency the saliency ratio decreased. The increase in the saliency ratio for frequencies below 1 kHz was assumed to result from the skin effect in the induced currents in the rotor (forcing

more of the flux to the rotor surface where the modified slot with determines the inductance). The decrease in saliency ratio for frequencies over 5 kHz where assumed to be caused by the skin effect in the laminations. The actual lamination thickness used in [13] was not given.

4.3.1 Inductance measurements on the IPMSM

The measurements in this section were made on a IPMSM (Test Machine 1) with 0,35 mm laminations both in stator and rotor. The frequency dependency was measured by using the inverter. The rotor was locked and a high frequency balanced carrier signal was injected in the machine. The currents where logged and the characteristic ellipse plot in stationary stator reference where plotted. In order to determine the d and q axis characteristic current the length of the major and minor axis where representing the d- and q-axis current. The terminal impedance where represented by dividing the carrier voltage amplitude with the characteristic d- and q-axis current. The standard switching frequency for the system was 10 kHz. The frequency range of the carrier signal was limited by the switching frequency. In order to produce higher carrier signal the switching frequency of the inverter was increased. The practical maximum switching frequency was 40 kHz (DSP run time, and dead time limitations). The dead time in the inverter was fixed to 3 us. In order to avoid large dead time effects the DC-bus voltage was lowered from 300 V to 86 V, thus the pu voltage command could be bigger for lower voltages. Two measurement series was taken: f_{sw} =10kHz covered the frequency from 100 to 1000 Hz, f_{sw} =40kHz covered from 500 to 8100 Hz. The lower limit for the f_{sw} =40kHz test was caused by the dead time becoming large compared to the commanded duty cycle for low output voltages (the lowest duty cycle used was 0.4 for f_c= 500 Hz). In addition to the continuous high frequency carrier measurements, transient excitation was applied. The transient excitation can be considered as an equivalent 20 kHz signal by considering the first harmonic representation [36]. In Figure 4.5.1 the saliency ratio as a function of the carrier frequency is plotted. The saliency ratio increase in the entire frequency region (maximum=0.44 at 8100Hz). The transient excitation resulted in a saliency ratio at 0.43. Thus the maximum saliency ratio is assumed to be located between 8.1 and 20 kHz.

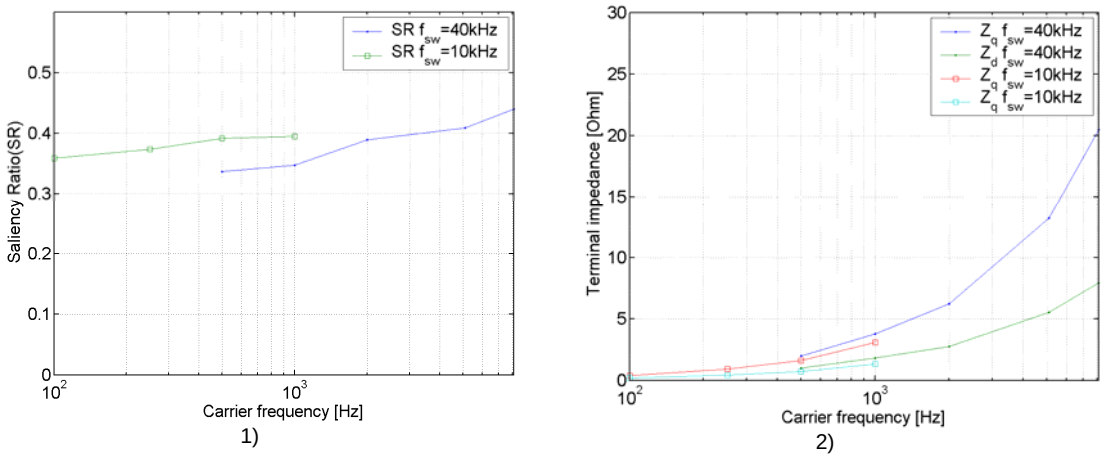

Figure 4.5 Measurements on Test Machine 1, 1: saliency ratio, 2: terminal impedance

The saliency ratio decrease for frequencies higher than 20 kHz is assumed to be caused by lamination skin effect. If skin effect in the laminations is extreme the high frequency flux distributes on the surface of the stator teeth (only leakage flux) and no detection of the rotor saliency is possible. At such extreme skin effect there would also be little penetration in the stator teeth and yoke where the saturation based saliencies are located. As the saliency ratio increase for the frequency region in Figure 4.5.1 there can not be an extreme skin effect in the laminations. At 20 kHz the skin effect is reducing the saliency ratio but not to a great extend. The terminal impedance is plotted in Figure 4.5.2. A logarithmic x-axis is used in order to visualize the transition between the f_{sw} =10kHz and f_{sw} =40kHz measurement series. Due to the inverter dead time the voltage applied to the machine is reduced for the f_{sw} =40kHz measurement series compared to the f_{sw} =10kHz measurement series. As the commanded voltage is used in the estimation of the terminal impedance the estimated terminal impedance is larger compared to the f_{sw} =10kHz measurement series. Despite the difference in the actual and commanded voltage the trends in the measurements are equal. When the terminal impedance is plotted on a linear x-axis (Figure 4.6.1) a linear relationship between impedance and frequency can be seen from 100 Hz to 8.1 Hz. The apparent knee at 1 kHz is due to the dead time effect for the f_{sw} =10 kHz measurement series. The linear relationship indicates that the impedance is dominated by the reactance in the entire frequency range. In Figure 4.6.2 the inductance is plotted (the resistance is neglected). The inductance decreases in the entire frequency range. If the plot of the effective area (Figure 4.3.2) is compared to the inductance plot (Figure 4.6.2) a close relation can be seen. The decrease in the inductance is thus assumed to be caused by the skin effect in the laminations. The main conclusion from the frequency test is that a portion of high frequency flux penetrates into the rotor for the entire frequency range (100-8100 Hz). In the transient test (20 kHz) the saliency ratio is reduced and the skin effect in the laminations is reducing the amount of “main” flux penetration in rotor and stator.

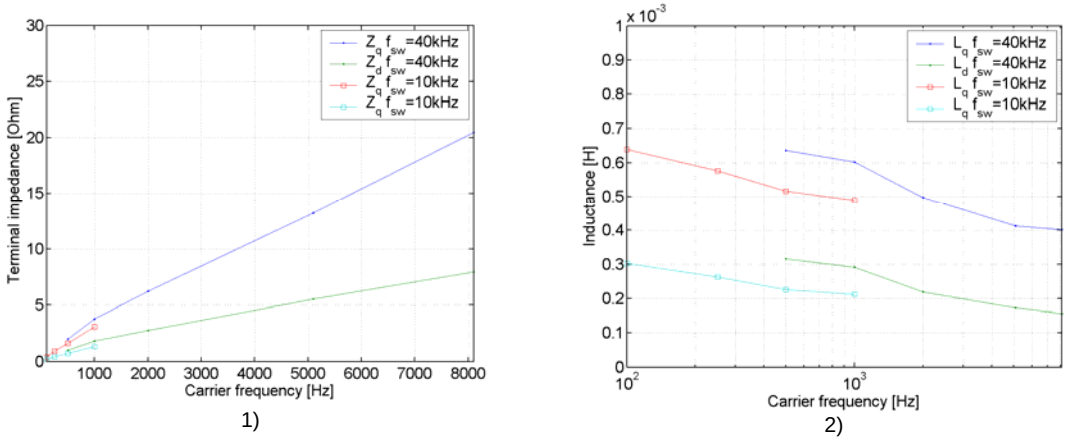

1) 2)

Figure 4.6 Measurements on Test Machine 1, 1: terminal impedance (linear x-axis), 2: 2: dq-inductance

The reduction is not extreme but the skin effect is increasing in the entire frequency region (100- 20 kHz). The increasing saliency ratio in the frequency region 100- 8100 Hz is assumed to be cased by induced currents in the permanent magnets. This effect adds to the saliency and contributes more than the reduction of "main" flux in the rotor and stator as a result of the lamination skin effect. At 20 kHz the saliency ratio is decaying, the leakage inductance is less sensitive to frequency compared to the main inductance (the leakage flux crosses a larger air gap than the main flux). From the measurement series presented in Chapter 3 the levels of main and leakage flux may be evaluated (transient excitation 20 kHz equivalent). According to the saliency model in Chapter 3 there should be a 90 degree shift in the saliency position depending on if the variation in the main or in the leakage flux dominates. In this work the position dependency in the main flux dominates over the leakage flux. This was verified by locking the rotor and applying signal injection at various frequencies (0.1-8kHz). Under this test the estimated saliency position (d-axis estimate) was equal for all frequencies. From the estimated inductances in Table 3.2 (estimated with transient excitation, 20 kHz equivalent) the transient flux linkage components may be estimated:

$$L = \frac{\Psi}{I} = \frac{N\phi}{I} \tag{4.4}$$

The inductance measurements give a good indication of the flux linkage components and they also indicate the level of main and leakage flux. In the definition of inductance (4.4) one of the factors that give an uncertainty in the flux levels is the number of turns (N) that the actual flux links trough. The main flux links all the turns in the winding but this is not the case for the leakage flux. Even tough the flux levels cannot be estimated directly from this kind of test the flux linkage values give an indication of the leakage and main flux level. In this work the amount of main flux was surprisingly high considering the transient excitation used for the measurements (20 kHz equivalent).

Table 4.1 Transient flux linkage distribution (20 kHz equivalent)

Flux linkage components	Amount of total (constant or position dependent)
Main flux linkage constant part	83 %: $L_{a0}/(L_{a0}+L_{a\sigma})$
Leakage flux linkage constant part	17 %: $L_{a\sigma}/(L_{a0}+L_{a\sigma})$
Main flux linkage position dependent part	70 %: $L_g/(L_g+L_{a\sigma ts}-L_{a\sigma ys})$
Leakage flux linkage position dependent part	30%: $(L_{a\sigma ts}-L_{a\sigma ys})/(L_g+L_{a\sigma ts}-L_{a\sigma ys})$

When considering the results in Table 4.1 one must recall that this machine (Test Machine 1) has a rated frequency equal 167 Hz. During field weakening the maximal fundamental frequency is approximately 500-600 Hz. Thus this machine is a special designed machine with thin lamination compared to a standard machine designed for 50 Hz. The results in Table 4.1 show that the position dependent part of the main flux is larger than the position dependent part of the leakage flux. The inductance estimates in Table 3.2 indicates that the flux in the main flux path dominates the resulting flux for excitation frequencies ranging from 0.1 to 20 kHz.

4.3.2 Inductance measurements on a axial flux PMSM

Test Machine 2, the axial flux PMSM, has different materials compared to the radial flux machine. The cores are made of iron powder, the magnets are surface mounted and the yoke is made of solid iron. The machine is illustrated in Figure 3.14 and Figure 3.15. This machine has a different high frequency response compared to the machines with laminated stator and rotor. As these measurements where made in an early stage of the PhD work the inductance was not directly measured. In this early stage position dependency in the high frequency current response was measured. The measurements still gives an indication of the frequency dependency in the position dependent inductance term. The frequency dependency in the “inductance” was measured with balanced three phase voltage applied to the stator windings. The rotor was locked and the current response in the stationary alpha/beta frame was logged for different rotor positions. Saliency was detectable when the carrier frequency was 125 (saliency ratio approximately 0.08). This is shown in Figure 4.7. The major axis of the ellipse indicates the double rotor position. The saliency measured at 125 Hz is a saturation based saliency in the yoke between the magnets (verified by FEM simulations). As the frequency was increased the saliency ratio approached zero and the alpha beta currents became circular (Figure 4.8). This indicates that the high frequency flux no longer penetrates into the rotor yoke. Induced currents are likely to occur both in the permanent magnets and the solid iron in the yoke.

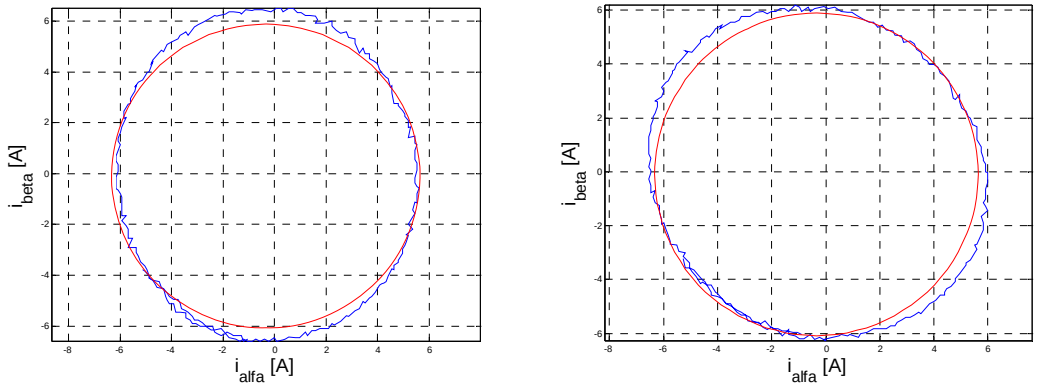

Figure 4.7 I alpha and I beta for two positions; excitation 125 Hz - 6 A(blue), the red circle indicates the case if the machine is symmetrical

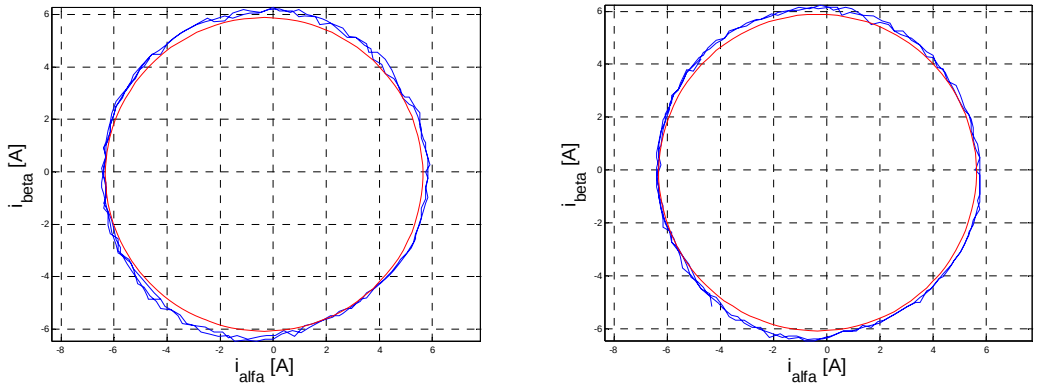

Figure 4.8 I alpha and I beta for two positions; excitation 250 Hz - 6 A, the red circle indicates the case if the machine is symmetrical

The measurements performed at the axial flux PMSM (Test Machine 2) shows that the high frequency flux distribution can be highly frequency dependent for some machines. Transient excitation where also tried on Test Machine 2. The transient excitation based scheme could not detect position dependency.

4.4 Chapter Conclusions

In this chapter the different excitation signals used in sensorless control is evaluated in terms of high frequency flux distribution in the machine. In general there are two types excitation for high frequency injection schemes: continuous high frequency injection in the range 500 – 2000 Hz and transient excitation with equivalent frequency at 10-20

kHz. The saliency ratio was evaluated on two machines for different excitation methods and different excitation frequencies.

For sensorless control of AC machines the high frequency flux distribution is of great interest. This distribution describes the saliency regions that the high frequency flux can detect. In this chapter the effects of lamination skin effect is described. Traditionally the effect of lamination skin effect has been described as forcing the high frequency flux to distribute around the stator slot as a leakage flux. The term “high frequency” is rather undefined. Based on the work in Chapter 3 and the work in this Chapter the flux distribution was evaluated for an IPMSM. The experiments performed in these two chapters indicate that parts of the carrier flux penetrated the rotor structure in the frequency range 0.1 to 20 kHz. Table 4.1 shows estimates of the flux linkages associated with the different inductance terms developed in Chapter 3. The percentages given in Table 4.1 can be used indirectly to evaluate the portions of leakage flux and main flux when transient excitation is used to estimate the inductance. The saliency characteristics of the IPMSM indicates that the schemes based on high frequency injection (HFCI-R and HFCI-P) and the schemes based on transient excitation can be used to detect the saliency due to the rotor saliency (relative permeability in magnets and induced currents in the magnets).

The second machine was an axial flux PMSM with surface mounted magnets. This machine had a saturation based saliency in the yoke behind the magnets. Due to the solid structure of the yoke and the permanent magnets the saliency was only detectable at low frequency carrier injection (125 Hz). The magnets cover most of the surface facing the windings and the induced currents in magnets and yoke prevent the high frequency flux from penetration into the yoke. When the carrier signal was 250 Hz or higher (and for the transient excitation) no saliency could be detected in the machine The frequency dependency of the saliency makes the machine not suitable for high frequency (500 Hz and higher) injection based sensorless control. The same machine is revisited in Chapter 10 where a redesign approach is used in order to introduce saliency in the high frequency flux paths.

5 EXPERIMENTAL SETUP

5.1 Electrical Machines

Four different machines were used in this thesis. The machine used for testing of the different schemes was an Interior Permanent Magnet Synchronous Machine (IPMSM). This machine is referred to as Test Machine 1. Test Machine 1 has 0.35 mm thick laminations in stator and rotor, skewed rotor and virtually no cogging torque. Test Machine 1 has a single saliency and is ideal for injection based sensorless control. Initially the machine was water cooled. The original machine data is given in Table 5.1. These values where not used in the setup. The inverter available for this work was 20 kW. Thus the machine was de-rated to the parameters in Table 5.2 and the water cooling was not used.

Table 5.1 Test Machine 1 original motor data

P_N [kW]	U_N [V]	I_N [A]	n_N [rpm]	R_s [Ω]	L_d[mH]	L_q[mH]	p
30	110	181	2500	0.011	0.123	0.381	4

It should be noted that the rated frequency for this machine is 167 Hz. The machine was tested at 500 Hz during field weakening at 8000 rpm. This illustrates some of the high frequency flux characteristics in this machine; the machine can be operated at very high fundamental frequency.

Table 5.2 Test Machine 1 de-rated motor data

P_N [kW]	U_N [V]	I_N [A]	n_N [rpm]	R_s [Ω]	L_d[mH]	L_q[mH]	p
15	110	90	2500	0.011	0.123	0.381	4

Table 5.3 Test Machines 2-4 motor data

P_N [W]	U_N [V]	I_N [A]	n_N [rpm]	R_s [Ω]	L_d[mH] (50Hz)	L_q[mH] (50Hz)	p
250	12	13	150	0.115	0.131	0.153	19

The other type machine was an axial flux permanent synchronous machine. Three different designs of this machine were used. Ratings for these machines were identical (Table 5.3). Test Machines 2-4 are designed to be integrated in the wheels of wheelchairs. The magnets are surface mounted. Test Machines 2-4 are disc shaped and had a high number of poles. The first prototype (labelled Test Machine 2) was a concept prototype. The initial saliency measurements where tested on this machine and this work were also the basis for the work done in [36]. The next stage was an optimized machine, this machine has reduced air gap and reduced magnet thickness (labelled test Machine 3). The last machine is the machine that was redesigned for sensorless control (labelled test Machine 4).

5.2 Inverter

The inverter and rectifier used in the experimental work are developed in the Power Electronics group at NTNU and at SINTEF Energy AS. The inverter ratings are 20 kW, DC-voltage 0- 650V, 3300uF Capacitor bank, 70 A maximum continuous current at 300 V DC and recommended switching frequency in the range 0 – 25 kHz. The converter module has gate drivers, hardware dead time generation and current limitations. The hardware dead time in this converter is approximately 1.6 us [63].

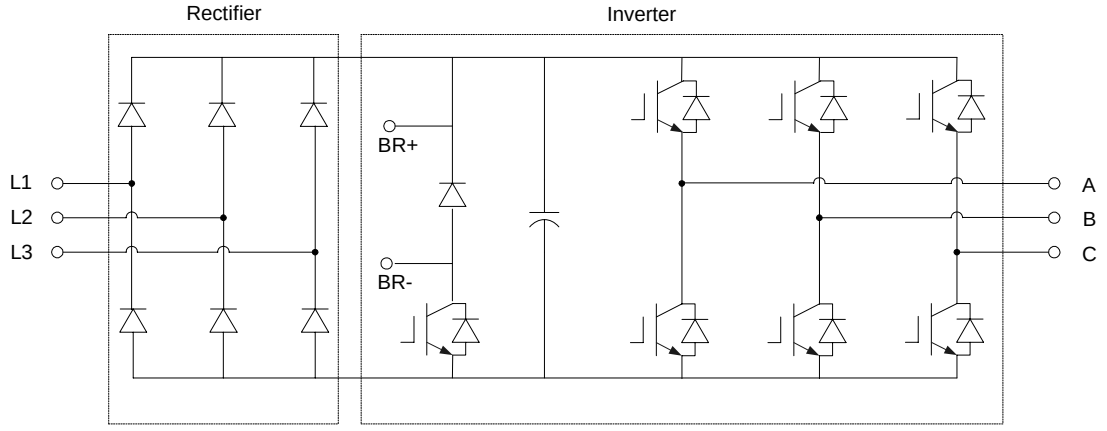

Figure 5.1 Inverter and rectifier

5.2.1 Effects of phase current zero crossing

There is a delay between the turn on command and the actual turn on of the IGBT. The same phenomena can be found for the turn off sequence. In [57,68] these effects were analysed in order to approximate the resulting delay, the analyses is repeated here for convenience. There are several contributors to these delays: delay between DSP output to IGBT drivers (d-Figure 5.2) and delay from drivers to the actual gate emitter signal change (denoted $t_{d(on)}$ and $t_{d(off)}$ in Figure 5.2). In addition the IGBT it self adds delays according to the IGBT's turn on and turn off characteristics. As the rise time of the current is a part of the delay the delays will be dependent on the amplitude of the current in the inverter leg. Thus in order to avoid cross conduction in the leg a delay is added in the control signal for the turn on operation. This delay will be denoted blanking time (t_{bl}). The blanking time can be realized in the DSP or in hardware as a part of the inverter. In the experimental set up both options are available but the hardware solution is used. The operation of an inverter leg is dependent on the current flow in the leg and the on/off condition of the switches. First we consider the two possible turn off cases:

- if the current is flowing into the inverter leg and the upper switch (T_{A+}) turns off (and the lower switch T_{A-} turns on after a delay)
- if the current is flowing out of the branch and the lower switch (T_{A-}) is turned off (and the upper switch T_{A+} turns on after a delay)

Under these conditions the turn off delay can be approximated as:

$$t_{\Delta 1} \approx t_{d(off)} + \frac{t_{rv}}{2} \tag{5.1}$$

Turn on delay will appear if:

- the current is flowing out of the inverter leg and the lower switch (T_{A-}) turns off (and the upper switch T_{A+} turns on after a delay)
- the current is flowing into the branch and the lower switch (T_{A+}) is turned off (and the upper switch T_{A-} turns on after a delay)

Under these conditions the turn on delay can be approximated as:

$$t_{\Delta 2} \approx t_{bl} + t_{d(on)} + t_{ri} + \frac{t_{fv}}{2} \tag{5.2}$$

In the approximation of $t_{\Delta 2}$ the effects of t_{fv2} is assumed to be small. The resulting delay can be approximated as the blanking time and the difference of the turn on and turn off delay. This delay is typically called the dead time:

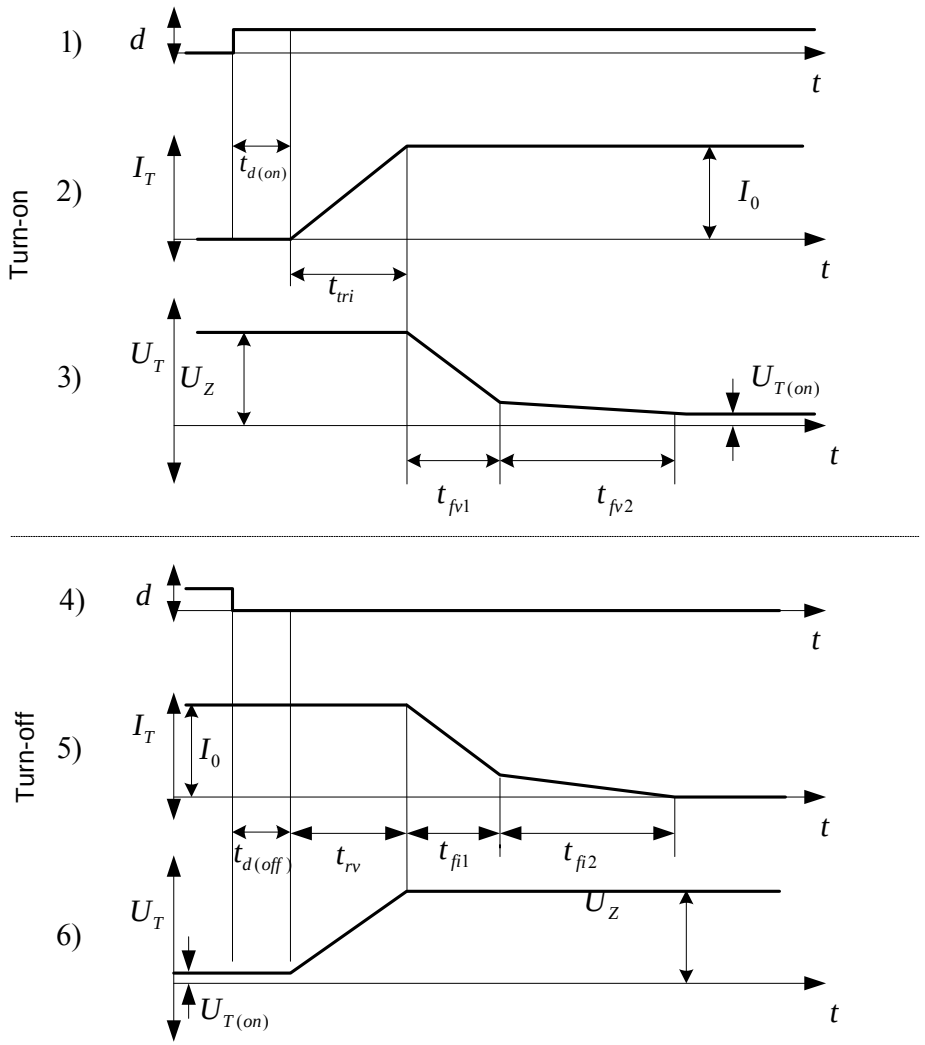

Figure 5.2 Approximated turn-on/off waveforms for the inverter with IGBT's

$$\Delta t \approx t_{bl} + \left(t_{d(on)} + t_{tri} + \frac{t_{fv1}}{2} \right) - \left(t_{d(off)} + \frac{t_{rv}}{2} \right) \qquad (5.3)$$

From the test data on this inverter [63] the typical dead time is 1.64 us. In [68] the dead time effect was analysed, this analysis is repeated here in order to describe the dead time effect: the dead time effect can be described by considering one inverter leg. In order to describe the dead time we consider inverter leg A (Figure 5.3). The output voltage is U_{AN} in the analyses: the dead time is represented as a delay between the control signal "on" command and the real switching on action in the IGBT. Figure 5.4.1 and 2 shows how the control signal for the upper (T_{A+}) and lower (T_{A-}) IGBT. The delay for T_{A+} is indicated by Δt in Figure 5.4.3.

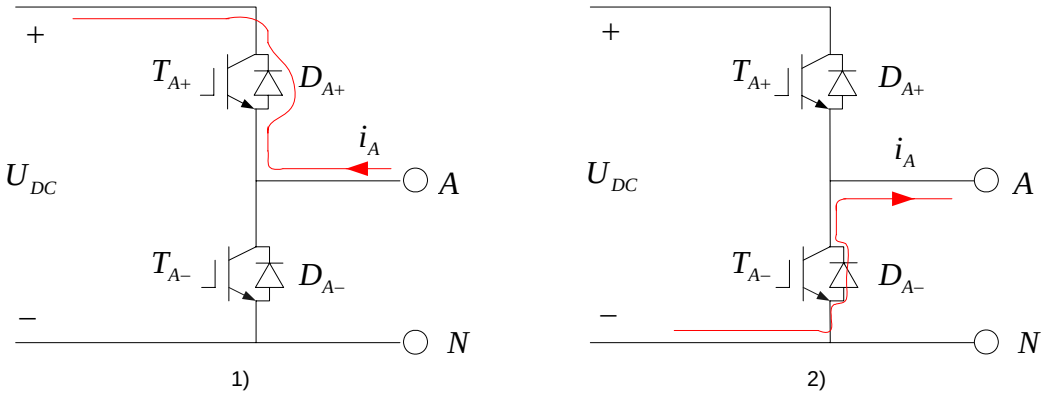

Figure 5.3 One inverter leg, 1) negative current, T_{A+}, T_{A-} off2) positive current, , T_{A+}, T_{A-} off

During the dead time both IGBT's are off: the voltage U_{AN} then depends on the direction of the current in the inverter leg. If the current is negative it flow trough the upper freewheeling diode (D_{A+}) and the resulting voltage is positive. The output voltage will have a gain compared to an ideal operation with no dead time. This gain is indicated in Figure 5.4.6. When the current is positive (Figure 5.3.2) it flows in the lower freewheeling diode (D_{A+}). The result is a loss in the resulting voltage as the diode clamps to the lower voltage level.

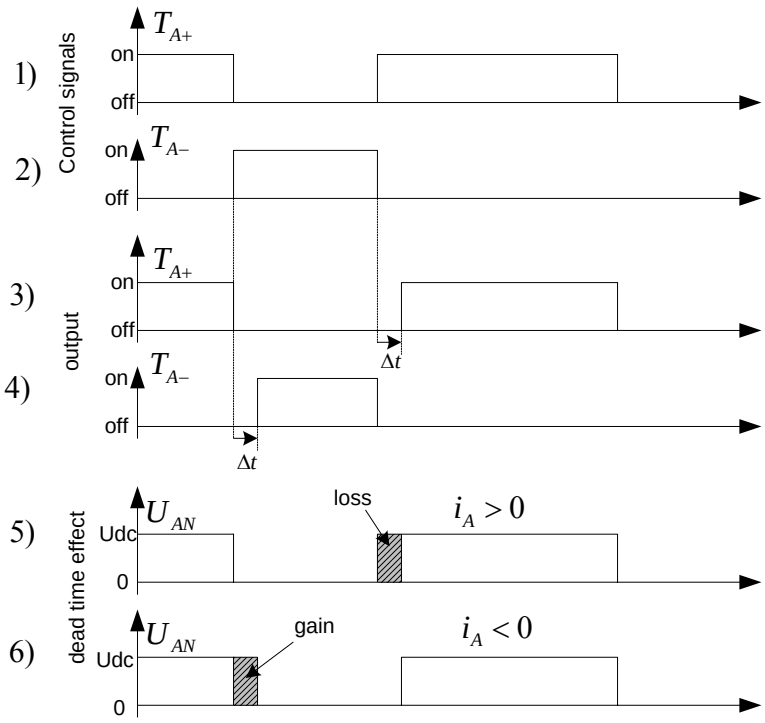

Figure 5.4 Dead time effect

Figure 5.4.5 indicates the voltage loss. If the effect of the dead time is evaluated over one switching period the change in the output voltage can be described as:

$$i_A > 0: \quad \Delta U_{AN} = -\frac{\Delta t}{T_{sw}} U_{DC} \tag{5.4}$$

$$i_A < 0: \quad \Delta U_{AN} = +\frac{\Delta t}{T_{sw}} U_{DC} \tag{5.5}$$

In addition to the dead time the IGBT's has forward voltage drop characteristics. Figure 5.5.1 shows the forward voltage characteristics for the Semikron IGBT [70] used in the inverter. The forward voltage is usually divided in two parts: one part is constant and dependent on the direction of the current in the IGBT and one part is dependent of the current magnitude. The latter can be modelled as an additional stator resistance. The constant part is modelled together with the dead time effect. The same effect can be seen from the freewheeling diode. The forward voltage drop in the diode (Figure 5.5.2) is very similar to the IGBT forward voltage drop. In the model the diode and IGBT forward voltage characteristics will be regarded as equal. Thus the resulting voltage error that changes with the sign of the phase currents is:

$$U_F = (U_{TD} + \frac{\Delta t}{T_{sw}} U_{DC}) \cdot sign(i) \tag{5.6}$$

Where u_{TD} describes the constant forward voltage drop in the IGBT and diode. In [69] and [70] the dead time effect was modelled as a space vector quantity. The dq-modelling of the dead time effect found in [70] is repeated here for convenience: in Figure 5.6.1 and Table 5.1: the error vectors are described for the space vector sectors in the machine.

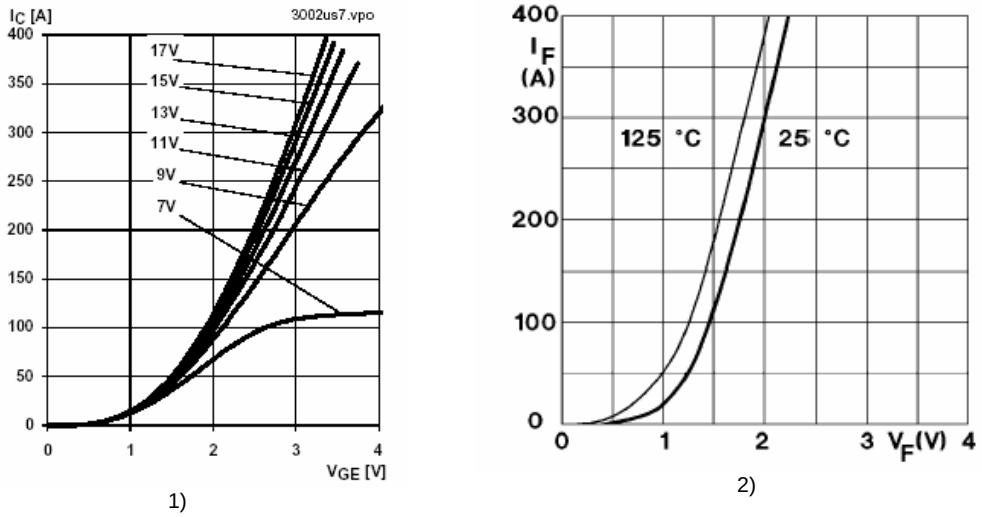

Figure 5.5 Characteristics Semikron 400 GB 123 D, 1) IGBT forward characteristics, 120*C, 2) Diode forward characteristics

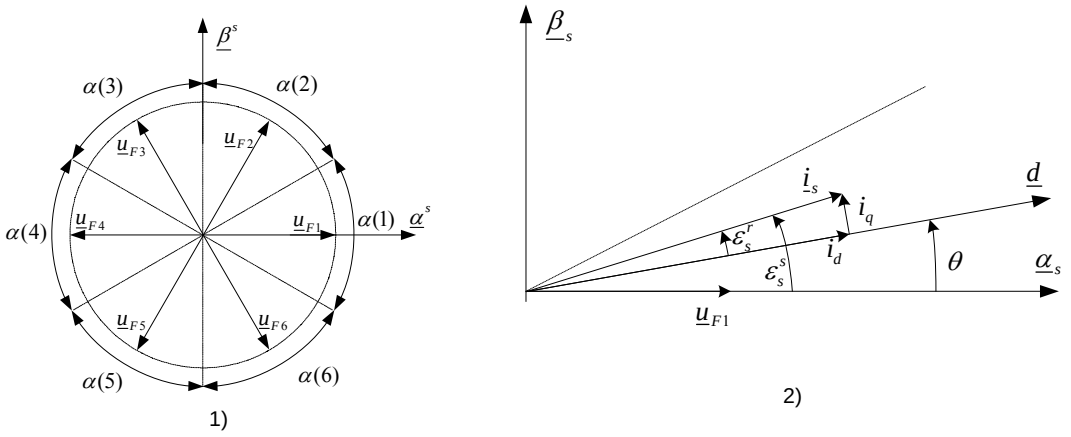

Figure 5.6 1)Location of the sectors between the zero crossings $\alpha(1)-\alpha(6)$ and the space vector representation of the zero crossing errors, 2) Transformation of the error space vector in a rotating coordinate system

The sectors $\alpha(1)-\alpha(6)$ describes the sectors where the error vector $\underline{U}_F$ is constant. Figure 5.6.2 shows the coordinate system used for decomposition of the error vector. The angle between the d-axis and the stator current can be expressed as:

$$\tan(\varepsilon_s^r) = \frac{i_q}{i_d} \tag{5.7}$$

Table 5.1 Sectors with constant signs of phase currents

Sector	sign(i_a)	sign(i_b)	sign(i_c)	$\underline{u}_F$
$\alpha(1)$	1	-1	-1	$4/3u_F e^{j0}$
$\alpha(2)$	1	1	-1	$4/3u_F e^{j\frac{\pi}{3}}$
$\alpha(3)$	-1	1	-1	$4/3u_F e^{j\frac{2\pi}{3}}$
$\alpha(4)$	-1	1	1	$4/3u_F e^{j\pi}$
$\alpha(5)$	-1	-1	1	$4/3u_F e^{-j\frac{2\pi}{3}}$
$\alpha(6)$	-1	-1	1	$4/3u_F e^{-j\frac{2\pi}{3}}$

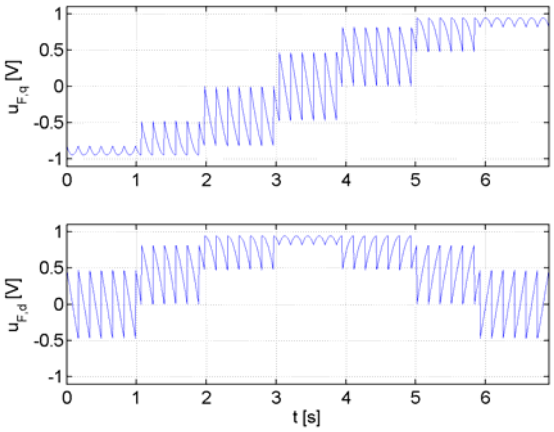

Figure 5.7 Decomposed dead time effect in dq-axis. Machine rotating, ε_s^r varying as: 0-1s: ε_s^r =-90, 1-2s: ε_s^r =-60, 2-3s: ε_s^r =-30, 3-4s: ε_s^r =0, 4-5s: ε_s^r =30, 5-6s: ε_s^r =60, 6-7s: ε_s^r =90

When $\underline{i}_s$ is located in sector $\alpha(1)$ the dead time error can be decomposed as:

$$u_{F,d} = u_{F1}\cos(\varepsilon_s^s - \varepsilon_s^r) \tag{5.8}$$

$$u_{F,q} = u_{F1}\sin(\varepsilon_s^s - \varepsilon_s^r) \tag{5.9}$$

Figure 5.7 describes the decomposed dead time effect for different angles ε_s^r and rotating machine. In this simulation the dead time voltage vector is created depending in the current vector location. The $\alpha\beta$-components are transformed to the dq-reference frame according to the angle ε_s^r. In this work the reluctance torque has not been utilized and the dq-currents are controlled as: $i_q^*=i_s$, $i_d^*=0$. For this control strategy the angle ε_s^r always is equal 90 degrees. In Figure 5.7 we see that the dead time effect is largest for the d-axis voltage and that the influence in the q-axis is minimal. This effect was also found in the experimental work.

5.2.2 Space Vector Pulse Width Modulation

Symmetrical space vector pulse with modulation was used for voltage modulation in this work. The space vector modulation principle is build upon producing an average representation of the commanded voltage within the switching period. The commanded voltage in the dq-system is transformed to the stationary $\alpha\beta$ - system. The inverter gives 8 possible voltage combinations (Figure 5.8.1). The representation of the average voltage can be illustrated by assuming a voltage command in the first quadrant (0-60 degrees). The reference voltage can be decomposed in the two basis vectors $\underline{e}_1$ and $\underline{e}_2$ and the duration of each pulse can be derived as:

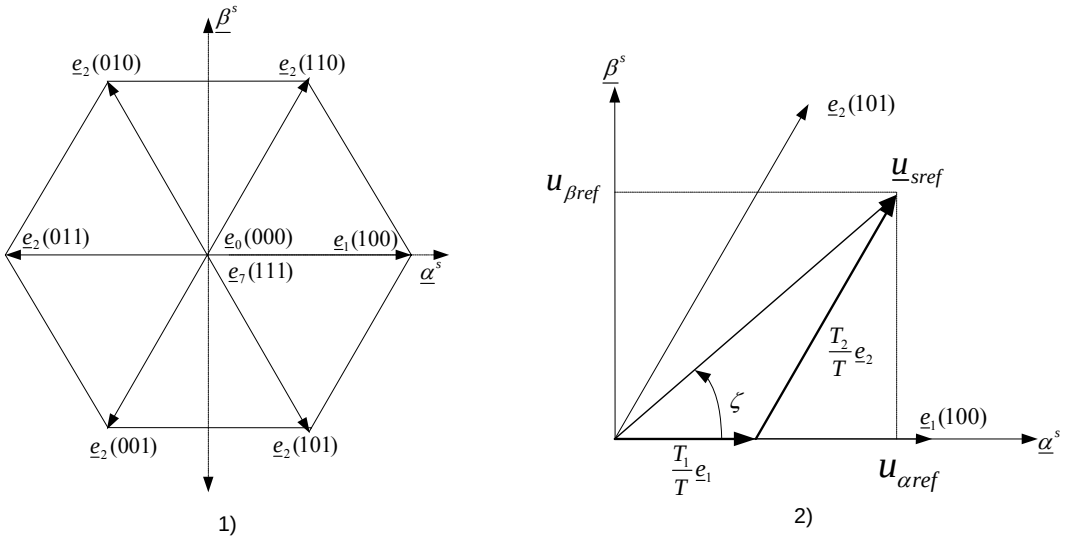

Figure 5.8 Space vectors inverter, 1) available space vectors, 2) space vector modulation

$$T_1 = u_{sref} T_{sw} \sin(\frac{\pi}{6} - \zeta) \tag{5.10}$$

$$T_2 = u_{sref} T_{sw} \sin(\zeta) \tag{5.11}$$

$$T_0 = T_{sw} - T_1 - T_2 \tag{5.12}$$

In the DSP the symmetrical space vector modulation is realized by compare units and a counter. Figure 5.9 illustrates how the realization is done in the DSP. There are two zero vectors used in Figure 5.9: $\underline{e}_0$ at the beginning and end, $\underline{e}_7$ in the centre. In the transient based excitation the centre zero vector time region is used for pulse generation.

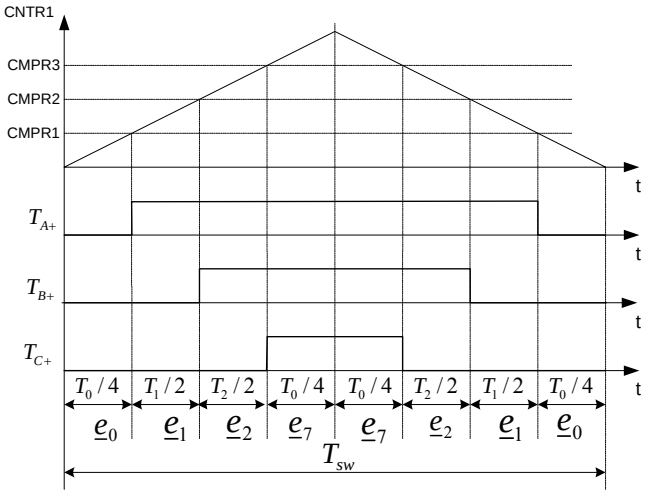

Figure 5.9 Symmetrical Vector Pulse Width Modulation

5.3 System description

The test system used in the evaluation of schemes is based on Test Machine 1 (IPMSM) and the inverter described in the previous chapter. An overview of the system is presented in Figure 5.10. A three phase variac was applied in front of the rectifier in order to allow variation of the DC bus voltage. A load machine was not included in the test stand (due to time limitations) and the inertia of the rotor where utilized in order to perform high load currents in short intervals. All three currents where measured by LT300-S current transducers. The technical specifications for the current transducers are given in Table 5.5. (three turns was used in the LEM sensors, thus real rated current equals 100 A).

Table 5.5 LT300-S Current Transducer data

		Dynamic performance		
I_N[A]	Overall accuracy	Linearity error	di/dt – followed	Bandwidth (-1dB)
300	0.5% of I_N	<0.1 % of I_N	50A/us	0-150kHz

The DSP board was an experimental board developed by Aker Kvaerner, SINTEF, and NTNU. The DSP is a 32 bit fixed point industrial DSP (TMS320F2812). The DSP has a 12 bit analogue to digital converter (ADC). The effective resolution is 9 bit as the DSP is still an early version (bad internal voltage reference).

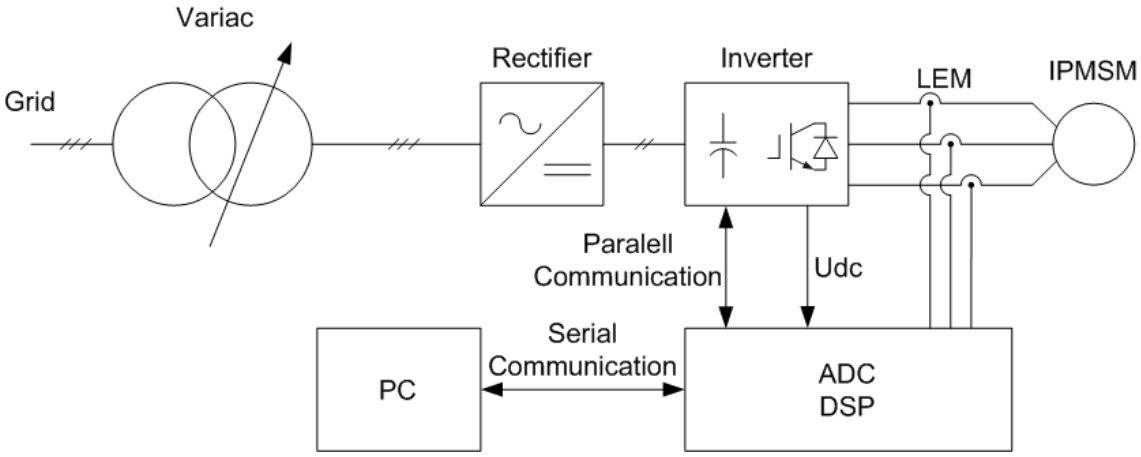

Figure 5.10 Test setup -overview

5.4 Experimental work strategy

The experimental work is not presented as one single chapter in this work. Due to the many schemes involved the experimental work is presented for each scheme. The results are discussed in Chapter 9. The strategy in the experimental work is to document the fundamental characteristics of the scheme evaluated. Also, in order to evaluate how these schemes can be integrated into standard drives several aspects have to be evaluated:

- Additional losses in power electronics
- Switching frequency
- Current regulator bandwidth
- Speed regulator bandwidth
- Demands on Current sensors
- DC-bus voltage reservation due to carrier/excitation signal
- Parameter sensitivity
- Stability/Reliability
- Acoustic noise
- DSP requirements (complexity of schemes)

All these aspects are not covered by the work done in this thesis as the time and equipment for this work was limited. Three schemes are tested in this work: rotating high frequency carrier injection (HFCI-R), pulsating high frequency carrier injection (HFCI-R) and transient excitation (TE). The switching frequency in the original system was 10 kHz. This switching frequency was used as the base value for the comparison of switching losses associated with each scheme. The scheme based on transient excitation will introduce additional switching operation and the switching frequency was lowered to 5 kHz. For each scheme the tuning of the current regulators are discussed, different issues are associated for each scheme. The performance of each scheme is evaluated using two tests:

- Speed reversal test +/- 0.1 pu speed reference
- Transient test +/- 0.5 pu i_q reference (45A)

The speed reversal test results in a large transient q-axis current, multiple fundamental zero crossings and zero speed transition. From this test the robustness against transient current and inverter non linearity can be evaluated. The estimation errors and lags at constant speed can also be evaluated just after the speed reversal. The transient test is performed with a square wave reference signal in the q-axis current regulator. Two

reference frequencies are tested: 12.5 Hz and 25 Hz. At 12.5 Hz the variation in the position is approximately 40 electrical degrees and the speed varies from -0.036 to 0.036 pu (90 rpm). In the 25 Hz test the variation in the position is approximately 10 electrical degrees and the speed varies from -0.018 to 0.018 pu (45 rpm). The transient test illustrates the dynamic operation of the schemes.

Chapter 6, 7 and 8 describes the implementation and experimental work for each method. In Chapter 9 the results from the tests are compared and some of the issues regarding integration with standard systems are evaluated. The effects from inverter non linearity are discussed for the three methods in Chapter 9.

6 HIGH FREQUENCY CARRIER INJECTION – ROTATING

The basic scheme is described in the first section. In the next section some modified schemes are presented. The first modification is a simplification of the rotating Synchronous frame filter, the second modification is a simple decoupling approach for the Synchronous Frame filter. In the chapter conclusions the main features of this scheme is summarised and the performance with the decoupling scheme is evaluated.

6.1 Description of Scheme

In this chapter the implementation of the HFCI-R scheme is described. This work is based on the work done by Professor R.D. Lorenz and he's graduate students at University of Wisconsin, Madison, USA [2,13, 39]. In [2,13] the method was tested on induction machines and in [39] it was tested with an IPMSM.

6.1.1 Carrier injection

The carrier injection is implemented as a voltage injection. Current injection is also possible but this kind of injection place extreme requirements on current regulator bandwidth. Figure 6.1 show a principal view of the scheme. The carrier voltage is superimposed on the fundamental voltage after the current controllers. The measured current is divided in two parts in the synchronous frame filter: one for the current regulators and one for the observer.

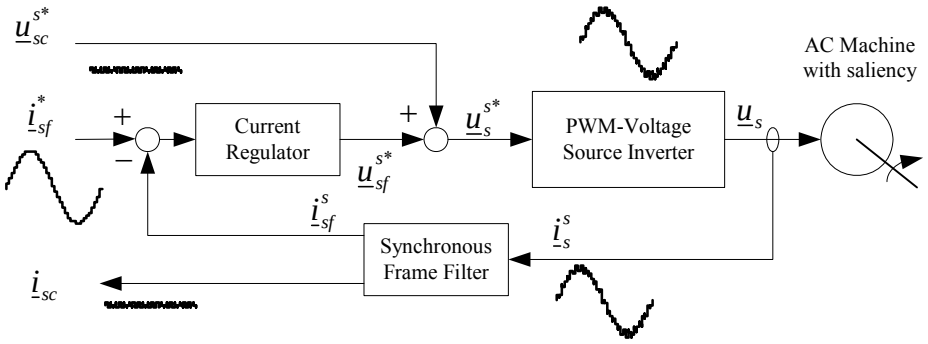

Figure 6.1 Injection of high frequency carrier signal

The derivation in this Chapter is based on a single saliency model. The single saliency model is described in detail in Chapter 3. The high frequency current response can be described by inverting the inductance matrix (6.1) in stator reference frame:

$$L_s^s = \begin{bmatrix} \sum L - \Delta L\cos(2\theta) & -\Delta L\sin(2\theta) \\ -\Delta L\sin(2\theta) & \sum L + \Delta L\cos(2\theta) \end{bmatrix} \tag{6.1}$$

Where:

$$\sum L = \frac{L_d + L_q}{2}, \Delta L = \frac{L_q - L_d}{2} \tag{6.2}$$

The inverse of (6.1) can be written as:

$$L_s^{s-1} = \frac{1}{L_d L_q}\begin{bmatrix} \sum L - \Delta L\cos(2\theta) & \Delta L\sin(2\theta) \\ \Delta L\sin(2\theta) & \sum L + \Delta L\cos(2\theta) \end{bmatrix} \tag{6.3}$$

If we solve for constant and differential parts, one obtains:

$$L_s^{s-1} = \frac{1}{L_d L_q}\left(\sum L\begin{bmatrix} 1 & 0 \\ 0 & 1 \end{bmatrix} + \Delta L\begin{bmatrix} -\cos(2\theta) & \sin(2\theta) \\ \sin(2\theta) & \cos(2\theta) \end{bmatrix}\right) \tag{6.4}$$

If a symmetrical rotating three phase voltage is applied the resulting current would be:

$$I_{s\_c}^s = I_{cp}\begin{bmatrix} \cos(\omega_c t) \\ \sin(\omega_c t) \end{bmatrix} + I_{cn}\begin{bmatrix} -\cos(2\theta)\cos(\omega_c t) + \sin(2\theta)\sin(\omega_c t) \\ \sin(2\theta)\cos(\omega_c t) + \cos(2\theta)\sin(\omega_c t) \end{bmatrix} \tag{6.5}$$

By using trigonometric simplifications:

$$I_{s\_c}^{s} = I_{cp}\begin{bmatrix}\cos(\omega_c t)\\ \sin(\omega_c t)\end{bmatrix} + I_{cn}\begin{bmatrix}\cos(2\theta - \omega_c t)\\ \sin(2\theta - \omega_c t)\end{bmatrix} \tag{6.6}$$

Where:

$$I_{cp} = \frac{L_d + L_q}{2L_d L_q}\frac{U_{s\_c}^{s}}{\omega_c} \tag{6.7}$$

$$I_{cn} = \frac{\left(L_q - L_d\right)}{2L_d L_q}\frac{U_{s\_c}^{s}}{\omega_c} \tag{6.8}$$

Thus a balanced high frequency voltage results in two high frequency current terms: one positive rotation and one negative rotating. The negative rotating term contains information on the saliency position.

6.1.2 Synchronous Frame filtering

The separation of the position dependent carrier frequency and the fundamental current can be done in several ways. One approach is based on low pass filters in the negative carrier frame for the observer output, and a low pass filter in the dq-frame for current controller feedback. A second approach [2] is the usage of a synchronous frame filter with high pass filters. The high pass filters have zero magnitude for any constant (DC) signal and have the ability to completely eliminate a specified frequency. If we consider a simple PMSM control that only regulates the q-axis current the resulting current would be:

$$I_{s\_c}^{s} = I_{cp}\begin{bmatrix}\cos(\omega_c t)\\ \sin(\omega_c t)\end{bmatrix} + I_{cn}\begin{bmatrix}\cos(2\theta - \omega_c t)\\ \sin(2\theta - \omega_c t)\end{bmatrix} + I_{sf}\begin{bmatrix}\cos(\omega t)\\ \sin(\omega t)\end{bmatrix} \tag{6.9}$$

Common for both outputs from the filter is that the positive rotating carrier signal should be removed (first term in (6.9)). This task is therefore the first in the synchronous frame filter. The current is rotated to positive rotating carrier reference frame and filtered by a first order high pass filter (hp1). For the current regulator output the second term in (6.9) should also be removed. This term contains the estimated double rotor position and the negative rotating carrier angle, this frame is labelled cn'. The current is then filtered by a first order high pass filter (hp2) and transformed to the dq- reference frame. This current is used as the feedback for the current controllers. The lower branch is designed for the separation of the position dependent part of the carrier signal. When the signal enters the lower branch the positive carrier signal is already removed, then only the fundamental current needs to be removed (third term in (6.9)).

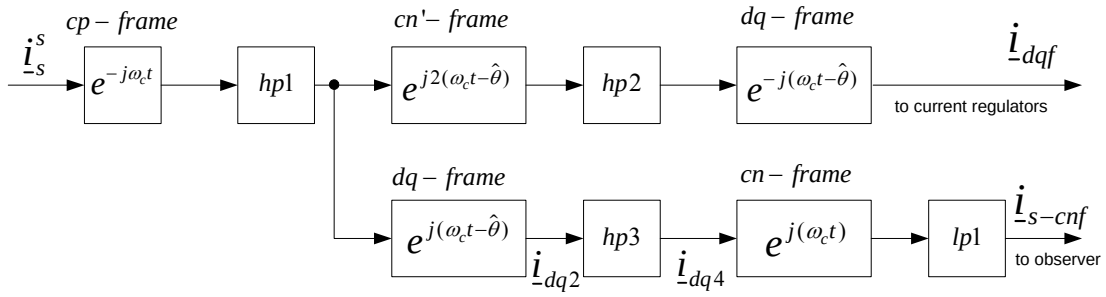

Figure 6.2 Synchronous frame filtering

This is done by transforming the current to the rotating dq-frame and high pass filtering (hp3). The remaining current should then be the second term in (6.9). When this current is transformed to the negative rotating carrier frame the current forms a vector with magnitude equal i_{cn} rotating with the double rotor position. During acceleration the q-current can change very quickly, the high pass filter in the dq-frame does not filter of all the fundamental current as we have a high frequency change in the dq reference frame. The remaining fundamental current will appear at the observer input with carrier frequency; this can be filtered off by a low pass filter (lp1). The amplitude of the remaining fundamental current is several times larger than the position dependent carrier current (typically comparable to the fundamental current amplitude at the time instant after the transient). The bode plot for the synchronous frame filter (Figure 6.3) gives a graphical impression of the function of the synchronous frame filter. The low pass filter is not included in Figure 6.3. The transformation of the filter transfer functions from the respective reference frames are done by substituting s with $(s-j\omega_c)$ for the positive frame and $(s-j\omega_{dq})$ for the dq frame. The resulting expression for the observer branch is:

$$\frac{i_s}{i_{s-cn}} = \frac{s - j\omega_c}{s - j\omega_c + \omega_{cpf}} \cdot \frac{s - j\omega_{dq}}{s - j\omega_{dq} + \omega_{dqf}} \tag{6.10}$$

Where $\omega_{dqf} = \omega_n \cdot n$. The current controller branch becomes:

$$\frac{i_s}{i_{s-cn}} = \frac{s - j\omega_c}{s - j\omega_c + \omega_{cpf}} \cdot \frac{s + j\omega_c}{s + j\omega_c + \omega_{cnf}} \tag{6.11}$$

There are three approaches that reduce the problems with the transient operation: low pass filtering before the position dependent part is fed to the heterodyning term (Figure 6.9 and Figure 6.4.1-LP-A), low pass filtering after the heterodyning term [39] (Figure 6.4.1-LP-B), decoupling of the fundamental current (Figure 6.4.2).

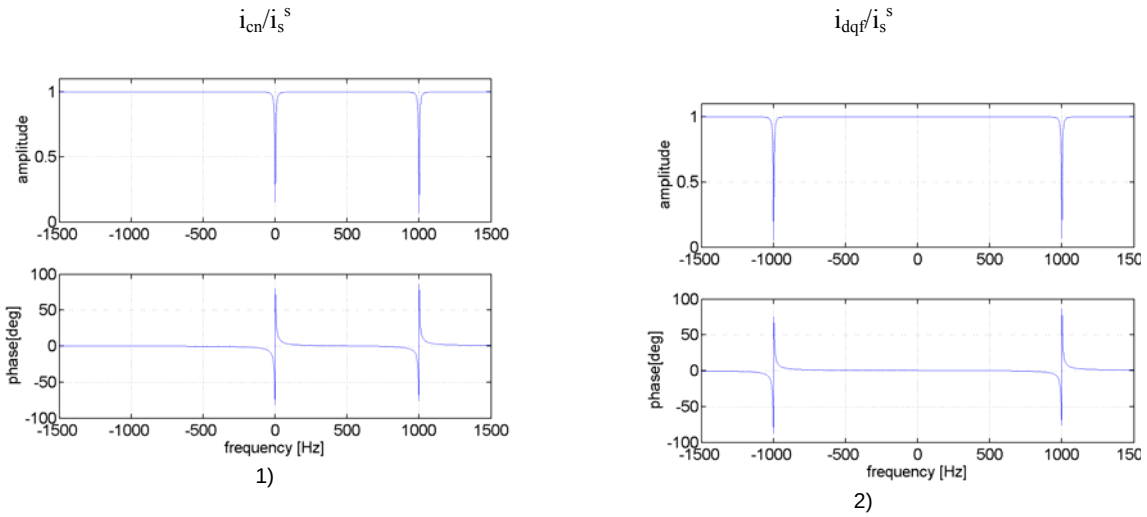

Figure 6.3 Bode plot synchronous frame filter.1:observer filter. 2: current regulator filter. Hp1, hp2 and hp3 cut off frequency at 5Hz, n=0 rpm.

The heterodyning term generates the error signal to the observer (defined in the next sub Chapter). When the low pass filter is placed after the heterodyning term there will be less position dependent error in the estimates. In this work the low pas filter is placed before the heterodyning term (as in Figure 6.2 and Figure 6.4.1-LP-A) in order to evaluate the influence from the phase current zero crossings and transient operation. If low pass filtering is implemented as mentioned above, and the cut off frequency is one magnitude lower than the carrier frequency, the notch filtering characteristics in the synchronous frame filter is lost: the low pass filters bode plot will overlap the frequency region for the notch filtering performed in the synchronous frame filter. The resulting expression for the observer branch:

$$\frac{i_s^s}{i_{c-cnf}} = \frac{s - j\omega_c}{s - j\omega_c + \omega_{cpf}} \cdot \frac{s + j\omega_c}{s + j\omega_c + \omega_{cnf}} \cdot \frac{\omega_{lp}^2}{(s - j\omega_c)^2 + j1.414 \cdot (s - j\omega_c) \cdot \omega_{lp} + \omega_{lp}^2} \tag{6.12}$$

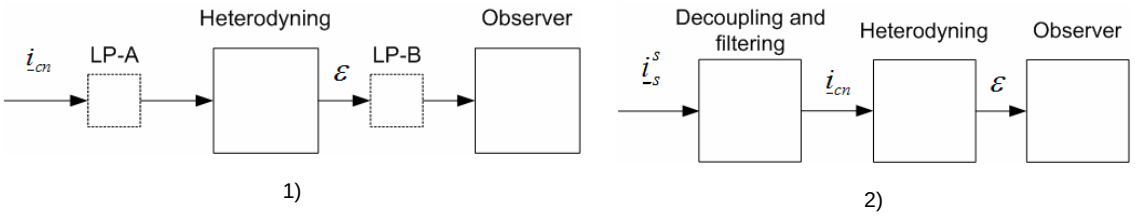

Figure 6.4 Alternative solutions for enhanced transient operation. 1) low pass filters, 2) decoupling scheme

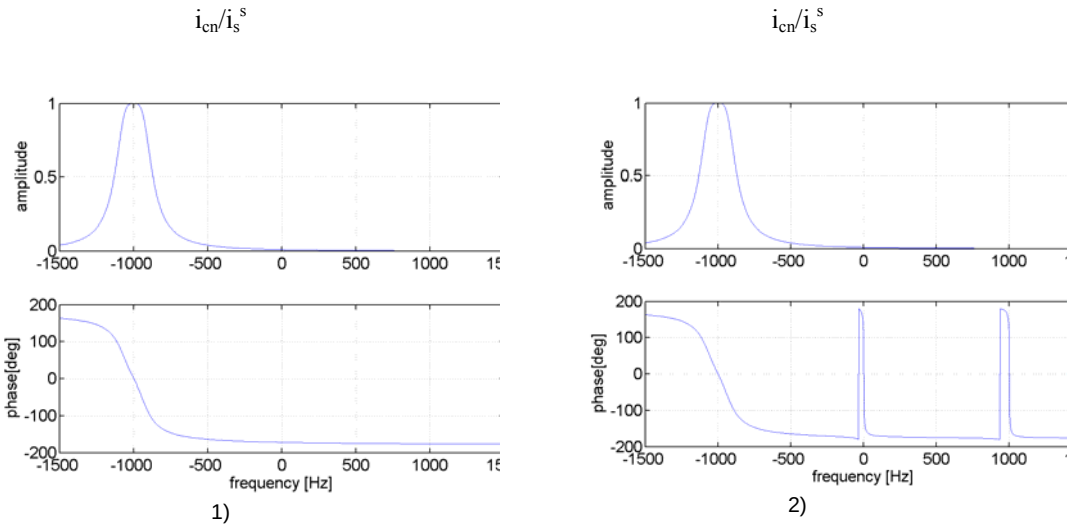

Figure 6.5 Bode plot. 1: 100 Hz lp filter in negative carrier frame, 2: combined effect of lp (100 Hz) filter in negative frame and hp1 and hp3 at 5 Hz

The synchronous frame filter can be reduced to the filter shown in Figure 6.6. Even though the high pass filters completely eliminates the current at the frequency in the frame, the low pass filter gives approximately the same effect. The low pass filtering introduces a lag in the speed and position estimate. The lag can be approximately compensated by a linear function and the speed estimate. The speed estimate used in the compensation is an internal state from the observer. This estimate is typical noisy and must be filtered by a low pass filter. A fundamental current observer was presented in [29]. According the authors the fundamental current observer could remove the effects of the fundamental current zero crossing, transients from a step in the q-axis current and DC bus voltage variations. The fundamental current observer was tuned for 200 Hz bandwidth.

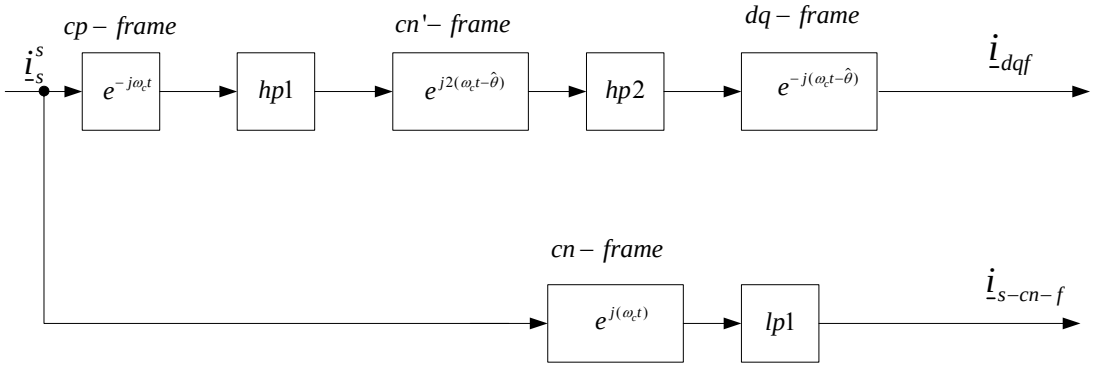

Figure 6.6 Simplified synchronous frame filter

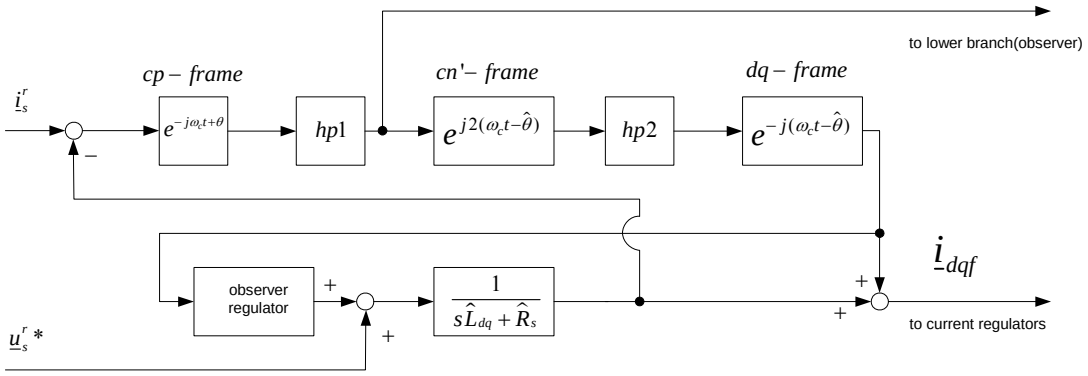

Figure 6.7 Fundamental current observer used for decoupling [29]

The fundamental current observer contains estimates of both the stator resistance and the d and q axis inductance. A simpler approach is tested in this thesis (Figure 6.8). The fundamental current is directly decoupled in the synchronous frame filter. This approach is much simpler than the use of a fundamental current observer, and it contains no machine parameters. This decoupling scheme will be revisited in the experimental work.

6.1.3 Observer/Heterodyning

Common for all the implemented schemes is the use of an observer in order to track the rotor position. The focus of this work has been to verify the ability to extract position information with different excitation methods, thus the observer topology has not been the main focus in this work. There are several methods that can lead to position and speed estimate: extended Luenberger observer, arc tang function and separate positive d-axis correction algorithm, PLL solutions and Kalman filters [1]. In this work an extended Luenberger observer structure [3] is used.

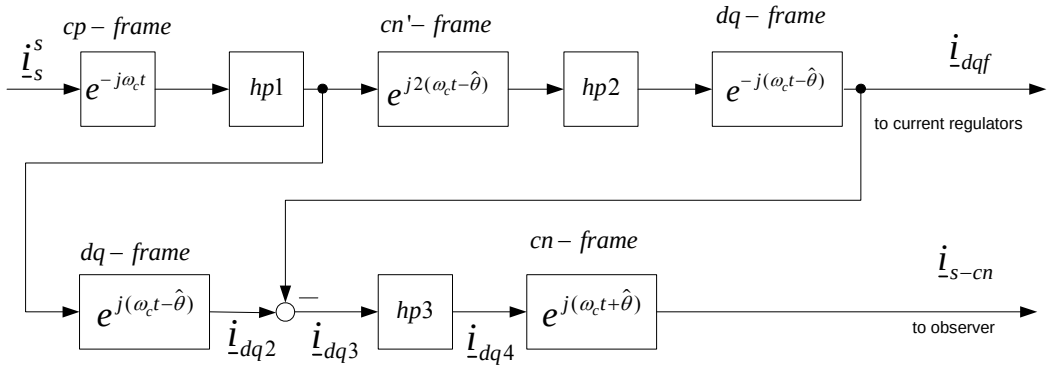

Figure 6.8 Fundamental current decoupling

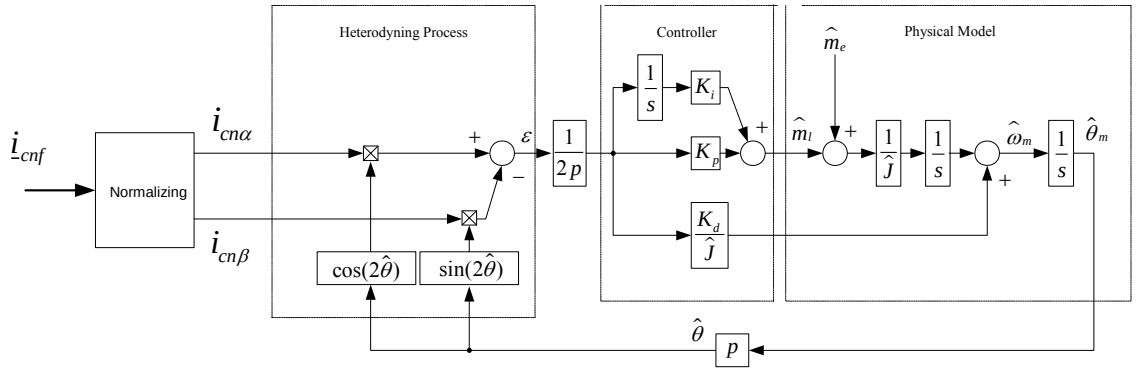

Figure 6.9 Luenberger style observer, heterodyning and normalizing term

The position information gives double rotor position, thus the positive d-axis is determined during commissioning stage and the position (theta) is tracked with an observer. The electrical position is converted to mechanical position by using the pole pairs p (alternatively all quantities in per unit system). The observer includes the mechanical model of the machine and load. In the first stage the error signal for the observer is made by heterodyning. The heterodyning stage is simply the cross product of the estimated saliency vector (always unity amplitude) and the position signal vector. If we assume the positioning signal has amplitude equal I_{cn} we get:

$$\varepsilon = I_{cn} x 1 \angle \hat{\theta} = I_{cn} \sin(2(\theta - \hat{\theta})) \tag{6.13}$$

For small errors the error term can be approximated as:

$$\varepsilon \approx 2 I_{cn} (\theta - \hat{\theta}) \tag{6.14}$$

In Figure 6.9 the factor two from the linear approximation is included as a scaling term before the observer. The bandwidth of the observer can be selected using the approximation of the error term for small errors. A simple pole placement technique is used in order to give the observer the bandwidth needed for the actual application. The poles are placed with a factor 5 between them in order to reduce parameter sensitivity for the observer. The amplitude of the positioning signal enters the observer and they will influence the three gains in the observer. In order to decouple this effect a normalizing term is used in order to scale the position signals before they enter the observer:

$$i_{\alpha n}^{cn} = \frac{i_{\alpha}^{cn}}{\sqrt{(i_{\alpha}^{cn})^2 + (i_{\beta}^{cn})^2}} \tag{6.15}$$

$$i_{\beta n}^{cn} = \frac{i_{\beta}^{cn}}{\sqrt{(i_{\alpha}^{cn})^2 + (i_{\beta}^{cn})^2}} \tag{6.16}$$

With the normalized positioning signals the tuning of the observer becomes easier as the bandwidth does not change with carrier signal amplitude. Discrete design was used in the implementation and pole placement. The discrete design is described in the next section. The s-plane transfer function for the closed loop system becomes:

$$H_{obs} = \frac{\hat{\theta}}{\theta} = \frac{H_0}{1+H_0} = \frac{\frac{1}{\hat{J}}(K_d s^2 + sK_p + K_i)}{s^3 + \frac{K_d}{\hat{J}}s^2 + \frac{K_p}{\hat{J}}s + \frac{K_i}{\hat{J}}} \tag{6.17}$$

If one consider the combined effect of the torque feed forward and the estimate of the load torque the combined effect must be expressed. The effect from the feed forward on the estimated position can be expressed as:

$$\frac{\hat{\theta}}{\hat{m}_e} = \frac{s}{\hat{J}s^3 + K_d s^2 + K_p s + K_i} \tag{6.18}$$

the real relationship (m_l=0):

$$\frac{\theta}{m_e} = \frac{1}{Js^2} \tag{6.19}$$

If these two expressions are combined the relation ship between the feed forward torque and the estimation accuracy becomes:

$$\frac{\hat{\theta}}{\theta} = \frac{Js^3(\frac{\hat{m}_e}{m_e})}{\hat{J}s^3 + K_d s^2 + K_p s + K_i} \tag{6.20}$$

The resulting effect in the observer is the feed forward effect together with the standard transfer function. The combined effect is evaluated by summation of (6.17) and (6.20):

$$\frac{\hat{\theta}}{\theta} = \frac{Js^3(\frac{\hat{m}_e}{m_e}) + K_d s^2 + K_p s + K_i}{\hat{J}s^3 + K_d s^2 + K_p s + K_i} \tag{6.21}$$

In this work the reluctance moment is not used ($i_d^* = 0$) and the electromechanical torque can be estimated as:

$$\hat{m}_e = \hat{\psi}_m \cdot i_q \tag{6.22}$$

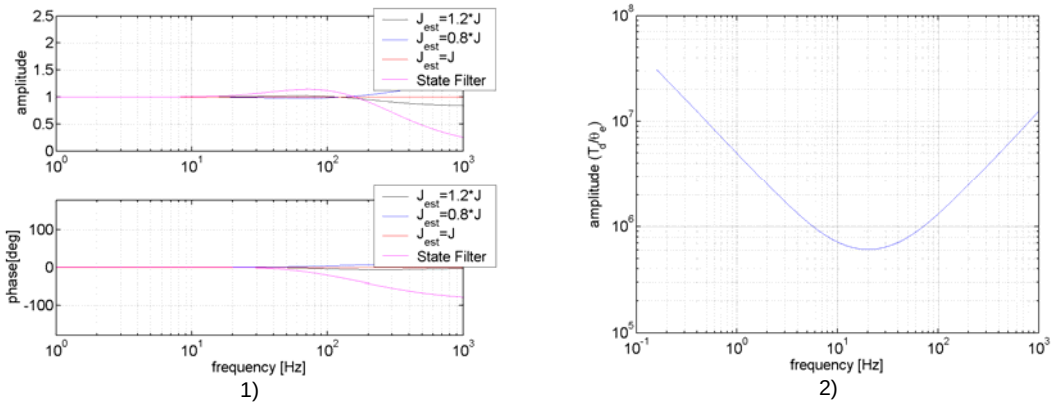

1) 2)

Figure 6.10 Observer, poles in 10, 50 and 250 Hz, J=0.07 Nms^2 ,1: Observer sensitivity $\hat{\theta}/\theta$, 2:Disturbance rejection

The estimated position accuracy can be expressed as:

$$\frac{\hat{\theta}}{\theta} = \frac{Js^3(\frac{\hat{\psi}_m}{\psi_m}) + K_d s^2 + K_p s + K_i}{\hat{J}s^3 + K_d s^2 + K_p s + K_i} \tag{6.23}$$

The disturbance rejection can be represented by the transfer function:

$$\frac{m_l}{\theta - \hat{\theta}} = \frac{m_l}{\theta_e} \tag{6.24}$$

The real system is:

$$\theta = \frac{m_e - m_l}{Js^2} \tag{6.25}$$

The observer gives:

$$\hat{\theta} = \frac{1}{s}\left[\frac{1}{\hat{J}s}\left(\theta_e\left(\frac{K_i}{s} + K_p\right) + \hat{m}_e\right) + \theta_e \frac{K_d}{\hat{J}}\right] \tag{6.26}$$

(6.24),(6.25)and (6.26) are combined :

$$\theta - \hat{\theta} = \theta_e = \frac{m_e}{Js^2} - \frac{\hat{m}_e}{Js^2} + \frac{m_l}{Js^2} - \theta_e\left(\frac{K_i}{\hat{J}s^3} + \frac{K_p}{\hat{J}s^2} + \frac{K_d}{\hat{J}s}\right) \tag{6.27}$$

The influence of the disturbance with respect to the position error can be describes as:

$$\frac{m_l}{\theta_e} = Js^2 + \frac{J}{\hat{J}}(K_p + K_d s + K_i \frac{1}{s}) \tag{6.28}$$

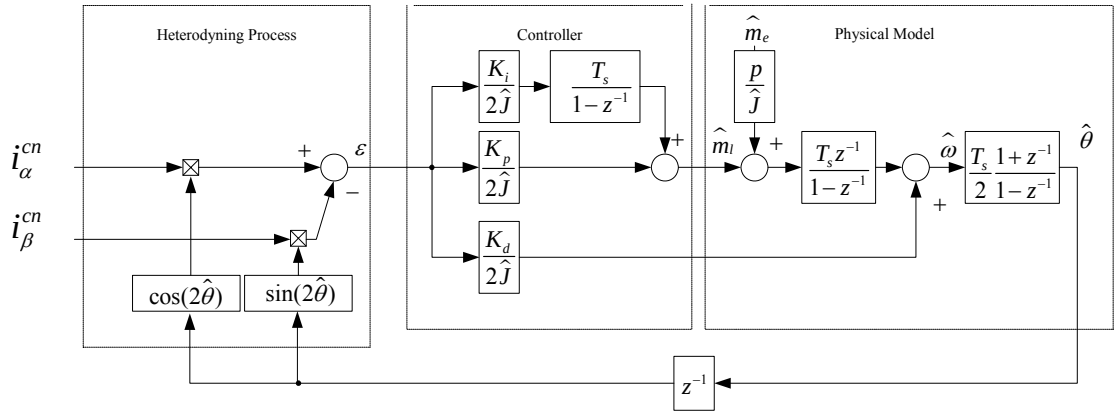

Figure 6.11 Discreet representation of observer

The disturbance rejection describes the amount of disturbance torque needed on different frequencies in order to make a 1 electrical degree error. This function will be used in the evaluations of the final tunings for the different methods. As there is no load machine connected to the machine this is the only evaluation one get on the disturbance rejection. In general large values in the disturbance rejection gives good disturbance rejection. In the DSP the observer is implemented in a discreet version. When a fixed point DSP is used there are several modifications that simplify the implementation: in Figure 6.11 the estimated inertia is included in the gains, in addition to this the sampling times can also included in the gains in order to represent the gains on a suitable fixt point format. The factor 1/2 in the gains represents the linearization of the error term(6.14). The estimated inertia is included in the gains in order to tune the State Filter representation (no torque feed forward) without the estimated inertia. When the torque feed forward is used the estimated inertia and the pole-pairs (p) is used as scaling.

6.2 Experimental work on HFCI-R

The experimental work was performed on test machine 1 (IPMSM). As the test setup had no load machine the inertia of the machine it self was used as load during acceleration. Two types tests where performed: a speed reversal test and a transient test. The speed reversal test performs a speed reversal from 250 rpm to -250 rpm (0.1 pu speed). The speed reversal test covers the speed range that this method should cover, it reveals the zero crossing effects and it shows the performance of the synchronous frame filter during a quick change in the q-axis current. In the transient test a square wave reference (45 A) is applied to the q-axis current regulator. The test shows the dynamics (and distortions) in the estimated speed and rotor position, the relationship between the saliency position and the q-axis current and the performance during extreme q-axis current change. Since there was no load machine in the test setup the disturbance rejection properties could not be tested. These properties are described by the disturbance rejection function(6.28).

6.2.1 Current regulators

In all sensorless schemes based on voltage carrier signal some strategy must be chosen in order to prevent the current regulators to follow the carrier signal. In [35] the bandwidths of the current regulators were selected lower than the carrier signal frequency. In this work the synchronous frame filter found in [29] is used for the current feedback. The synchronous frame filter is made adaptive by using the estimated position in the frame where the position dependent part of the carrier signal is removed. In theory the synchronous frame filter removes the carrier signal components from the stator current and the current regulator bandwidth can be selected higher. In the practical implementation there will be some errors in the estimated rotor position and there may be some carrier signal components entering the current controller feedback. Thus the current regulators must be tuned according to the performance of the position estimate and the synchronous frame filter. Figure 6.12 show the inputs and outputs for a step change in the speed reference.

The bandwidth (ω_b) of the current regulators where determined by measuring the 10-90% rise time for a step response.

$$\omega_b = \frac{\ln 9}{t_r}[rad/s] \tag{6.29}$$

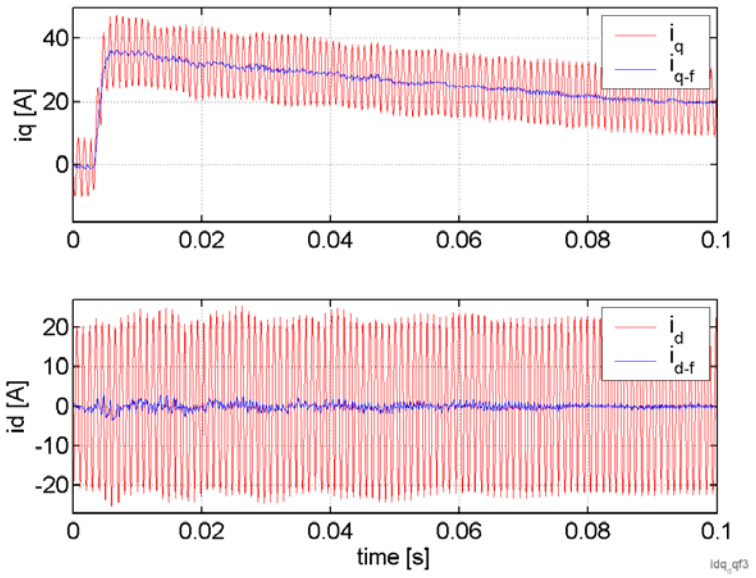

Figure 6.12 Synchronous frame filtering for current regulator feedback:Vc=30 V, fc=1000Hz, hp1-3=100Hz (rated current equals 90 A)

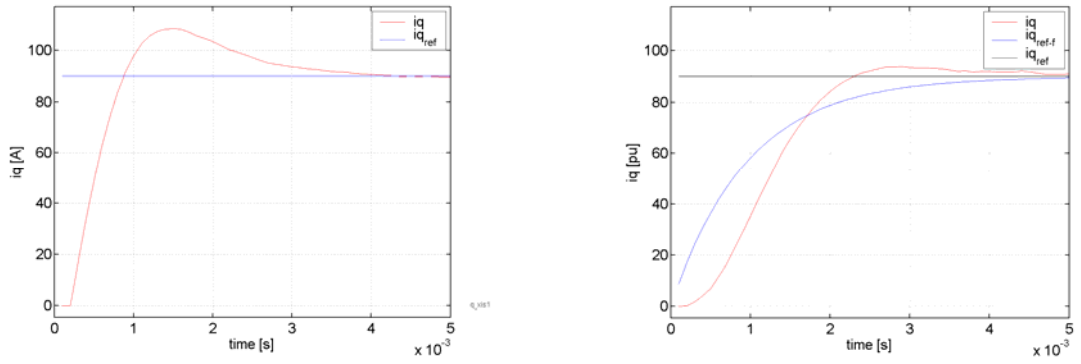

Figure 6.13 Left: 1.0 pu step change in q-axis regulator. Right: 1.0 pu step change with pre filter on reference.

Initially there were some problems during the speed reversal tests. The quick change in the stator current resulted in loss of orientation. This was mainly due to the high pass filtering in the dq-frame. When the q-axis current changed very quickly the high pass filter in the dq-frame could not remove the fundamental current. In order to slow down the change in the current a pre filter was applied on the reference for the regulator. According to (6.29) the current regulator bandwidth was approximately 700 Hz before the pre filter was introduced, with the pre filter the bandwidth was reduced to approximately 350 Hz. The pre filtering did not improve the transient operation of the synchronous filter, but due to the smooth current response it was used during the experimental work in this Chapter. It should be noted that the gains in the regulator was not changed, only the reference current was pre filtered. Thus any deviations from reference current still faced a 700 Hz bandwidth.

6.2.2 Selection of carrier voltage magnitude

The selection of carrier voltage magnitude relates to many aspects: current sensor accuracy, magnitude of transient current distortion and magnitude of zero crossing effects. A speed reversal test was used to show the position dependent part of the carrier signal during transient operation of the system.

The typical resulting frequency from a transient in the negative rotating carrier reference frame is at the same frequency as the carrier. The typical amplitude is comparable to the q-axis change in amplitude. In Figure 6.14 transients from speed reversals is shown. The interpretation of the different currents is shown in Figure 6.2. The speed controller outputs a step in the i_q reference equal almost 50 amps. The size of the transient in the carrier position signal is at the same size as the transient in i_q.

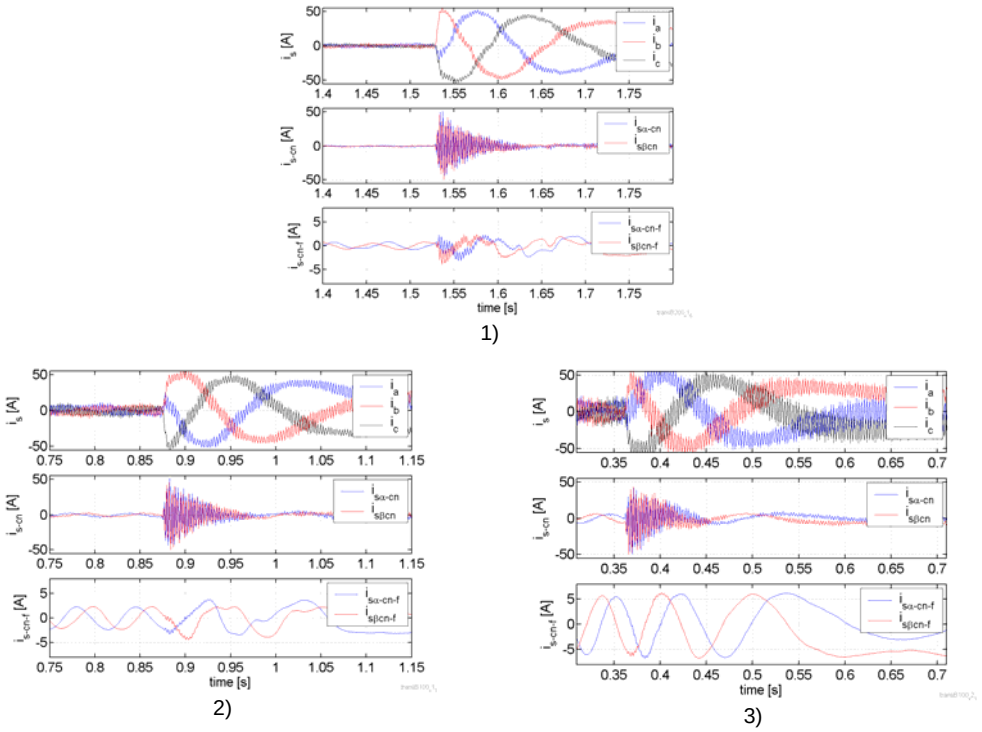

Figure 6.14 Speed reversal -370/370 rpm – transient impact on carrier in negative rotating carrier reference frame. Carrier frequency 1000 Hz ,hp1-3= 5Hz,1: lp1 200 Hz and Vc=7.5 V. 2: lp1= 100 Hz, Vc=15.0 V, 3:lp1=100 Hz, Vc=30 V

The second plot in Figure 6.14-1 show the position carrier current after the synchronous filter. The transient dominates the position signal and a low pass filter can be used in order to remove the high frequency disturbance. In Figure 6.14-1 a second order Butter Worth filter with cut off frequency at 200 Hz was used. The filtered carrier signal is shown in the lower plot in Figure 6.14-1. In this implementation the transient has bigger amplitude than the position dependent carrier and the tracking will be lost during the transient. In order to reduce the impact on the position estimation due to transient operation the carrier voltage was increased to 15 V. The cut off frequency in the low pass filter after the synchronous filter was lowered to 100 Hz. With these settings the position tracking was not failing during the transient test but there where large errors (approximately 20-30 el. degrees) during the transient due to fundamental current zero crossing. In Figure 6.14-2 the time instants of the large position errors can be derived from the fundamental current zero crossings. In the final test (Figure 6.14-3) the carrier amplitude was increased to Vc=30 V (amplitude). With this carrier signal the impact from the zero crossings are minimized as the amplitude of the position signal becomes sufficient larger than the influence from the fundamental current zero crossing. In the rest of this subchapter 30 V is used as the default carrier amplitude. The resulting high frequency phase current was approximately 20 A (0.22 pu) in peak value.

6.2.3 Transient and zero crossing effects on the estimates

The fundamental current zero crossing effect in the position dependent part of the carrier can be evaluated by applying a speed reversal and logging the response after the synchronous frame filter and lp1 in Figure 6.3. In this test only the fundamental excitation is used: Figure 6.15 shows that there is virtually no influence from the fundamental phase zero crossing when *no carrier signal* is applied.

Figure 6.16 shows the influence on position estimate from fundamental current zero crossings when the carrier is applied. The labels t1-t5 indicates where the position error peaks are located: there is a close relation between the error peaks and the fundamental phase current zero crossings. This indicates that the fundamental current zero crossings impose transients in the same frequency region as the negative rotating carrier signal. These transients are difficult to remove by filtering due to the frequency overlap with the position dependent carrier signal. A detailed analysis of these phenomena is presented in Chapter 9.

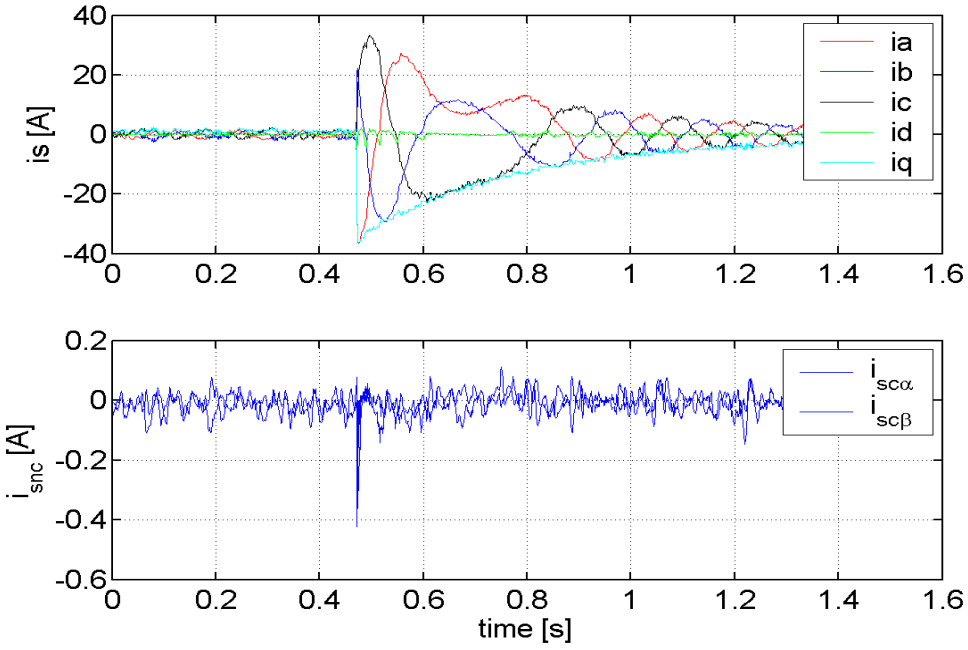

Figure 6.15 Resulting Current in negative frame after synchronous frame filter and low pass filter 1 (100 Hz) during a speed reversal, no carrier signal injection

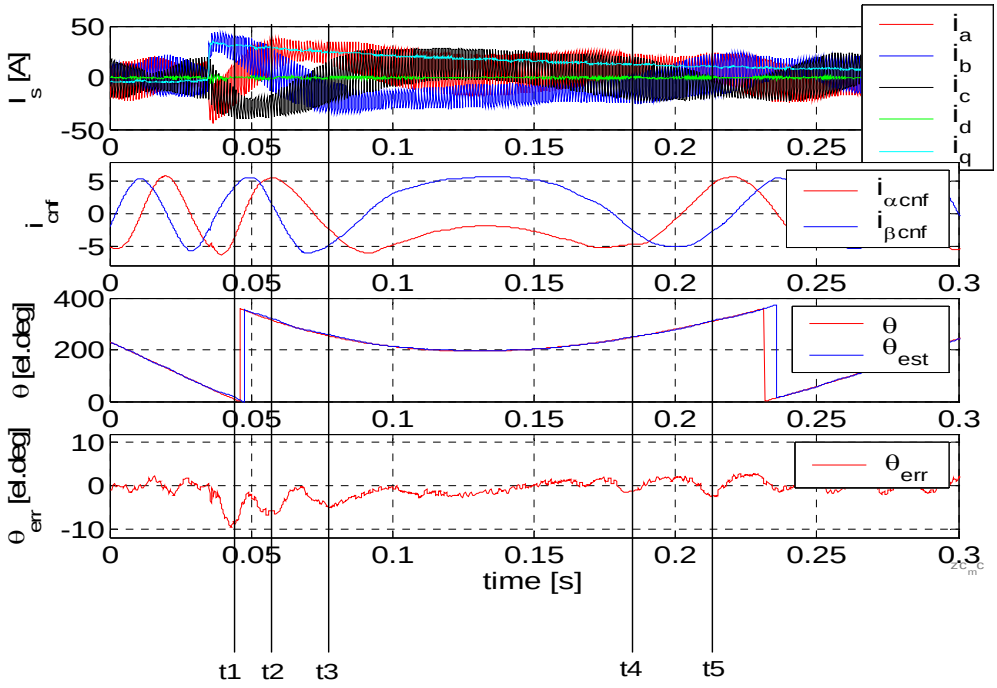

Figure 6.16 Fundamental current zero crossing effect on position estimate when carrier is applied

6.2.4 Tracking and transient test with standard and simplified scheme

The standard scheme (Figure 6.2) and the simplified scheme (Figure 6.6) were tested with the speed reversal test. During these tests the carrier voltage amplitude was 30V. There was a speed dependent lag in the estimated speed and rotor position. The lag was mainly due to the low pass filtering used (lp1) but some lag also relates to the observer and other lags in the current loop and DSP. A linear approximation could be used to compensate for the speed dependent lag in the position estimate. From the speed reversal test the speed dependent correction is estimated. For the implementation with the second order butter filter at 100 Hz the delay at 0.1 pu speed is approximately 13.5 electrical degrees. There is also a load dependent offset in the position estimate due to i_q. The load dependent offset is due to the interaction between the flux from the magnet and the flux form the load current. This interaction creates a spatial shift in the resulting stator flux and a shift in the saturation based saliency. This effect was described in detail in Chapter 3. The size of this offset is determined with transient operation in the next section. From these measurements the offset due to i_q is approximately 5 electrical degrees (negative) for a 90A change in i_q.

$$\hat{\theta} = \hat{\theta}' + \Delta_1 \cdot \hat{n} + \Delta_2 \cdot i_q \tag{6.30}$$

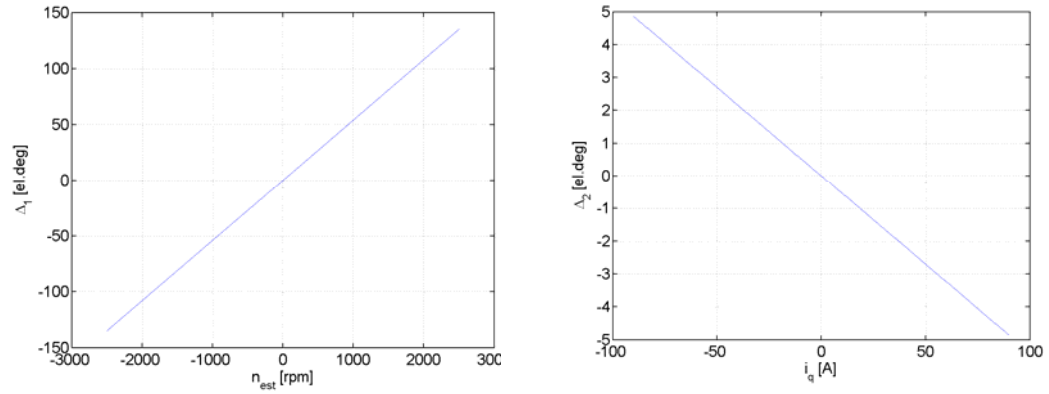

Figure 6.17 Correction functions used for HFCI rotating

In order to compare the different schemes the same pole placement strategy was used for all schemes: the poles where placed with 5 times frequency separation. The observer poles where tuned up (as far as possible); the upper limit where determined by a maximum +/- 10 electrical degrees error in the position estimate. This may not be an optimal pole placement in respect to parameter sensitivity and noise rejection for all schemes, but it gives an easy way of comparing different schemes. If the torque feed forward term was used the transient test for high frequencies turns into a test of how good the estimated inertia is. In the comparison of the schemes the performance without the estimated inertia and torque feed forward will be used. In Figure 6.18 speed reversal tests are shown. The correction term $\Delta_1 n$ is used for all plots. The basic solution with the synchronous filter is plotted in Figure 6.18.1. If this plot is compared to the simplified scheme (Figure 6.18.2) there is virtually no difference (the simplified scheme is illustrated in Figure 6.6). Torque feed forward was not used in Figure 6.18-1 and 2. Transient tests where also performed in order to verify the similar characteristics and these tests also confirmed that the operation was equal. As the performance was equal only the standard synchronous frame solution is presented for the remaining tests. The effects from torque feed forward were also tested: in Figure 6.18-3 and 4 the estimated inertia is set equal to $\hat{J} \approx 0.5J$ and $\hat{J} \approx J$. As the speed reversal is slow compared to the observer pole location (10, 50, 250 Hz) the feed forward term has virtually no effect. This can also bee seen if considering the sensitivity function in Figure 6.10. The large errors in the position estimate in the time instant after the commanded speed step is related the fundamental current zero crossings.

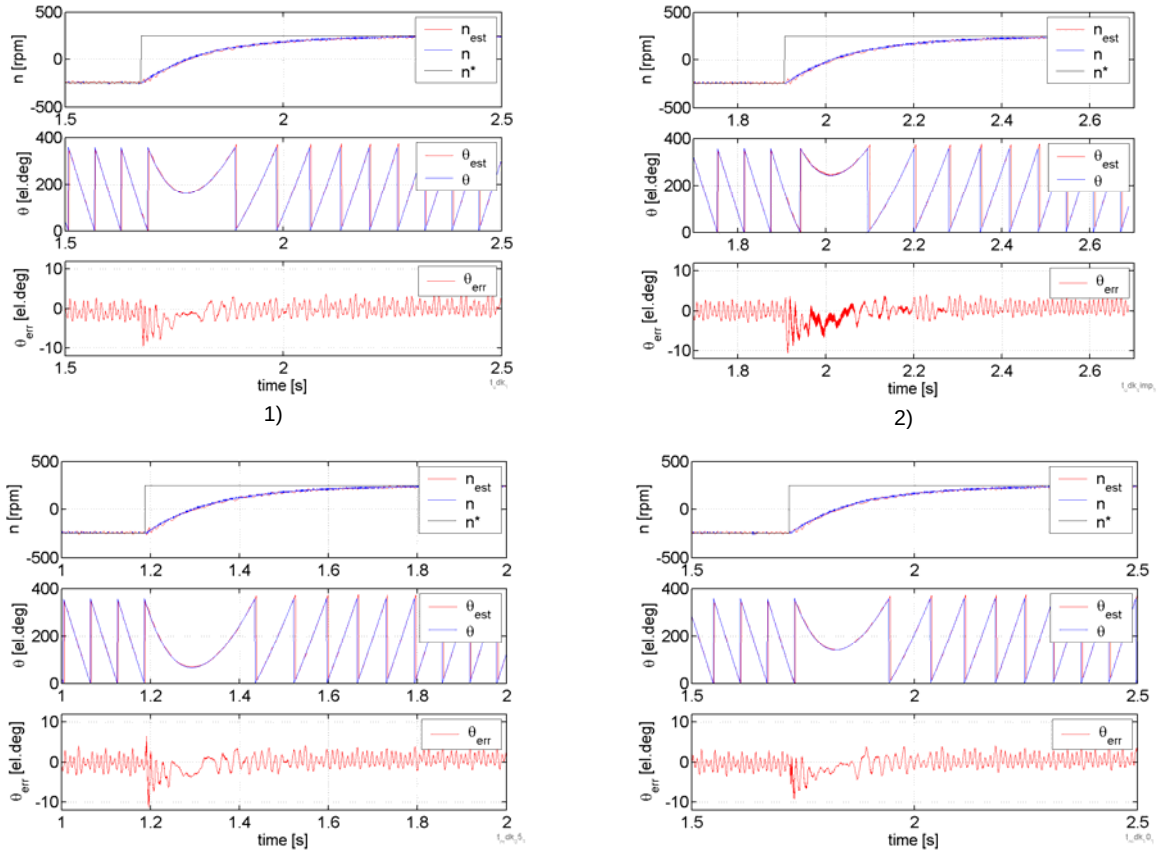

Figure 6.18 Speed reversal -250/250 rpm, observer poles:10, 50, 250Hz, no load. 1) Synchronous filter, 2) Alternative filtering, 3) Synchronous filter Torque feed forward ($\hat{J} \approx 0.5J$) , 4) Synchronous filter Torque feed forward ($\hat{J} \approx J$)

In order to verify the extreme transient operation square wave i_q reference (+/- 45 A) were applied. As the reference frequency was increased the speed and position estimates begin to degrade. The fast transition from + 45 A to – 45 A leads to phase current zero crossing and heavy transient content from the fundamental current. Figure 6.19 shows the transient test at 12.5 Hz and 25 Hz. Correction terms were not used for the tests in Figure 6.19. Two major contributions to the position error are: the fundamental current goes trough zero, and the saliency is shifted due to the high q-axis current. In addition the synchronous frame filter suffers from the rapid change in the q-axis current. The high pass filtering in the dq-frame (Figure 6.2) cannot reject the rapid change in the q-axis current. This current must be filtered off in the low pass filter in the negative rotating frame (lp1 in Figure 6.2). The resulting effect in the speed and position estimate is an error in the time instant the q-axis current is changed. In Figure 6.19- 3 and 4 the feed forward term is used ($\hat{J} \approx J$).

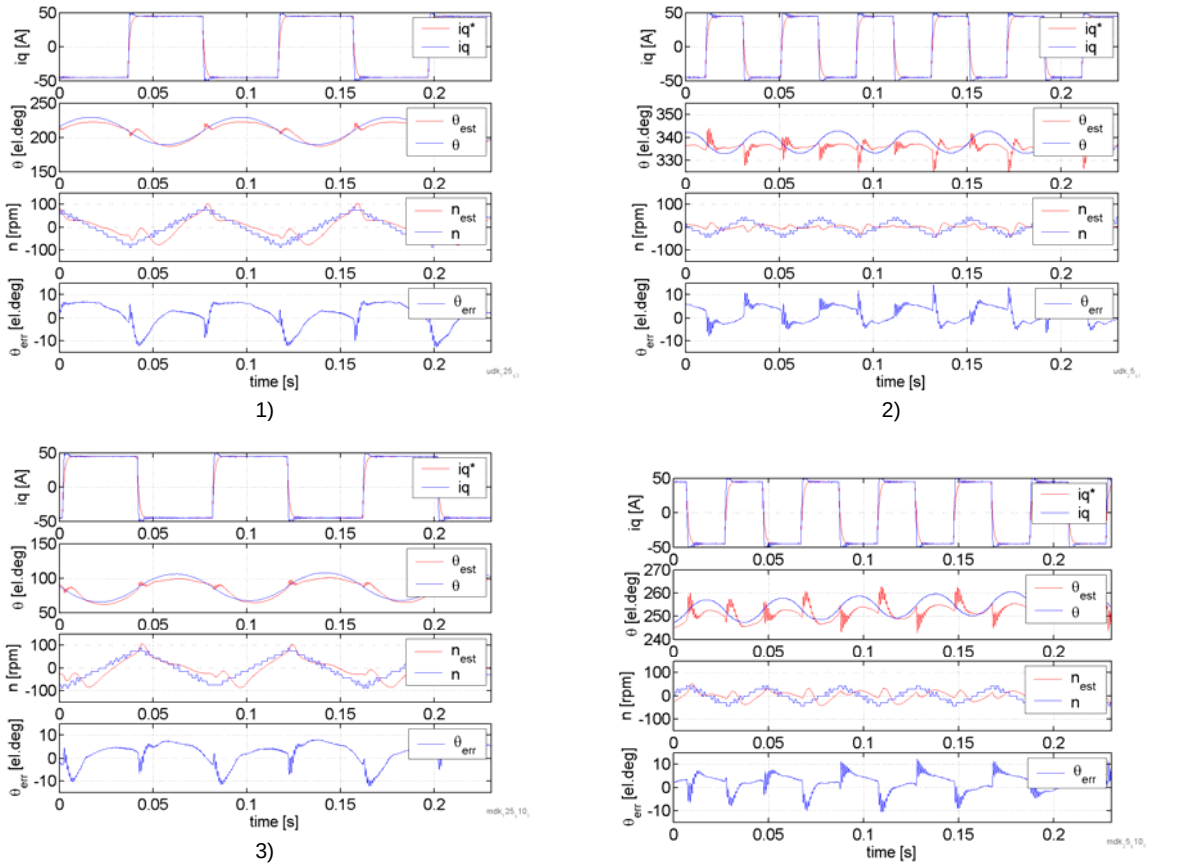

Figure 6.19 Transient test, Synchronous frame filtering, Observer poles at 10, 50 and 250 Hz,1) no torque feed forward 12.5Hz, 2) No torque feed forward 25Hz, 3)Torque feed forward 12.5 Hz ($\hat{J} = J$) 4) Torque feed forward 25 Hz ($\hat{J} = J$)

The 12.5 Hz test (Figure 6.19- 1 and Figure 6.19- 3) are quite similar due to the low test frequency compared to the observer pole placement. As the frequency was increased the feed forward torque improved the estimates (Figure 6.19- 1 and Figure 6.19- 3). The AFF diagram in Figure 6.10 also indicates this type of effect form the feed forward term. In order to fully illustrate the potential effects of the torque feed forward a different observer tuning approach is presented in Figure 6.20: the observer poles are placed slower than the test frequency. This tuning result in a lower disturbance rejection and the estimates apparently becomes much better. The observer poles were detuned to 0.2, 1 and 5 Hz, the test sequence was 12.5 and 25 Hz (Figure 6.20). If this type observer tuning was used for comparison of the different schemes the tests results would be fairly equal as this merely is a test showing how good the estimate of inertia is and how the torque feed forward term improves bandwidth of the observer. This type tuning will result in a more parameter sensitive scheme and it will not be used in the final comparison of schemes.

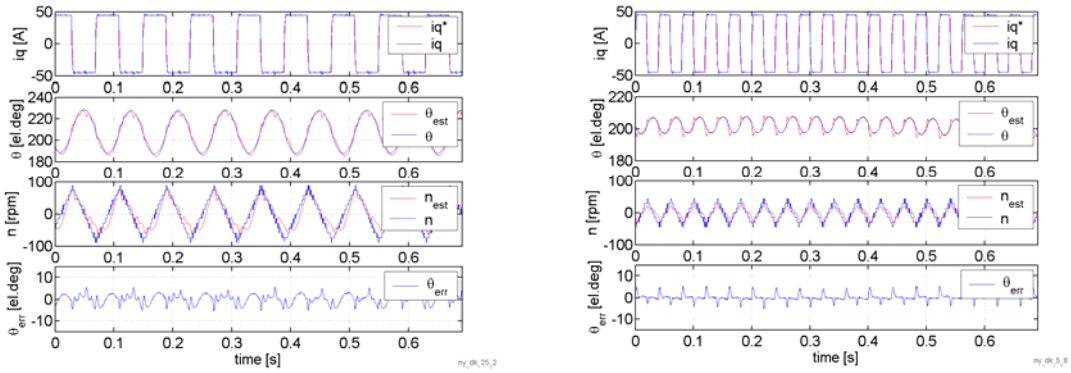

Figure 6.20 Transient test with standard synchronous frame filtering.1: 12.5 Hz alternating iq reference. 2: 25 Hz alternating iq reference. Observer poles 0.2, 1 and 5 Hz, $\hat{J} \approx J$

6.2.5 Decoupling of fundamental current

Two approaches were tried with the configurations in Figure 6.8: narrow notch filtering (hp1-3=1-10Hz Figure 6.2) and wide notch filtering (hp1-3=50-100Hz Figure 6.2). The narrow notch filtering aimed to decouple both the zero crossing and the transient fundamental effect. The wide notch filtering aimed at decoupling only the transient fundamental effect.

Figure 6.21 the current response during a speed reversal with narrow notch filtering. The labelling is referring to Figure 6.8 were i_{d3} is the resulting current after the decoupling. In this test the position from the encoder was used in the synchronous frame

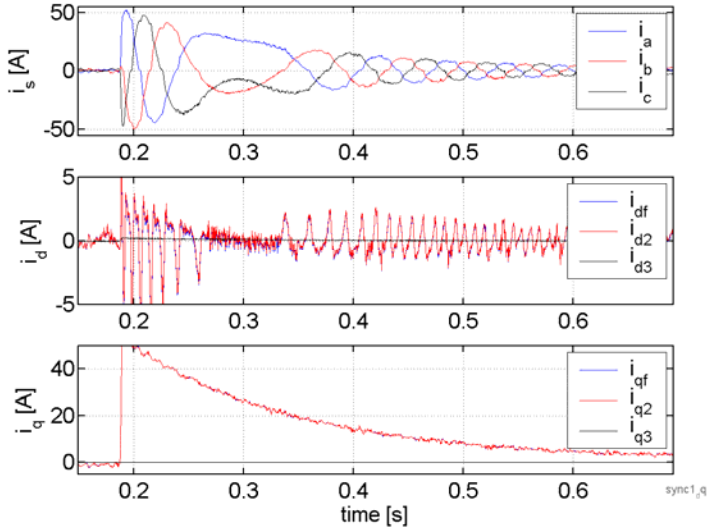

Figure 6.21 Fundamental current zero crossing effect, 375 rpm speed reversal, no hf excitation, hp(1-3) filters at fc= 5 Hz, rotor position from encoder, no signal injection

filter. When the *encoder position* was used all the frames in the synchronous frame filter were based on measured or commanded variables. This made the reference frames as accurate as possible. From a series of tests full decoupling was found when the cut off frequency for the high pass filters was tuned to ≤5 Hz. Figure 6.22 shows the same test with the carrier voltage applied. The zero crossing and the transient fundamental current effect was eliminated even when the carrier amplitude was lowered to 7.5 V. Compared to the carrier signal in Figure 6.14 the quality of the position dependent carrier was improved and the need for low pass filtering was eliminated. When the synchronous frame filter was tried with the *estimated rotor position* the results where not as good. The narrow notch filtering has one serious problem: when the estimated rotor position has errors the feed back in the observer contains carrier signal. In addition the lag of the carrier signal in the feedback alters from +90 to -90 when the error is small positive or small negative. Even tough the narrow notch filtering was not successfully implemented with the estimated position the tests gives an idea of the potential performance of the scheme based on HFCI-R when the zero crossing effects are decoupled.

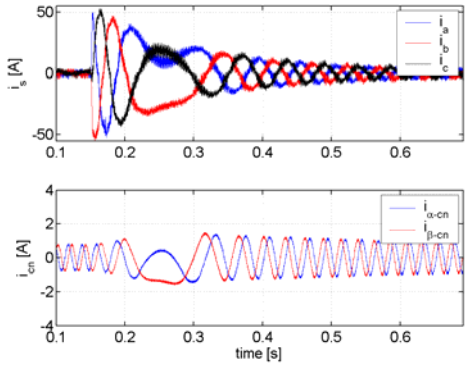

1)

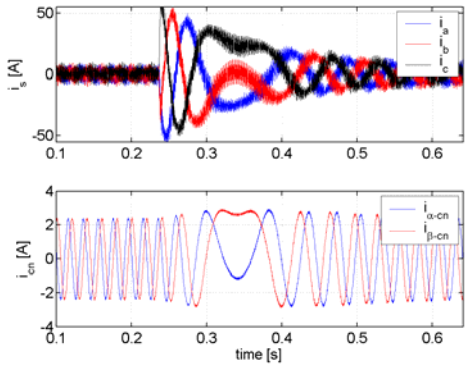

2)

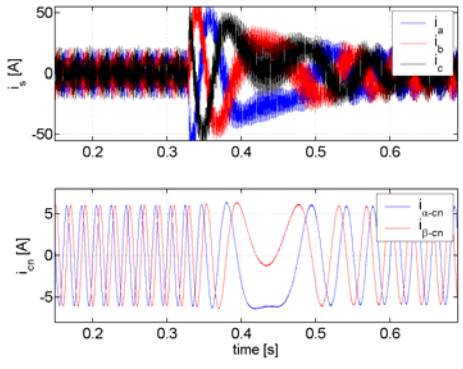

3)

Figure 6.22 Speed reversal -370/370 rpm – transient impact on carrier in negative rotating carrier reference frame. Carrier frequency 1000 Hz, hp1-3=5Hz, rotor position from encoder used in filters,1: Vc=7.5 V. 2: Vc=15.0 V, 3: Vc=30V

The wide notch filtering (hp1-3=50-100Hz Figure 6.2) was aimed at decoupling of the fundamental current, but no decoupling of the zero crossing effect. 100 Hz cut off frequency was selected for the high pass filters (1 to 3 in Figure 6.8): the resulting decoupling removed the impact from the transient fundamental current and the low pass filter before the observer was not needed. In the tuning of this approach there was one serious problem as the observer could not be tuned at high bandwidths. If the observer was tuned with a high bandwidth the noise sensitivity became too big and the performance degraded. As the original solution with the low pass filter in the negative reference frame also removed the transient current (and the observer poles could be located at 10, 50 and 250 Hz) the decoupling scheme with wide notch filtering did not enhance the operation of the scheme.

6.3 Chapter conclusions

Based on the work found in [2, 13, 39] the scheme based on rotating carrier injection was implemented. The implementation in this thesis is a simple implementation where the bandwidths obtained by no means are optimal. In [39] a 100 Hz bandwidth was proved with an IPMSM and the same scheme. The bandwidth test in [39] was a test with sinus varying load. For comparison with the work done in this thesis the test without the torque feed forward must be used. In this thesis the comparable bandwidth was approximately 12.5 Hz (Figure 6.19.1). The reason for the large difference is mainly the effects of the fundamental zero crossings and the low cut-off frequency used in the low pass filter (lp1 in Figure 6.2). In addition the test in Figure 6.19 is more extreme as a large square wave torque reference was used. In the square wave test there are large transients and a saliency shift due to the large q-axis current. In this thesis the recognition of the challenges for each scheme is the focus rather than optimal implementation of each scheme. For the HFCI-R based scheme the following challenges where found:

- the synchronous frame filter alone does not reject transient response in the dq-currents. A low pass filter is needed in order to remove transients in dq-current (Figure 6.2). Alternatively a fundamental current decoupling scheme could be used [29].
- the effect of fundamental phase current zero crossings limits the bandwidth of the system and the accuracy in the estimated speed and position

If low pass filtering is used after the synchronous frame filtering in Figure 6.2 the performance would be equal to the simplified scheme in Figure 6.6. The torque feed forward arrangement in the observer enhance the observer when applied frequencies are close to or higher than the observer poles.

A simple scheme for fundamental current decoupling is presented in this Chapter. In the tuning of the decoupled system the bandwidths could not be as high as for the arrangement in Figure 6.2. The decoupled system with narrow notch filtering is presented merely to show how the potential improvement could be if the fundamental current is decoupled. For future work the decoupling scheme in [29] could be implemented or a dead time compensation scheme could be implemented. Both these methods could improve the performance of the system.

In the initial analyses the carrier voltage amplitude had to be 30 V in order to produce reliable position and speed estimation. With this carrier voltage and the observer poles in 10, 50 and 250 Hz the maximum frequency in the transient test was found to be 12.5 Hz. In the comparison of schemes the following results will be used: speed reversal - Figure 6.18.1, transient test - Figure 6.19.1, disturbance rejection - Figure 6.10.2.

7 HIGH FREQUENCY CARRIER INJECTION-PULSATING

7.1 Description of scheme

The schemes based on injection of pulsating high frequency injection are many. Both d and q axis injection can be found in the literature [3, 25]. In this work d-axis injection is implemented due to two factors: minimum torque production from the carrier signal and minimum influence from fundamental current zero crossing. Minimum torque production from carrier signal will be true for surface mounted PMSM where only the q-axis current is torque producing. For an IPMSM the carrier injection in the d-axis will not be the minimum torque producing angle due to the reluctance torque. As the carrier frequency is high any pulsating torque components due to the carrier will be effectively filtered by the rotor inertia, more interesting is the acoustic noise as a result of the torque production. The influence from transient operation of the drive is documented in this chapter: very little influence from fundamental zero crossing is found. A new filtering approach is presented based on synchronous frame filtering. The new filtering technique allows the current regulators to be tuned more freely.

7.1.1 Carrier injection and observer

The injection scheme is very similar to HFCI-R scheme. The high frequency component is added to the d-axis output voltage. The carrier signal in the estimated dq-frame can be expressed as (j-included in order to simplify resulting current):

$$\underline{U}_c^{\hat{r}} = \begin{bmatrix} U_{\hat{d}c} \\ U_{\hat{q}c} \end{bmatrix} = j \begin{bmatrix} U_{sc}\cos(\omega_c t) \\ 0 \end{bmatrix} \tag{7.1}$$

In order to derive a expression for the carrier current the inductance matrix must be transformed to the estimated rotor reference frame by the difference between the estimated rotor position and the real rotor position ($\Delta\theta = \theta - \hat{\theta}$):

$$\underline{L}_s^{\hat{r}} = \frac{1}{L_d L_q}\left(\sum L\begin{bmatrix}1 & 0\\ 0 & 1\end{bmatrix} + \Delta L\begin{bmatrix}-\cos(2\Delta\theta) & \sin(2\Delta\theta)\\ \sin(2\Delta\theta) & \cos(2\Delta\theta)\end{bmatrix}\right) \tag{7.2}$$

If the resistive drop is neglected the high frequency response can be derived as:

$$\underline{I}_{sc}^{\hat{r}} \approx \begin{bmatrix} I_{\hat{d}c} \\ I_{\hat{q}c}\end{bmatrix} = \frac{U_{sc}}{\omega_c L_d L_q}\begin{bmatrix}\left(\sum L + \Delta L\cos(2\Delta\theta)\right)\cos(\omega_c t) \\ -\Delta L\sin(2\Delta\theta)\cos(\omega_c t)\end{bmatrix} \tag{7.3}$$

In order to derive a term proportional to the position error the q-axis current is demodulated by multiplication of $\sin(\omega_c t)$ followed by a low pass filter (LPF):

$$e \approx LPF(i_{qc}^r \sin(\omega_c t)) = -\frac{U_{sc}}{4\omega_c}\frac{(L_d - L_q)}{L_d L_q}\sin(2(\theta - \widehat{\theta})) \tag{7.4}$$

$$\widehat{K}_e = \frac{U_{s\_c}(\hat{L}_d - \hat{L}_q)}{4\omega_c \hat{L}_d \hat{L}_q} \tag{7.5}$$

It should be noted that the amplitude of the error signal is only half the amplitude compared to the HFCI-R based scheme. In Figure 7.1 an outline of the scheme is shown: in order to remove as much of the fundamental current as possible a high pass filter is added in the dq-fame. This filter is optional and the effect of the high pass filter is presented in the experimental work. In order to tune the observer the error term is scaled according to the estimated error amplitude(7.5). Due to the linearization of the sinus term in (7.4) a factor 2 must also be included in the scaling term.

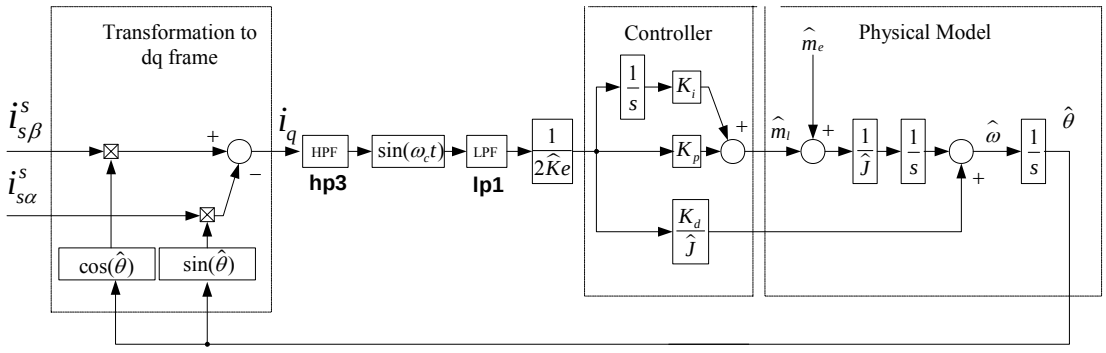

Figure 7.1 Error term and observer for HFCI-P

7.1.2 Synchronous frame filtering

The high carrier frequency will lead to limitations in the tuning of the current regulators. Some implementations use a low bandwidth current regulator that would not act on the high frequency injection. In [25] the d-axis current regulator feedback was simply filtered by a low pass filter. The low pass filter must be approximately one decade lower than the carrier signal in order to properly remove influence from the carrier injection. In this thesis a synchronous fame filter solution is suggested in order to remove the carrier frequency from the fundamental current. The implementation of the filter is slightly different from the synchronous frame filter used in the previous chapter. The injected voltage can represented as two rotating voltage vectors [2] (transformation matrixes in Appendix A):

$$\underline{U}^s_{s\_c} = \underline{T}^{-r}_{ss} \cdot U^s_{s\_c} j \begin{bmatrix} \cos(\omega_c t) \\ 0 \end{bmatrix} = \frac{U^s_{s\_c}}{2} j(e^{j(\hat{\theta}+\omega_c t)} + e^{j(\hat{\theta}-\omega_c t)}) \tag{7.6}$$

The carrier current components can be expressed by using the inversed inductance matrix (6.4) and the voltage components in (7.6):

$$\underline{I}^s_{s\_c} = \frac{1}{j\omega_c} L_s^{s-1} \underline{U}^s_{s\_c} \tag{7.7}$$

The decomposition of positive and negative rotating current components are derived in same manner as in (6.5) and (6.6).The currents in stationary stator reference frame can be expressed as:

$$\underline{I}^s_{s\_c} = I_{c0} e^{j(\hat{\theta}+\omega_c t)} + I_{c1} e^{j(2\theta-\hat{\theta}-\omega_c t)} + I_{c0} e^{j(\hat{\theta}-\omega_c t)} + I_{c1} e^{j(2\theta-\hat{\theta}+\omega_c t)} \tag{7.8}$$

Where

$$I_{c0} = \frac{U^s_{s\_c}(L_d + L_q)}{4\omega_c L_d L_q}, I_{c1} = \frac{U^s_{s\_c}(L_d - L_q)}{4\omega_c L_d L_q} \tag{7.9}$$

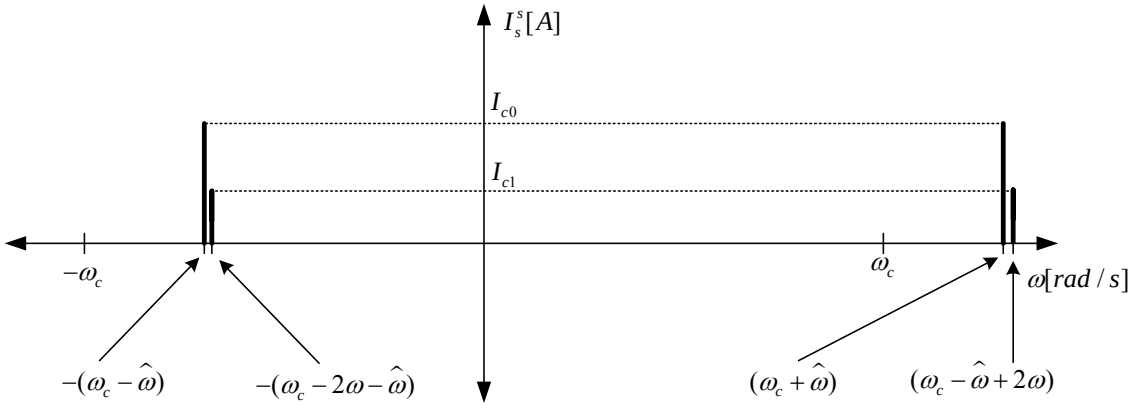

Figure 7.2 Frequency spectra for pulsating high frequency injection in d-axis

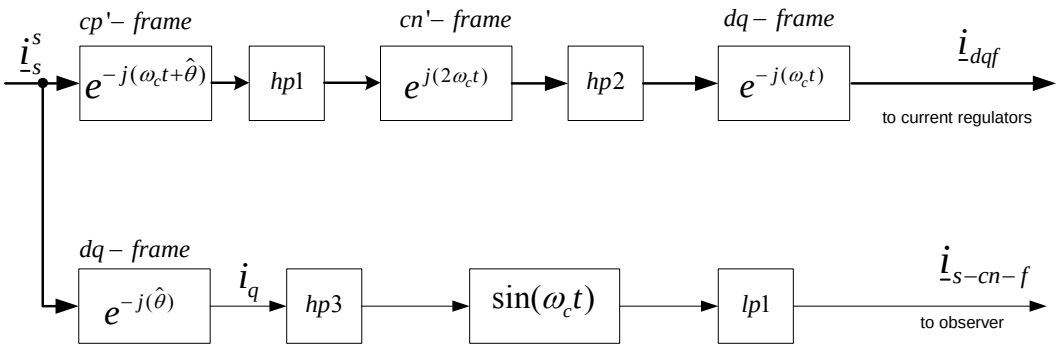

Figure 7.3 Synchronous frame filtering and signal demodulation for HFCI pulsating scheme.

Figure 7.2 illustrates the frequency spectra in stationary reference frame. There are two components rotating in negative direction and two components rotating in the positive direction. The difference in location for the negative (and positive) rotating pair equals the error in the estimated speed. In order to utilize the synchronous frame filter in an optimal manner the filter should be made adaptive (use the estimated position). A modified synchronous frame filter is presented in Figure 7.3. The cp' frame is located at $\omega_c t+\hat{\theta}$ while the cn' frame is located at $-\omega_c t+\hat{\theta}$. When the estimated speed and position is correct the synchronous frame filter completely eliminates the high frequency components. As there always will be some error in the estimates high pass filter 1 and 2 are tuned with 50-100 Hz cut off frequency. Figure 7.4 illustrates the AFF diagrams for the two filter solutions: Figure 7.4.1 illustrates a first order 100 Hz low pass filter and Figure 7.4.2 illustrates the synchronous frame filter with high pass cut off frequency at 50 Hz. The solution with synchronous frame filter allows the bandwidth of the current regulators to be higher compared to the low pass solution.

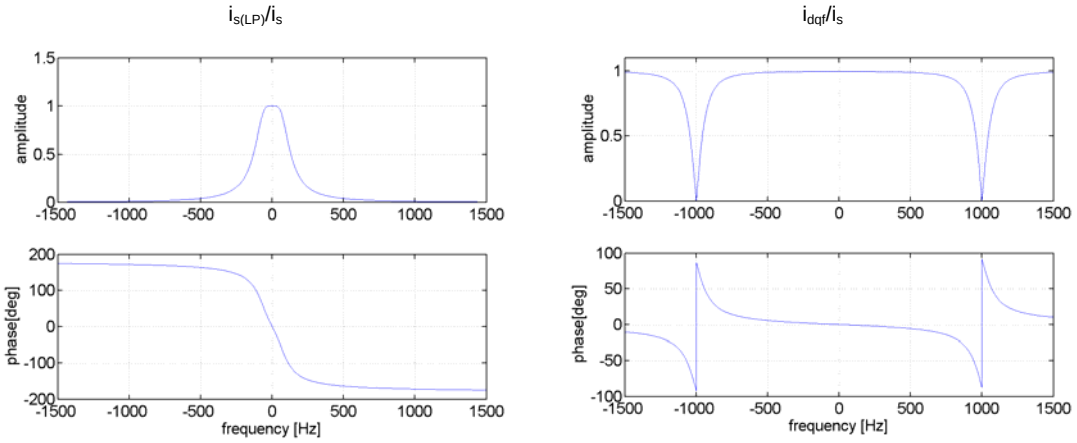

Figure 7.4 AFF diagrams for current feedback filtering f_c=1kHz, 1) standard solution with 100 Hz low pass filter, 2) Synchronous Frame filter (n=0) hp1-2=50Hz

7.2 Experimental work on HFCI-P

In the experimental work Test Machine 1 (IPMSM) was used in all tests. In order to derive the characteristics of the scheme the same tests is used as in the previous chapter: speed reversal and transient test.

7.2.1 Current regulators

The current regulators were tuned with the same bandwidth as for the HFCI-R scheme. Pre filtering of reference value was also used here and the resulting bandwidth is approximately 350 Hz (700 Hz for disturbance – no pre filter effect in feedback loop). The synchronous frame filtering in Figure 7.3 is used in the current feedback loop with 75 Hz cut off frequency in the high pass filters. A speed reversal test is plotted in Figure 7.5, the filtering removes nearly all the carrier signal content.

7.2.2 Amplitude of carrier voltage

When selecting the carrier voltage amplitude the first requirement is that the current measurements accuracy is sufficient for measurements of the position dependent part of the carrier. The current measurement error is discussed in Chapter 9. The error term (7.4) containing the position dependent part of the carrier was measured for different carrier voltage magnitudes. The pulsating excitation was fixed in the stator reference alpha axis and the machine was rotated by hand while the error term was logged. The results from 15 V carrier voltage amplitude is shown in Figure 7.6.1. The experimental setup uses an inverter with 10kHz switching frequency with a 3us dead time. At this switching frequency the dead time influence the voltage quality for low voltage commands. The 15 V carrier voltage amplitude represents 0.1 pu of the system voltage. The inverter will introduce a non linearity at this small voltage command. When the voltage command is increased to 30V the dead time has less influence on the resulting voltage. The error term for Vc=30 V is presented in Figure 7.6.2 .In this work both 15 and 30 V carrier was tested.

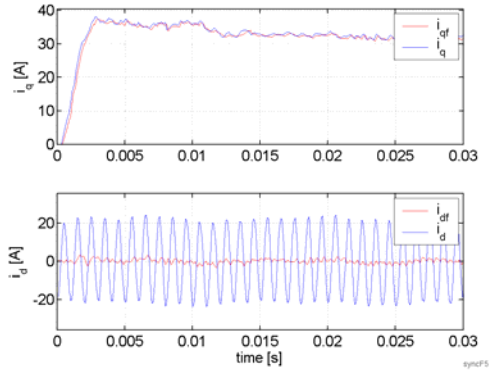

Figure 7.5 Synchronous frame filtering of current controller feedback during a speed reversal hp1 and 2 = 75 Hz, f_c=1kHz, Vc=30V

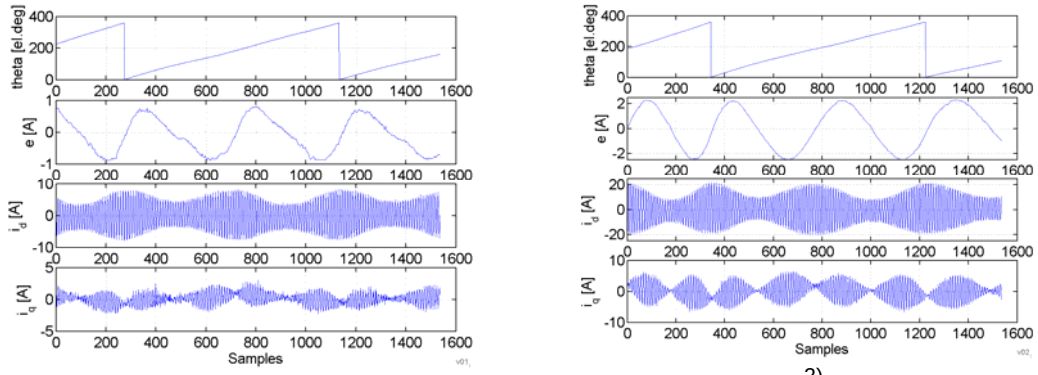

Figure 7.6 Carrier signal and error signal to observer, left Vc=15V right Vc=30 V

When the carrier signal was 15 V the acoustic noise was reduced. In order to compare the scheme to the HFCI-R scheme the performance for the 30 V carrier was used as this gives the same carrier current magnitude as for the HFCI-R implementation.

7.2.3 Transient and zero crossing effect

The basic implementation found in [35] uses no high pass filter in the dq-frame. In a later thesis by [73] the usage of a high pass filter in the dq-frame was suggested. In this section the effect of this high pass filter is evaluated. Two speed reversal tests are shown in Figure 7.7. They illustrate how the fundamental current leads to high frequency content in the error term. Figure 7.7.1 shows the results from a speed reversal test when no high pass filter is used in the error term (hp3 in Figure 7.3). After the demodulating term the fundamental q-axis current appears with frequency approximately equal to the carrier frequency and amplitude equal to the q-axis current. The signal is filtered by a 2. order low pass butter worth filter with cut off frequency equal 200 Hz. The filter does not suppress all the high frequency content and some high frequency components exist in the error term. During the experimental work the cut off frequency was lowered to 100 Hz for some tests but the effect was still present and the presented tests all uses the 200 Hz low pass filter. A higher order filter may improve the performance (not implemented here). As for the synchronous frame filter a high pass filter can be implemented in the dq-reference frame in order to remove the fundamental current before the demodulating. The high pass filter removes the fundamental current in stationary operation. Under transient operation (step reference in current or speed reversal) the current changes quickly and the all the fundamental current passes the high pass filter. Figure 7.7.2 shows the improvement from the high pass filter: when the q-axis current changes slowly all the fundamental current is removed, when the current changes quickly the effect is equal to the implementation with no high pass filter. In the experimental work the high pass filter was used in order to improve the steady state operation.

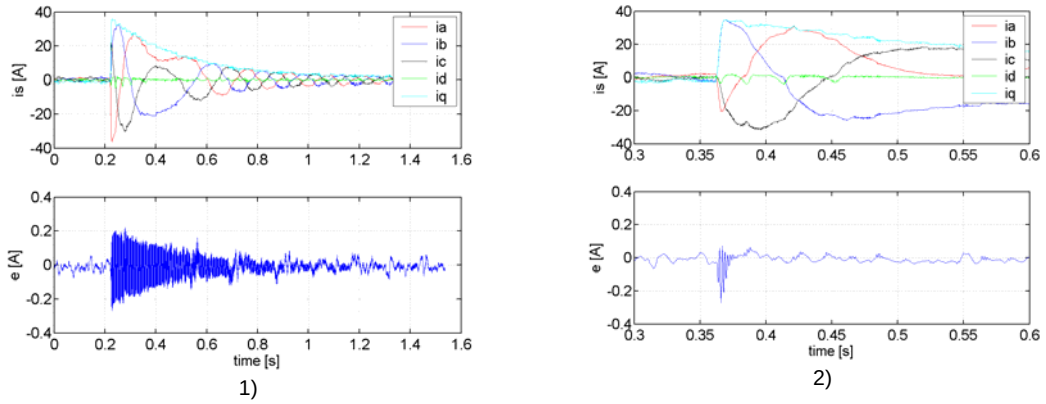

Figure 7.7 Impact on position dependent carrier signal during speed reversal (no signal injection), 1) no high pass filter in dq-frame, 2)100 Hz high pass filter in dq frame

In the HFCI-R scheme the errors during speed reversal could be related the fundamental current zero crossings. A comparable plot can be seen in Figure 7.8; there are no detectable error that can be related to the fundamental current zero crossing. A detailed analysis of these phenomena is presented in Chapter 9.

7.2.4 Speed reversal and transient test

The speed reversal and transient tests where performed with Test Machine 1 (IPMSM). Two carrier voltage amplitudes where tested: 15 and 30 V. The 30 V test is used for comparison with the HFCI-R scheme in order to evaluate the schemes with the same carrier magnitude. When the carrier voltage was 15 V the acoustic noise was dramatically reduced. As acoustic noise is also a criteria used in the comparison the performance with the 15 V carrier was also documented. In order to compare the performance an identical tuning approach was used for all the schemes; the observer bandwidth was increased until the estimated position and speed was at best performance for the 12.5 Hz transient test. The three observer poles where placed with 5 times frequency separation (i.e. poles in p1, p2 and p3 placed as p3=2*pi*(5*f2), p2=2*pi*(5*f1)). The speed reversal and transient tests are done with no feed forward torque in the observer in order to find the characteristics of the scheme. In Figure 7.8.1 the speed reversal test for Vc=15 V and observer poles in 1, 5, and 25 Hz is presented. When the poles where placed more to the left in the complex plane the position error was larger and the system started to oscillate when the poles were located in 2, 10 and 50 Hz. When the carrier voltage was increased to 30 V the performance was improved as the transient and zero crossing effects are smaller compared to the carrier amplitude. The results for 30 V carrier and poles in 2, 10 and 50 Hz is shown in Figure 7.8.2.

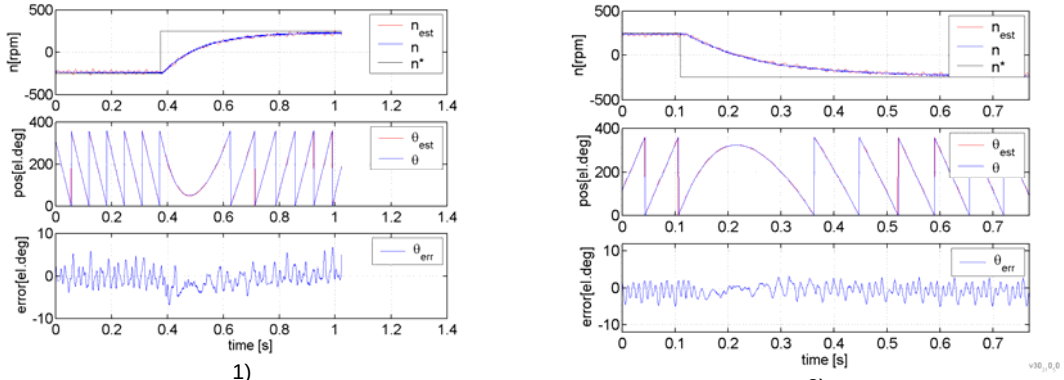

Figure 7.8 Step change (0.2 pu) in speed reference, no torque feed forward 1) Vc=15V observer poles 1, 5, 25 Hz, 2) Vc=30 V, observer poles in 2, 10, 50Hz

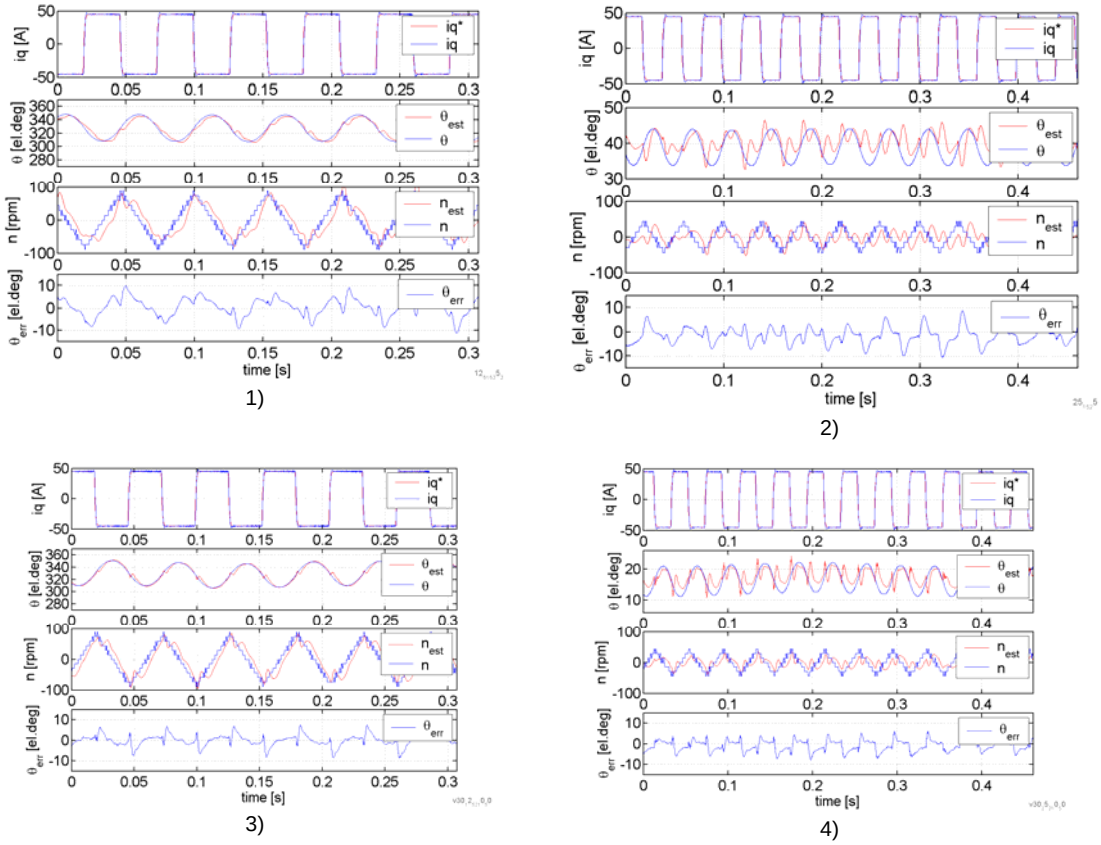

Figure 7.9 Transient test, no torque feed forward, lp1=200Hz, hp1=100Hz 1)Vc=15V 12.5 Hz test , observer poles in 1, 5 and 25 Hz, 2) Vc=15V 25 Hz test, observer poles in 1, 5 and 25 Hz, 3)Vc=30V 12.5 Hz test, observer poles in 2, 10 and 50 Hz, 4)Vc=30V 25 Hz test, observer poles in 2, 10 and 50 Hz

Transient tests are presented in Figure 7.9. In the transient test the q-axis reference current is a square wave (12.5 and 25 Hz) +/-45A. The motor shaft oscillates and the performances of the estimates are evaluated. In Figure 7.9-1 and 2 the carrier amplitude was 15 V and the observer poles where located in 1, 5 and 25 Hz. Under the 12.5 Hz test the position estimate is within the +/- 10 degrees limit, but the speed estimate is deformed. The maximum speed during this test is only 4% of the rated speed thus the speed error in percentage of the rated speed is maximum 2%. At the time instant of the current step there are transient effects in the estimated speed and position: the fundamental phase current crosses zero and the quick change in the q-axis current gives a distortion as showed in Figure 7.7. In addition the saliency will have a shift due to the change in the load current. When the test frequency is increased to 25Hz the change in position is comparable to the effect from the transient effects and the speed and position estimates fails. When the carrier voltage was increased to 30 V the influence from the transients is smaller compared to the carrier voltage and the poles in the observer could be placed in 2, 5 and 50 Hz. The 12.5 Hz test (Figure 7.9.3) shows an excellent position estimate: the scheme quickly compensates for the position change but also here the speed estimate is deformed. The speed estimate is an internal state in the observer and it is highly sensitive to noise when the observer is tuned at high bandwidths. When the test frequency was increased to 25 Hz (Figure 7.9.3) the transient effects are comparable to the position change and the estimates fails. The bode plot and the disturbance rejection function (defined in Chapter 6) is plotted in Figure 7.10 for the poles used in the 15 and 30 V carrier implementation.

The scheme was also tested with the torque feed forward term included in the observer. The observer poles where placed at 0.2, 1 and 5 Hz in order to reduce the sensitivity to the transient effects. This type tuning reduces the disturbance rejection ability as the bandwidth of the estimated load torque reduces. The 12.5 and 25 Hz transient test is shown in Figure 7.11 for $\hat{J} \approx J$. Both speed and position estimates are excellent

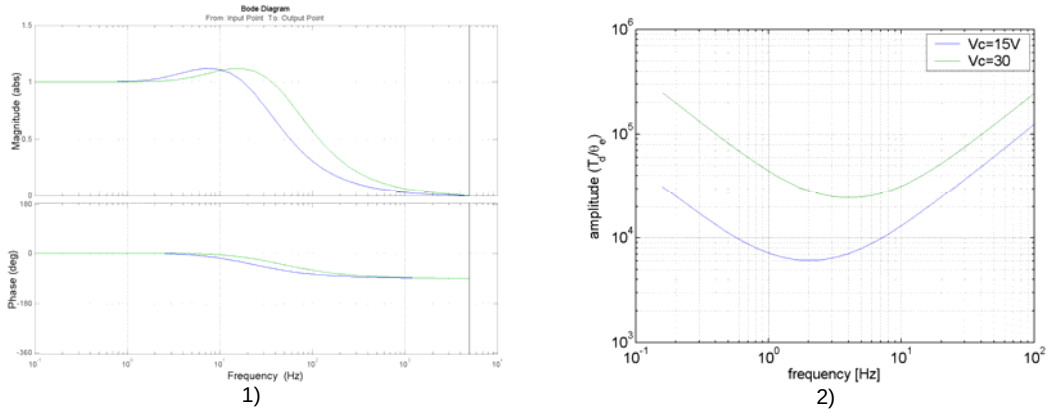

1) 2)

Figure 7.10 Vc=15V Observer poles in 1, 5, 25 Hz (blue) and Vc=30 V observer poles in 1, 5, 25 Hz (green), 1) AFF diagram for estimated position over real position 2) Disturbance rejection function

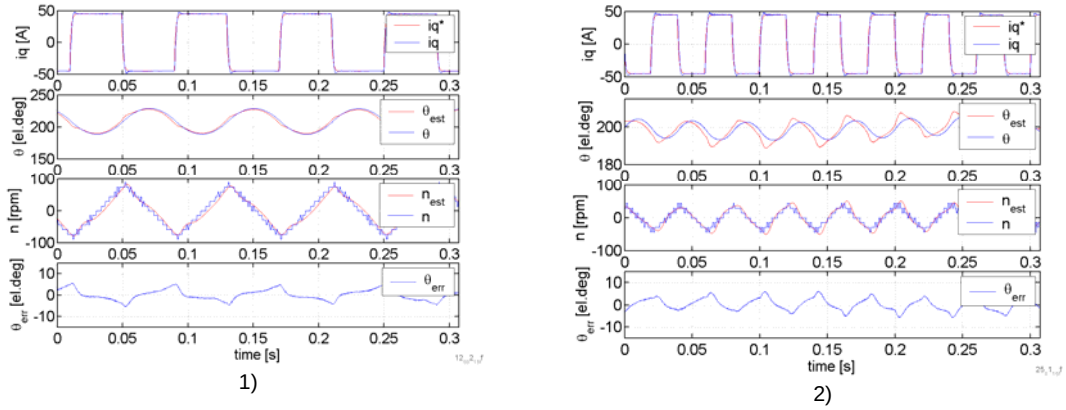

1) 2)

Figure 7.11 Transient test Vc=15 V, Observer poles in 0.2, 1, 5 Hz, torque feed forward,lp1=100Hz, hp1=200Hz, $\hat{J} \approx J$ 1) 12.5 Hz test 2)25 Hz test

compared with the estimates without the torque feed forward. In the 25 Hz test some transient effects can still be seen in the position and speed estimate. In Chapter 6 the disturbance rejection and parameter sensitivity functions where defined. Figure 7.12.1 shows the parameter sensitivity for the torque feed forward solution (0.1, 1 and 5 Hz poles) is plotted. The disturbance rejection function for the same pole placement is shown in Figure 7.12.2.

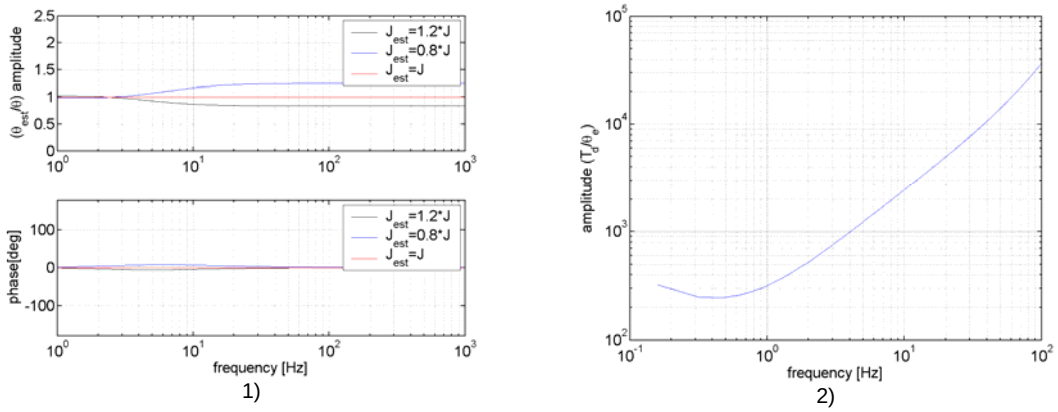

1) 2)

Figure 7.12 Torque feed forward, poles in 0.2, 1, 5 Hz 1)Parameter sensitivity 2) disturbance rejection

7.3 Chapter Conclusions

Based on the work done in [3, 25] the scheme based on pulsating high frequency d-axis injection has been implemented. The successful operation with 15V carrier amplitude indicates that the combined zero crossing effects from fundamental and carrier is smaller compared to the HFCI-R scheme.

There is a different mechanism that limits the bandwidth of the HFCI-P scheme: due to the "search algorithm" nature of the scheme the carrier current injection angle is a result of the estimated position. This includes the lag from filters, electrical time constants and lag in observer. In the HFCI-R scheme the carrier voltage is injected in the stationary stator reference frame independent of the position estimate. In the HFCI-R scheme the observer is an add-on compared to the HFCI-P scheme where the estimated position is included in the injection angle.

In order to prevent the carrier injection from influencing the current regulators two approaches is common:

- The feedback to current regulators are filtered by a low pass filter [22, 25, 30]
- The current regulator bandwidth selected sufficiently lower than the carrier frequency [3, 4]

In this work synchronous frame filtering is suggested to filter the feedback to the current regulators. This allows for higher current regulator bandwidth compared to the existing methods.

For the comparison of schemes in Chapter 9 the following results will be used: speed reversal test from Figure 7.8.2, transient test from Figure 7.9.3, and the disturbance rejection function from Figure 7.10.2 (Vc=30 V). All of these test where made with no torque feed forward and the observer poles in 2, 10 and 50 Hz. It should be noted that the normalizing term used in this tuning (observer tuning) is an estimate containing machine parameters. The observer pole placement and the disturbance rejection must therefore be regarded as approximately results. In worst case the observer poles may drift due to changes in the estimated parameters and lead to unstable operation. In [73] stable operation was guarantied by using saturated estimates of inductance in the tuning of the observer.

8 TRANSIENT EXCITATION

There is a variety of different schemes that uses transient excitation for sensorless control or initial position estimation [1, 66, 67]. In comparison of different schemes [2] it has been claimed that the transient excitation based schemes have lower bandwidth and disturbance rejection ability. A new scheme based on transient excitation is presented in this chapter. The new scheme estimates the rotor position based on a single measurement sequence. In the experimental part of this chapter the characteristics of the new scheme is documented and used in the comparison of schemes in chapter 9.

8.1 Description of Scheme

The scheme is based on the INFORM (INdirect Flux detection by On-line Reactance Measurement) method [1] and the excitation principle found in [7] where the transient excitation is integrated in the zero vector. In contrast to the basic INFORM method the modified scheme make a position estimation based on one measuring sequence and an offset. Thus a new independent position estimate can be made in each switching period.

8.1.1 Stator current derivative trajectory

The basis for the transient excitation methods are the same as the basis for the high frequency injection based methods. If back EMF and stator resistance is neglected the remaining stator voltage equation is:

$$\underline{U}_s^s = \underline{L}_s^s \frac{d\underline{I}_s^s}{dt} \tag{8.1}$$

In the implemented scheme the back EMF is not neglected but removed by a differential measurement. This technique will be covered in the next section. The derivative of the stator current can be expressed by introducing the inverse inductance matrix:

$$\frac{d\underline{I}_s^s}{dt} = \underline{L}_s^{s-1}\underline{U}_s^s = \frac{1}{L_d L_q}\left(\sum L\begin{bmatrix}1 & 0\\ 0 & 1\end{bmatrix} - \Delta L\begin{bmatrix}\cos(2\theta) & -\sin(2\theta)\\ -\sin(2\theta) & -\cos(2\theta)\end{bmatrix}\right)\underline{U}_s^s \quad (8.2)$$

The voltage pulses used in this approach is directed in the stationary stator α direction. On vector form, with excitation in the α -axis, the derivative can be expressed as:

$$\frac{d\underline{I}_s^s}{dt} = (y_0 + \Delta y \cdot e^{-j2\theta})U_{s\alpha}^s \quad (8.3)$$

Where:

$$y_0 = \frac{L_d + L_q}{2L_d L_q}, \Delta y = \frac{L_d - L_q}{2L_d L_q} \quad (8.4)$$

The current response from a voltage step in the stationary stator α direction with the duration Δt is in each phase:

$$\Delta I_{sa,1}^s = \Delta t \cdot U_{s\alpha}^s \cdot [y_0 - \Delta y \cdot \cos(2\theta)] \quad (8.5)$$

$$\Delta I_{sb,1}^s = \Delta t \cdot U_{s\alpha}^s \cdot [y_0 - \Delta y \cdot \cos(2\theta - 4\pi/3)] \quad (8.6)$$

$$\Delta I_{sc,1}^s = \Delta t \cdot U_{s\alpha}^s \cdot [y_0 - \Delta y \cdot \cos(2\theta - 2\pi/3)] \quad (8.7)$$

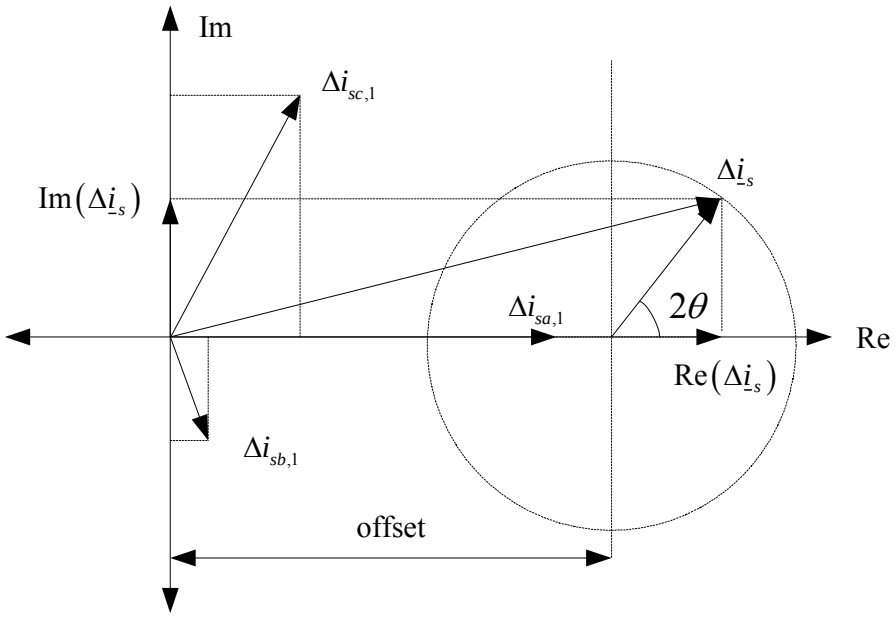

Figure 8.1 Stator current derivative trajectory

The stator current derivative can be expressed by the change in the stator current during a time interval Δt :

$$\Delta \underline{I}_s^s \approx \Delta I_{sa,1}^s + \Delta I_{sb,1}^s e^{j\frac{2\pi}{3}} + \Delta I_{sc,1}^s e^{-j\frac{2\pi}{3}} \tag{8.8}$$

As the machine rotates the stator current derivative trajectory forms a circle in the complex plane (Figure 8.1). In this scheme the offset in the real axis is subtracted and the remaining stator current derivative used for the position and speed estimation.

8.1.2 Excitation

When the machine rotates there will be back EMF in the stator voltage. If the estimate of the stator current is made from a differential measurement the back EMF term is eliminated. Thus two voltage vectors are used as excitation: on in the positive- and one in the negative stationary stator α direction:

$$U_{s\alpha,1}^s - U_{s\alpha,2}^s = L_s^s \left(\frac{\Delta \underline{I}_{s,1}^s}{\Delta t} - \frac{\Delta \underline{I}_{s,2}^s}{\Delta t} \right) \tag{8.9}$$

The voltage pulse used is of equal duration and opposite polarity:

$$\left(\Delta \underline{I}_{s,1}^s - \Delta \underline{I}_{s,2}^s \right) = 2U_{s\alpha}^s L_s^{s-1} \Delta t \tag{8.10}$$

In order to minimize the deviation from the average stator current space vector, two additional voltage pulses are used (the small pulses t1-t2 and t4-t5 in Figure 8.2). In the PWM scheme used for the standard drive system a symmetrical space vector modulation is used. At low speed the induced voltage is small and there is a large zero vector in the modulation. Figure 8.2 illustrates the transient excitation in the zero vector. The current is sampled at time instances t2, t3 and t4. The delta currents are formed as (same for all three phases):

$$\Delta i_{sa,1} = i_{sa}(t4) - 2 \cdot i_{sa}(t3) + i_{sa}(t2) \tag{8.11}$$

$$\Delta i_{sb,1} = i_{sb}(t4) - 2 \cdot i_{sb}(t3) + i_{sb}(t2) \tag{8.12}$$

$$\Delta i_{sc,1} = i_{sc}(t4) - 2 \cdot i_{sc}(t3) + i_{sc}(t2) \tag{8.13}$$

The three delta values in (8.11),(8.12) and (8.13) are combined in order to get the imaginary and real part of the $d\underline{i}_s / dt$ trajectory.

$$\mathrm{Re}(\Delta \underline{i}_s) = \Delta i_{sa,1} - 0.5 \cdot (\Delta i_{sc,1} + \Delta i_{sb,1}) \tag{8.14}$$

$$\mathrm{Im}(\Delta \underline{i}_s) = \frac{\sqrt{3}}{2} (\Delta i_{b,1} - \Delta i_{c,1}) \tag{8.15}$$

$$\underline{c} = (\mathrm{Re}(\Delta \underline{i}_s) - offset) + j\, \mathrm{Im}(\Delta \underline{i}_s) \tag{8.16}$$

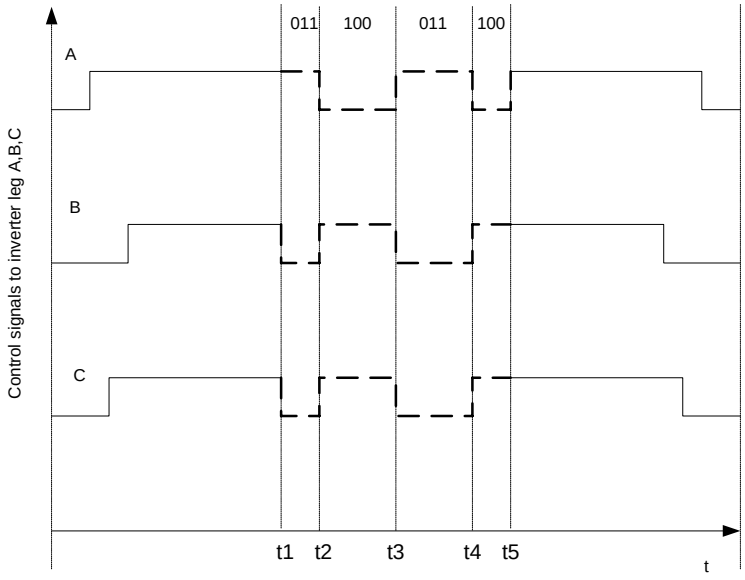

Figure 8.2 Transient excitation in the zero vector

8.1.3 Observer and normalizing terms

As for the two other schemes the transient excitation is combined with the observer described in Chapter 1. The complex vector in (8.16) rotates with the double rotor position. The vector is normalized before entering the heterodyning (exactly as the HFCI-R scheme in Chapter 1). After the cross product (heterodyning) the error term is divided by two in order to compensate for the linear approximation of the sine term and divided by the pole pairs p in order to get the mechanical position. The mechanical rotor position appears at the output of the observer and this is multiplied with the pole pairs p in order to get the electrical position. The discrete implementation of the observer is covered in Chapter 6.

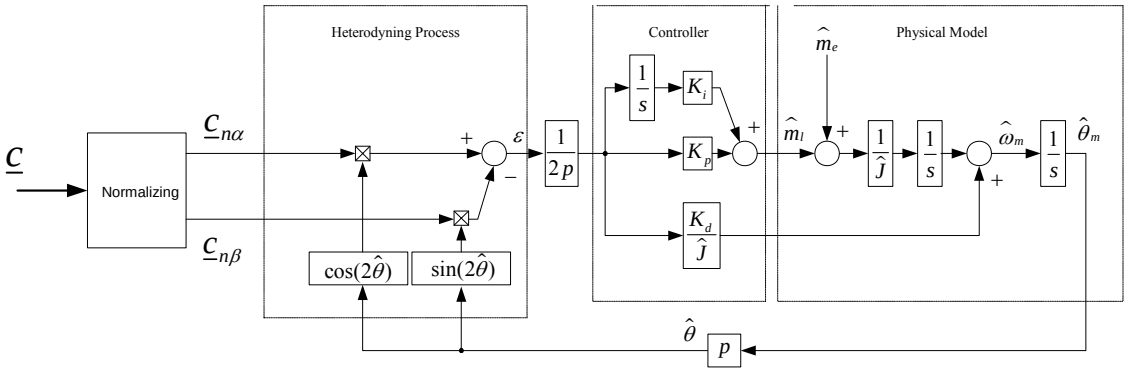

Figure 8.3 Observer and normalizing term

8.1.4 Transient excitation in intervals

If the transient excitation is applied in every switching period the number of switching operations increases with a factor 3 compared to standard symmetrical space vector. In order to reduce the additional switching losses due to the transient excitation the transient excitation can be applied in intervals. The switching losses from this type implementation is compared to the other schemes are presented in Chapter 9. Each transient excitation sequence produce a position estimate and the interval between the excitation sequences can be selected freely. In this implementation the speed is assumed constant between the excitation sequences i.e. the speed estimate is updated after every excitation sequence. The position estimate is updated with the speed estimate between the excitation sequences. The observer presented in Chapter 6 is used also for this implementation and the observer is applied in the same interval as the transient excitation.

8.2 Experimental work on Transient Excitation

The switching frequency was lowered to 5 kHz for the transient based excitation schemes in order to properly fit the transient excitation in the zero vector. All tests where performed with Test Machine 1 (IPMSM). In order to compare the performance of this scheme to the other two schemes the same tests are performed as in Chapter 6 and 7: speed reversal and transient test.

8.2.1 Current regulators

Compared to the high frequency injection based schemes the tuning of the current regulators is quite different for the transient excitation based scheme. As the transient excitation is an isolated event the current regulators are tuned according to standard optimal design procedures [74]. The only influence from the transient excitation is that the maximum available average voltage is reduced and that there may be a small deviation from the stator current vector due to the transient excitation. The optimal tuning criteria used for the tuning was:

$$T_{id} = \frac{L_d}{r_s} - \frac{T_s}{2} \tag{8.17}$$

$$T_{iq} = \frac{L_q}{r_s} - \frac{T_s}{2} \tag{8.18}$$

$$K_{pd} = \frac{\frac{L_d}{r_s} - \frac{T_s}{2}}{K_s(2T_{sum} + T_s)} \tag{8.19}$$

$$K_{pq} = \frac{\frac{L_q}{r_s} - \frac{T_s}{2}}{K_s(2T_{sum} + T_s)} \tag{8.20}$$

Where T_{sum} represents the sum of the delay in the inverter, current measurements and filters. In the setup the current regulators where tuned slightly lower than the optimal values in order to reduce the overshoot. The resulting experimental bandwidth (10-90% rise time based) was 833 Hz.

8.2.2 Selection of time intervals in measurement sequence

There are several factors that determine the selection of time intervals in the measurement sequence. The most obvious demand is that the change in the current must be reasonable larger than the current measurement accuracy. This demand is met by adjusting the time interval t2-t3 and t3-t4 in Figure 8.4 until the change in the current is sufficient for the current measurement equipment. In Figure 8.4 this interval equals 25 us. In addition to the current measurement accuracy issue there is large transients in the current due to the switching of the IGBT's. These transients may cause problems for the current measurements. Time region t1-t2 and t4-t5 are used in order to minimize the deviation from the stator current vector. In this work the time interval t1-t2 was the limiting factor in the tuning of the time intervals due to the switching transients. When the t1-t2 interval was to short the current measurements where influenced by the switching transients and the performance degraded. The final time period for the time interval t1-t2 and t4-t5 was 12.5 us. The total measurement sequence was 75 us. In the work with the transient excitation a 5kHz switching frequency was used.

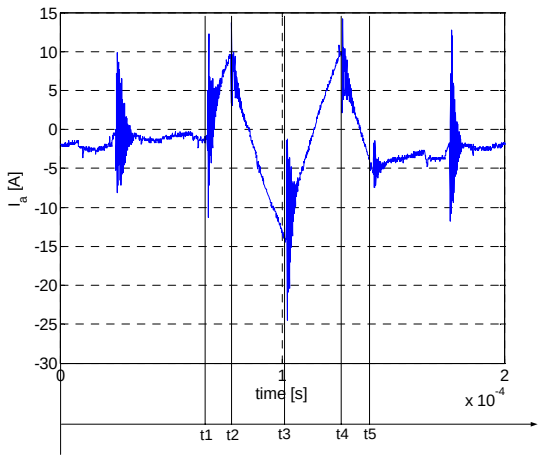

Figure 8.4 Transient excitation measurement sequence, 5 kHz switching period

Thus 37.5% of the total duty cycle was occupied by the measurement sequence. In the experimental setup the DC link voltage is high compared to the IPMSM rated voltage; the machine could be controlled with transient excitation in the entire speed region.

8.2.3 Tracking and transient tests

All the tests in this chapter are performed without the feed forward torque in the observer. Two series of measurements are presented: one series has the transient excitation integrated in every switching period and one series has the transient excitation integrated in every 10^{th} switching period. The low pass filters on the current measurements had a very high cut off frequency (30kHz). Due to the high cut off frequency in the low pass filters and the transients from the switching there are some high frequency noise in the $\underline{c}$ vector(8.16). Due to the high frequency noise two pole placement approaches are presented. The first approach is the approach that was used for the schemes in Chapter 6 and 7. The second approach has more experimental placed poles in order to reduce sensitivity for high frequency noise.

8.2.3.1 Transient Excitation in every switching period

When the transient excitation was applied in every switching period the observer poles was placed at 10, 50 and 250 Hz (as for the HFCI-R scheme). At higher bandwidths the scheme was more sensitive to the high frequency noise and the performance degraded. For the speed reversal test the position error was well within +/- 10 electrical degrees (Figure 8.5). The disturbance rejection properties with this tuning are equal to the properties found with the HFCI-R scheme. The position error has different characteristics compared to the schemes in Chapter 6 and 7: the main contribution to the position error stems from offset in the stator current derivative trajectory (Figure 8.1) and switching noise. Offsets in the stator current trajectory can be influenced by operating condition of the machine, ADC gains, delays in current sampling and dead time effects. For the HFCI-R scheme the largest error could be found in the instant after the speed command was applied. In the transient excitation the error is of equal size during the speed reversal. Thus the zero crossing effect is not dominant in this scheme.

In the transient test (Figure 8.6) two observer pole sets are presented. The first test is performed with the same pole placement approach as in Chapter 6 and 7. The observer poles are located at 10, 50 and 250 Hz (this figures will be used for comparison of schemes). At 12.5 Hz test signal the speed and position estimate are well within the acceptable error band. When the frequency is increased to 25 Hz (Figure 8.6.2) the speed estimate fails and the position estimate is noisy. The observer is too sensitive to the high frequency noise and the poles are moved in order to improve the performance. The pole in 250 Hz was moved to 200 Hz in order to reduce the impact from the high frequency noise, and the pole in 10 Hz was moved to 4 Hz in order to reduce the "overshoot" in the resulting AFF diagram. With this observer poles the 12.5 and 25Hz test performs with acceptable accuracy both for position and speed estimates.

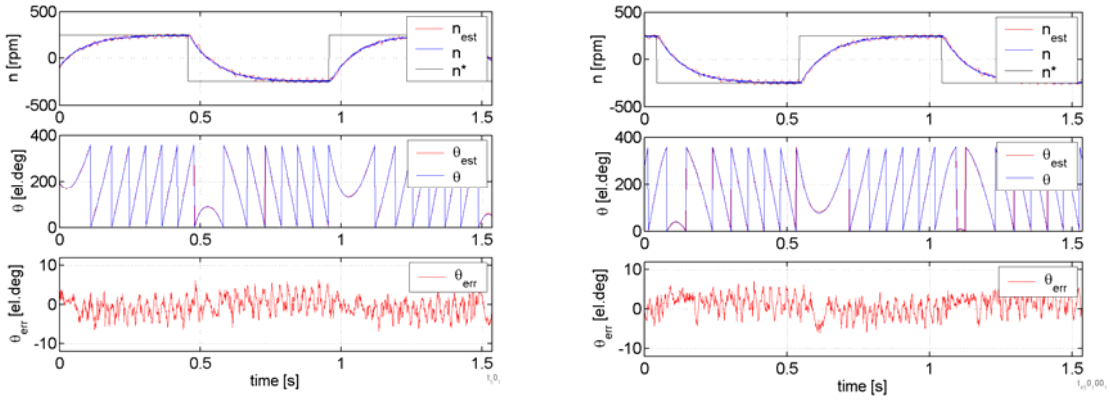

1) 2)

Figure 8.5 Speed reversal +/-250 rpm. 1)poles in 10, 50 and 250 Hz, 2)poles in 4, 50, 200 Hz

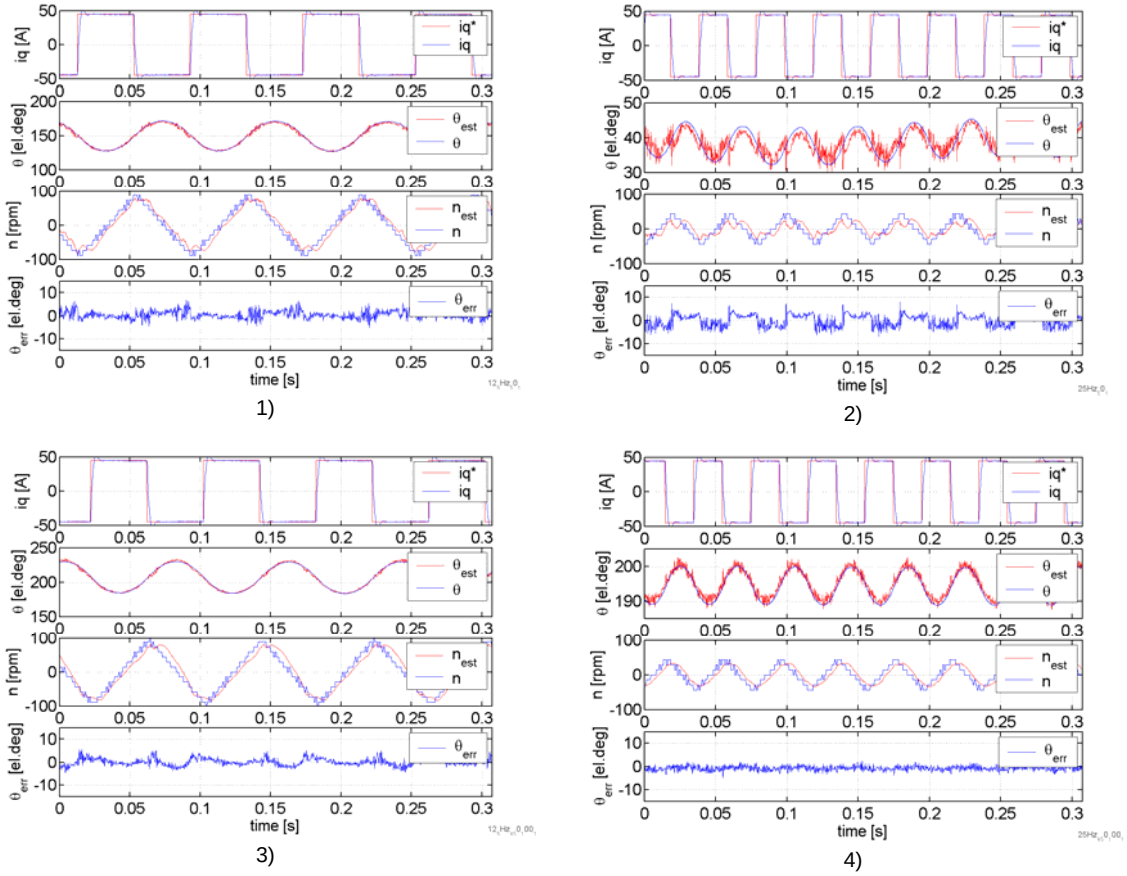

1) 2)

3) 4)

Figure 8.6 Transient test i_{qr}=+/- 45 A, 1) test frequency=12.5 Hz, observer poles in 50Hz, 2) test frequency=25 Hz, observer poles in 50Hz, 3) test frequency=12.5 Hz, observer poles in 4,50,100Hz , 4) test frequency=25 Hz, observer poles in 4,50,100Hz

Compared to the HFCI-R scheme the transient performance is improved: zero crossings of the phase currents do not influence the estimates in the same manner. The saliency shift can be estimated from Figure 8.6.1 and 2: for a 90A shift in the q-axis current the saliency moves approximately 5 electrical degrees. The small shift due to q-axis current can be interpreted as an indication of that the rotor inherent saliency dominates over the saturation based saliencies (as in the saliency modelling in Chapter 3).

8.2.3.2 Transient Excitation in every 10th switching period

In order to document how the transient excitation based schemes work when applied in intervals a modification of the scheme was made. In this scheme the transient excitation was integrated in every 10th switching period. The observer was also used every 10th switching period (executed on a 500 Hz bases). In the interval between the transient excitation the speed was assumed constant and the position estimate was updated using the speed estimate. Due to the increased sampling time for the observer the observer poles had to be placed at lower frequencies. In order to compare the scheme with the other schemes the 5 times separation of the poles was also used for this tuning. The optimal performance for the 12.5 Hz transient test was found with poles in 0.6, 3, 15 Hz. Figure 8.7.1 shows the speed reversal test for this pole location. Due to the low observer bandwidth there is a speed dependent error in the position estimate. This error was corrected by a simple linear function shown in Figure 8.7.2.

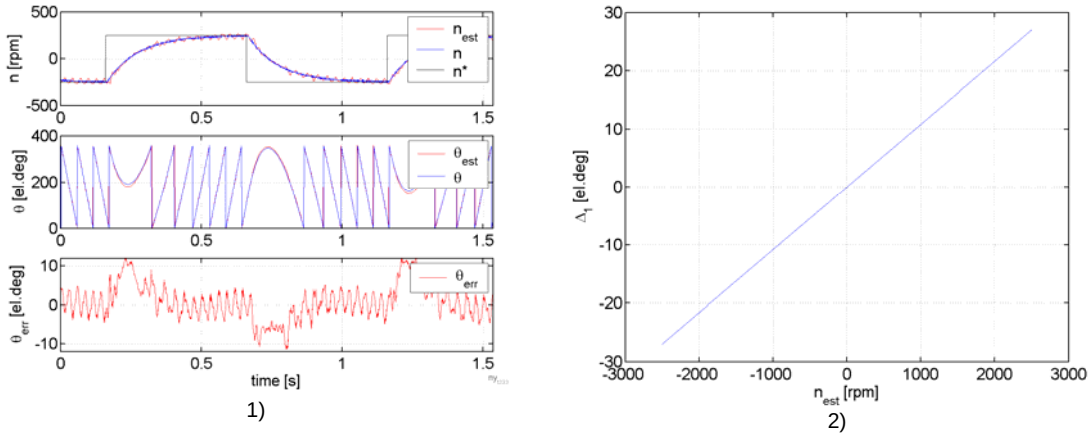

Figure 8.7 Speed reversal test +/250 rpm, transient excitation every 10th switching period, Observer poles in 0.6,3 and 15 Hz, 1) Position and speed estimates (correction function used) 2) Correction function for rotor position estimate

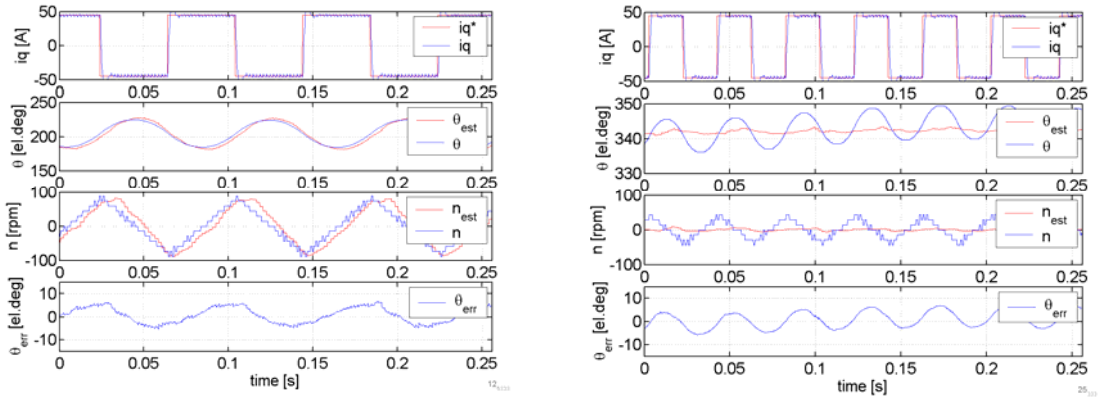

1) 2)

Figure 8.8 Transient test iq*=+/- 45A, Observer poles in 0.6, 3, 15 Hz 1)Test frequency=12.5 Hz, 2)Test frequency=25 Hz

In the transient test (Figure 8.8.1) the approach with poles in 0.6, 3 and 15 Hz performed within the specified accuracy both for speed and position estimate at the 12.5 Hz test. When the 25 Hz test (Figure 8.8.2) was applied the scheme failed due to low observer bandwidth.

The speed reversal test was particular poor with the pole placement strategy used for the comparison of schemes. With a more experimental approach in the pole placement, the performance increased and the speed dependent error was reduced. In the comparison of schemes the plots from Figure 8.7 and Figure 8.8 will be used.

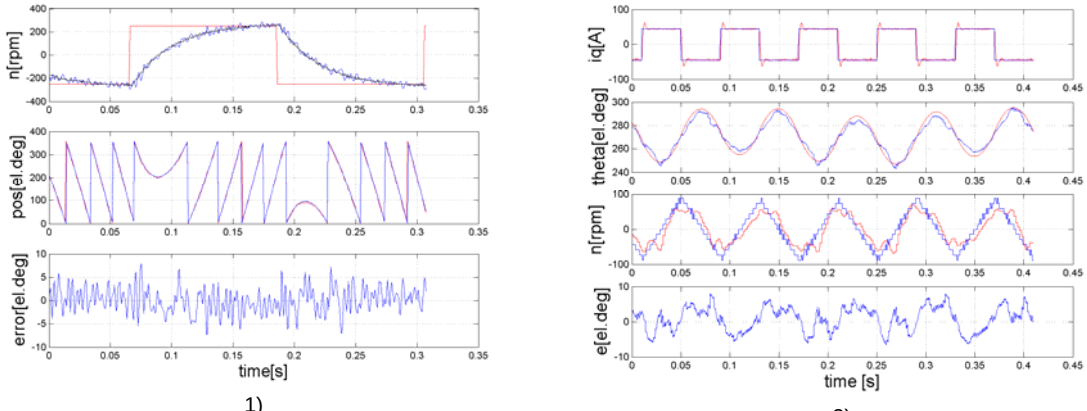

1) 2)

Figure 8.9 Experimental pole placement, transient excitation every 10th switching period, 1) Speed reversal test +/250 rpm (no correction function used), 2)Transient test iq*=+/- 45A, , test frequency=12.5 Hz

8.3 Chapter Conclusions

In this chapter a new scheme is presented based the work found in [1, 7]. The new scheme use transient excitation and gives an updated position estimate every switching period. The scheme shows the characteristic properties of transient excitation based schemes. During the speed reversal and transient tests, no fundamental zero crossing effects where found. The scheme uses an offset that depends on machine parameters. This offset was not changing noticeably during any of the tests applied in this thesis. The observer bandwidth and disturbance rejection was equal to the HFCI-R based scheme when the poles in the observer located at 10, 50 and 250 Hz (Figure 8.8.1). For the comparison of schemes the approach with observer poles at 10, 50 and 250 Hz is used: speed reversal test (Figure 8.5.1), transient test (Figure 8.8.1).

The analogue low pass filters on the current measurements interface had a very high cut off frequency (30kHz). As there is no low pass filters before the observer there are high frequency noise in the $\underline{c}$-vector(8.16). This noise was better rejected when the observer poles where separated and placed at 4, 50, 200 Hz. An improved transient test is presented in Figure 8.6.3 and 4.

In order to describe transient excitation based schemes where excitation is applied in intervals a modified version of the new scheme was implemented. The transient excitation was integrated in the zero vector every 10^{th} switching period. A simple update approach was used in the interval between the transient excitation: the speed was assumed constant and the position was updated with the estimated speed. The observer updated the speed and position on a 500 Hz basis. As the observer sampling time decreases the bandwidth and disturbance rejection decreases approximately proportional. For the comparison of schemes the approach with observer poles at equal frequency are used: speed reversal test (Figure 8.7.1), transient test (Figure 8.8.1). Also Experimental pole placement was also advantageous (Figure 8.9) for the interval based transient excitation.

9 EVALUATION OF METHODS

It is difficult to compare the performance of the three schemes implemented in Chapter 6, 7 and 8. Every scheme has different characteristics and there are several ways of enhancing the performance in each scheme. In this comparison the simple implementation of each scheme will be compared (no individual enhancements used). By using the same strategy for the pole placement and no torque feed forward torque in the observer the characteristics of the different schemes will be analysed. This is by no means the optimal possible performance in each case, but in this work the characteristics of each scheme are the focus. In addition to the performance in the tests other characteristics will also be evaluated as: current sensor requirements, additional loss in the power electronics, stability, integration into existing schemes, acoustic noise, voltage reservation and parameter sensitivity.

9.1 Performance

In the comparison of performance the speed reversal test, transient test (12.5 Hz) and the disturbance rejection will be compared. In Figure 9.1 the results are revisited for comparison purposes. There are several characteristics that can be interpreted from the test results: in the speed reversal test for the HFCI-R scheme (Figure 9.1.1) the largest error appears at phase current zero crossing when the fundamental current has the largest amplitude (the resulting current vector). The same phenomena can be seen for the transient test (Figure 9.1.2) where there is an increased error at the time instant of the q-axis current step. The zero crossing effect and the demand for low pass filtering in the carrier negative frame are assumed the limiting factor for the HFCI-R scheme in this experimental setup. For a different setup the zero crossing effect may have different impact, but the sensitivity to the zero crossing is evident. The speed estimate is an internal state and this estimate is very sensitive to distortions in the carrier signal at high observer bandwidths.

In the HFCI-P implementation the limitation on observer bandwidth are a combination of the zero crossing effects and the low pass filter placed in the observer structure. The

maximum bandwidth was found with poles in 2, 10 and 50 Hz. The HFCI-R scheme could be tuned with poles in 10, 50 and 250 Hz and resulted in a better disturbance rejection function (Figure 9.2). However, if the results in Figure 9.1.2 and 4 is compared, the HFCI-P scheme has less error in the position estimate and better speed estimate. Thus, even if the HFCI-R scheme could be tuned for a higher bandwidth the HFCI-P scheme outperforms the HFCI-R scheme in the transient test. The HFCI-R scheme was also tested with poles in 2, 10 and 50 Hz but the results where not improved: the zero crossing effects had the same influence on the estimates. The phase current zero crossing effect is smaller for the HFCI-P scheme compared to the HFCI-R scheme. This is evident from the test results in Figure 9.1.and the testing done with 15 V carrier signal: when the HFCI-R scheme was tested with 15 V carrier the position estimate had error larger than 20 electrical degrees, for the HFCI-P based scheme the tests with 15V carrier could be performed with a position estimate within +/- 10 electrical degrees.

The scheme with integrated transient excitation in every switching period performed noticeably better then the other schemes in the transient test. There are no phase current zero crossing effects and the speed estimate is of high quality in the transient test (Figure 9.1.6). The disturbance rejection function is plotted in Figure 9.2 where the label “TE1” represents the scheme with transient excitation in every switching period. The periodic errors in the speed reversal test are mainly a result of offset in the stator derivative current trajectory. There are several contributors to this effect: load dependency, direction of excitation compared to direction of magnet, current sampling delays and ADC gain errors. The influence from direction of excitation compared to direction of magnet is assumed to give the largest effect. The 25 Hz transient test is not presented in this chapter. When comparing the methods is should be noted that only the transient based excitation scheme could perform success fully on this test. The 25 Hz test is presented in Figure 8.6.4. In order to reduce the high frequency noise content the poles where placed in 4, 50 and 100 Hz in this test.

When the transient excitation is applied in intervals the observer was only executed every 10^{th} switching period. This resulted in a 500 Hz repetition rate for the observer. Due to the slow repetition rate the bandwidth and disturbance rejection was lowered in approximately the same rate as the interval number. In the speed reversal test in Figure 9.1.7 a speed dependent lag was present. This lag is compensated for by a liner function in Figure 9.1.7. In addition to the speed dependent lag there is also a lag in the acceleration phase. In this scheme there are several factors that may enhance the performance: the observer could be executed at the switching frequency with the torque feed forward term and the pole placement could be performed in a more optimal manner (Figure 8.9). Due to the low bandwidth the disturbance rejection function has the lowest value compared to the other schemes (Figure 9.2.2).

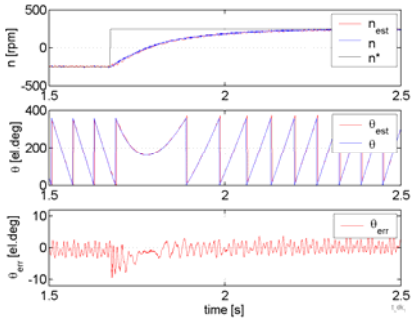

1) HFCI-R

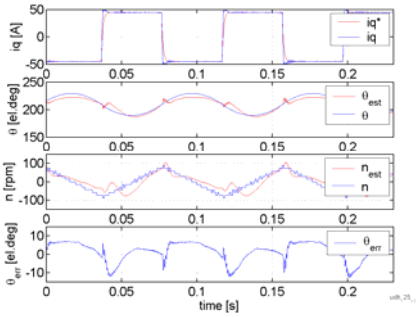

2) HFCI-R

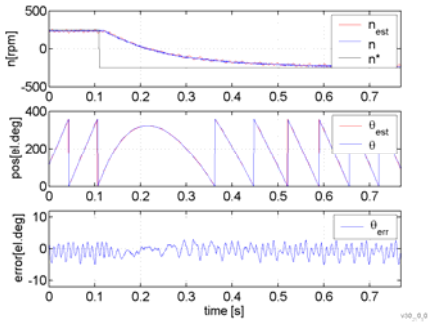

3) HFCI-P

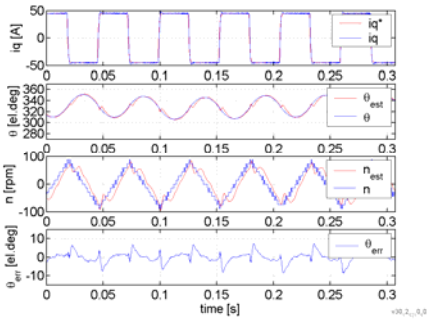

4) HFCI-P

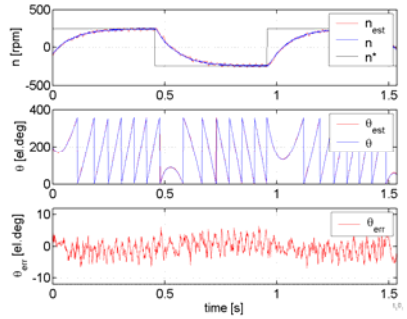

5) Transient Excitation-every switching period

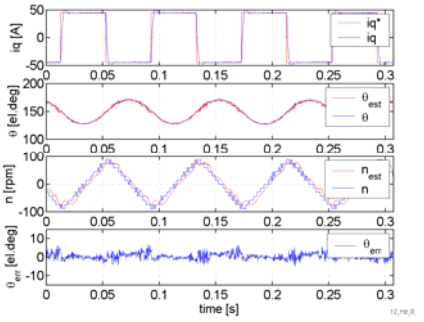

6) Transient Excitation-every switching period

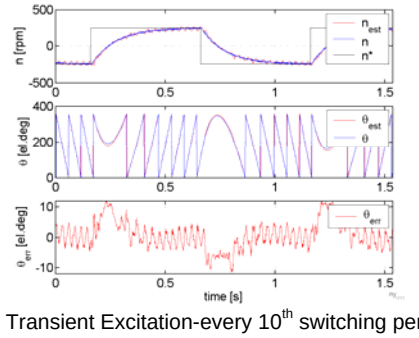

7) Transient Excitation-every 10th switching period

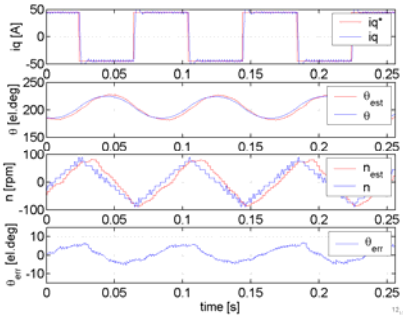

8) Transient Excitation-every 10th switching period

Figure 9.1 Speed reversal and transient test (12.5 Hz): 1-2) HFCI-R, 3-4)HFCI-P, 5-6)Transient excitation in every switching period, 7-8) Transient excitation in every 10th switching period

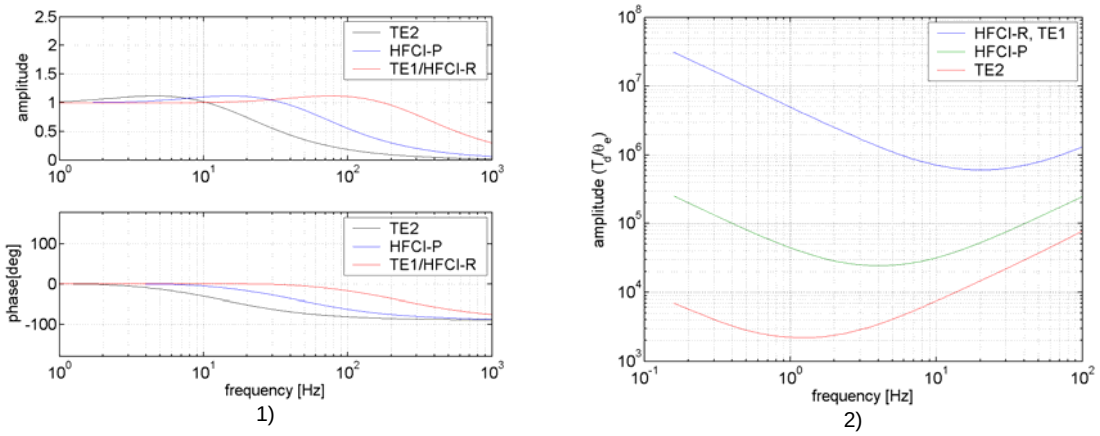

Figure 9.2 Characteristics:1) $\hat{\theta}/\theta$-AFF function for the different schemes at maximum bandwidth, 2) Disturbance rejection function: TE1-transient excitation included in every switching period, TE2-transient excitation included in every 10^{th} switching period

9.2 Drive issues

There are several issues that must be regarded when an injection based sensorless scheme is integrated into a standard drive system. Usually the main objective for implementing a sensorless scheme is cost savings. In order to get the full cost picture the penalties of inserting an injection based sensorless system must be considered. The sensorless scheme may lead to lower available output voltage, additional losses in the machine and inverter, DSP requirements, switching frequency limitations, current sensor requirements and acoustic noise emission.

9.2.1 DC-voltage reservation

All the injection based schemes requires some reservation of voltage due to the extra excitation. The different schemes implemented in this scheme required different reservation of voltage. In the high frequency injection based schemes the output of the current regulators must be limited to a level large enough to supply the carrier voltage at all operating conditions. In the tuning of the schemes in this work, the HFCI-R scheme needed a 30 V carrier amplitude (20% of the duty cycle) in order to overcome influence from fundamental current zero crossings and transients from the fundamental current. The HFCI-P scheme could operate with carrier amplitude equal 15 V, but the best performance was found with carrier amplitude equal 30 V. When the transient excitation was included in every switching period the voltage reservation was made by reserving a region of the zero vectors. The region reserved was 37.5 % of the full duty cycle. When the transient excitation is applied in intervals the voltage reservation is only needed every 10^{th} switching period: the average voltage reservation then becomes 2.75%. All these methods should be used in combination with an alternative non injection based schemes at speed above approximately 0.1 pu. If the schemes are

properly combined with an alternative high speed scheme the voltage reservation does not have to be a limitation. In the "transient test" with the HFCI-R the q-axis voltage reference never exceeded 0.5 pu. In general the level of voltage command depends on the tuning of the current regulator but for low speeds below 0.1 pu the voltage reservation is not regarded as a limiting factor due to the low back EMF in this speed region.

9.2.2 Demands on current sensors

Current sensor and Analogue to Digital Converters (ADC) accuracy has been the limiting factor for several sensorless approaches. This is especially important when the saliency ratio is small and when the maximum current is large compared to the rated current (high torque demands short term). If the contributors to the error term are considered without normalizing functions for the different schemes, we get an idea of how the position dependent current level is. In the HFCI-R scheme the negative rotating vector has amplitude as in (9.1). The level of position dependent current is determined of the carrier frequency, carrier voltage and the saliency ratio of the machine. If we consider the error term for the HFCI-P scheme the error term is only half the size as the HFCI-R scheme for the same carrier voltage.

$$e_{HFCI-R} = \frac{L_q - L_d}{2L_qL_d}\frac{U_{sc}^s}{\omega_c}\sin(2(\theta - \hat{\theta})) \tag{9.1}$$

$$e_{HFCI-p} = \frac{L_q - L_d}{4L_qL_d}\frac{U_{sc}^s}{\omega_c}\sin(2(\theta - \hat{\theta})) \tag{9.2}$$

The transient excitation based scheme has a slightly different derivation of the un-scaled error term to the observer. In this analyse only one voltage pulse is considered as this defines the current sensor accuracy demand. In the implemented scheme a differential measurement is used in the error term. This will not be representative for the measurement accuracy as it contains two separate measurements. In (9.3) $U_{s\alpha}^s = U_{DC-BUS}$ and the only parameter for adjustment of the current level is the duration of the voltage pulse applied.

$$\Delta I_{sa,1}^s = \Delta t U_{s\alpha}^s \left[y_0 - \Delta y \cos(2\theta) \right] \tag{9.3}$$

$$\Delta y = \frac{L_q - L_d}{2L_qL_d} \tag{9.4}$$

$$e_{TE} = \frac{L_q - L_d}{2L_qL_d}\Delta t U_{s\alpha}^s \sin(2(\theta - \hat{\theta})) \tag{9.5}$$

TABLE 9.1 Signal to noise ratio for position dependent part of current

Method	e[A]	SNR – LEM
HFCI-R (Uc=30V)	5.2	11.6
HFCI-P (Uc=30V)	2.1	5.7
TE	4	8.9

In the experimental set up the current sensors has 0.5% overall accuracy on a 90A rated current this gives the current measurements accuracy equal +/- 0.45A. In addition to the LEM measurement accuracy there is a quantification error due to the digital representation in the DSP. The ADC in this set up has a 12 bit resolution. The DSP is still at an alpha version and the effective resolution is maximum 10 bit. This gives a quantification error equal 0.18 A. Thus in this set up the LEM accuracy is the limiting factor for the current measurement accuracy. There have been several approaches to improve the demand on the current measurements. Common for these approaches is that the ADC resolution is improved and the LEM accuracy is unchanged. In [29] the HFCI-R method was used for an induction machine. A decoupling scheme for the fundamental current was implemented in a software/hardware combination where the carrier current could be supplied separate to the ADC. In [59] a sample and hold arrangement was used in combination with transient excitation. The sample and hold circuits where combined with analogue summation and the differential of the stator current was feed to the ADC.

9.2.3 Additional losses in the Power Electronics

The high frequency injection based schemes does not add any additional losses in the power electronics as the carrier voltage is superimposed on the fundamental excitation. The transient excitation based scheme increases the number of switching actions on average. When comparing the schemes the reduced switching frequency also has to be considered. In general the high frequency injection based schemes requires a high switching frequency in order to produce a high quality carrier signal. The transient based excitation on the other hand does not require a high fundamental switching frequency but it needs to produce voltage pulses in addition to the fundamental switching. In this work two approaches are evaluated: transient excitation integrated in every switching period and transient excitation integrated in every 10^{th} switching period. In the symmetrical space vector routine each IGBT switch twice in every switching period. When the transient excitation is integrated in the zero vector each IGBT switches 6 times in every switching period. The number of switching operation can be compared over a time interval t as following:

$$n_{10kHz} = \frac{t}{T_{s5kHz}} 2 \tag{9.6}$$

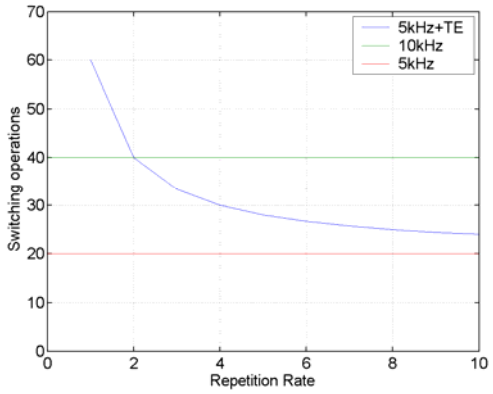

Figure 9.3 Switching operations during a 2ms time interval, 5 and 10 kHz standard symmetrical space vector, 5 kHz with transient excitation integrated on intervals(5kHz+TE)

$$n_{5kHz} = \frac{t}{T_{s5kHz}} 2 \tag{9.7}$$

$$n_{5kHz+TE} = \frac{t}{T_{s5kHz}} \left(\frac{6}{k} + (2 - \frac{2}{k}) \right) \tag{9.8}$$

Where k represent the repetition rate of the transient excitation. If we consider a 2ms time interval the 10th interval is included for a 5kHz system. In Figure 9.3 the numbers of switching operations in each IGBT is plotted. When the transient excitation is integrated in every 2.switching period the switching losses are equal to the 10 kHz scheme. The implemented scheme with transient excitation every 10th switching frequency has only 60 % of the switching losses compared to the 10 kHz scheme.

9.2.4 Current regulator limitations

All the schemes reduce the current regulator maximum voltage output due to the reduced voltage available for the fundamental excitation. This is not the main limitation as the back EMF is minimal during low speed operation. The main limitation on current regulator bandwidth is the interaction between the high frequency carrier signal and the current regulators. In this work synchronous frame filtering is used for the HFCI-P and HFCI-R schemes. The current regulator bandwidth must be selected sufficiently lower than the carrier frequency as the high pass filters in the synchronous frame filter are tuned to 75 – 100 Hz in this work. A 700 Hz current regulator bandwidth (defined by the 10-90% rise time – Chapter 6) could be obtained without noticeable interaction between the fundamental and carrier current. In addition the current reference was pre-filtered in order to slow down the transient operation. The pre filter implementation was optionally and resulted in a 350 Hz current regulator bandwidth. In the transient excitation based scheme the excitation is an isolated event and the current regulators

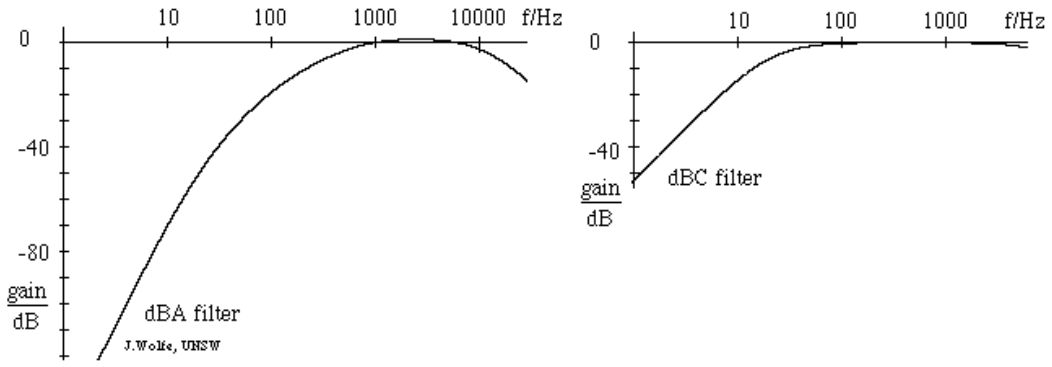

Figure 9.4 Sound Filters in the dB-meter [73]

could be tuned in accordance to optimal tuning procedures. Even if the switching frequency was lowered to 5 kHz the current regulator bandwidth could be higher than the other schemes. The experimental current regulator bandwidth for the transient excitation based scheme was found to be 833 Hz.

9.2.5 Acoustic noise

All the implemented schemes resulted in additional acoustic noise. The acoustic noise is highly dependent on the amplitude of the injected voltage amplitude, carrier frequency and intervals for the transient excitation. In order to get an idea of the noise level from the different schemes a dB metre was used to measure the noise (Onsoku Sound Meter SM-6). The dB-meter has two filters available for noise measurements: dBA and dBC. The dBA filter is supposed to be representative for audio noise in the frequency region of the human ear. The dBC filter has a flat characteristic more sensitive to high frequency noise. Figure 9.4 shows the filter characteristics [73] for the dB meter. In the measurements done in this work the dBA filter was used in order to describe the audio noise as in the human ear. The dB-meter was mounted one metre from the IPMSM (Figure 9.5) and the noise was measured for two operating conditions in each scheme. The first operating condition was no load at standstill. The second operating condition was constant speed 0.1 pu and no load. In order to compare the noise measurements to a standard drive solution the machine was first tested with no signal injection: at zero speed the noise was not measurable with the dB meter (minimum range 40dBA). For the rest of the measurements the noise was considerable larger and all measurements could be done within the range of the dB-meter.

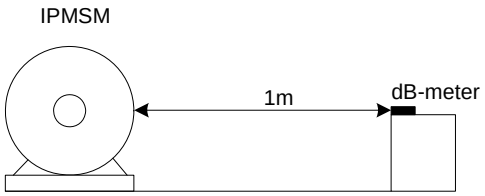

Figure 9.5 Principal view of acoustic noise measurement

Table 9.1 Acoustic noise measurement (fc=1000Hz for HFCI-P and HFCI-R)

Speed	No injection	HFCI-R (Vc=30V)	HFCI-P (Vc=30V)	HFCI-P (Vc=15V)	TE1 (in every f_{sw})	TE2 (in every 10^{th} f_{sw})
	[dBA]	[dBA]	[dBA]	[dBA]	[dBA]	[dBA]
n=0	<40	75	57	55	64	54
n=0.1pu	47	75	71	64	65.5	56.5

The results of the acoustic noise measurements are presented in Table 9.1. These results should be used with care as the noise measurement was a primitive measurement compared to the professional noise measurement techniques. From the simple noise measurement it was evident that the HFCI-P and TE2 scheme had lowest noise at zero speed. When the machine was operating at constant speed the TE2 scheme had lowest noise. The HFCI-R scheme had highest noise for both operating conditions. The noise observations done in this work is not sufficient to give a general statement regarding acoustic noise emission for the methods. In order to give a general statement a series of machines should be tested.

9.2.6 Integration in standard drive systems

When an injection based sensorless scheme is integrated in an existing drive system it is preferred that the program structure, current sensors and cooling requirements are unchanged. The HFCI-R and HFCI-P schemes offer integration as an add-on to an existing system. The carrier voltage is added after the current regulators and the filtering and observer and be added as a separate routine. The synchronous frame filter may seem like a large effort to a DSP, but in [3] a transformed representation is developed where no coordinate transforms are needed. The observer may also seem like a large effort to the DSP but the actual implantation is not large. The simplest form of HFCI-R could be the simplified scheme presented in Chapter 6 and a simple PLL tracking device. At an early stage of this project the HFCI-R scheme was implemented with a 16 bit fix-point DSP (TMS320c240). The implementation required assembly coding but the system could operate at 10 kHz. The transient excitation based systems requires more adjustments when combined with a standard drive system. The interrupt arrangement must be altered in order to apply the voltage pulses. In addition the sampling instants of current must be altered. In the scheme presented in this work the available computing time also reduces (compared to a standard 5 kHz implementation) as the vital parts of the program must be executed in the time span after the last voltage pulse (t5 in Figure 8.2). The maximum runtime for inner loop functions at 5 kHz was 100us before the transient excitation was included. After the transient excitation was included the maximum runtime was reduced to 62.5us. There is no need for additional filtering but a tracking device like the Luenberger observer or a PLL arrangement is required. The

additional losses in the power electronics may also lead to increased cooling requirements for the power electronics.

9.3 Scheme characteristics

9.3.1 Inverter non linearity

The dead time in the inverter legs will introduce a non linearity in the resulting voltage and current. In Chapter 6 and 7 the dead time effects on the fundamental excitation was demonstrated. The dead time effect was largest in the d-axis current as the deformation of the current during he zero crossing has largest effect in this axis. The d-axis current regulator tries to compensate for the non linearity but fails with the bandwidths used in this work. When the bandwidth was increased the zero crossing effect on the fundamental current was decreased as the error was compensated by the current regulators. These observations are fully in agreement of the theoretical derivation found in Chapter 5 and in [70].

9.3.1.1 Fundamental excitation and inverter non linearity

The effect in the error term (input to the observer) from the fundamental current zero crossing alone was documented in Figure 6.15 and Figure 7.7. In the HFCI-R scheme the dq-currents are transformed to the negative carrier reference frame and low pass filtered by a 100 Hz 2.order butter worth filter. In the negative carrier reference frame the dead time effects appears with a frequency equal $\omega - \omega_c$ thus they are effectively filtered off by the low pass filter. This can be seen in Figure 6.15 where the dead time effect from the fundamental current hardly can be related to the variations in the error term. The same effect can be seen for the HFCI-P scheme: in the demodulation term the q-axis current is multiplied with $\sin(\omega_c t)$ and the effects seen in the dq-frame appears at a frequency equal $\omega - \omega_c$. The demodulated signal is low pass filtered by a 200 Hz 2. order butter worth filter. Thus also for this scheme any "low frequency" effects in the dq frame is filtered off after the demodulation. In addition the HFCI-P scheme uses the q-axis current as the input for the error generation term. This term contains very little dead time effect. The error term for the HFCI-P scheme is plotted In Figure 7.7.2; the dead time effects cannot be seen in the error term. From the measurements done with the *fundamental excitation alone* it can be concluded that the dead time effect from the fundamental current alone does not influence the error terms for the HFCI-R and HFCI-P scheme.

9.3.1.2 High frequency signal injection and inverter non linearity

When a carrier signal is superimposed to the fundamental excitation the dead time effect is quite different. If we consider an operating point right after a speed reversal the q-

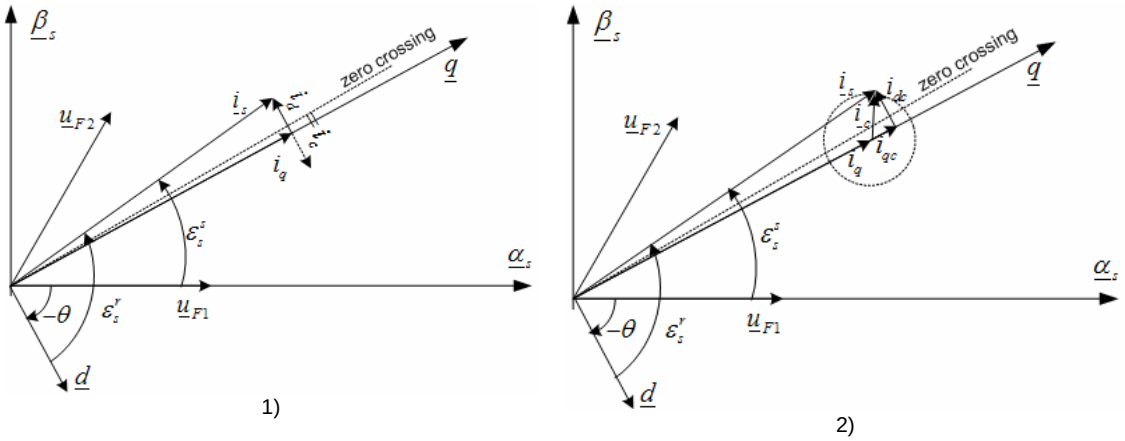

Figure 9.6 Phase current zero crossing due to carrier signal, 1)HFCI-P, 2)HFCI-R

axis current is large. Figure 9.6.1 illustrates this operating point when the b-phase current approaches zero. First we evaluate the effects for the HFCI-P scheme: the carrier pulsates in the d-axis and creates multiple zero crossings in the b-phase current. The effect can be simulated using (9.9) in the dq derivation of the dead time voltage (as in Chapter 5).

$$\varepsilon_s^r = 90 + \operatorname{atan}\left(\frac{i_d}{i_q}\right)\sin(\omega_c t) \tag{9.9}$$

Figure 9.7.1 shows the dead time effect without the carrier injection. Figure 9.7.2 shows the effects when the carrier is superimposed: the dead time voltage is modulated with the carrier frequency. The resulting voltage in each axis becomes:

$$u_d = u_d^* + u_{d,c} + u_{F,d} \tag{9.10}$$

$$u_q = u_q^* + u_{F,q} \tag{9.11}$$

The high frequency modulation in $\underline{u}_F$ has a 6 times periodicity with the electrical position. This modulation is very close to the modulation created by the saliency in the machine as this has a periodicity of twice the electrical position. *In the HFCI-P scheme* the error term is created by demodulating and low pass filtering the q-axis current. The high frequency terms in $\underline{u}_F$ will pass trough the low pass filtering after the demodulation term. When the estimated position equals the real position a disturbance proportional to high frequency portion of $u_{F,q}$ will enter the observer.

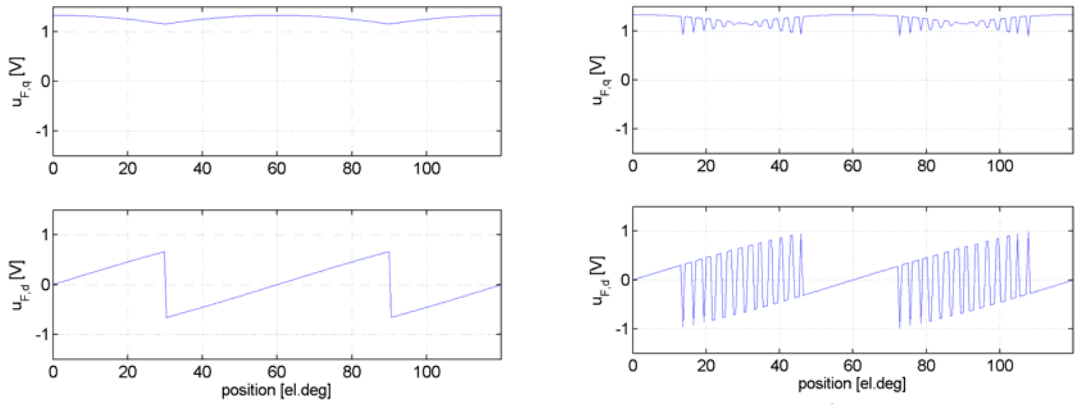

Figure 9.7 Simulated dead time effect $i_s^*=i_q$, u_F=1V, f_c=500 Hz, fundamental frequency 1Hz, 1) no carrier signal, 2) carrier signal pulsating in d-axis i_q/i_d=2.75

$$e = LPF(\sin(\omega_c t) i_q) = \frac{(LPF(\sin(\omega_c t)\cdot u_{F,q}))(L_d + L_q)}{4\omega_c L_d L_q}) + \left(\frac{(u_c + LPF(\sin(\omega_c t)\cdot u_{F,d}))(L_d - L_q)}{4\omega_c L_d L_q} \right) \sin(2\Delta\theta) \tag{9.12}$$

When there is an error in the position estimate there will be a term proportional to the position error and an additional disturbance term from the dead time voltage (9.12). As the high frequency modulation in $u_{F,q}$ is small the influence from the dead time is small in the HFCI-P scheme. Even during transients the experimental work shows that the dead time effect on the position estimate is small.

The same operating condition is also considered for the HFCI-R scheme Figure 9.6.2. The superimposed carrier rotates and creates multiple phase zero crossings. The variations in ε_s^r can be expressed as:

$$\varepsilon_s^r = 90 + \text{atan}\left(\frac{i_{d\_c}}{i_q} \right) \sin(\omega_c t) \tag{9.13}$$

The carrier is injected in the stationary stator reference frame and the high frequency pulsations in the dead time voltage will have frequency $\omega_c - \omega$ in the rotor reference frame. A simulation of the dead time voltage is given in Figure 9.8. For comparison with the HFCI-P scheme the dead time voltage is plotted in dq-reference frame in Figure 9.8.1. The effect is almost identical as the fundamental excitation rotates with 1Hz compared to the carrier at 500 Hz (in Figure 9.7.2 the high frequency component is

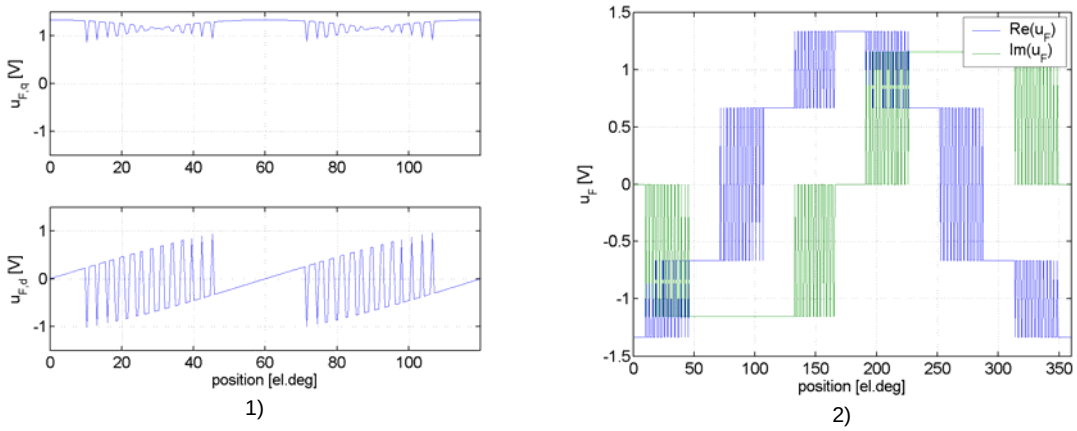

Figure 9.8 Simulated dead time effect HFCI-R, $\underline{i}_s^*=i_q$, $u_F=1V$, $f_c=500$ Hz, fundamental frequency 1Hz, $i_q/i_{d\_c}=2.75$, 1)dq-frame, 2)stationary reference frame

500 Hz compared to 499 Hz in Figure 9.8.1). In Figure 9.8.2 the dead time voltage is plotted in the stationary stator reference frame. The DC offsets are effectively filtered off in the low pass filter in the negative carrier reference frame. The high frequency modulation creates a signal modulated with 6 times periodicity compared to the electrical position. This modulation will appear in the negative carrier reference frame with only 3 times frequency separation compared to the position dependent term. In contrast to the HFCI-P scheme, the HFCI-R scheme uses the entire negative rotating carrier component. Thus the distortion from the entire dead time vector will act as a disturbance. This disturbance will have 6 times periodicity with the estimated position (electric). The simulations of the dead time voltage indicated that there will be voltages modulated with the carrier frequency and a periodicity 6 times the electrical frequency. In order to simulate the impact on the position and speed estimates from the dead time voltage the impedance have to be included. The position varying terms in the inductance matrix will add additional harmonics. In the simulation the analyses will be simplified by using only the constant part of the inductance matrix. For the HFCI-R scheme the resulting current from the dead time voltage can be approximated as:

$$\underline{i}_{u_F}^{cn} \approx j\frac{(L_d+L_q)\underline{u}_F^{cn}}{2L_dL_q\omega_c} \tag{9.14}$$

From Chapter 5 the dead time voltage in the experimental set up was found to be approximately 4.9 V. The analyses will be performed in two steps: first we evaluate the error in the angle in the position dependent carrier. Then we include the normalizing term and express the effect in the input of the observer in order to make a direct comparison with the HFCI-P scheme. The influence from the dead time voltage in the

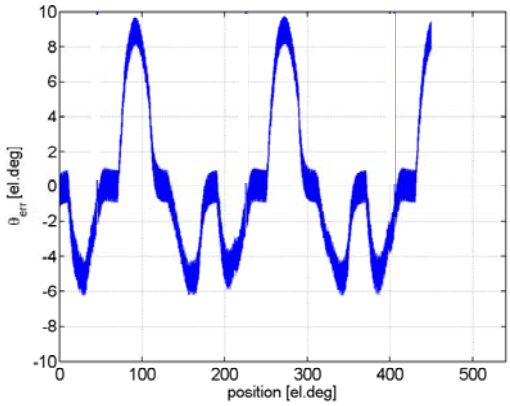

Figure 9.9 Simulated influence from dead time in position dependent part of the carrier signal in negative carrier reference frame, fc=500Hz, lp=100Hz(first order) , Vc=30V, u_F=4.9V

negative carrier position dependent current was simulated and plotted in Figure 9.9. The maximum deviation is approximately 8 electrical degrees. The simulated deviation is comparable with the measured errors in the position estimate right after a speed reversal command. In Figure 9.10 a simulation of the error terms to the observer is plotted. In the simulation a 100 Hz first order low pass filter was applied, transformation and normalizing where performed as in the actual implementation. In these plots the error terms are presented in per unit system. The per unit representation is used as the input to the observers are scaled in both the HFCI-R and the HFCI-P scheme. When there is an error in the estimate the HFCI-P scheme will be more influenced by dead time effects. These effects are documented by the test results in the experimental work. From the simulations and the experiments it is evident that the HFCI-P scheme is less sensitive to inverter non linearity compared to the HFCI-R scheme.

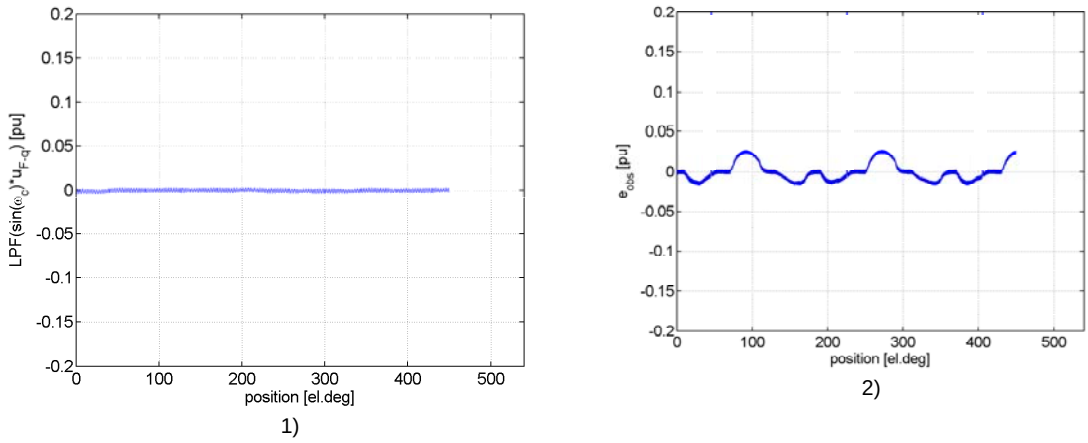

Figure 9.10 Simulated influence from dead time on error signal to observer , $\hat{\theta} = \theta$, Uc=30 V, U_F=4.9 V, fc=500 Hz, lp=100Hz (first order), pu referred to input to observer after normalizing term, 1)HFCI-P, 2)HFCI-R

In Figure 6.16 the combined effect of fundamental and high frequency carrier is shown for the HFCI-R scheme. There is a close relation between the fundamental current zero crossing and the error in the position estimate. This indicates that the combined effect of the fundamental and the carrier zero crossing is the reason for the relative large errors at the fundamental zero crossing. In the HFCI-P scheme this effect is not as large. This can be seen from Figure 7.8.2 where the position error in the time region 0.15 -0.3 s is smaller than the steady state (constant speed) position error. In addition the HFCI-P scheme could operate with Vc=15 V and accuracy within +/- 10 electrical degrees for the speed reversal and the transient test. When this was tried with the HFCI-R scheme the position error was 20-30 electrical degrees and loss of orientation appeared occasionally. From the tests and analysis it is evident that the HFCI-P scheme is less influenced by the phase current zero crossing effect compared to the HFCI-R scheme.

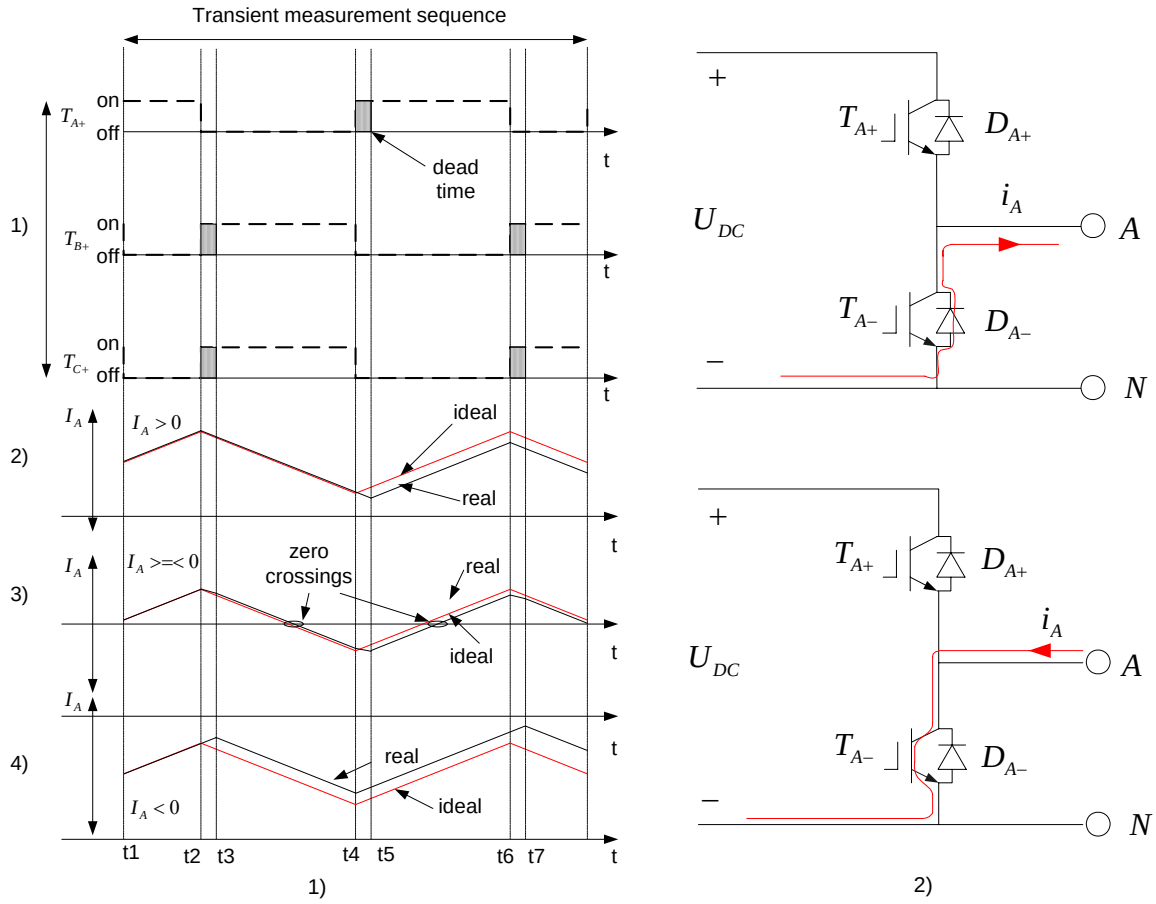

Figure 9.11 Transient measurement sequence, back EMF=0, 1) dead time effects , 2) zero crossing effect

9.3.1.3 Transient excitation and inverter non linearity

The dead time effect and the current zero crossing effect cannot be modelled combined for the transient excitation without a detailed analyses: the dead time will appear as a delay between the switch on command and the actual switching action. Figure 9.11.1.1 illustrate the switching commands for the three upper legs in the inverter ((T_{A+}, T_{B+}, T_{C+}) and the timing for the actual switching operation. During the dead time (Figure 9.11.1.1: t2- t3, t4- t5, t6- t7) all the switches are off and the direction of the current in inverter legs determines the actual voltage vector in this time region. The back EMF will influence the current during the transient excitation sequence but for the purposes of analysing the dead time and zero crossing effects the output voltage from the converter is used as bases for the analysis. In order to illustrate the dead time and zero crossing effect the current in inverter leg *A* is analysed during a transient excitation sequence. Figure 9.11.1.2 illustrates the dead time effect when the inverter currents are equal the currents in Figure 9.12.1 (t2). The first dead time appear in the time region t2-t3 (Figure 9.11.1.2): all switches are off and the A-phase voltage clamps to the negative DC bus. The voltage vector is directed in the negative phase a-direction.

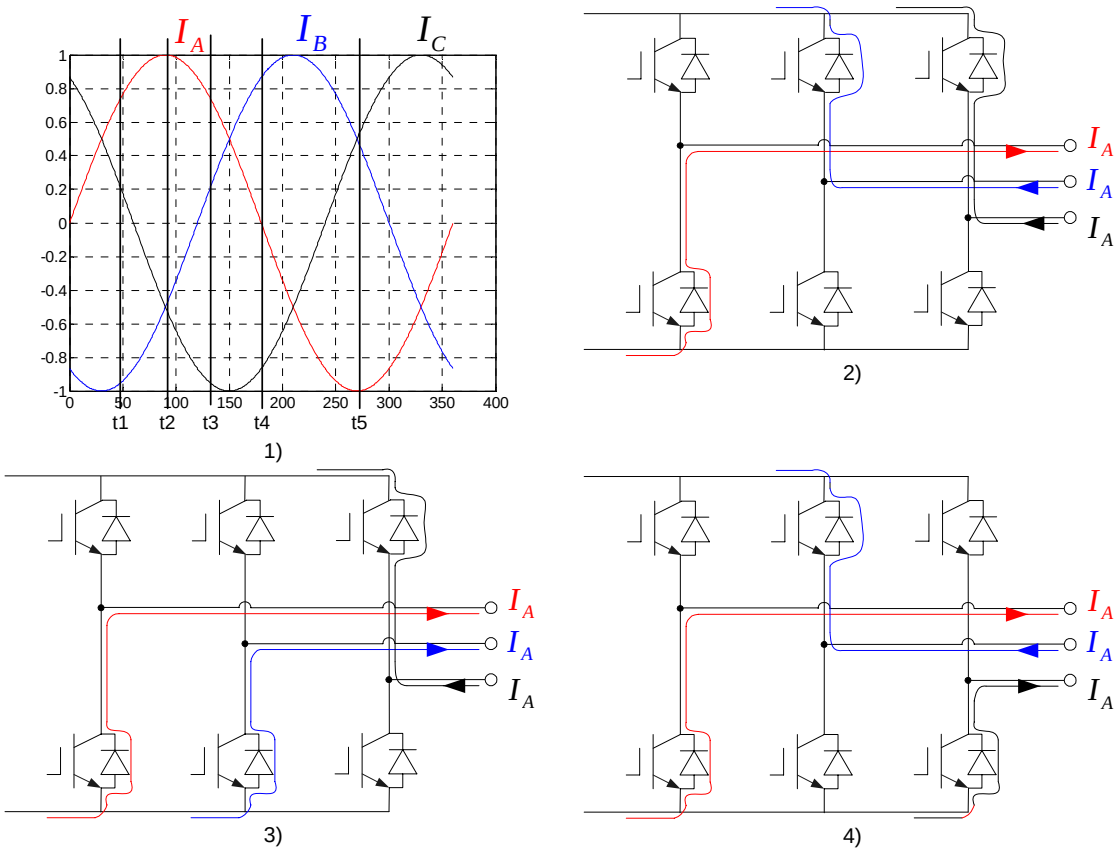

Figure 9.12 Diode clamping effect during dead time, 1)timing instances for three phase current, 2) I_A positive, I_B ,I_C-negative (t2), 3) I_A , I_B positive, I_C-negative,(t3), 4) I_A , I_C positive, I_B-negative (t1)

For the two other dead times (t4-t5, t6-t7) the effect is equal and the result is a smaller change in the current in the time region t4-t6, and an ideal change in time region t2-t4. This will influence the estimated stator current derivative: the offset will be smaller and the radius of the circle will be smaller compared to the ideal case. In addition the resulting stator current vector will have an offset compared to the initial value. In Figure 9.11.1.4 I_A is negative during the transient excitation sequence. In this example the operating condition showed in Figure 9.12.1 (t5) is used. In the dead time interval (t2-t3) the current flows in D_{A+} and the derivative of the current is the same as in time region t1-t2. The change of current is smaller in the region t2-t4 compared to t4-t6 (this will have current change as the ideal). This will influence the estimated stator current trajectory: the offset will be smaller and the radius of the circle will be smaller. As a result of the dead times the resulting stator current vector will have an offset compared to the initial value. Figure 9.11.1.3 describes a phase current zero crossing during the transient measurement sequence. The operating condition is equal Figure 9.12.1 (t4). During the actual zero crossing in the time region t3-t4 T_{A-} , T_{B+} and T_{C+} are on. When the current is positive, the current flows in D_{A-} (Figure 9.11.2). When the direction of

the current goes negative, the current flows in T_{A-} (Figure 9.11.3). The characteristic forward voltage drop of the diode and the IGBT is shown in Chapter 5. The forward drop is very similar for D_{A-} and T_{A-} : when the voltage across the device is close to zero there is diode characteristic knee voltage. For these devices this knee appears at approximately 1.5 V (Figure 5.4). The effect of the knee voltage is a deformation on the resulting voltage and the change of current smaller in the time regions t2-t4 and t4-t5. As the total voltage across the circuit is the DC-link voltage (300V) the actual zero crossing effect is small. This can be seen in Figure 8.4 where the actual zero crossings have very little influence on the derivative of the current. The dead time effect is different from the two other cases: in this example the operating condition close to Figure 9.12.1 (t4): at the first dead time I_A and I_B are positive and I_C is negative. The voltage vector in the time region t2-t3 (Figure 9.11.1) is directed in the C-phase direction. If we neglect the saliency in the machine the effect of the dead time voltage can be approximated as representing the derivative with half the ideal value in phase A. At the second dead time (t4-t5) I_A and I_C are negative and I_B is positive. The voltage vector in this time region is directed in the negative B-phase direction. If we neglect the saliency in the machine the effect of the dead time voltage can be approximated as representing the derivative with half the ideal value in phase A. The last dead time (t6-t7) will have the same properties as the first dead time (t2-t3). The consequences for the measurement of the derivative in phase A is a slightly smaller value compared to the ideal operation. From the three examples shown in Figure 9.11 and the clamping effect shown in Figure 9.12 it is evident that the transient based excitation scheme also is influenced by the dead time effects. The voltage vector in the dead time period depends on the current direction in all the inverter legs. The six dead time voltage vectors defined in Figure 5.5.1 will be active in accordance to the angle of the current space vector. The estimated stator current derivative is calculated using the change in current during time intervals t2-t4 and t4-t6 in Figure 9.11:

$$\Delta \underline{I}_1(t_2 - t_4) = \underline{L}_s^{s-1} \cdot ((t_3 - t_2) \cdot \underline{u}_{Fi} - (t_4 - t_3)\underline{u}_\alpha) \tag{9.15}$$

$$\Delta \underline{I}_2(t_4 - t_6) = \underline{L}_s^{s-1} \cdot ((t_5 - t_4) \cdot \underline{u}_{Fj} + (t_6 - t_5) \cdot \underline{u}_\alpha) \tag{9.16}$$

In order to remove the influence from back EMF the delta currents are subtracted ((t3-t2)=(t5-t4) and (t4-t3)=(t6-t5) substituted):

$$\Delta \underline{I}_1 - \Delta \underline{I}_2 = \underline{L}_s^{s-1} \cdot ((t_3 - t_2) \cdot (\underline{u}_{Fi} - \underline{u}_{Fj}) - 2 \cdot (t_4 - t_3)\underline{u}_\alpha) \tag{9.17}$$

Thus when the phase currents do not cross zero $\underline{u}_{Fi} = \underline{u}_{Fj}$ and the dead time effect cancels. When the phase current crosses zero the resulting “dead time voltage” in (9.17) becomes:

$$\underline{u}_{dt} = (\underline{u}_{Fi} - \underline{u}_{Fj}) \tag{9.18}$$

The resulting time voltage integral in (9.17) becomes:

$$\underline{u}_{res} = (t_3 - t_2)\cdot(\underline{u}_{Fi} - \underline{u}_{Fj}) - 2\cdot(t_4 - t_3)\underline{u}_{\alpha} \qquad (9.19)$$

The effects is summarised in Table 9.1 where the dead time is 1.6 us and the time region t2-t4 is 25 us. The maximum deviation from the mean amplitude of $\underline{u}_{res}$ is +/- 3.76 %. The resulting error from this type error is discussed in the next section.

Table 9.1 Dead time effect on transient excitation

$u_{Fi} - u_{Fj}$	$u_{Fi} - u_{Fj}$ (vectors)	$\underline{u}_{dt}[V]$	$\underline{u}_{res}[V\mu s]$
$u_{F1} - u_{F2}$	$e^{-j0} - e^{-j60}$	$1\angle -60$	$47.6\angle -1.7$
$u_{F2} - u_{F3}$	$e^{-j60} - e^{-j120}$	$1\angle 0$	$48.4\angle 0$
$u_{F3} - u_{F4}$	$e^{-j120} - e^{-j180}$	$1\angle 60$	$47.6\angle 1.7$
$u_{F4} - u_{F5}$	$e^{-j180} - e^{-j240}$	$1\angle 120$	$46\angle 1.7$
$u_{F5} - u_{F6}$	$e^{-j240} - e^{-j300}$	$1\angle 180$	$45\angle 0$
$u_{F6} - u_{F1}$	$e^{-j300} - e^{-j0}$	$1\angle -120$	$46\angle -1.7$

9.3.2 Parameter sensitivity

When the observer structure is used with feed forward term there will be parameter sensitivity due to inertia, permanent magnet flux and dq-inductance estimates. The parameter sensitivity functions are presented in Chapter 6. This sensitivity is equal for all the schemes when applied with the torque feed forward observer and equal bandwidths. The HFCI-R scheme does not use any machine parameters when implemented with the normalizing function before the observer. If the normalizing function is not used the amplitude of the negative rotating carrier can lead to migration of the eigenvalues in the observer. When the HFCI-R scheme is implemented without the feed forward torque and with the normalizing functions the inertia estimate can be included in the observer gains and no machine parameters are used. In the HFCI-P scheme the normalizing function (with no machine parameters) cannot be used before the observer. In order to scale the error signal the dq inductance must be estimated. The effect of errors in the estimate is eigenvalue migration for the observer. In the transient excitation based scheme the offset in the stator current derivative needs to be estimated. The offset contains the transient dq-inductance.

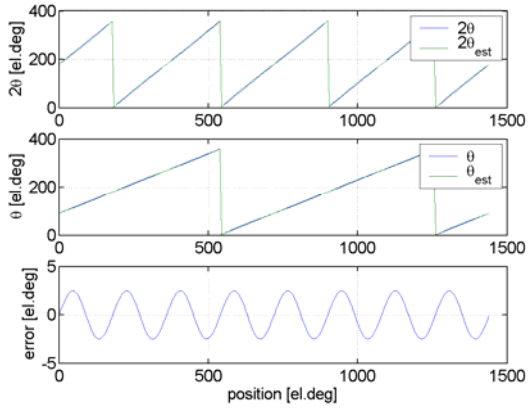

Figure 9.13 Error due to 3.76% error in the offset term used in the Transient based excitation scheme

If there is errors in the offset estimate the estimated angle will have a periodic error. The error from a 6.8 % error in the offset estimate is shown in Figure 9.13. The position dependent part of the derivative stator current trajectory rotates with two times the electrical position. When the electrical position is derived the error from the offset is also divided by two. The resulting error will have a 4 times periodicity with the electrical position.

9.3.3 Stability

The stability issues will not be discussed in detail in this work. In [2] the stability of the Luenberger Style observer and heterodyning term was discussed. For the comparison of schemes there is one difference in the three schemes evaluated: in the HFCI-R and transient excitation based scheme the vector containing position information could be normalized before entering the heterodyning term. Thus there will be no eigenvalue migration due to a change in the amplitude of the carrier signal. In the HFCI-P scheme the normalizing term contains machine parameters: thus for different operating conditions of the machine there will be eigenvalue migration in the observer. In [73] saturated inductance estimates where used in order to guarantee real poles in the PLL scheme.

9.4 Application range

In general all the sensorless schemes evaluated in this thesis are aimed for medium to high bandwidth applications. The high bandwidth category is referred to as the category with servo capability. These systems typically have low system inertia in order to enable fast transitions. Ratings close to the ratings in the sensored servo solutions are the ultimate goal for the sensorless solutions. These systems are often positioning systems where the machine has a large rotor length compared to the rotor radius in order to minimize the inertia. In the medium bandwidth class typical applications would be electric cars, truck, wheelchairs. These applications are dominated by larger system

inertia. Thus the demand for high bandwidth in estimation is not as high. There is often a focus on high bandwidth for the sensorless schemes but the schemes are also well suited for low bandwidth systems. Typical for low bandwidth systems is that the disturbance rejection does not have to be fast: pumps, fans, propulsion. In this work the different schemes has been implemented without optimizing each scheme. The potential improvement is largest with the HFCI-R scheme where the dead time influenced the position estimate. In an optimized scheme a dead time compensation scheme should be implemented. The HFCI-R scheme have double signal to noise ratio for the current measurement arrangement and would potentially be better for high bandwidth solutions compared to the HFCI-P scheme. In addition the HFCI-P scheme is implemented with a low pass filter in the observer loop. Thus for high bandwidth applications the HFCI-R scheme and the Transient excitation based scheme are candidates. For medium and low bandwidth the HFCI-P scheme and the Transient based scheme with excitation applied in intervals are candidates. The continuous injection based schemes needs a high switching frequency (>5kHz) in order to produce a high frequency carrier (>500 Hz) with sufficient quality. The transient based scheme used in intervals gives a position update for every excitation sequence and can be used in any interval given that the demand for bandwidth is low. Thus for applications with low switching frequency and low bandwidth demands the transient based scheme is a candidate. During the work done in the experimental work it was evident that the HFCI-P scheme was not influenced much from the dead time effect. Even tough the bandwidth could not be as high as for the HFCI-R scheme it gives and advantage; for machines with small saliencies the scheme performs better. If dead time compensation does not solve the problems for the HFCI-R scheme the HFCI-P scheme will be superior for application where a machine with a small saliency is used (for example surface mounted PMSM). This is due to the dead time components easily get large compared to the position dependent part of the carrier signal.

In applications where the current sensors have poor characteristics the Transient based excitation applied in intervals have an advantage. The current in the measurement sequence can be made large by allowing the pulse duration to be larger. In the INFORM [1] method the measurement sequence is separate from the fundamental excitation (not integrated in the zero vector): thus the pulse with in the measurement sequence can be made larger and a the accuracy demands on the current sensors can be lowered. In the continuous injection based schemes the carrier amplitude can also be increased but this will deteriorate the performance faster compared to the transient based scheme.

9.5 Chapter conclusions

In the comparison of schemes it must be stressed that the individual schemes was not optimized. The work done in this thesis has been focused on the characteristics of the schemes in terms of transient operation and dead time effects rather than the optimal implementation. Table 9.3 summarizes the characteristics found from the test result and the analyses. The content in Table 9.3 should be used with care as there are a lot of

different approaches when implementing these schemes. In general there are a large set of parameters for each scheme that can change the results in Table 9.3. For example an increase of the carrier frequency allows the current regulator bandwidth to increase but the DC voltage reservation must be increased in order to maintain carrier signal amplitude (and accuracy in current measurements). As another example decoupling techniques and different filtering can change the observer bandwidth and disturbance rejection function. Keeping in mind the above limitations the results can be used to derive some of the characteristics of the schemes. In drives systems the losses in the power electronics, switching frequency and current regulator bandwidth closely related. The losses in the power electronics determines the need for cooling in the inverter: when a sensorless scheme is integrated with a standard drive system it is advantageous that the cooling requirements are not changed. The additional switching losses for the transient based excitation were 50 % when the excitation was applied in every switching period. As the switching losses in the power electronics typically are 50% of the total losses the overall power electronic losses are increased by 25% compared to the 10 kHz implementation. The continuous based injection schemes do not add any additional losses in the power electronics. When the transient excitation based scheme is applied in every second switching period (f_{sw}=5 kHz) the switching losses are equal to the continuous injection based schemes (f_{sw}=10 kHz). It is interesting to evaluate the current regulator bandwidth obtained for the different schemes: in the continuous injection based schemes the current regulator bandwidth was limited to 700 Hz in order to avoid interaction between the carrier signal and the current regulators. In the tests a pre-filter was used and the resulting bandwidth was 350 Hz. In the transient exaction based scheme the current regulators where tuned according to optimal design: the maximum bandwidth for this scheme where 833 Hz. Thus even tough the switching frequency was higher for the continuous based injection schemes the maximum current regulator bandwidth was lower.

Table 9.3 Comparison of methods

	HFCI-R	HFCI-P	TE	TE 10th
f_{sw}	10 kHz	10 kHz	5 kHz	5 kHz
Current regulator bandwidth	350 Hz[1)]	350 Hz[1)]	833 Hz	833 Hz
Test performance	3	2	1(best)	4
Observer bandwidth	600 Hz[2)]	110 Hz[2)]	600 Hz[2)]	30 Hz[2)]
Disturbance rejection	1[3)]	2[3)]	1[3)]	3[3)]
Zero crossing Robustness	3	2	1	1
Total loss in power electronics	100%[4)]	100%[4)]	125%[4)]	80%[4)]
Parameter sensitivity	No	No[5)]	Yes	Yes
Easy integration with standard systems	1	1	2	2
Signal to noise ratio on position dependent current –LEM sensor	11.6	5.7	8.9	8.9
DC voltage reservation	30%	15-30%	37.5%	2.75%
Acoustic noise	75dBA[6)] 75dBA[7)]	57dBA[6)] 71dBA[7)]	64dBA[6)] 65.5dBA[7)]	54dBA[6)] 56.5dBA[7)]

[1)]Pre filter used on reference value, maximum bandwidth without the pre filter was 700Hz. Bandwidth was determined by the 10-90% rise time

[2)]Theoretical bandwidth with gains from test run

[3)]Theoretical disturbance rejection with gains from test run: 1-describes the best disturbance rejection properties

[4)]Total losses: switching losses + conduction losses compared to symmetrical space vector implementation with 10 kHz switching frequency

[5)]Machine parameters used in normalizing term

[6)]Acoustic noise at stand still and signal injection (HFCI-P, Vc= 30V)

[7)]Acoustic noise at 0.1 pu speed with signal injection (HFCI-P, Vc =30V)

In Table 9.3 the performance is rated from 1 to 4 where 1 represents the best performance. In this rating the speed and position quality during the speed reversal and transient test are used as a base for the ratings. The torque feed forward term is not applied during these tests. The transient excitation based scheme gives considerable better performance when both the speed and position estimate are evaluated. The HFCI-R scheme is rated as second best and the HFCI-P scheme is rated as third best. The transient based scheme applied every 10^{th} witching period shows the poorest performance due to the poor performance during the speed reversal test. It should be noted that the interval based scheme will have better speed reversal performance with a more experimental pole placement [71].

The bandwidth of the schemes was not tested experimentally (sinusoidal load variations based test). Due to inverter non linearity and transient noise the theoretical bandwidth is not representative for the system. The actual bandwidths for the estimates are considerable lower than the theoretical bandwidth due to the inverter non linearity and the transient disturbance from the fundamental current. The theoretical bandwidth can be used to compare the schemes in order to determine lags and capability with ideal operating conditions. The transient tests done with no torque feed forward can be regarded as a disturbance rejection test. In Table 9.3 the disturbance rejection functions are used in order to rate the disturbance rejection functions.

The major difference between the continuous injection based schemes and the transient excitation based schemes are the influence from dead time. The continuous injection based schemes separates the position dependent by frequency separation. In general any frequency component close to the negative carrier frequency in the stator current can show up as a disturbance in the position estimate. In this chapter the effect from fundamental zero crossings where discussed for the three schemes. The analyses show how the carrier signal introduces a dead time effect modulated by the carrier frequency. This modulation has 6 times periodicity to the position (electrical). The HFCI-R scheme is most sensitive to this error as it uses the negative carrier vector as an input to the heterodyning term. In the HFCI-P scheme the q-axis current is used as bases for the input to the observer. The analyses and test shows that the dead time effect is minimal in the q-axis current under the control strategy used in this work ($i_s^*=i_q$). Also in the transient based scheme there are effects from inverter dead time. These effects are minimal in the test performed in this work. The dead time effect is assumed the main difference between the schemes evaluated in this work.

10 REDESIGN FOR SENSORLESS CONTROL

Redesign of electrical machines in order to increase the saliency ratio has successfully been done for several types of machines. The first redesign approaches was focused on introducing saliency in the leakage inductance in induction machines: [2, 13] used modified rotor slots, [34, 35] used modified rotor bars. For IPMSM there has typically been a saliency present due to the rotor design and teeth saturation. These machines are usually very well suited for true sensorless control and they will not be discussed in this chapter. For surface mount PMSM the saliency is usually due to stator teeth saturation. For some "off the shelf" machines sensorless control is possible due to a 10-15% saliency. This saliency is typically based on saturation in stator teeth and yoke. For other machines the saliency is smaller and true sensorless control is harder to archive. In this Chapter different redesign approaches for PMSM are discussed. In the first section various redesign approaches found in publications are discussed. At the end of the Chapter a redesign approach on an axial flux PMSM (Test Machine 2) is presented.

10.1 State of the Art Redesign for Sensorless Control

There are several publications on enhancing the saliency ratio by redesign of electrical machines. For different types AC machines the strategy for designing saliency into the machine are quite different. PMSM are the main focus for this thesis and only this type of machines will be evaluated in this Chapter. The saliency ration can be influenced by several machine properties:

- Rotor magnetic design
- Tooth saturation
- Yoke saturation
- Stator slot modification
- Lamination (direction)
- Slot filling/wedges

The proposed changes have different features as some influence leakage inductance and some influence main inductance. The load dependency also differs for the different modifications. The radial flux machines are the most common PM machines. For IPMSM there usually is a large difference in the dq-inductance due to the rotor design and due to stator teeth saturation. In case of stator yoke saturation this will add more saliency to the machine as all these three saliencies are spatially working on the same flux path (in the main flux path). The radial flux machines are often designed with laminated stator and rotor, thus portions of the high frequency flux can penetrate in the main flux path. In the surface mounted PMSM the saliency is often smaller compared to the IPMSM and sensorless control can be hard to realize. The surface mounted PMSM are therefore the focus for this Chapter.

10.1.1 Surface mounted PMSM

In a surface mounted radial PMSM there are several ways of introducing saliency; rotor design, tooth/core saturation, semi magnetic slot wedges and iron filling between magnets. In the next sub chapters examples of these redesign approaches will be referred from publications.

10.1.1.1 Rotor design

The rotor design may be used in order to produce saliency in the machine. In [72] the rotor was altered in order to give the machine saliency, the redesign changes the machine from a pure surface mount into a machine where the magnets have some iron between the magnets. A conceptual description of the redesign is presented in Figure 10.1. The machine has an outer rotor structure with an internal stator. In Figure 10.1 only the details from the rotor are given as they illustrate the modification to the machine. The redesign introduced varying saliency ratios into the machines depending

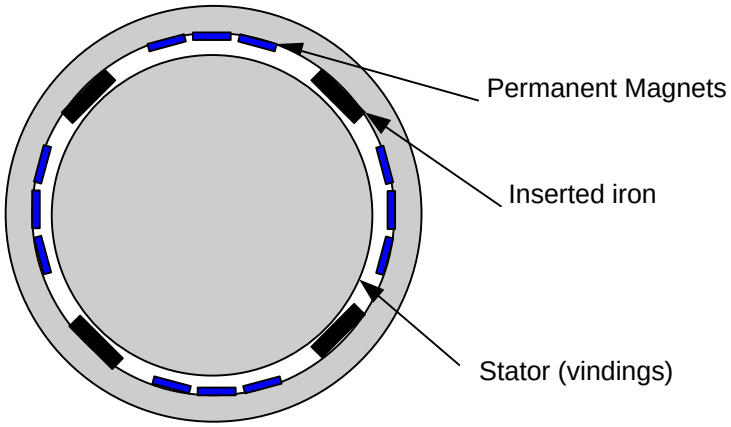

Figure 10.1 Redesign approach on PMSM [72]

on the shape of the insert iron. The maximum saliency ratio obtained was 0.287.The INFORM method [1] was used to measure the saliency.

10.1.1.2 Tooth/core saturation

In [1] and [30] "of the self", surface mounted PMSM, was used with sensorless control. In these machines the saturation in the stator teeth and rotor yoke was assumed to be the basis for the saliency in the machines. The saturation level in the stator teeth and rotor yoke are design parameters. The stator teeth and yoke flux density are typically checked after initial design, loss calculations and optimization criteria are checked and gives inputs to an iterative design procedure. The saturation based saliency will depend upon the lamination selected for the machine. For example the laminations M235-35A from Surehamar (Congent) have approximately a linear relationship between relative permeability and flux density from 0.4 T up to 1.3. If one aim for saturation based saliency the maximum flux density in the machine design procedure should be no more than 1.3 T for this type lamination (above this level the relative permeability becomes non linear to the flux density). Optimal design will wary in accordance to the criteria function used for the design. If low prise is important (optimal) the machine design-procedure will result in a machine with high flux/current density and minimum amount of iron, copper and magnets. If efficiency is important the losses are minimized, this is primary done by reducing the copper loss ($i^2 \cdot r$) by increasing parallel branches in the stator winding (or increasing the wire dimension). In addition the iron losses can be reduced by reducing the flux density in the machine. In (10.1) an example of optimal design criteria function is given.

$$\lambda = k_1 P_{loss} + k_2 (c_{Fe} m_{Fe} + c_{Cu} m_{Cu} + c_{PM} m_{PM}) + k_3 D \qquad (10.1)$$

In (10.1) the different terms are weighted according to the significance of the different factors. The first term in (10.1) represents the losses in the machine, k1 represent the

significance of the losses to the overall cost. The next them represent the cost of the materials used in the machine and the third term includes a penalty (cost) on the diameter on the machine (D). In order to illustrate the losses in the machine a typical loss calculation is presented (friction losses not considered):

$$P_{loss} \approx P_{Cu} + P_{Fe} \tag{10.2}$$

$$P_{Cu} = 3R_s I_s^2 \tag{10.3}$$

$$P_{Fe} \approx 2.8 f^{1.6} (B_{t-\max}^2 m_t + B_{y-\max}^2 m_y) \cdot 10^{-3} \tag{10.4}$$

Where $B_{t-\max}$ and $B_{y-\max}$ represents the maximum flux density in the stator teeth and yoke, m_t and m_y represents the mass of the laminations associated with teeth's and yoke. In general introducing/increasing saturation based saliency in a machine will result in increased iron losses.

10.1.1.3 Stator slot modification

The design of the stator slot geometry affects the leakage flux. For surface mounted machines the effective air-gap is large. Due to the high frequency on the carrier signal, and the large air gap, only a small portion of the high frequency flux will penetrate into the rotor structure. If a modification in the leakage flux path is introduced the high frequency leakage flux are likely to be modulated. In [37] the stator slot was closed in order to produce a position dependent variation in the leakage flux path. The variation in the leakage inductance was based on saturation of the bridge over the stator slot. The design on a surface mounted PMSM resulted in a saliency ratio equal 0.14 (ΔL/ΣL) compared to no saliency initially. The saliency ratio was dependent on the loading of the machine and at full load the saliency ratio was approximately 0.067.

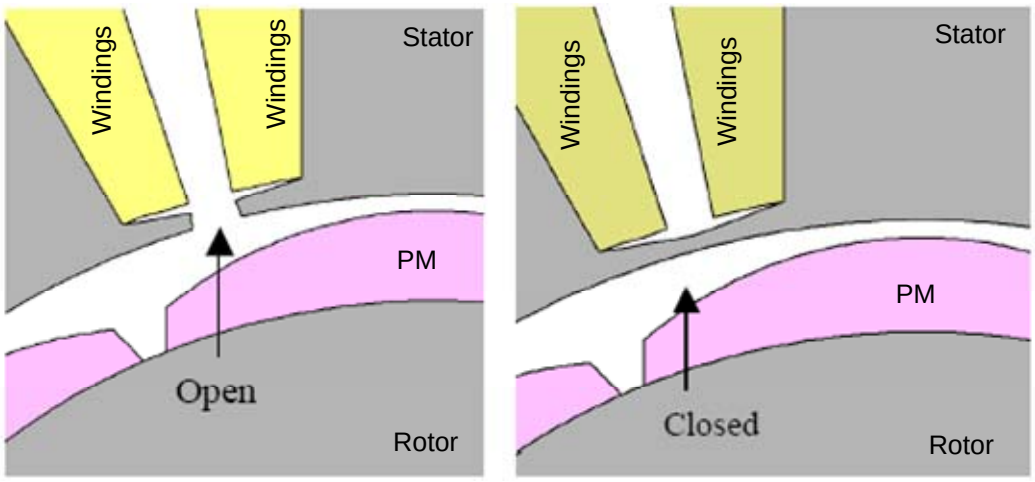

Figure 10.2 Stator slot modification [37]

10.1.1.4 Lamination direction

In non oriented lamination material the magnetic properties should be the same in all directions. In [38] the magnetic properties of laminated was evaluated. The relative permeability does not depend on the rolling direction (production line) for fundamental excitation at rated frequency [38]. When the frequency is increased there is a difference in the permeability depending on the rolling direction and the transverse direction. Test machines where made with all lamination aligned in rolling direction and with shifted lamination orientation (minimum common orientation). The machine with oriented lamination direction showed a saliency due to lamination direction at approximately 20% ($\Delta L/\Sigma L$) the machine with shifted lamination orientation showed almost zero saliency. It should be noted that this type of saliency will be dependent on twice the mechanical period compared to twice electrical for the saturation induced saliencies.

10.1.1.5 Combined effects

When considering design of machines for sensorless control the sources of saliency in the machine should be encountered for. One should also consider where the resulting flux from the excitation distributes in the machine. If the excitation results in a flux that is distributed in the leakage flux paths the modifications should be done in these regions. In chapter 3 the saliency modelling shows that the saliency is the difference of main flux and leakage flux variations. Table 5.1 gives an overview of the design options and the region of the machine that varies:

Table 10.1 Modification and region in change due to the modification

	Main flux path	Leakage flux path
Rotor design	X	
Stator Tooth Saturation	X	X
Stator Yoke saturation	X	
Stator slot design		X
Lamination directions	X	X

The saliency from lamination direction will be periodic with twice mechanical revolution, thus it appears as multiple saliency with for instance saturation induced saliency on a machines with more than one pole pair. The laminations should be shifted

if one tries to design saturation based saliency into the machine and the machine has more than one pole pair. If the carrier flux is assumed to distribute in the main flux path (laminations and few barriers) combined effort can be made; rotor design, tooth saturation and core saturation can be introduced as a singe saliency in the machine. If the carrier flux is assumed to distribute in the leakage flux path stator slot design can be used to introduce a saliency.

10.2 Redesign of a axial flux PMSM

When a machine is considered for redesign for sensorless control there is a lot of factors that has to be considered: optimal design criteria, usage of the machine (load profile), materials used in the machine, noise, cost, complexity of change, reliability of design (mechanical). In this work the saliency ratio is evaluated for different redesign approaches. Based on this work the approach with most synergy effects and minimum penalties was selected for prototyping.

10.2.1 Machine Characteristic

Test machine 2 was designed for usage in a wheelchair application. The machine was optimised for low cost, high torque and efficiency. A saturation based saliency was present in the initial design. This saliency was frequency dependent and low portion of position dependent inductance (approximately 5% saliency) [36]. In order to extract saliency information from the machine the excitation signal frequency had to be as low as 125 Hz. This saliency was problematic in two ways: the saliency was very small and the carrier frequency had to be very low. The small saliency leads to problems with the accuracy of the current sensors. The low frequency leads to problems with the frequency separation needed for the HFCI schemes (synchronous reference frame filter or demodulation). Transient excitation based schemes could not be used as this excitation could not extract the saliency information from the machine. Test machine 2 is a commercial prototype machine. Figure 10.3 shows a principal view of the machine. In Figure 10.3.1 side view of the stator is shown. The yellow areas represent the coils, the grey areas represents the iron powder cores. In Figure 10.3.2 one

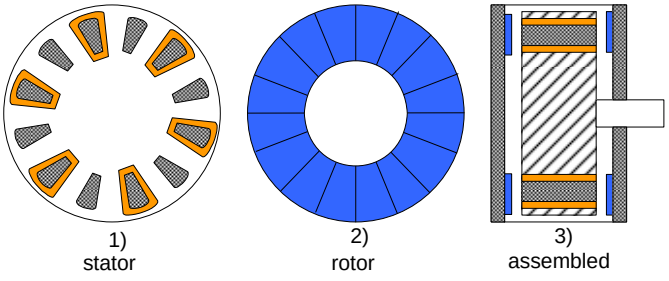

Figure 10.3 Axial flux PMSM principal view

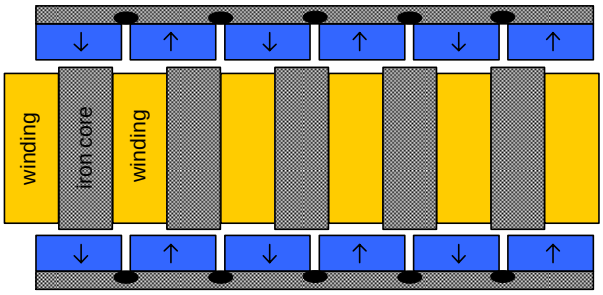

Figure 10.4 Axial flux PMSM principal view – two dimensional view

of the rotor sides are shown; the magnets (blue colour) fronts the drawing, a solid iron disc cowers the backside of the magnets. In Figure 10.3.3 the assembled machine is shown. The same colour code is used for the permanent magnets, coils and core materials. The shaft is stationary in this machine (mounted on the wheelchair) and the rotor rotates. In the actual application the machine is integrated into the wheel. In the analyses of the magnetic design a two dimensional representation of the machine is useful. Figure 10.4 illustrates the surface of an axial cut in the centre of the iron powder core in Figure 10.3.3.

The black areas between the magnets represent the areas of local saturation in the rotor yoke. Some special features of this design may be of particular interest for the redesign evaluation of the machine: the effective air-gap is large, the magnets cover most of the surface of the rotor, the windings are concentrated, iron powder stator cores and the yoke behind the magnets are solid iron (no lamination).

10.2.2 FEM simulations

The Finite Element Method was used to verify the different redesign approaches. As FemLab was used by the machine design group and for teaching purposes at the University this FEM program was used for the simulations. The simulations in FemLab was by no means straight forward: in order to incorporate the saturation effects and combination of stationary and time dependent sources a group of people worked with FemLab over a period of one year. A master thesis [43] and two student projects was written on the subject and one paper war published [44]. FemLab in Sweden (supplier of software) was consulted in the development of the models. The material characteristics for the iron powder cores were supplied by Høganes in Sweden. In this chapter a brief description of the FEM simulation are presented. The field from the permanent magnets where modelled as a static field. This simplification was applicable due to the high frequency of the carrier signal compared with the main field frequency. The signal injection was modelled by sinusoidal high frequency (500 to 10000Hz) current. Two sub domains (“transient” and “time harmonic”) was used in FemLab in

order to incorporate the field from the current in the windings and the field from the permanent magnets. The resulting flux density was used in an iterative solver together with the curves for the relative permeability in order to incorporate the saturation in the machine. The inductance calculation where made by evaluating the magnetic energy:

$$W_{magn} = \frac{1}{2}\int_{Si} (J \cdot \mathbf{A}) \cdot dSi \qquad (10.5)$$

Where J is the specified current density in the core, A is the magnetic vector potential and Si is the winding area. In order to get a simulation that could be performed within a reasonable time some simplifications where made: only one coil was evaluated and symmetry simplifications where made. The most important simplifications are listed here in order to get an overview:

- end effects not included
- relative permeability assumed constant between 0 and 0.5 T for core and yoke
- relative permeability correction for minor loops (field from high frequency carrier superimposed on field from permanent magnet) not included
- rotor rotation not included
- relative permeability curve for wedge and disc material assumed to be of equal shape of the iron powder core (supplier could not give sufficient material data)
- the individual leaders in the coil was represented by a current density in the area occupied by the leaders (proximity effect not included)

There are several of these simplifications that may have large impact on the field calculation: the evaluated machine is a “disc” type machine, thus the end effects could be large. The assumption of constant permeability at low flux densities was crucial in order to get convergence in the results. The minor loops may reduce the relative permeability in all the materials and as a result the penetration dept may be altered. Due to the many simplifications the results from the FEM simulations cannot be regarded as absolute. The FEM results where rather used to show trends in the inductance (and saliency ratio) as a result of the different redesigns.

10.2.3 Evaluation of redesign approaches

Several redesign approaches where discussed for the machine; more saturation in the stator cores (main flux path), local saturation in stator cores (end effects), increased saturation in the rotor yoke, altered rotor redesign and leakage flux path modifications. The main design goal was to introduce a saliency in the machine that could be detected with signal injection based methods using a carrier frequency from 500 to 2000 Hz or transient excitation with equivalent frequency at 20 kHz. Preferably the redesign should

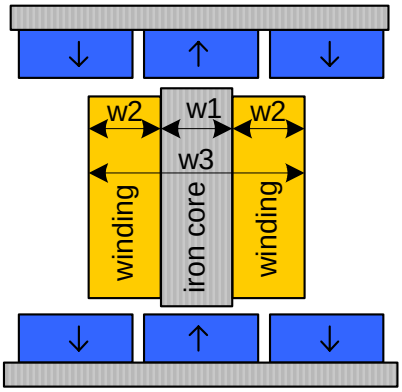

Figure 10.5 Core saturation increased due to reduction of core area

also lead to increased machine performance as reduced cogging torque, reduced iron losses or better utilization of materials used in the design. As the machine is a low cost product the redesign should not increase the manufacturing cost or material cost more than the cost reduction from removal of the position sensor.

10.2.3.1 Core saturation

Saliency due to core saturation can be directly compared with teeth saturation for radial flux PMSM. In order to increase the saturation effect in the core the core area can be reduced. If some of the iron is removed there are room for more copper, this may lead to better utilization of the permanent magnets (less magnets needed to produce same torque). The concept is illustrated in Figure 10.5; the total width w3 is held constant, core width (w1) is reduced and winding width (w2) is increased accordingly. The saturated area is included in the leakage flux path thus the carrier injection (500-2000 Hz) and transient excitation could detect the saliency. This concept was discussed and synergy was found on overall cost; if the core could be smaller there would be more room for copper. If more copper could be inserted the permanent magnets could be smaller (or better utilized). There was a severe drawback: the maximum torque specification could not be met with the reduced core area.

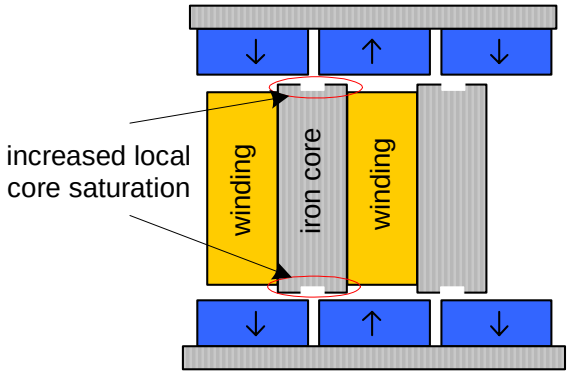

Figure 10.6 Increased local saturation in core

10.2.3.2 Local core saturation

When the core is located between the magnets there are some local saturation in the section of the core closest to the magnets. From the initial design and the initial experiments performed on the machine these effects where not measurable. Different core design (Figure 10.6) was evaluated in order to create a bigger local saturation. Also for this redesign there was some synergy on machine performance; the cogging torque could potentially be reduced. The inductance variation would be in the region of the leakage flux and usage of carrier injection (500-200Hz) and transient excitation could be possible. The concept was discussed but the production cost was increased due to the complex shape of the core and the increased complexity in assembly of the machine.

10.2.3.3 Yoke saturation

Yoke saturation was originally the only measurable saliency present from the initial design. Due to the large air-gap the synchronous reactance was very low and the flux from the permanent magnets dominates the resulting flux. The yoke saliency would therefore be very little influenced by the load condition of the machine. If the saturation level in the yoke where increased (by reducing w10 in Figure 10.7) there would be some penalties; more iron loss and less utilization of the permanent magnets. Due to the problematic frequency dependency on the rotor yoke saliency and the lack of synergy effect this approach was not implemented.

10.2.3.4 Rotor redesign

Iron insert between the magnets (Figure 10.8) was considered in order to produce an inherent saliency due to rotor design. No synergy effects could be found for this modification. The modification may lead to increased leakage flux from the permanent magnets and increased losses in the rotor. The region of inductance variations are in the main flux path but still close to the core (1mm air-gap). The modification may work with carrier injection (500-2000 Hz) and transient excitation.

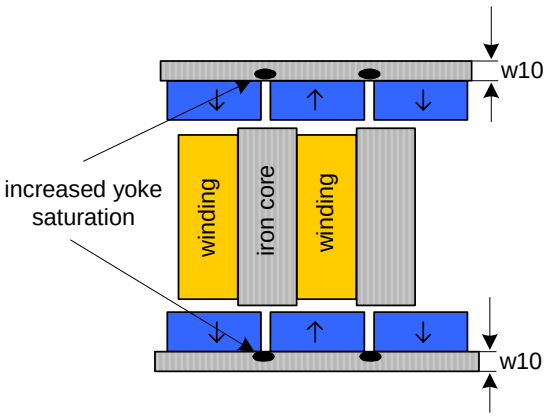

Figure 10.7 Increased yoke saturation

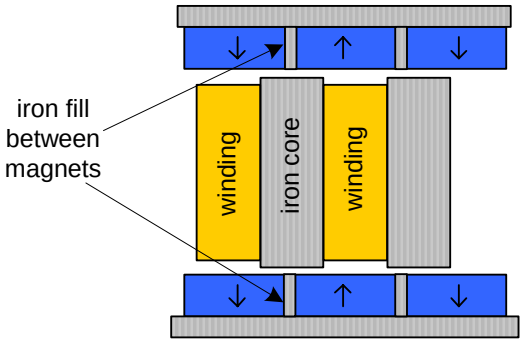

Figure 10.8 Iron fill between magnets

The penalties from this modifications where not severe and the redesign was evaluated in FemLab. The simulations show approximately a saliency ratio 0.18 $(\Delta L / \sum L)$ due to the modification. The redesign is not easily implemented in the machine as the distance between the magnets are small and the original rotor yoke is made of a solid iron disc. The redesign was not tested with a prototype due to the increased complexity in the rotor structure.

10.2.3.5 Leakage inductance modifications

The stator winding fills the volume between the stator cores. The leakage flux is concentrated to the stator winding volume. If a thin magnetic material is inserted between the cores this could have impact on the leakage flux. If the inserted material has variations in the flux density according to the rotor position there may be a position dependent portion of the leakage inductance. This concept was evaluated with two approaches: a semi magnetic disk could be used on top of the core (Figure 10.9.1) or mount a thin layer of semi magnetic material between the cores (Figure 10.9.2). The disc approach lead to increased effective air gap as the disc material was supposed to have less permeability compared to the iron powder core.

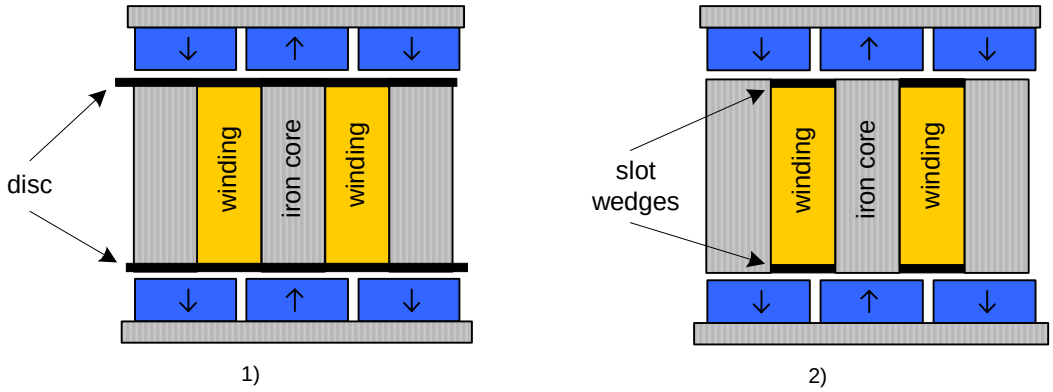

Figure 10.9 Leakage inductance modification. 1: semi-magnetic disc covering the surface of the core and winding, 2:semi magnetic slot wedges between the iron cores

This approach required changes in the original dimensions for the machine and was therefore not considered for prototyping. The slot wedge solution was easily realizable in a new prototype, and it had several synergy effects to the machine performance. A detailed description of the slot wedge redesign is covered in the next chapter.

10.2.4 Redesign based leakage flux variation

Of all the redesign candidates evaluated the redesign based on insertion of semi magnetic slot wedges was selected as the most promising. Semi magnetic slot wedges has been used for induction machines in order to reduce torque harmonics [41] and iron losses [40]. The same concept has been used in axial flux PM machines; in [42] slot wedges was used successfully to reduce iron losses and cogging torque. The cogging torque in the axial flux PM machine stems from the forces acting between an individual iron core and a nearby permanent magnet. The semi magnetic slot wedges are placed in-between the iron cores and thereby smoothen the magnetic properties along the air gap. As a result of insertion of semi magnetic slot wedges the cogging torque was reduced by 60% in [41]. As the machine rotates the flux from the permanent magnets leads to flux pulsations in the iron powder cores. The discrete nature of the stator (copper/iron powder) leads to high local flux density in the iron powder cores. This effect was (core power loss) reduced by 48% in [42] by insertion of semi magnetic slot wedges. Thus a synergy effect can potentially be found: introducing semi magnetic slot wedges may enable sensorless control and reduce loss and cogging torque. In order to evaluate the potential saliency increase the insertion of semi magnetic slot wedges was simulated in FemLab. The simulations were done as a combined effort from [43] and the author. In order to simulate the slot wedge approach the permeability as a function of the flux density was needed. As the slot wedge material was not selected at the time of the simulations the properties from the core material was downscaled in order to simulate a semi magnetic slot wedge. The downscaled curves for the relative permeability are shown in Figure 10.10.

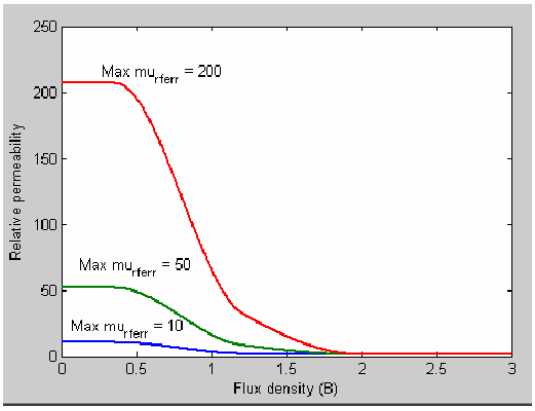

Figure 10.10 Relative permeability curves for slot wedge material used in FEM simulations

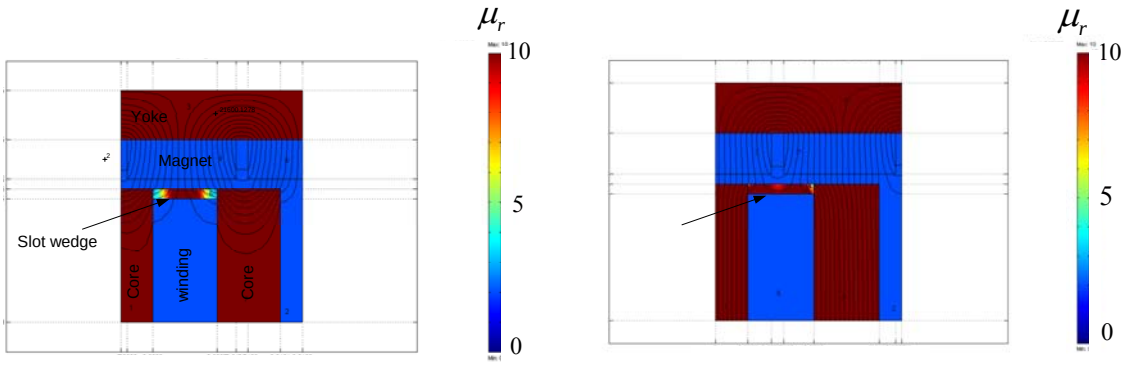

1) 2)

Figure 10.11 FEM simulation of relative permeability for two different rotor positions based on flux from permanent magnets; 1) q-axis, 2) d-axis (maximum relative permeability limited to 10)

Figure 10.11 shows a simulation of relative permeability in a small section of the machine. In Figure 10.11.1 the winding is oriented in the q-axis. The flux lines and relative permeability is a result of the flux from the permanent magnets alone. In Figure 10.11.2 the same structure is simulated with the winding in the d-axis. If the relative permeability is compared for the two positions the slot wedge is more saturated when the winding is oriented in the q-axis.

In order to evaluate the inductance variation the flux from the winding must be evaluated. The simulations where run with combined field from magnets and carrier signal as the basis for the iterative solver. Figure 10.12 shows the flux lines and the flux density from a 500 Hz carrier signal in the winding. The difference in the saturation level in the slot wedge results in a large difference in the leakage flux distribution in the structure.

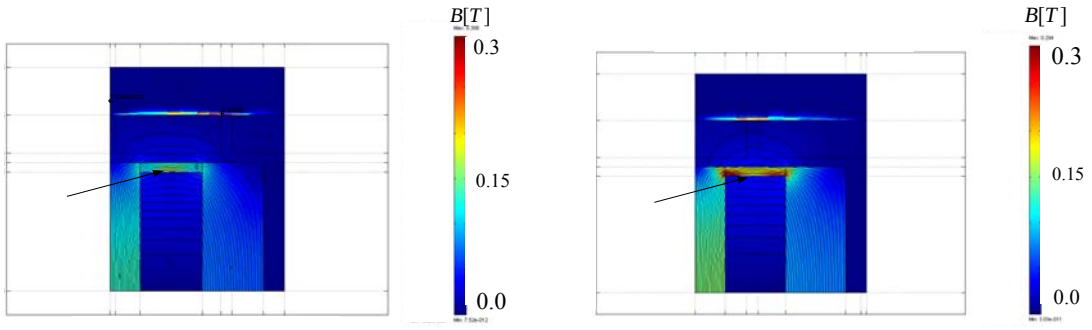

1) 2)

Figure 10.12 Flux density as a result of a 500 Hz carrier in the winding; 1) q-axis, 2) d-axis

The slot wedge approach was evaluated with three different relative permeability curves (Figure 10.10). The saliency ratio varied from 0.07 to 0.14 depending on the relative permeability curve used in the simulation. The trend was increasing saliency ratio for increasing maximum relative permeability (10, 50, 200 - Figure 10.10). Different carrier frequencies were also tried: the saliency ratio was approximately constant for frequencies from 0.5 to 10 kHz. The load dependency of the saliency was also simulated; the simulations all had converges problems and no results from these simulations are given here. From the saliency modelling in Chapter 3 a general assumption can be made: when the machine is loaded the q-axis current increase (control strategy $i_q = i_s^*, i_d = 0$). The load current will drive the slot wedge more into saturation, as this approach is based on saturated slot wedge when the rotor is in the q-axis the load dependent effect will add to the effect from the permanent magnets. Thus the saliency ratio is supposed to increase with increasing load. In order to build a prototype, suppliers of semi magnetic slot wedges was contacted in order to get a slot wedge with the comparable relative permeability as used for the FEM simulations. The only supplier that delivered slot wedges at short notice was Camawi Electricals & Electronics. The permeability description on the MAGNATUFF slot wedges from Camawi only described two points on the BH curve: at H=100A/cm μ_r=7.5 and at H=200A/cm μ_r=6.1. Thus the permeability of these slot wedges was considerably lower than permeability used in the simulations. The prototype based on slot wedge insertion cold be archived with small costs and a prototype was build with the MAGNATUFF wedges in order to evaluate changes in the inductance (trends rather than a full sensorless capability). The actual prototype (test Machine 4) is showed in Figure 10.13. The slot wedges are the grey parts to the right of the machine in Figure 10.13.1, the iron powder cores are the black ovals distributed around the periphery of the stator. In Figure 10.13.2 the slot wedges are mounted between the iron powder cores.

1) 2)

Figure 10.13 Test Machine 4. Insertion of slot wedges, 1) before slot wedge insertion, 2) after slot wedge insertion

10.2.5 Redesign results

In order to evaluate the effects of the slot wedges both Test Machine 3 (no slot wedges) and Test Machine 4 (with slot wedges) was tested. The goal in the redesign approach was to introduce a saliency detectable with a carrier frequency in the range 500 Hz to 20 kHz. The slot wedge material in the actual prototype was not the same as the material used in the simulations. The expected saliency ratio is therefore well below 0.07 (estimated saliency ratio from the FEM simulations). The effect of the slot wedge material is evaluated by comparing the saliency ratio from Test Machine 3 and Test Machine 4. The tests where performed on a commercial prototype drive system designed by SmartMotor AS. The details of this system are not presented in this thesis. Two factors must be mentioned: the DC link voltage was 24 V and the LEM sensors had an overall accuracy equal 2% (of 50 A). Two test signals where used during the testing of the machines: sinusoidal signal and transient signal. The transient excitation was equal the transient excitation used in Chapter 8. During the testing with transient excitation the changes in the current during a voltage step where only about 1 A. Due to the low accuracy in the LEM sensors a small saliency could hardly be measured from such small change in the current. The transient excitation did not give any useful estimates of the saliency ratio. The second test signal was a high frequency balanced sinusoidal voltage. The challenge with the LEM accuracy was met by increasing the voltage amplitude. Figure 10.14 shows the test results from the test with sinusoidal excitation: the alphas vs. beta components of the stator current are plotted. If there is a saliency present in the machine these plots will be elliptical. The saliency ratio can be estimated by evaluating the length of the major axis and the length of the minor axis.

$$SR = \frac{\Delta L}{\Sigma L} = \frac{L_q - L_d}{L_q + L_d} \approx \frac{|i|_{major\_axis} - |i|_{\min or\_axis}}{|i|_{major\_axis} + |i|_{\min or\_axis}} \tag{10.6}$$

The test results from TestMachine 3 did not show any measurable saliency at either 500 or 1000 Hz. In the test results from TestMachine 4 (Figure 10.14- 2 and 4) a small saliency could be estimated:

Table 10.2 Saliency estimates for Test Machine 4 (slot wedge insertion)

Test frequency [Hz]	Saliency Ratio
500	0.030
1000	0.048

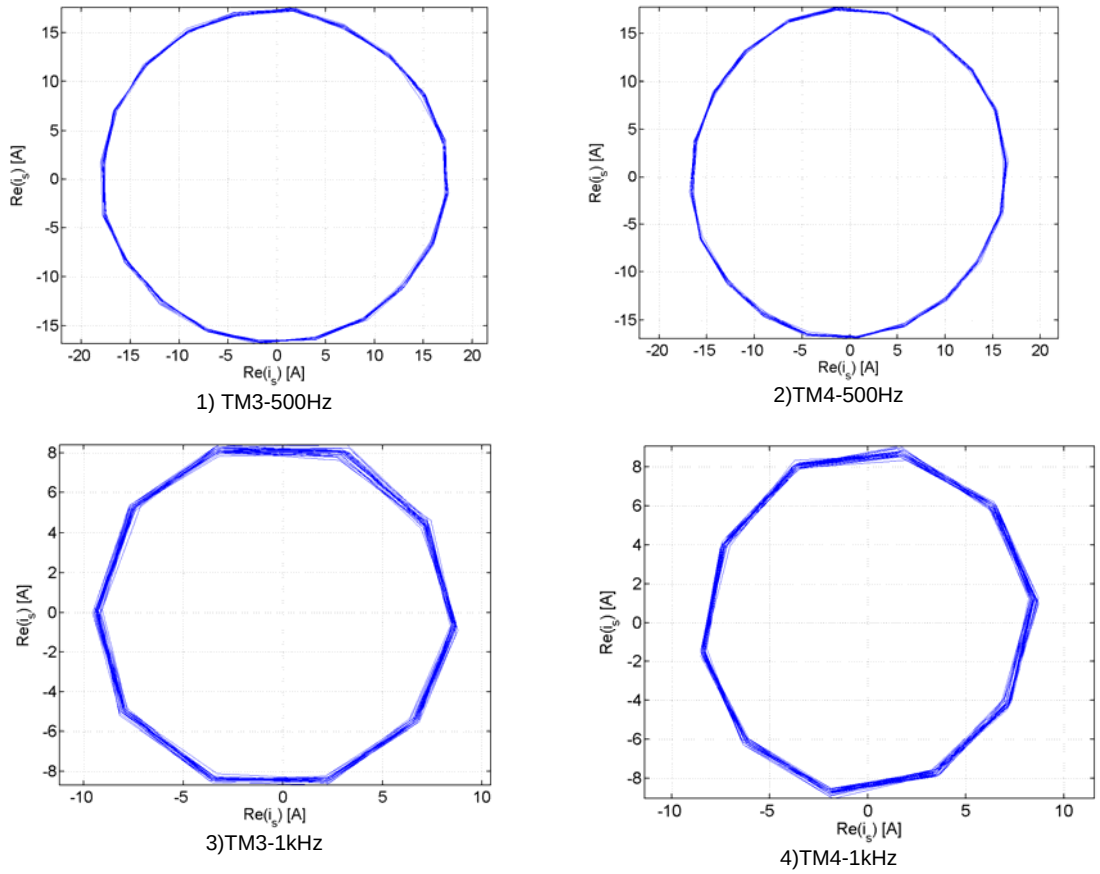

Figure 10.14 Alpha vs. beta component of carrier signal, rotor locked in one position, 1)Test Machine 3 – 500 Hz, 2)Test machine 4 – 500 Hz, 3)Test Machine 3 – 1kHz, 4)Test Machine 4 -1kHz

The estimated saliency ratios from the measurements are in good agreement with the simulated saliency ratio if the low permeability in the real slot wedges is taken into account. The redesign shows that the saliency ratio can be increased by insertion of semi magnetic slot wedges. The saliency ratio is still too small for on-line rotor position estimation. The limiting factors for on line estimation are: low accuracy in the LEM sensors, influence from dead time and other sources of noise in the system. In order to further increase the saliency ratio a slot wedge material with higher relative permeability should be used (for example Somaloy550).

10.3 Chapter conclusions

Several redesign approaches where discussed in this Chapter. The approach based on introduction of position dependent saturation in the leakage flux paths where selected as

this redesign had several potential synergy effects. From theory studies and FEM simulations the potential synergy effects where identified as:

- Introduction of saliency in leakage flux path
- Reduction of iron losses
- Reduction of cogging torque

The drawback from the redesign was assumed to be increased leakage flux. A prototype of the Axial Flux PMSM was redesigned with semi-magnetic slot wedges. In this thesis only the saliency of the machine was measured. The cogging torque and iron losses was not evaluated.

The saliency ratio was evaluated for Test Machine 3. No saliency could be detected with the current sensors in the commercial prototype for sinusoidal (0.5 and 1 kHz) and transient excitation (20 kHz equivalent).

Test Machine 4 was redesigned with semi magnetic slot wedges to increase the saliency ratio at higher excitation frequencies. The machine was tested with sinusoidal excitation (0.5 and 1kHz) and with transient excitation (equivalent 20 kHz). The transient excitation could not be used to detect the saliency as the change in the current was too small compared to the accuracy in the LEM sensors. With the sinusoidal excitation the amplitude of the signal was increased in order to improve the current measurement accuracy. The saliency ratio was estimated to be approximately 0.03 at 500 Hz test frequency and 0.048 at 1000 Hz test frequency. The saliency ratio was lower than the Saliency ratio found from the FEM simulations (SR=0.07). The lower saliency ratio is assumed to be caused by two factors: only one coil is evaluated in the FEM simulations. In the prototype one phase are made from a series connection of three coils. The decrease in the saliency ratio due to the series coupling is described in(1.58). In addition the relative permeability in the slot wedges in the prototype was lower than the value used in the FEM simulation.

The redesign effect on load dependency, iron loss and cogging torque was not evaluated in this work but scheduled for future work.

11 SUMMARY AND FUTURE WORK

11.1 Summary and Conclusions

This thesis covers a range of different topics within the field of sensorless control. Each chapter ends with a conclusion this section summarises the main conclusions from this work.

In Chapter 1 the classical machine modelling was presented and a special case for concentrated coil axial flux machine was developed.

In Chapter 2 the state of the art sensorless control was presented. In the first sections the basic back EMF based methods where presented. The low and zero speed limitations for these methods where pointed out. One way of overcoming the problems with the back EMF based methods are to use signal injections based methods.

Chapter 3 presented a saliency model that combined the different contributors of single saliency for PMSM. The main findings in this Chapter were the 90 degrees spatial displacement between the saturation based saliency from the main and the leakage flux. A new dq-axis machine model was developed that contained the second order effects of saturation in the main and the leakage flux path. A model was derived for both radial and axial flux PMSM.

Chapter 4 presents some evaluations of the high frequency flux distribution in a PMSM with sinusoidal or transient excitation. The saliency ratio as a function of the excitation frequency was tested for excitation frequency from 100 Hz to 8100 Hz with sinusoidal excitation and with transient excitation (20 kHz equivalent). From the measurements of mutual inductance and the inductance model developed in Chapter 3 an estimate of flux linkages indicated the flux distribution in the machine. In the IPMSM a considerable amount of flux was penetrating into the rotor even for the 8.1 kHz and the transient excitation. In the axial flux PMSM the flux distribution concentrated to the leakage paths at approximately 250 Hz.

Chapter 5 presents the experimental setup. The basics on dead time effect were discussed. The main conclusion was that the distortion from the dead time in the

inverter had different size for the d- and q-axis when the drive was controlled with iq*=is and id*=0.

Chapter 6 presents the sensorless scheme based on injection of rotating high frequency sinusoidal voltage [2, 3, 4 and 13]. A new decoupling scheme was tested but not found to enhance the performance of the system. The scheme was tested with step commands in speed and with transient tests in iq reference. The scheme worked satisfactory for medium bandwidth performance. One of the main limiting factors was the impact from the dead times in the inverter.

Chapter 7 presents the sensorless scheme based on injection of pulsating high frequency sinusoidal voltage in the q-axis [22-26]. A new approach with a synchronous frame filter was developed. The usage of a synchronous frame filter for filtering of the feed back to the current regulators enabled higher bandwidths for the current regulators compared to the standard solutions. The scheme was tested with step commands in speed and with transient tests in q-axis current reference. The scheme worked satisfactory for medium bandwidth performance. The dead time effects were found to have less impact in this scheme compared to the HFCI-R scheme. The filtering technique in the position estimation loop was found to be the limiting factor in this implementation.

Chapter 8 presents a new scheme based on transient excitation [1-7]. This scheme performed better on all tests compared to the HFCI-P and HFCI-R scheme. The main difference was found to the small impact from the dead time and low demands for filtering in the position estimation loop. The scheme introduces some additional switching operations and the switching frequency was lowered to 5 kHz. If the transient excitation was applied every second switching period the average number of switching actions was the same as the HFCI-P and HCFI-R running at 10 kHz.

Chapter 9 presents a comparison of the three schemes presented in chapter 6, 7 and 8. The comparison is made from the test results and from other issues concerning integration into standard drive systems. The scheme based on transient excitation performed better on the experimental tests compared to the HFCI-R and HFCI-P. When considering the ease of integration with standard drives the HFCI-P and HFCI-R schemes are easier to implement as no special switching or sampling is needed.

Chapter 10 presents a redesign of an axial flux PMSM. Several methods for enhancing the saliency ratio were evaluated and the method based on modification of the leakage field was selected for analyses and prototyping. The modification was done by inserting semi magnetic slot wedges between the iron powder cores. The redesign had several potential synergy effects as reduced iron losses, reduced cogging torque and increased saliency ratio. A prototype was build with semi magnetic slot wedges with low relative permeability. Only the saliency ratio was tested in this work; the saliency ratio increased from un-measurable to 0.03 (500 Hz) and 0.048 (1kHz).

11.2 Future Work

There are a lot of challenges in the area of sensorless control of PMSM. The IPMSM traditionally are very well suited for injection based sensorless control. All three schemes tested in this thesis worked within the test criteria (minimum accuracy +/- 10 electrical degrees) with the IPMSM. The saliency in a surface mounted PMSM is typically smaller compared to the IPMSM. The surface mounted designs therefore offer the greatest challenge with injection based sensorless control. In order to evaluate sensorless control principles, and functionality, a wide range of topics must be cowered: control theory, power electronics, microprocessors, electromagnetism, FEM simulations, machine design and sensor technology. One person in the time frame of a PhD program cannot cover all these aspect. In this work some of the important issues are treated but by no means fully developed. This last chapter contains some suggestions to future work:

In the original plan a load machine was included in the test setup. As time elapsed the plan was changed and the inertia of the machine was used as load. If a load machine was integrated in the test setup some additional tests could be performed: the system bandwidth (obtained by sinusoidal load variations) and the load rejection properties. In future work a load machine should be included in the system.

Only two machine prototypes have been tested in this work. In future work a larger selection of machines should be evaluated in order to get a wider picture of the application range of the sensorless schemes.

Integration of the sensorless schemes into standard drive systems are not performed in this work. A combination of the injection based and the back EMF based schemes will be the goal of this activity. This task was scheduled for future work. The activity has already been started at the University with promising results (integration of TE excitation into an experimental drive with standard software). Integration of the HFCI-R scheme has already been tested with good results in [73].

Improvement of the accuracy and reduction of the noise content in current measurements are two of the most important issues when developing sensorless schemes for machines with small saliencies. Research on the current sensors, AD-converters and integrated design are key issues when developing sensorless control systems for electrical machines with limited saliency.

The implementation done in this thesis has been basic implementations with a low degree of optimalization for each scheme. For the HFCI-R based scheme the limiting

factor (at increasing bandwidth) was found to be the dead time effect from the inverter. One interesting approach could be to implement active compensation for the dead time together with the signal injection scheme (the same could also be tested for the two other schemes). In general the robustness to dead time effects is an interesting topic for future work.

The concept of including drive issues into the machine design are one of the most interesting aspects of sensorless control for machines with limited saliency. In this work a redesign approach was tested for an axial flux machine with limited saliency. Several redesign approaches was evaluated and the usage of semi magnetic slot wedges was found to be one of the most promising approaches for this prototype. The focus of this work was aimed at finding a redesign approach with low cost and preferably with synergy effects to other machine parameters. The work done in Chapter 10 showed that insertion of semi magnetic slot wedges did introduce a position dependent term in the leakage inductance. The size of the variation was not sufficient to enable sensorless control; in future work a slot wedge with higher relative permeability should be used in the machine. This may increase the saliency ratio and enable sensorless control. In addition the synergy effects on cogging toque and iron losses should be evaluated for this type of redesign.

REFERENCES

[1] Schroedl, M; *"Sensorless Control of A.C. Machines"*, Ph.D. thesis, Wien, 1992

[2] Degner, MW; *"Flux, Position, and Velocity Estimation in AC Machines Using carrier signal injection"*, Ph.D. Dissertation, Dep. Of Mechanical Engineering, University of Wisconsin - Madison 1998

[3] Corley, MJ, Lorenz, RD; "*Rotor position and velocity estimation for a salient-pole permanent magnet synchronous machine at standstill and high speeds"* Industry Applications, IEEE Transactions on , Volume: 34 Issue:4,July-Aug.1998 Page(s): 784 -789

[4] Corley, MJ, Lorenz, RD; "*Rotor position and velocity estimation for a permanent magnet synchronous machine at standstill and high speeds",* Industry Applications Conference, 1996. Thirty-First IAS Annual Meeting, IAS '96., Conference Record of the 1996 IEEE , Volume: 1 , 1996 Page(s): 36 -41 vol.1

[5] Briz, F, Degner, MW, Guerrero JM, Zamarron, A , Lorenz, RD; "*Implementation issues affecting the performance of carrier signal injection based sensorless controlled AC drives",* Industry Applications Conference, 2001. Thirty-Sixth IAS Annual Meeting. Conference Record of the2001 IEEE , Volume: 4 2001 Page(s): 2645 -2652 vol.4

[6] Leksell, M, Harnefors, L, Nee, HP; *" Machine Design Considerations for Sensorless Control of PM Motors"*, Proceedings of the International Conference on Electrical Machines, Istanbul, September 1998

[7] Wolbank, TM, Machl, J; "A modified PWM scheme in order to obtain spatial information of ac machines without mechanical sensor", 2002 IEEE, ISBN 0-7803-7404-5/02

[8] Fitzgerald, A E, Kigsley, Jr.C, Umans, SD; *"Electrichal Machinery"*, McGraw-Hill Inc. 1983

[9] Buhler, HR; *"Einfurung in die Theorie der geregelter Drehstromantriebe"* Band 1: Grundlagen. Band 2:Anwendungen. Birkhauser Verlag, Basel 1977

[10] Nilsen, R; *"Modelling, Identification and control of Induction Machine"*, Doktor Ingeniør-avhandling, The Norwegian Institute of Technology (NTH) 1987

[11] Åndanes, A K; *"High Efficiency, High Performance permanent magnet synchronous motor dirves"*, Doktor Ingeniør-avhandling, The Norwegian Institute of Technology (NTH) 1991

[12] Vas, P; "Sensorless Vector And Direct Torque Control", Oxford University Press 1998

[13] Jansen, PL; *"The Integration of State Estimation, Control, and Design for Induction Machines"*, Ph.D. Dissertation, Dept. of Electrical and Computer Engineering, University of Wisconsin – Madison, 1993.

[14] Ovrebo, S, Nilsen R; "New self sensing scheme based on INFORM,

heterodyning and Luenberger observer", EMDC 2003 Madison, Wisconsin, USA

[15] Hartman, C; *"Optimal Design av aksialmagnetiserte PM maskiner"*, Master thesis, Norwegian University of Science and Technology 1999

[16] Gabriel, R; *"Feldorientierte Regulerung einer Asynchronmaschine mit einem Mikrorechner"*, Dr.Ing Dissertation, University Carolo-Wilhelmina, Braunschweig,, Germany 1982

[17] Blaschke, F; "Method and Apparatus for determining the initial rotor angle in a rotating field machine", US patent 3,909,688 30.Sept 1975

[18] Harnefors, L, Nee, HP; *"A General Algorithm for Speed and Position Estimation of AC Motors"*, IEEE transactions on Industrial Electronics vol 47,No.1, Feb2000

[19] Chen, Z, Tomita, M, Ichikawa, S, Doki, S, Okuma, S; *"Sensorless Control of Interior Permanent Magnet Synchronus Motor by Estimation of an extended Electromotive Force"*, Industry Applications Conference, 2000. Conference Record of the 2000 IEEE , Volume: 3 , 8-12 Oct. 2000, Pages:1814 - 1819 vol.3

[20] Kim, H, Harke, MC, Lorenz, RD; *"Sensorless Control of Interior Permanent Magnet Machine Drives with Zero-Phase-Lag Position Estimation"*, Industry Applications Conference, 2002. 37th IAS Annual Meeting. Conference Record of the , Volume: 3 , 13-18 Oct. 2002 Pages:1661 - 1667 vol.3

[21] Cilia, J, Asher, GM, Bradley, KJ; "Sensorless position detection for vector controlled induction motor drives using an asymmetric outer-section cage", proc. Of IEEE-IAS 1996 pp 286-292

[22] Jung, H, Sul, S; "Sensorless Field-Oriented Control of an Induction Machine by High-Frequency Signal Injection", IEEE transactions Industry Applications 1999

[23] Ha, J, Sul, S; "*Sensorless field orientation control of an induction machine by high frequency signal injection"*, Industry Applications Conference, 1997. Thirty-Second IAS Annual Meeting, IAS '97

[24] Kang, S, Ha, J, Sul, S; "*Position controlled synchronous reluctance motor without rotational transducer"*, Industry Applications Conference, 1998. Thirty-Third IAS Annual Meeting. The 1998 IEEE

[25] Ha, J, Ide, K, Sawa, T, Sul, S; *"Sensorless position control and initial position estimation of an interior permanent magnet motor"*, Thirty-Sixth IAS Annual Meeting. Conference Record of the 2001 IEEE

[26] Jang, J, Sul, S, Ha, J, Ide, K, Sawamura, M; *"Sensorless drive of SMPM motor by high frequency signal injection"* APEC 2002. Seventeenth Annual IEEE , Volume: 1 , 10-14 March 2002

[27] Hu, J, Wu, B; "New integration algorithms for estimating motor flux over a wide speed range" IEEE Trans. Power Electron. 1998

[28] Consoli, A, Scarcella, G, Testa, A; "A New Zero-Frequency Flux-Position Detection Approach for Direct-Field-Oriented-Control Drives", IEEE Trans. on industry appl. 2000

[29] Briz, F, Diez, A, Degner, MW; "Dynamic operation of carrier signal injection based sensorless, direct field oriented AC drives" IEEEIndustry Applications Conference, 1999

[30] Linke, M, Kennel, R, Holtz J; "Sensorless Speed and Position Control of Synchronous Machines using Alternating Carrier Injection", IEMDC Madison 2003

[31] Moreira, JC, Lipo, TA; "Direct field orientation control using the third harmonic component of the stator voltage", Proc. ICEM'90

[32] Kreindler, L, Moreira, JC, Testa, A, Lipo, T A; "Direct field orientation controller using the stator phase voltage third harmonic" , Conf. Rec. IEEE-IAS Annu. Meeting 1992

[33] Ogasawara, S, Akagi, H; "Implementation and position control performance of a position-sensorless IPM motor drive system based on magnetic saliency" , IEEE Transactions on Industry Applications, 1998

[34] Cilia, J ;"Sensorless Speed and Position Control of Induction Motor Drives", PhD. Thesis at the University of Nottingham , UK, October 1997

[35] Teske, N; "Sensorless Position Control of Induction Machines using High Frequency Signal Injection", PhD. Thesis at the University of Nottingham , UK, October 2001

[36] Ovrebo, S, "Comparison of excitation signals for low and zero speed estimation of the rotor position in a axial flux PMSM", NORPIE2002

[37] Ha, J, Jang, J, Sul, S; "Design and Selection of AC Machines for Saliency-Based Sensorless Control" IEEE 2002

[38] Wolbank, TM, Machl, J; "Anisotropy in Induction Machine Lamination and its Influence on Mechanical Sensorless Control and Conditioning Monitoring", EPE Toulouse 2003-10-22

[39] Jansen, PL, Corley, MJ, Lorenz, RD; "Flux, Position, and Velocity estimation in AC machines at zero and low speed via tracking of high frequency saliencies" EPE 1995, Sevilla

[40] Salon, S, Burow, D, DeBortoli, M, Slavik, C; "*Effects of slot closure and magnetic saturation on induction machine behavior Magnetics*", IEEE Transactions on , Volume: 30 , Issue: 5 , Sep 1994, Pages:3697 – 3700

[41] Anazawa, Y, Kaga, A, Akagami, H, Watabe, S, Makino, M; *"Prevention of harmonic torques in squirrel cage induction motors by means of soft ferrite magnetic wedges"*, Magnetics, IEEE Transactions on , Volume: 18 , Issue: 6 , Nov 1982 Pages:1550 – 1552

[42] Caricchi, F, Capponi, FG, Crescimbini, F, Solero, L; "Experimental study on reducing cogging torque and core power loss in axial-flux permanent-magnet machines with slotted winding", Industry Applications Conference, 2002. 37th IAS Annual Meeting. Conference Record of the , Volume: 2 , 13-18 Oct. 2002

Pages:1295 - 1302 vol.2

[43] Kvåle, LO; *"Identifying magnetic salience with the Finit Element Method"*, Master Thesis, Norwegian University of Science and Technology, 2003

[44] Kvåle, LO, Ovrebo, S, Nilssen, R; *"Identifying Magnetic Saliency with the Finite Element Method"*, The Nordic MATLAB Conference 2003, Copenhagen, Denmark, October 21-22, 2003

[45] Aime, ML, Degner, M.W, Lorenz, RD; *"Saturation measurements in AC machines using carrier signal injection"*, IAS, 1998. The 1998 IEEE , Volume: 1 , 12-15 Oct. 1998 Pages:159 - 166 vol.1

[46] Leppanen, VM; "Low-frequency signal-injection method for speed sensorless vector control of induction motors", PhD thesis, Helsinki University of Technology 2003

[47] Kenny, BH; "Deadbeat Direct Torque Control of Induction Machines using Self-Sensing at Low and Zero Speed", PhD Thesis, University of Wisconsin-Madison, USA, 2001

[48] Sng, EKK, Ah-Choy, L, Lipo, TA; *" New observer-based DFO scheme for speed sensorless field-oriented drives for low-zero-speed operation"*, Power Electronics, IEEE Transactions on , Volume: 13 , Issue: 5 , Sept. 1998 Pages:959 – 968

[49] Kereszty, T, Leppanen, VM, Luomi, J; "Sensorless Control of Surface Magnet Sychronous Motors at Low Speeds Using Low-Frequency Signal Injection", IAS Salt Lake City 2003, Pages: 1150-1156

[50] Luukko, J; "Direct Torque Control of Permanent Magnet Syncronous Machines – Analyses and Implementation", PhD thesis, Lappenranta University of Technology 2000

[51] Nestli, TF, Nilsen, R; *"Evaluation and comparison of predictor models for rotor flux calculation in induction motors"*, Power Electronics Specialists Conference, PESC '94 Record., 25th Annual IEEE , 20-25 June 1994 Pages:729 - 737 vol.1

[52] Hasse, K; "Zur Dynamik drehzahlgreregelter Antriebe mit stromrichtergespeisten Asynchronkurzschublaufermotoren", Dissertation, Darmstadt, Germany, 1969

[53] Blaschke, F; "Das Verfahren der Feldorienterung zur Regelung der Drenfeldmashine" Dissertation, Erlangen, Germany, 1974

[54] Gullvik, W; *"Sensorløs styring av Permanentmagnetisert synkronmaskin"* , Master thesis, Norwegian University of Science and Technology, Trondheim, Norway 2000

[55] Nagel, NJ; *"Complex Vector Analysis and Sensorless Control of a Switched Reluctance Motor"*, PhD Dissertation, Dep. Of Mechanical Engineering, University of Wisconsin – Madison, 1999

[56] Harke, M; *"Spatial Modelling And State Estimation of a Universal Motor"*, Master Thesis, Dep. Of Mechanical Engineering, University of Wisconsin – Madison, 1999

[57] Nestli, TF; *"Modelling and identificatation of induction machines"*, PhD thesis, NTH, Trondheim, Norway, 1995

[58] Ogasawara, S, Akagi, H; *"An approach to real-time position estimation at zero and low speed for a PM motor based on saliency",* Industry Applications, IEEE Transactions on , Volume: 34 , Issue: 1 , Jan.-Feb. 1998 Pages:163 - 168

[59] Ogasawara, S, Akagi, H; " Implementation and position control performance of a position-sensorless IPM motor drive system based on magnetic saliency", Industry Applications, IEEE Transactions on , Volume: 34 , Issue: 4 , July-Aug. 1998 Pages:806 – 812

[60] Robeischl, E, Schroedl, M, Salutt, K; *"Improwed INFORM-measurements sequence and evaluation for senseless permanent magnet synchronous motor drives"*, 10th International Power Electroncs and Motion Control Conference, 9-11 September 2002, Cavtat Dubrovnik, Croatia

[61] Robeischl, E, Schroedl, M; *"Optimized INFORM-measurement sequence for sensorless PM synchronous motor drives with respect to minimum current distortion",* Industry Applications Conference, 2002. 37th IAS Annual Meeting. Conference Record of the , Volume: 1 , 13-18 Oct. 2002 Pages:92 - 98 vol.1

[62] Nandi, S, Toliyat, HA, Parlos, AG; *"Performance analysis of a single phase induction motor under eccentric conditions ",* Industry Applications Conference, 1997. Thirty-Second IAS Annual Meeting, IAS '97., Conference Record of the 1997 IEEE , Volume: 1 , 5-9 Oct. 1997 Pages:174 - 181 vol.1

[63] Ljokelsoy, K., Kolstad, H; *"Testprotokoll – 20 kW IGBT omformer"*, Sintef Enegiforskning AS, Trondheim, Norway, 2001

[64] Gyselinck, J, Vandevelde, L, Melkebeek, J, Dular, P, Henrotte, F, Legros, W; *"Calculation of eddy currents and associated losses in electrical steel laminations"*, IEEE Transactions on Magnetics, Volume: 35 , Issue: 3 , May 1999 Pages:1191 - 1194

[65] Worley, AC, Stephenson, JM;*"Eddy current behaviour in saturating laminations with impressed flux waveforms"*, Electrical Machines and Drives, 1993. Sixth International Conference on (Conf. Publ. No. 376) , 8-10 Sep 1993 ,Pages:229 – 233

[66] Ovrebo, S, Nilsen R; "New self sensing scheme based on INFORM, heterodyning and Luenberger observer", AUPEC 2003

[67] Yoshiaki, T; "Electrichal angle detecting device and synchronous motor drive device", European Patent Application EP0793337A2, 2002

[68] Mohan, N, Undeland, TM, Robbins, B; *"Power Electronics"* Second Edition, John Wiley & Sons, INC, 1989

[69] Holtz, J;*"Pulsewidth modulation for electronic power conversion"*, Proceedings of the IEEE , Volume: 82 , Issue: 8 , Aug. 1994 Pages:1194 – 1214

[70] Weichbold, P, Raumer, T; "Influence of Dead time Effects of PWM-VSI on Current Control", EPE 2001

[71] Wolfe, J; *"dB-filter Caracteristics"*, The University of New South Wales,Australia, web page; http://www.phys.unsw.edu.au/~jw/dB.html#definition

[72] Rieder, UH, Schroedl, M;"Optimization of Saliency Effects of External Rotor Permanent Magnet Synchronous Motors with Respect to Enhanced INFORM-Capability for Sensorless Control", EPE 2003

[73] Wallmark, O;"Control of Permanent-Magnet Sychronous Motors in Hybrid-Electric Vehicle Applications", Licenciate Thesis, Chalmers University of Technology, Sweden 2004

[74] Nilsen, R; "Elektriske Motordrifter", Compendium in class TET4120, NTNU, Trondheim, Norway 2004

[75] Myklebust, T. A;"Sensorless Control of PMSM Evaluating Magnetic Fields", Master Student Project Work NTNU, Trondheim, Norway, 2002

APPENDIX

A MACHINE MODELLING

A.1 Machine modelling

This appendix summarises the derivation of the machine equation in detail. It contains all transformations needed to transform a machine model from a per phase description to two axis representation in rotor reference frame or any other general reference frame. The machines used in this work have Y-connected stator windings. The neutral point is isolated thus no zero sequence current flows in the machine. The zero sequence quantities are therefore not included in the machine equations.

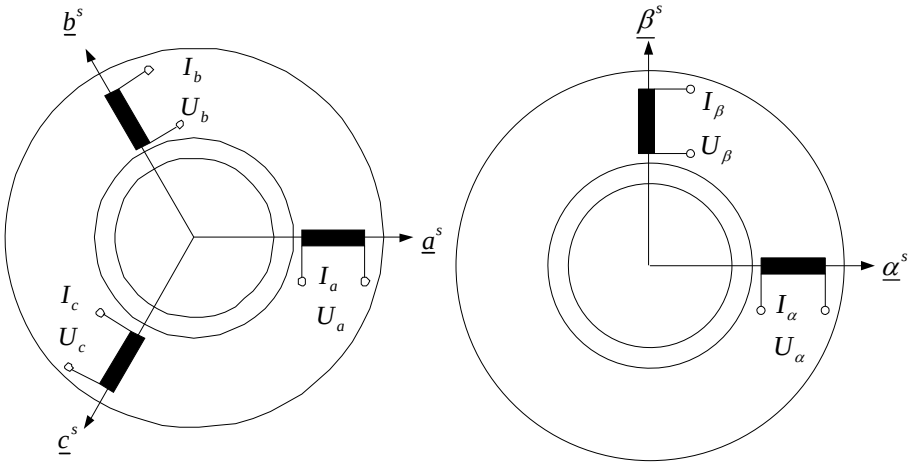

Figure 11.1 Three phase left, stator 2 axis representation right

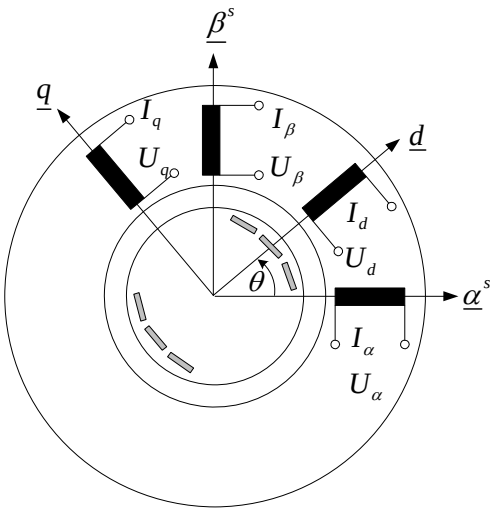

Figure 11.2 Relationship between $\alpha\beta$ and dq reference system

In literature several different notations are used to describe PMSM. For the rotating reference system fixed to the rotor the index d or q will be used. For the two axes reference system fixed to the stator the index α^s or β^s will be used. Figure 11.2 shows the relationship between the two reference systems. The currents in the tree phases are 120 degrees displaced from each other. The tree phase currents form a space vector in the machine. In this thesis a scaling factor (2/3) will be used so the space vector will have the same value as the phase current.

$$\underline{I}_s^S = \frac{2}{3}(I_{sa}^S \underline{a}^S + I_{sb}^S \underline{b}^S + I_{sc}^S \underline{c}^S) \tag{A.1}$$

During transformations it is useful to represent the equations on matrix form, defining;

$$\underline{I}_s^S = \begin{bmatrix} I_{sa}^S & I_{sb}^S & I_{sc}^S \end{bmatrix}^T \tag{A.2}$$

$$\underline{I}_s^s = \begin{bmatrix} I_{s\alpha}^s & I_{s\beta}^s \end{bmatrix}^T \tag{A.3}$$

$$\underline{I}_s^r = \begin{bmatrix} I_d & I_q \end{bmatrix}^T \tag{A.4}$$

$$\underline{U}_s^S = \begin{bmatrix} U_{sa}^S & U_{sb}^S & U_{sc}^S \end{bmatrix}^T \tag{A.5}$$

$$\underline{U}_s^s = \begin{bmatrix} U_{s\alpha}^s & U_{s\beta}^s \end{bmatrix}^T \tag{A.6}$$

$$\underline{U}_s^r = \begin{bmatrix} U_d & U_q \end{bmatrix}^T \tag{A.7}$$

$$R_s^S = \begin{bmatrix} R_s & 0 & 0 \\ 0 & R_s & 0 \\ 0 & 0 & R_s \end{bmatrix} \tag{A.8}$$

On matrix form the stator equations become;

$$\underline{U}_s^S = \underline{R}_s^S \underline{I}_s^S + \frac{d\underline{\Psi}_s^S}{dt} \tag{A.9}$$

The flux linkages

$$\underline{\Psi}_s^S = \underline{L}^S \underline{I}_s^S + \begin{bmatrix} \cos(\theta) \\ \cos(\theta - 120) \\ \cos(\theta + 120) \end{bmatrix} \Psi_m \tag{A.10}$$

Defining the transform matrix between abc system and $\alpha\beta$ system;

$$T_{ss}^s = \begin{bmatrix} \frac{2}{3} & -\frac{1}{3} & -\frac{1}{3} \\ 0 & \frac{1}{\sqrt{3}} & \frac{1}{\sqrt{3}} \end{bmatrix} \tag{A.11}$$

The inverse of this matrix define the transformation between $\alpha\beta$ system and abc system;

$$\underline{T}_{ss}^{-s} = \begin{bmatrix} 1 & 0 \\ -\frac{1}{2} & \frac{\sqrt{3}}{2} \\ -\frac{1}{2} & -\frac{\sqrt{3}}{2} \end{bmatrix} \tag{A.12}$$

From $\alpha\beta$ system to dq system the transform matrix becomes;

$$\underline{T}_{ss}^r = \begin{bmatrix} \cos(\theta) & \sin(\theta) \\ -\sin(\theta) & \cos(\theta) \end{bmatrix} \tag{A.13}$$

The inverse matrix describes the transformation between the dq system and the $\alpha\beta$ system;

$$\underline{T}_{ss}^{-r} = \begin{bmatrix} \cos(\theta) & -\sin(\theta) \\ \sin(\theta) & \cos(\theta) \end{bmatrix} \tag{A.14}$$

The direct transformation between the abc system and the dq system becomes;

$$\underline{T}^{k} = \underline{T}_{ss}^{s} \cdot \underline{T}_{ss}^{r} = \begin{bmatrix} \frac{2}{3}\cos(\theta_r) & \frac{2}{3}\cos(\theta_r - 120°) & \frac{2}{3}\cos(\theta_r + 120°) \\ -\frac{2}{3}\sin(\theta_r) & -\frac{2}{3}\sin(\theta_r - 120°) & -\frac{2}{3}\sin(\theta_r + 120°) \end{bmatrix} \quad \text{(A.15)}$$

The inverse of this matrix gives the transformation between the dq and abc system;

$$\underline{T}^{-k} = \begin{bmatrix} \cos(\theta_r) & -\sin(\theta_r) \\ \cos(\theta_r - 120°) & -\sin(\theta_r - 120°) \\ \cos(\theta_r + 120°) & -\sin(\theta_r + 120°) \end{bmatrix} \quad \text{(A.16)}$$

$$\underline{U}_s^S = \underline{T}^{-k}\underline{U}_s^r \quad \text{(A.17)}$$

$$\underline{I}_s^S = \underline{T}^{-k}\underline{I}_s^r \quad \text{(A.18)}$$

$$\underline{\Psi}_s^S = \underline{T}^{-k}\underline{\Psi}_s^r \quad \text{(A.19)}$$

If (A.17), (A.18) and (A.19) are substituted into (A.9) we get:

$$\underline{T}^{-k}\underline{U}_s^r = \underline{R}^S\underline{T}^{-k}\underline{I}_s^r + \frac{d}{dt}(\underline{T}^{-k}\underline{\Psi}_s^r) \quad \text{(A.20)}$$

Multiplying with $\underline{T}^{k}$ leaves the expression for the voltage equation in dq reference system;

$$\underline{U}_s^r = \underline{T}^{k}\underline{R}_s^S\underline{T}^{-k} + \underline{T}^{k}\frac{d}{dt}(\underline{T}^{-k}\underline{\Psi}_s^r) \quad \text{(A.21)}$$

$$\underline{U}_s^r = \underline{T}^{k}\underline{R}_s^S\underline{T}^{-k}\underline{I}_s^r + \underline{T}^{k}\frac{d\underline{T}^{-k}}{dt}\omega\underline{\Psi}_s^r + \frac{d}{dt}\underline{\Psi}_s^r \quad \text{(A.22)}$$

$$\underline{U}_s^r = \underline{R}_s^r\underline{I}_s^r + \underline{J}\omega\underline{\Psi}_s^r + \frac{d}{dt}\underline{\Psi}_s^r \quad \text{(A.23)}$$

$$\underline{R}_s^r = \underline{T}^{k}\underline{R}_s^S\underline{T}^{-k} = \begin{bmatrix} R_s & 0 \\ 0 & R_s \end{bmatrix} \quad \text{(A.24)}$$

$$\underline{J} = \underline{T}^{k} \frac{d\underline{T}^{-k}}{dt} = \begin{bmatrix} 0 & -1 \\ 1 & 0 \end{bmatrix} \tag{A.25}$$

$$\underline{\Psi}_s^r = \underline{T}^{k} \underline{\Psi}_s^S = \underline{T}^{k} \underline{L}_s^S \underline{T}^{-k} \underline{I}_s^r = L_s^r \underline{I}_s^r \tag{A.26}$$

The voltage equations are given for convenience in the PU system for rotor and stationary reference frame. For a symmetrical PMSM:

$$\underline{u}_s^r = \begin{bmatrix} u_d \\ u_q \end{bmatrix} = \begin{bmatrix} r_s + s\frac{1}{\omega_N} x_s & -nx_s \\ nx_s & r_s + s\frac{1}{\omega_N} x_s \end{bmatrix} \begin{bmatrix} i_d \\ i_q \end{bmatrix} + \begin{bmatrix} 0 \\ n \cdot \psi_m \end{bmatrix} \tag{A.27}$$

$$\underline{u}_s^s = \begin{bmatrix} u_\alpha \\ u_\beta \end{bmatrix} = \begin{bmatrix} r_s + s\frac{1}{\omega_N} x_s & 0 \\ 0 & r_s + s\frac{1}{\omega_N} x_s \end{bmatrix} \begin{bmatrix} i_\alpha \\ i_\beta \end{bmatrix} + n \cdot \psi_m \begin{bmatrix} -\sin\theta \\ \cos\theta \end{bmatrix} \tag{A.28}$$

s represents the derivative operator. For a IPMSM the equation becomes:

$$\underline{u}_s^r = \begin{bmatrix} u_d \\ u_q \end{bmatrix} = \begin{bmatrix} r_s + s\frac{1}{\omega_N} x_d & -nx_q \\ nx_d & r_s + s\frac{1}{\omega_N} x_q \end{bmatrix} \begin{bmatrix} i_d \\ i_q \end{bmatrix} + \begin{bmatrix} 0 \\ n\psi_m \end{bmatrix} \tag{A.29}$$

$$\underline{u}_s^s = \begin{bmatrix} u_\alpha \\ u_\beta \end{bmatrix} = \begin{bmatrix} r_s + s\frac{1}{\omega_N} x_\alpha & -nx_{\alpha\beta} \\ nx_{\alpha\beta} & r_s + s\frac{1}{\omega_N} x_\beta \end{bmatrix} \begin{bmatrix} i_\alpha \\ i_\beta \end{bmatrix} + n\psi_m \begin{bmatrix} -\sin\theta \\ \cos\theta \end{bmatrix} \tag{A.30}$$

$$x_\beta = \sum x - \Delta x \cos(2\theta) \tag{A.31}$$

$$x_\alpha = \sum x + \Delta x \cos(2\theta) \tag{A.32}$$

$$x_{\alpha\beta} = \Delta x \sin(2\theta) \tag{A.33}$$

Where:

$$x_d = \frac{\omega_N L_d}{Z_{base}} = \frac{(L_{s\sigma} + \frac{3}{2}(L_{s0} + L_g))\omega_N I_{base}}{U_{base}} \tag{A.34}$$

$$x_q = \frac{\omega_N L_q}{Z_{base}} = \frac{(L_{s\sigma} + \frac{3}{2}(L_{s0} - L_g))\omega_N I_{base}}{U_{base}} \tag{A.35}$$

$$\sum \mathrm{x} = \frac{\mathrm{x_d} + \mathrm{x_q}}{2} \tag{A.36}$$

$$\sum \mathrm{x} = \frac{\mathrm{x_d} - \mathrm{x_q}}{2} \tag{A.37}$$